RADIAL FLOW EFFECTS ON A RETREATING ROTOR BLADE

A Thesis
Presented to
The Academic Faculty

by

Vrishank Raghav S

In Partial Fulfillment
of the Requirements for the Degree
Doctor of Philosophy in the
School of Aerospace Engineering

Georgia Institute of Technology
May 2014

RADIAL FLOW EFFECTS ON A RETREATING ROTOR BLADE

Approved by:

Dr. Narayanan Komerath, Advisor
School of Aerospace Engineering
Georgia Institute of Technology

Dr. Karim Sabra
School of Mechanical Engineering
Georgia Institute of Technology

Dr. Dimitri Mavris
School of Aerospace Engineering
Georgia Institute of Technology

Dr. Peter Lorber
Sikorsky Corporation
United Technologies Corporation

Dr. Mark Costello
School of Aerospace Engineering
Georgia Institute of Technology

Date Approved: 6 January 2014

Dedicated to my family

ACKNOWLEDGEMENTS

This thesis would not have been possible without the selfless support of several people in my life. First, I would like to thank my parents and my family for their support throughout my endeavors. They have always inspired me to take up challenges and prepared me for a good life.

I thank my advisor Dr. Narayanan Komerath for being a constant source of inspiration and encouragement through out this work. His role has been imperative in the process of comprehension of the varied aspects of this work. Dr. Komerath has always been willing to listen and discuss the challenges in this work, I could not have asked for better advisor. His invaluable guidance, timely advice and enthusiasm have made this study an enriching learning experience and have enabled the successful completion of this thesis.

I also thank my committee members Dr. Dimitri Mavris, Dr. Mark Costello from the school of aerospace engineering, Dr. Karim Sabra from the school of mechanical engineering, and Dr. Peter Lorber from Sikorsky corporation for their time and valuable inputs towards improvement of this work. I would also like to thank Dr. James Gregory from the Ohio State University and Dr. Tom Thompson for their comments and feedback on my work. Dr. Thomas Doligalski and Dr. Fredrick Ferguson from the Army Research Office (ARO) the funding agency for this work for their constant financial support of my work.

I acknowledge the help of my colleagues in the wind tunnel. The graduate students who helped me with the experimental setups and data acquisition throughout the five years of my work down in the wind tunnel: Dustin Teuscher, Laura Hershberger, Felipe Ortega, Rafael Lozanno, Alex Forbes, Natasha Barbely, and Michael Mayo. The countless undergraduate students who helped in data acquisition and data reduction in the wind tunnel: Nicholas Motahari, Brandon Liberi, and Roger Lascorz to mention a few.

I thank Mr. Scott Eliot, Mr. Scott Moseley and Mr. Miller Russell from the aerospace workshop, whose help went a long way in assisting the completion of this work. Moreover

their company while working long hours in the basement definitely made the work seem effortless.

The extensive PIV measurements, post-processing and data analysis would not have been possible without the help and guidance of Dr. Steve Anderson and Dr. Callum Gray from LaVision Inc.

Finally, my acknowledgments will not be complete without thanking my friends for making my stay in Atlanta very memorable.

TABLE OF CONTENTS

LIST OF TABLES

LIST OF FIGURES

SUMMARY

Dynamic stall and reverse flow occurring on the retreating rotor blades of a helicopter rotor or a horizontal axis wind turbine operating at a yaw angle is a primary limitation on the performance of the associated vehicle or structure. Hitherto most of the studies have been conducted on two-dimensional airfoils and three-dimensional wings, which do not represent the reality of rotating blades which are subject to the coupled effects of reactive centrifugal and Coriolis forces unique to the rotating environment. These forces are expected to drive a strong radial flow, which in turn is expected to affect the aerodynamic phenomena on the retreating blade. However, the effect of centrifugal force induced span-wise flow (radial flow) on the aerodynamic phenomena on a retreating blade is not well understood and remains elusive.

The focus of this thesis is to investigate the effects of radial flow on a retreating rotor blade at different operating conditions. Dynamic stall and reverse flow are two separate aerodynamic phenomenon investigated in this work. Experiments are conducted on a rigid teetering two bladed rotor at high advance ratio in a low speed wind tunnel. Particle Image Velocimetry (PIV) measurements are used to quantify the flow field on the rotating blade. The velocity fields of the dynamic stall event from initiation of separation ($\psi = 220°$) to reattachment ($\psi = 320°$) is investigated. In particular the flow field at the yaw angle of $\psi = 270°$ is investigated in detail to understand the effect of "pure" radial flow induced only due to centrifugal forces. The results indicate that the radial flow causes the phase-averaged dynamic stall vortex to be pinned to the surface. In addition, cycle-to-cycle variations in the dynamic stall event over the rotating blade cause the phase-averaged vortex to appear spatially diffused.

The above results prompted the investigation of the radial velocity field during the dynamic stall event. Again, the $\psi = 270°$ was chosen, because this position allows for the decoupling of the radial flow due to yaw and radial flow due to centrifugal forces. Contrary

to the expected increase in mean radial velocity on moving outboard on the rotating blade, the measurements suggested that the mean radial velocity attenuated on moving outboard. Further investigations elucidated that an apparent shear layer instability was the physical mechanism of the attenuation of the mean radial velocity on moving outboard. In addition, quantitative comparisons indicated that the instability and associated co-rotating vortical structures were of first order importance in the radial velocity field. Hence these features must have a significant effect on the evolution of lift and pitching moment during dynamic stall.

Since the radial flow was shown to be of first order importance on a rotating blade undergoing dynamic stall. A quasi-analytical way to predict these co-rotating structures would be useful in understanding the role of these structures in a separated flow field. I hypothesized that if structures similar to those observed on the rotor could be found over a fundamental flow field such as over a rotating disk, that would open the way to link the rotor blade phenomena to quasi-analytical solutions and hence derive fundamental relationships. PIV measurements over a rotating disk in separated uniform stream showed the existence of co-rotating vortical structures. The co-rotating vortical structures were shown to occur at the upper edge of the radial velocity profile emanating from the inflection point of the profile. This suggests that this shear layer instability of the radial flow is a fundamental behavior of the flow generated due to centrifugal forces and should apply to radial flow on rotating blades. This investigation concludes the first part of the thesis which was focused studying the effect of radial flow on dynamic stall over a retreating blade.

The second part of the thesis focuses on the reverse flow on a retreating rotor blade. Aerodynamic load measurements, surface flow visualization via tufts and PIV is used to understand the effect of radial flow on reverse flow over a retreating rotor blade. The main hypothesis being tested here is the existence of vortex-induced lift on a yawed blade in reverse flow. Initially, experiments were conducted on a static blade to decouple the effects of rotation induced phenomena from yaw induced phenomena. Aerodynamic load measurements over a yawed static blade indicated that the lift-curve slope in reverse flow was significant. Surface flow visualization via tufts indicated the existence of a vortex

over the yawed static blade. Next, PIV measurements were gathered over the rotating blade to check for the existence of the vortex on the rotating blade between $240° \leq \psi \leq 270°$. The measurements clearly indicated the effect of radial flow which was to delay separation (formation of the vortex) to a higher angle of attack.

Nomenclature

Variables

α	Angle of attack of static yawed blade	deg
α_r	Angle of attack of rotor setup	deg
α_w	Angle of attack of wind turbine	deg
β_r	Blade pitch of rotor setup	deg
β_w	Blade pitch of wind turbine	deg
η	Non dimensional height above the surface	
Γ	Circulation	m^2/s
γ	Wind turbine yaw angle	deg
Γ_1	Normalized angular momentum	
μ_a	Advance ratio of rotor	
μ_d	Advance ratio of disk	
ω	Vorticity	1/s
ϕ_r	Induced angle of attack on rotor setup	deg
ϕ_w	Induced angle of attack on wind turbine	deg
ψ	Azimuthal angle	deg
ψ	Azimuthal location	deg
σ	Random error	
σ_i	Random measurement error in the image plane	

τ_s	Relaxation time for seed particles	s
C_D	Coefficient of drag	
C_L	Coefficient of lift	
C_M	Coefficient of moment	
d_p	Particle image diameter	
k	Reduced frequency	
r	Radial location	m
Re	Reynolds number	
u, v, w	Velocity component in x, y, z directions respectively	m/s
U_∞/V_∞	Freestream velocity for rotor setup	m/s
U_p	Seed particle velocity	m/s
U_r/V_r	Radial velocity	m/s
U_{ip}	Maximum in-plane component of flow velocity in PIV measurements	m/s
V_n	Velocity component normal to the TPP	m/s
V_c	Velocity component in the plane of the wind turbine	m/s
V_{TPP}	Velocity component parallel to the TPP for rotor setup	m/s
V_t	Tangential component of velocity to wind turbine blade	m/s
V_w	Freestream velocity for wind turbine	m/s
W_p	Maximum out-of-plane component of the flow velocity	m/s
x	Chordwise location	m
y	Spanwise location	m

z	Axial location	m
Z_s	Light sheet thickness	mm
$C_{L\alpha}$	Lift curve slope	
M	Magnification of the images in PIV	

Constants

μ	Absolute viscosity of air	Pa-s
ν	Kinematic viscosity of air	m^2/s
Ω	Rotation rate of rotor	rad/s
Ω_d	Rotation rate of disk	rad/s
ω_f	Flapping frequency	Hz
ρ	Density of ambient air	kg/m^3
ρ_p	Seed particle density	kg/m^3
a_o	Wind deficit factor	
c	Chord length	m
c_e	Empirical constant for random error	
R	Rotor radius	m
T	Temperature of ambient air	K

Abbreviations

DS Dynamic Stall

DSV Dynamic Stall Vortex

HARF High Advance Ratio Facility

$HAWT$ Horizontal Axis Wind Turbine

NAM Normalized Angular Momentum

PIV Particle Image Velocimetry

POD Proper Orthogonal Decomposition

RMS Root Mean Square

$SPIV$ Stereoscopic Particle Image Velocimetry

TPP Tip Path Plane

$VAWT$ Vertical Axis Wind Turbine

CHAPTER I

INTRODUCTION

The main rotor of a conventional helicopter is the primary source of propulsion, lift and control of the helicopter. The aerodynamics of the main rotor of a conventional helicopter in forward flight is intricate and it is well described by Figure 1 adopted from Bowles [9] and modifications adapted from Conlisk [24].

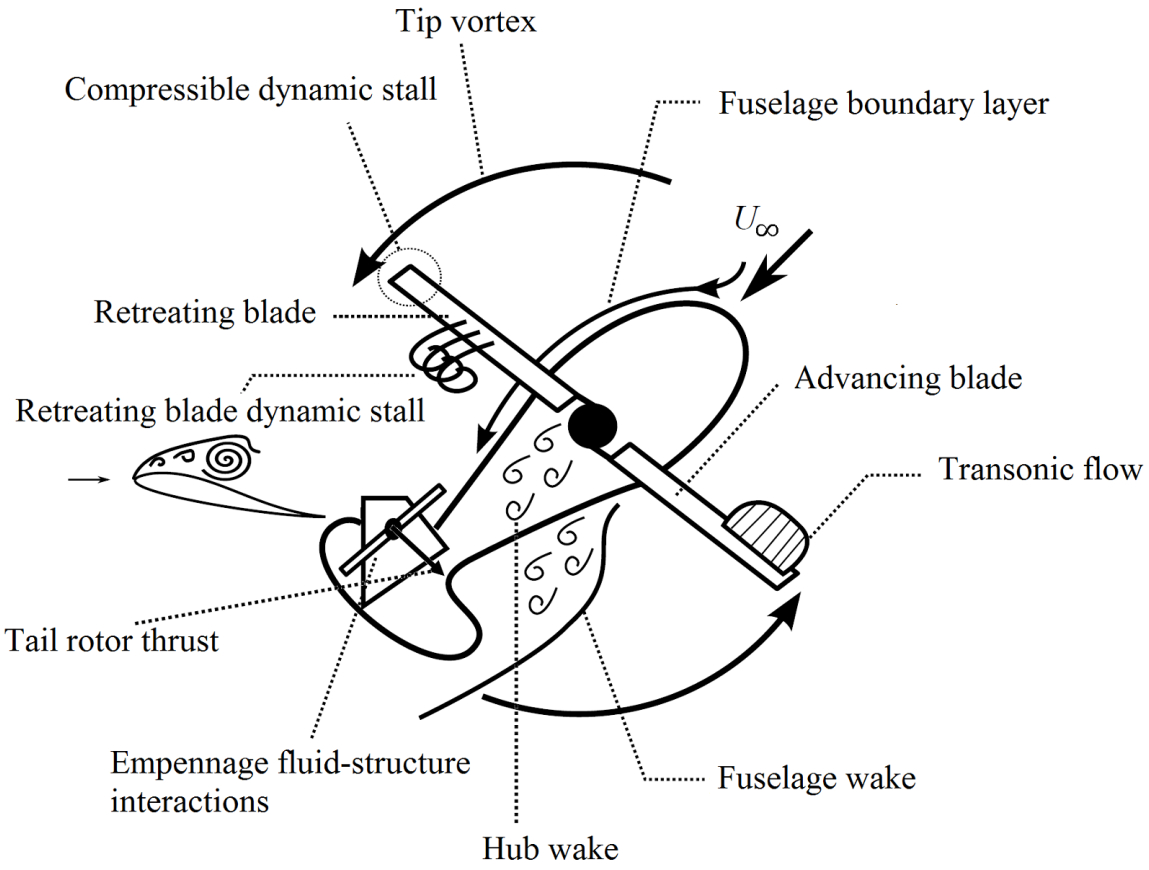

Figure 1: Various aerodynamic phenomena on a helicopter rotor in forward flight adopted from Bowles [9]

The focus of this thesis is on the retreating part of the rotating blades in forward flight. The retreating rotor blades experience two distinct aerodynamic regimes based on

the (advance ratio (μ_a) where advance ratio is defined as the ratio of forward flight speed to the rotation tip speed of the rotor). a) For $0.25 \leq \mu_a \leq 0.5$ the retreating rotor blade experiences dynamic stall, which is well known to be a primary limitation of the performance and handling qualities of a helicopter. b) For $\mu_a \geq 0.5$ the retreating rotor blade experiences significant reverse flow, where the effective freestream is directed from the trailing edge to the leading edge of the blade. Both these phenomena have been reported to occur on rotor blades of HAWT in yaw as well. This work investigates the radial flow effects on rotating blades with an emphasis on rotorcraft operations, which include: a) Helicopters at high forward flight velocity (high advance ratio). b) Helicopters under rapid maneuvering flight or in high-altitude flight. c) HAWT operating in yaw. Due to the spectrum of relevance fulfilling the objectives of this thesis would be a significant contribution to the rotorcraft community. The following sections briefly introduce each flow regime and its significance in limiting the operating conditions of rotorcraft.

1.1 Dynamic Stall

Dynamic stall manifests itself on wings experiencing high rates of unsteady pitching or plunging motion, causing angle of attack to reach significantly beyond the static stall angle. This results in the dynamic delay of stall, followed by a large drop in lift and excursions in pitching moment. When angle of attack drops down again, flow reattachment is delayed in a hysteresis loop. This phenomenon is predominantly seen on helicopter rotor blades, rapidly maneuvering fixed-wing aircraft, wind turbines blades, compressors, as well as birds, marine life and even insect wings. In some cases such as helicopters, wind turbines and compressors, dynamic stall becomes the primary limiting factor in the performance of the associated vehicle or structure. On the other hand, birds and insects use this phenomenon to extract higher lift and hence it is of great interest in biomimetic propulsion. Extensive experimental, computation and analytical work has focused over five decades on understanding and predicting dynamic stall.

The three main characteristics of dynamic stall include: a) A delay in stall with angle of attack exceeding the static stall limit. This is followed by shedding of a strong vortical

structure - the dynamic stall vortex (DSV) from the leading edge also referred to as the leading edge vortex (LEV) in the biomimetic propulsion literature. b) Convection of the DSV aft over the chord causing a non-linear pressure field, accompanied by large excursions in air loads. c) Delay of flow reattachment, resulting in substantial hysteresis. To better understand the complete process of dynamic stall Figure 2 adopted from Carr [13] is reproduced here. It depicts the development of the coefficients of normal force, pitching moment and the corresponding flow behavior for varying angles of attack. The study was conducted on a NACA 0012 airfoil oscillating in pitch, but the stall development is typical of virtually all airfoils experiencing fully developed dynamic stall.

As described in Carr [13] a chronology of dynamic-stall events starts at:

1. Point (a) in 2, where the pitching airfoil exceeds the static stall angle, with no apparent changes in the flow around the airfoil

2. The first indication of a "disturbance" in the flow appears at point (b), when the flow reversal is evident and the reversal progresses up to the leading edge.

3. The flow is no longer attached, and a very strong vortex begins near the leading edge (LEV) as shown by point (e)

4. The vortex then enlarges resulting in an overshoot of lift. The vortex then convects downstream towards the trailing edge causing variations in pitching moment. This vortex-shedding process is the most apparent characteristic of dynamic stall.

5. Further, as the blade begins the down stroke motion with a reduction of angle of attack, the vortex convects into the wake, and a fully separated flow develops on the airfoil. This is the stage of full separation - the lift stall accompanied by the pitching moment stall occurs. Thus producing the phenomenon known as dynamic stall.

6. As the angle attack reduces the flow reattaches from the leading edge to the trailing edge. The reattachment occurs with a hysteresis depending on the oscillation rate of the airfoil. Eventually, the aerodynamic loads return to the original values.

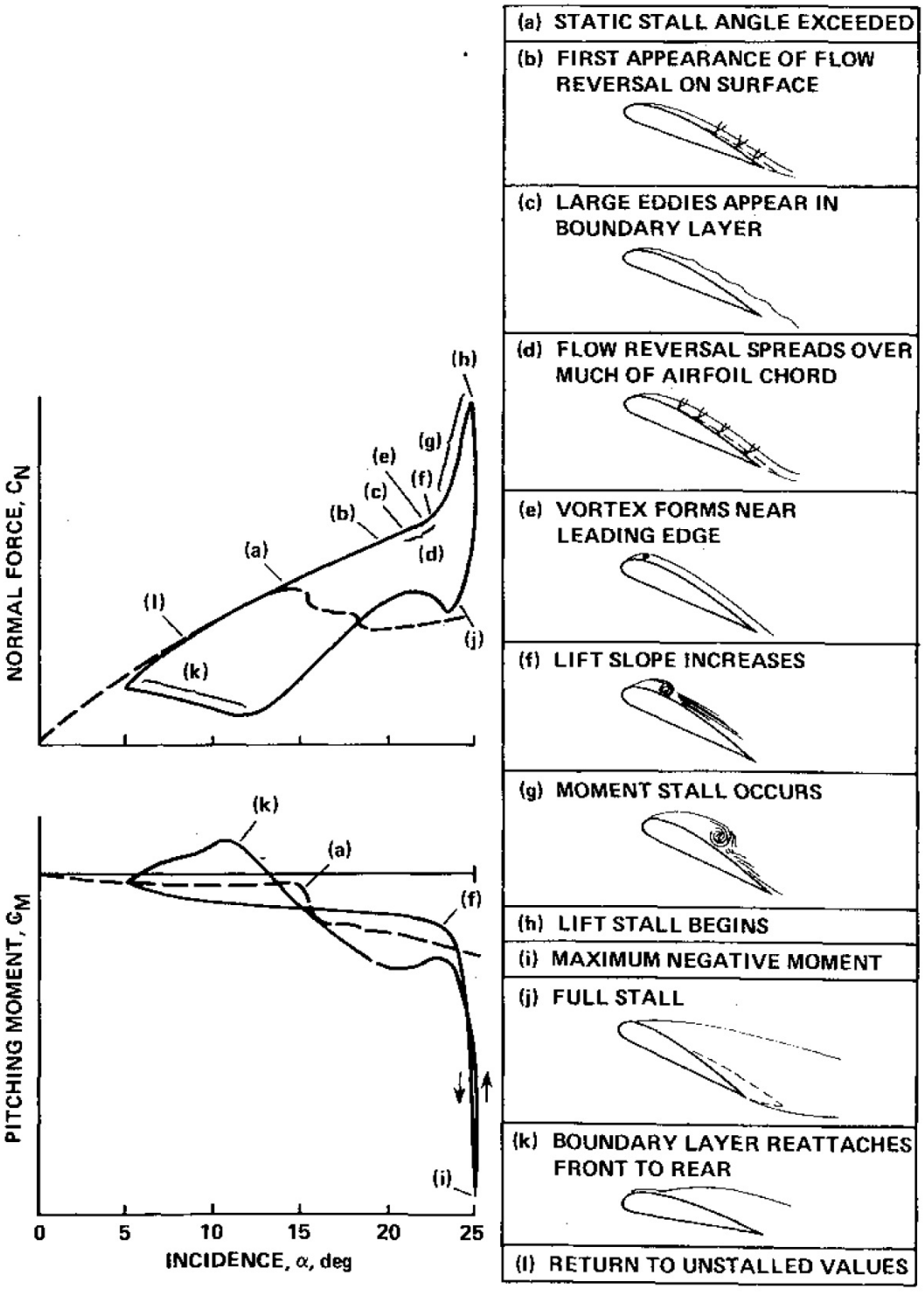

Figure 2: Events of dynamic stall on a NACA 0012 airfoil adopted from Carr [13].

Although dynamic stall is known to occur over various quadrants of the rotor blade based on advance ratio, maneuver type and blade loading [7], it predominantly occurs on the retreating blade of a helicopter in forward flight as shown in the Figure 3. Dynamic stall on the retreating blade imposes a limit on the flight envelope of the helicopter. The limitation primarily arises due to the following reasons:

1. Large excursions in pitching moments leading to abrupt growth in blade torsion.
2. Excessive load transmission to pitch-links, manifesting themselves in the pilot's stick, affecting handling qualities of the vehicle.
3. Increased airframe and cabin vibration.

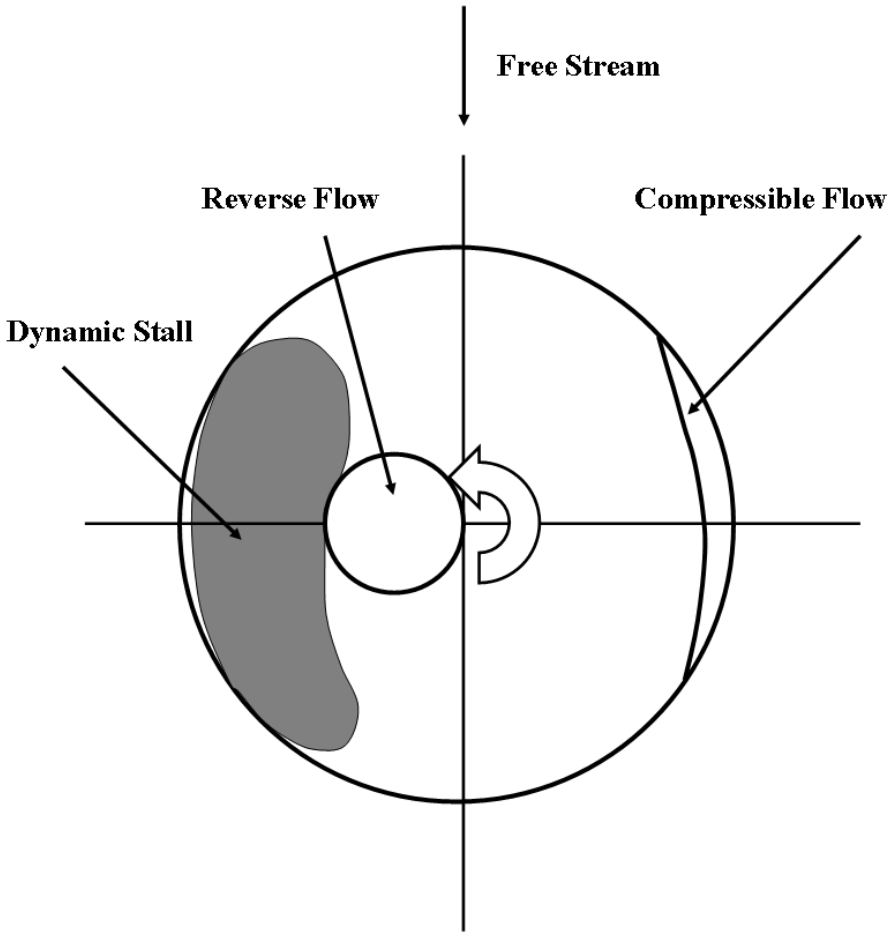

Figure 3: Azimuthal extent of dynamic stall at high forward flight velocities.

As mentioned earlier, dynamic stall also occurs on HAWT in yaw. One of the primary

limitations of the operating lifetime of wind turbines is the dynamic loading on the blades and generators, sometimes far in excess of their design loads [101, 100]. The unsteady loads produced during dynamic stall can be large enough to cause structural damage. It has been demonstrated by Veers [107] that a 30% error in prediction of the air loads leads to a 70% decrease in life expectancy of a HAWT.

Hitherto, the problem of dynamic stall was tackled by aerodynamicists by means of two-dimensional airfoil experimentation, which has been the key approach to understanding the phenomenon. McCroskey et al. [75] demonstrated that rotating blades of a helicopter could be simulated as oscillating airfoils/wings in a wind tunnel to conduct dynamic stall experiments. Although the two-dimensional nature of dynamic stall has been studied extensively (reviewed in Section 2.1), the three-dimensional behavior of the dynamic stall is not throughly comprehended. Centrifugal effects on the boundary layer are expected to drive a strong radial flow, but experiments have not provided evidence of the expected magnitude of these effects. The three dimensional nature of the dynamic stall and the intricacies that the strong radial acceleration a spinning rotor blade adds to the flow is a current research issue. The question "what is the role of radial flow on the dynamic stall process and post dynamic stall lift and pitching moment evolution?" remains unanswered.

1.2 Reverse flow

Reverse flow is characterized by the freestream moving from the trailing edge to the leading edge of the blade. This exotic aerodynamic regime manifests itself on the retreating part of rotating blades operating at significantly high advance ratios ($\mu_a \geq 0.5$). The behavior of the retreating blade at such high advance ratios is not clearly understood and is a primary limitation on the performance of the helicopter [85]. Although today most military and civil helicopters operate at low flight speeds ($0.1 < M < 0.2$), recent developments [108] in high-speed rotorcraft design quite easily exceed advance ratios of 0.5. Concepts such as slowed rotors for high-speed rotorcraft (for example see [20]) include the possibility of flying as fast as today's business jets (equivalent to $\mu_a \sim 1$) and yet benefiting from vertical take-off and landing (VTOL) capability. However, as mentioned earlier under high advance

ratio conditions, a significant portion of the rotor experiences flow from the trailing edge to the leading edge of the rotor blade (referred to as reverse flow as illustrated in Figure 4). This phenomenon of reverse flow has also been observed to occur on horizontal-axis wind turbine blades in yaw.

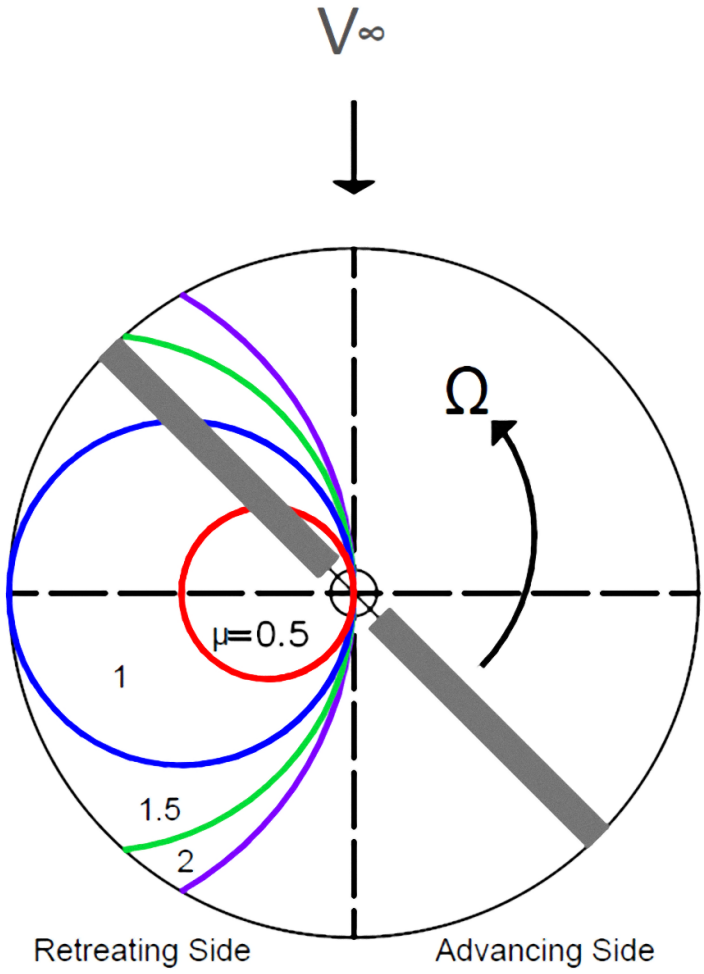

Figure 4: Extent of reverse-flow region at various advance ratios (μ_a)

Although research on reverse flow has been done in the past on airfoils at varying Reynolds number (see section 57 for a review), this particular significant relevance to high speed rotorcraft is a relatively nascent research area. Only recently experiments have been conducted on a slowed rotor, which suggest spikes in pitch link loads in the reverse flow regime. Again, the effect of radial flow unique to the rotating environment is crucial to understand this exotic flow regime.

1.3 Motivation and objectives

Both dynamic stall and reverse flow occurring on retreating rotor blades or on HAWT blades in yaw act as limiters of the performance of the associated vehicle/structure. As mentioned earlier dynamic stall over a rotor blade affects the performance in regards to power requirements, vibrations, handling qualities and structural fatigue. Flow field level insights of this phenomenon will help in improving predictions of loads associated with the event to improve helicopter speed and high-altitude performance, as well as the life and performance of large wind turbines. Similarly, the understanding of the flow field level details of the reverse flow aerodynamics of a rotating blade will help in designing efficient rotors for specific high advance ratio flight regimes and prediction of structural loads on yawed HAWT configurations.

These issues can be addressed with the knowledge of events behind the separation line on a rotor blade in dynamic stall. Here the radial acceleration and velocity field pose large unknowns in predicting rotor blade aerodynamics. Understanding the complete flow field would help in alleviating or at the least controlling the adverse effects of dynamic stall. Active flow control concepts could be used to achieve success with controlling dynamic stall, contributing to development of the field of high speed rotorcraft. Similarly, the knowledge of the effect of radial flow on reverse flow on rotating blades would help in ascertaining the expected aerodynamic loads in this exotic flow regime.

The motivation behind this work can be broadly categorized as scientific and engineering motivation. The scientific motivations are intended to answer fundamental questions in fluid mechanics, while the engineering motivations are to understand the implications of the fluid mechanics in the engineering community. The following is a description of each:

1. Scientific motivation Studying the velocity field over a retreating blade leads itself to several fundamental fluid mechanics questions. This work is intended to provide answers to the following:

   (a) Effect of rotating on the process of flow separation. Although the general effects of rotation on the initiation of separation are well understood, the effect of

rotation on post separated flow dynamics is not.

(b) The radial velocity and acceleration fields on a retreating blade undergoing stall is a major unknown.

(c) The characteristics of the above mentioned radial velocity field are also not well understood. The radial velocity profile could be susceptible to shear layer instabilities arising due to adverse pressure gradients in the flow field.

2. Engineering motivation The implications of the fluid mechanics in the engineering community is of primary importance in the this work, especially as applied to the rotorcraft community. Understanding the effects of radial flow on a retreating blade helps the rotorcraft community as discussed below

(a) A better understanding of effect of rotation on dynamic stall will help improve flight speed envelope and maneuverability of helicopters, while at the same time helping to reduce vibrations and improving handling qualities of the vehicle.

(b) Since dynamic stall also adversely affects HAWT in yaw, a better understanding of effect of rotating on dynamic stall helps improve the life span of a HAWT and at the same time help improve performance.

The principal objective of the work is to study the physics of the effects of radial flow on a retreating rotor blade as applied to the rotorcraft community. Two specific flows related to the flow over a retreating blade are investigated in this study: A) Dynamic stall and B) Reverse flow. The detailed set of objectives are provided below.

A Dynamic stall on the retreating blade

(a) Dynamic stall process

i. Characterize the process of separation and reattachment.

ii. Study the strength of the dynamic stall vortex via circulation estimates

iii. Investigate the effect of rotation on the dynamic stall event.

(b) Flow characteristics

i. Determine the separation line on the blade during dynamic stall.

ii. Characterize the radial flow on the rotating blade during dynamic stall

(c) Rotating disk analogy for radial flow

i. Explore the flow features on a rotating disk in a superimposed separated uniform stream.

ii. Study similarities of flow for the two cases of rotating disk and rotating blade in separated flow.

B Reverse flow on the retreating blade

(a) Static experiments

i. Investigate aerodynamic load characteristics of a static yawed blade in reverse flow.

ii. Augment prior load measurements with surface flow visualization to uncover blade surface flow features.

(b) Rotating experiments

i. Investigate the velocity fields on the lower surface of the rotating blade in reverse flow.

In summary, fulfilling these objectives makes a significant contribution towards the current understanding of dynamic stall on helicopter and HAWT rotor blades. The flow field level details of the aerodynamic phenomena on the retreating blade will allow for a better interpretation of the effects of radial flow on the retreating rotor blade. The size, strength, and position of the vortex determined from the velocity fields can be used to deduce the evolution of aerodynamic loads on the retreating blade. The planned three component (u,v,w) velocity measurements will provide further insights into the behavior of radial flow on the retreating blade. The radial flow measurements can be used to support the hypothesis for the significance of radial flow during dynamic stall. The fundamental investigation of the radial flow over a rotating disk in a superimposed separated uniform stream will help develop quasi-analytical method to predict flow features on a rotating blade

in separated flow. Eventually, these results could pave way for flow control techniques to minimize the effects dynamic stall on the performance of a helicopter as well as a HAWT. Furthermore, a knowledge of the reverse flow over a retreating rotor blade will help predict aerodynamic loads to the accuracy needed for design of very high advance ratio helicopter rotor as well as HAWT in yaw.

1.4 Planned approach

The figure on the next page illustrates a flowchart of the detailed research plan. This illustration should serve as a road map for this thesis, summarizing the main focal points in this work with the path taken to reach the conclusions. The blue blocks indicate the experiments/investigations conducted and the green ovals indicate the questions that are answered in order to fulfill the objectives of this work.

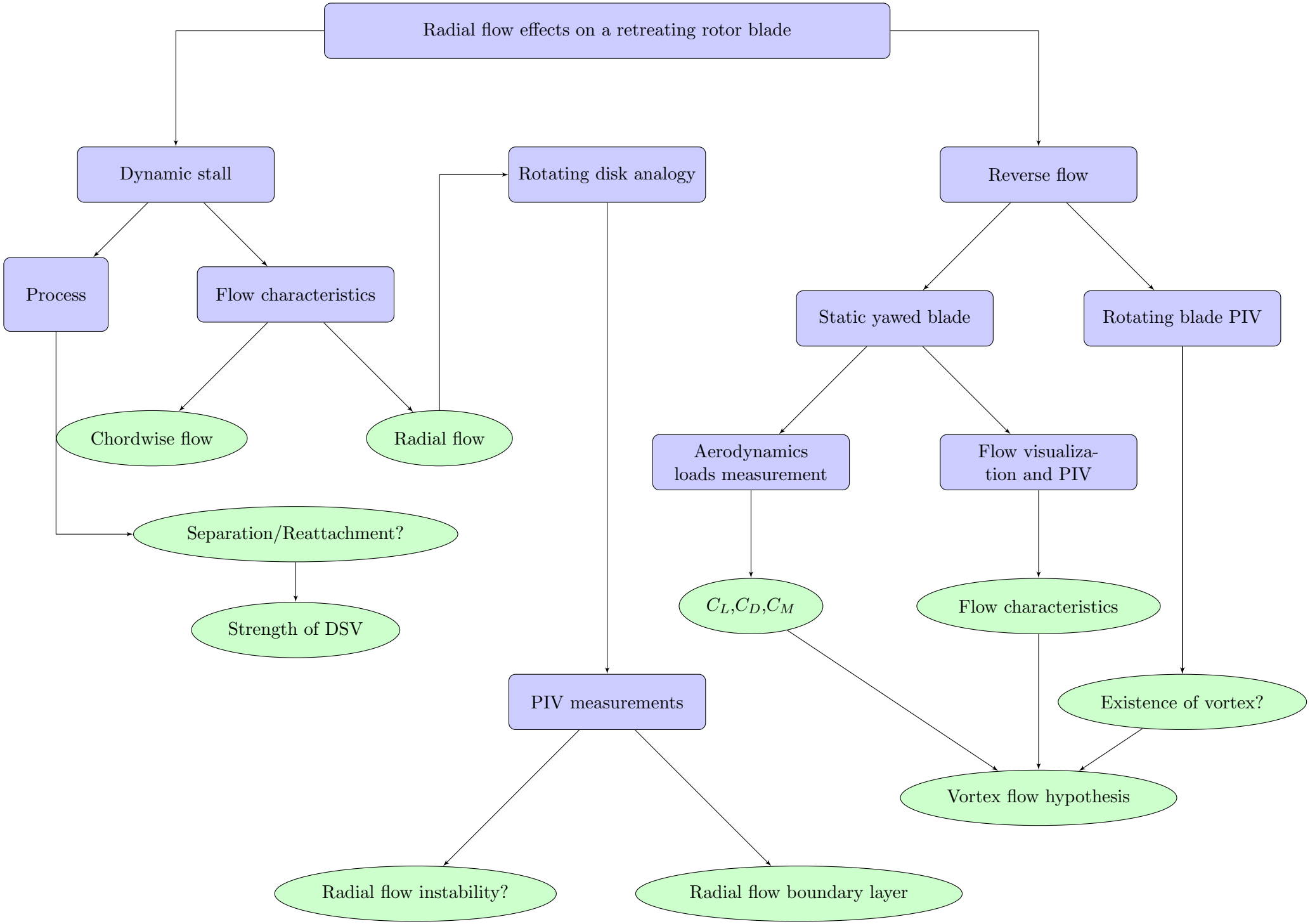
Radial flow effects on a retreating rotor blade
Dynamic stall
Process
Flow characteristics
Chordwise flow
Radial flow
Separation/Reattachment?
Strength of DSV
Rotating disk analogy
PIV measurements
Radial flow instability?
Radial flow boundary layer
Reverse flow
Static yawed blade
Aerodynamics loads measurement
C_L,C_D,C_M
Flow visualization and PIV
Flow characteristics
Rotating blade PIV
Existence of vortex?
Vortex flow hypothesis

1.5 Experimental Facilities

This section describes in detail the experimental facilities used in this investigation, which includes the low speed wind tunnel and the diagnostic equipment.

1.5.1 Low speed wind tunnel

The experiments were conducted in the John Harper 2.13m×2.74m low speed wind tunnel at the Georgia Institute of Technology, illustrated in Figure 5. It is a closed circuit tunnel built in the 1920's located in the basement of the Guggenheim building. The contraction ratio between the cross sectional area of the settling chamber to the cross sectional area of the test section is approximately 4:1. The closed circuit tunnel is powered by a three-phase 600hp induction motor. The motor is coupled to a fixed pitch single stage fan via a gearing mechanism with a 8:3 gear ratio. The wind tunnel speed is controlled by a variable frequency drive which is a closed loop controller with 0.1 % error in RPM setting. The wind tunnel dynamic pressure (q) was measured using a 10 Torr Baratron, a differential pressure transducer connected to a pitot-static tube located near the ceiling of the middle of the test section. Knowing the ambient pressure and temperature, the tunnel speed and Reynolds number were calculated using the expressions in Table 1.

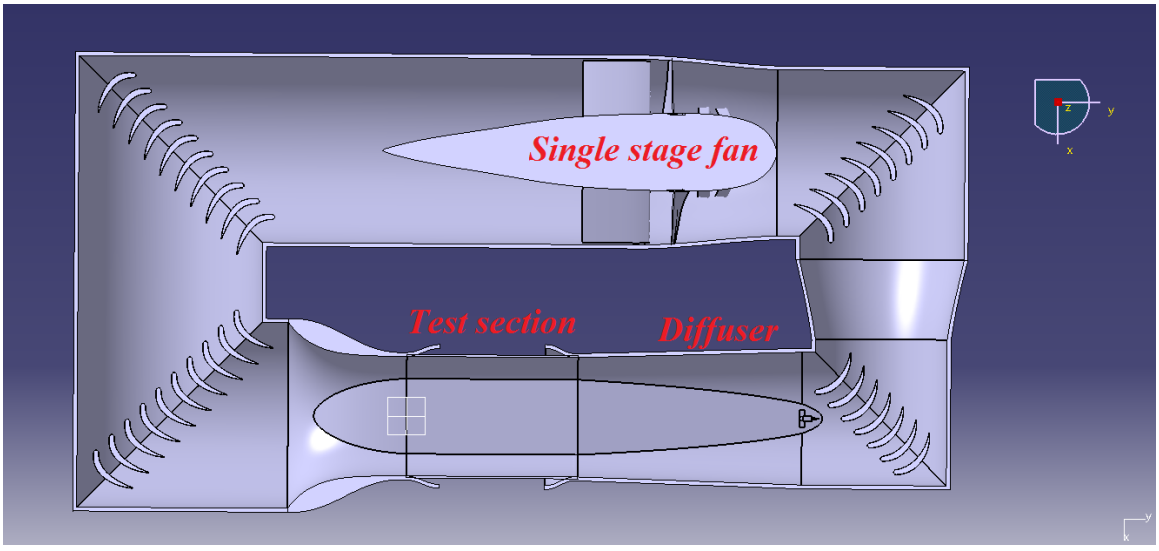

Figure 5: Drawing of the John Harper wind tunnel at Georgia Institute of Technology

Table 1: Sample calculation of flow conditions

Property	Estimate	Value	Units
ρ	$\frac{P}{R_g T}$	1.184	kg/m^3
μ	$\frac{C_1 T^{3/2}}{T+S}$	1.91×10^{-5}	$Pa\text{-}s$
V_∞	$\sqrt{\frac{2q}{\rho}}$	15.41	m/s
R_e	$\frac{\rho V_\infty c}{\mu}$	1.7×10^5	

$C_1 = 1.458 \times 10^{-6}$ and $S = 110.4\ K$ are Sutherland's constants.

The turbulence intensity of the wind tunnel is 0.05% measured at a freestream velocity of 102.67 ft/s (31.29 m/s). The turbulence intensity reported here is computed using data gathered after applying a 1 Hz high pass filter and a 2,500 Hz low pass filter to the velocity fluctuations measured using Constant Temperature Anemometry (CTA). Refer to section 1.5.5 for details on CTA and Appendix B for details on the turbulence intensity measurement and computation.

1.5.2 High advance ratio facility

The high advance ratio facility with manually adjustable cyclic and collective pitch was fabricated to study the flow characteristics of a rotating blade at high advance ratios. It was installed in the test section of the John Harper low speed wind tunnel described in the previous section with the motor positioned below the rotor. In order to simplify the operations a teetering rotor hub design was preferred. A photo-micro sensor (provided by Omron Electrnics - EE-SX1070) was installed on the shaft of the rotor to enable phase-locked data measurement. Further detailed specifications of the rotor used in this work are provided in Table 2. The blade used in the experimental investigations in this work was a rectangular, non-tapered blade with zero twist. The blade was comprehensively characterized by measuring the chord length, maximum thickness, location of the maximum thickness and the surface roughness at several span-wise locations. The length dimensions were measured using a 2 feet shop vernier caliper with a resolution of 0.01 in. The surface roughness measurements were gathered using a stylus based device, called the profilometer.

The measurements were made along the chord and the roughness along the span was not quantified due to dimensional constraints imposed by the profilometer. Table 3 summarizes the measurements made along with the average and standard deviation of the measurements. Although the standard deviation of the chord length, maximum thickness and location of maximum thickness are minimal, the standard deviation of the surface roughness is around 17.82% which is significantly high.

Table 2: High advance ratio facility rotor specifications

Description	Value	Units
Blade mass total	1.747	kg
Blade span	0.622	meter
Blade chord	0.178	meter
Blade aspect ratio	3.49	
Disc radius	0.889	meter
Solidity	0.0895	
Precone	1.6	Deg
Maximum collective	10	Deg
Maximum cyclic	6.5	Deg
Maximum TPP tilt	16	Deg
Motor	3.73	kW
Height	1.575	meter

Table 3: Detailed analysis of the blade geometry and surface roughness of the upper surface of the blade

Section Number	Distance from tip of the blade (in)	Chord length, c (in)	Max thickness (% c)	Location of max thickness from LE (% c)	Surface roughness (μ in)
1	0.70	6.95	12.81%	24.75%	25.00
2	1.94	6.99	12.88%	25.16%	28.75
3	2.96	7.02	12.75%	25.41%	42.50
4	3.95	7.00	12.79%	25.20%	36.25
5	4.86	7.03	12.79%	25.56%	35.00
6	5.96	7.03	12.79%	25.42%	27.50
7	6.96	7.02	12.82%	25.46%	26.25
8	7.97	7.00	12.86%	25.40%	33.75
9	8.96	7.00	12.79%	25.11%	28.75
10	9.95	6.94	12.90%	24.51%	30.00
11	10.94	6.95	12.89%	24.58%	30.00
12	11.98	6.93	12.91%	24.37%	31.25
13	12.94	6.95	12.88%	24.60%	30.00
14	13.94	6.95	12.88%	24.56%	26.50
15	14.92	7.05	12.77%	25.62%	23.00
16	15.95	6.94	12.97%	24.42%	21.25
17	16.94	7.05	12.77%	25.63%	-
18	17.97	7.05	12.77%	25.60%	-
AVERAGE		6.99	12.83%	25.08%	29.73
STD DEV (% off AVG)		0.61%	0.5%	1.86%	17.82%

1.5.3 Particle image velocimetry (PIV)

The flow diagnostics were performed on the rotor using PIV. Unless mentioned otherwise, in most of the experiments a LaVision PIV system was used for the diagnostics. The equipment used with the LaVision setup included a Litron Nano Nd:YAG PIV laser, an ImagerIntense CCD camera, and the DaVis imaging software. The laser was double pulsed and frequency doubled to produce 532nm visible light. The resulting beam diameter was about 3.5mm with a pulse width of 5ns. The ImagerIntense camera had a 1600(h) $\times$ 1200(v) pixel viewing area. The scan rate of the CCD sensor was 16MHz. The cameras and the laser unit were synchronized using a programmable timing unit (PTU).

The Figures 1.5.3 and 1.5.3 show the wiring scheme and typical timing used in the experiments. The data processing was done using the software provided by LaVision, the DaVis 7.2. Certain data acquisition parameters and processing techniques vary for each experiment depending on the measurements needed and the flow conditions. Hence the specifics are detailed in the respective chapters.

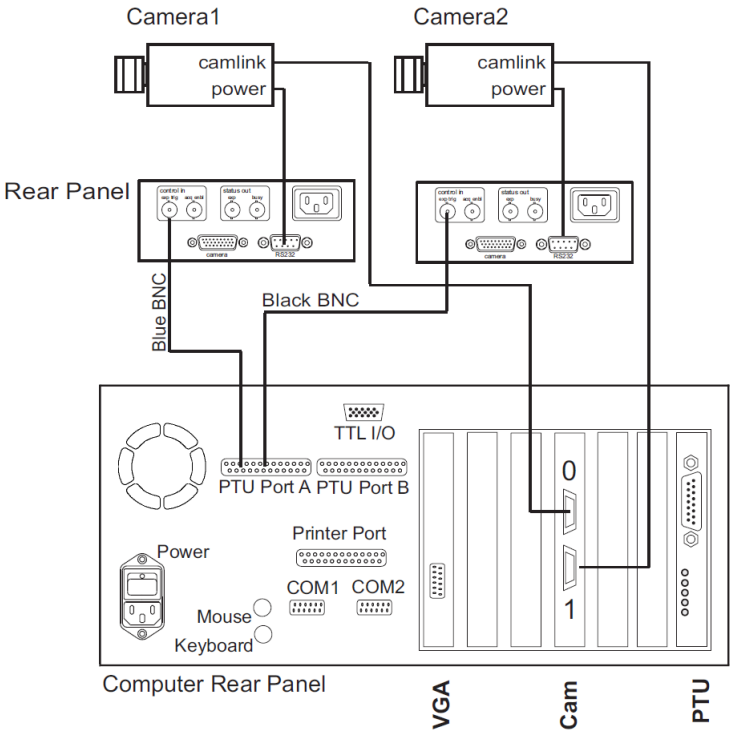

Figure 6: Camera wiring with camlink interface

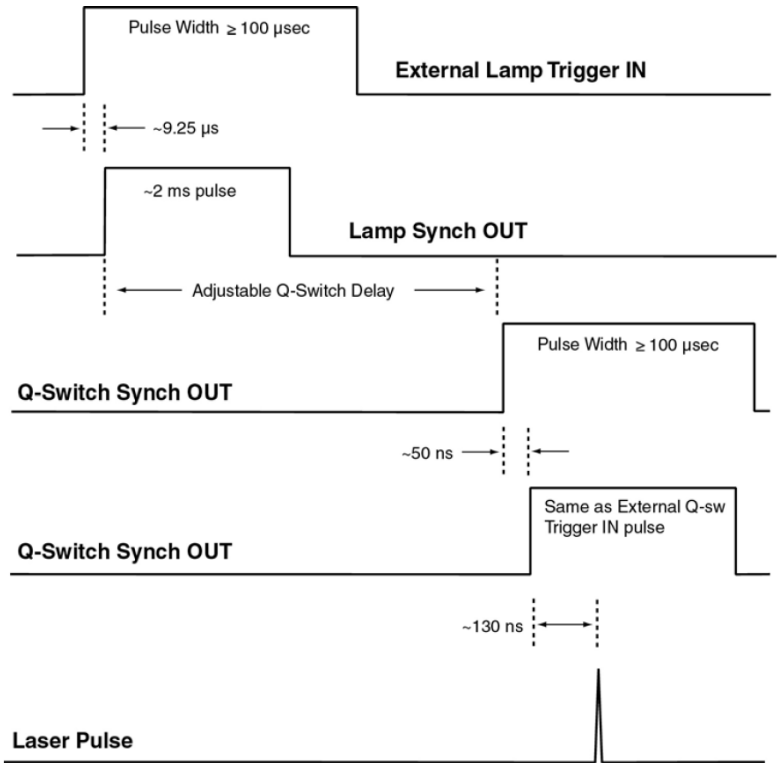

Figure 7: Timing diagram for a PIV experiment.

1.5.4 Aerodynamic loads measurement

Aerodynamic loads on the blade were measured using a 6-DOF ATI Delta load-cell transducer, capable of measuring three forces F_x, F_y, F_z and 3 moments M_x, M_y, and M_z. The load cell is interfaced to the computer via LABVIEW through an ATI signal conditioner as illustrated in Figure 8. The specifications of the ATI Delta load cell are provided in Table 4.

Table 4: Specifications of the ATI-Delta load cell

Measurement	Range	Sensitivity
F_x, F_y	165 N	$\frac{1}{32}$ N
F_z	495 N	$\frac{1}{16}$ N
T_x,T_y	15 Nm	$\frac{1}{528}$ Nm
T_z	15 Nm	$\frac{1}{528}$ Nm

In order to keep track of the forces and moments in every coordinate and convert them back into wind tunnel coordinates a rotation matrix $\mathbf{R}$ as shown below was used:

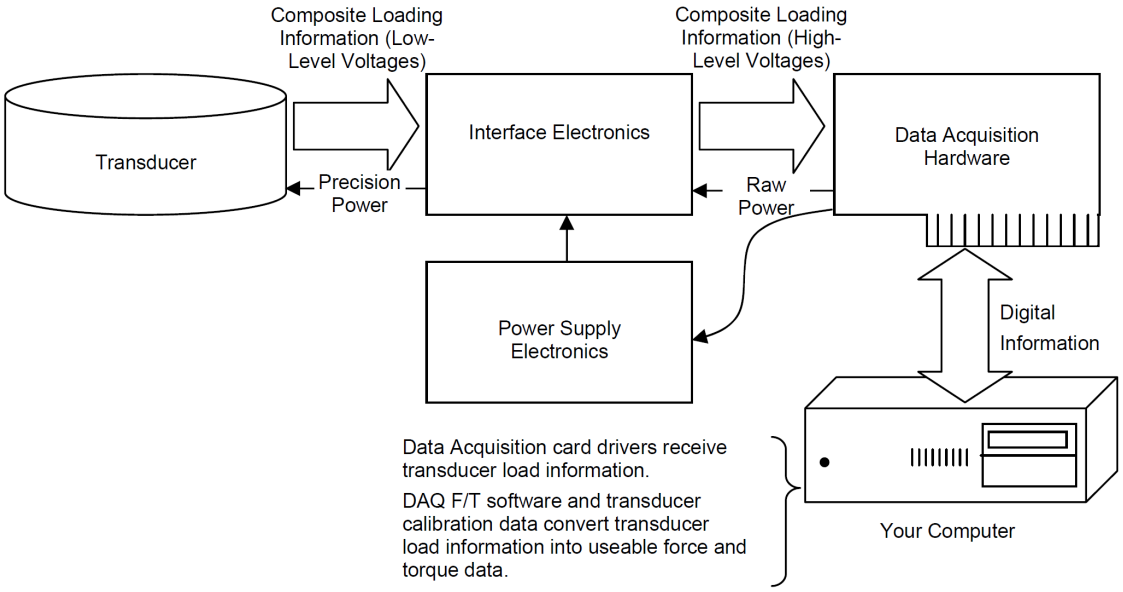

Figure 8: Force transducer wiring diagram for force and moment measurements taken from ATI force transducer manual

$$\mathbf{R} = \begin{pmatrix} -cos\theta cos\psi & -cos\psi sin\theta & -sin\psi \\ sin\theta & -cos\theta & 0 \\ -cos\theta sin\psi & -sin\theta sin\psi & cos\psi \end{pmatrix} \tag{1}$$

where θ is the pitch angle (angle of attack) of the blade and ψ is the yaw angle of the blade as defined in Chapter 6.

1.5.5 Constant temperature anemometry (CTA)

The velocity data required to compute turbulence intensity were gathered using CTA technique. The IFA-300 system provided by TSI was used to acquire data using a hot-film sensor (model 1201 from TSI made using a platinum film). The specifications are listed in Table 5 and the specific probe used is shown in Figure 9.

The wiring scheme used for a typical hotfilm probe for measurements is shown in Figure 10. Due to certain hardware limitations some modifications were made to the wiring diagram. For details please refer to the internal hotwire/hotfilm documentation manual available at the John Harper Wind Tunnel.

Table 5: Hot film probe specifications

Type	Specification
Probe Name	TSI Model No. 1201
Sensor Type	Single, Platinum Film
Sensor Size	3.2 mm
Maximum Exposure Temperature	60^oC
Typical Probe Resistance	5.58Ω
Typical Operating Resistance	8.88Ω

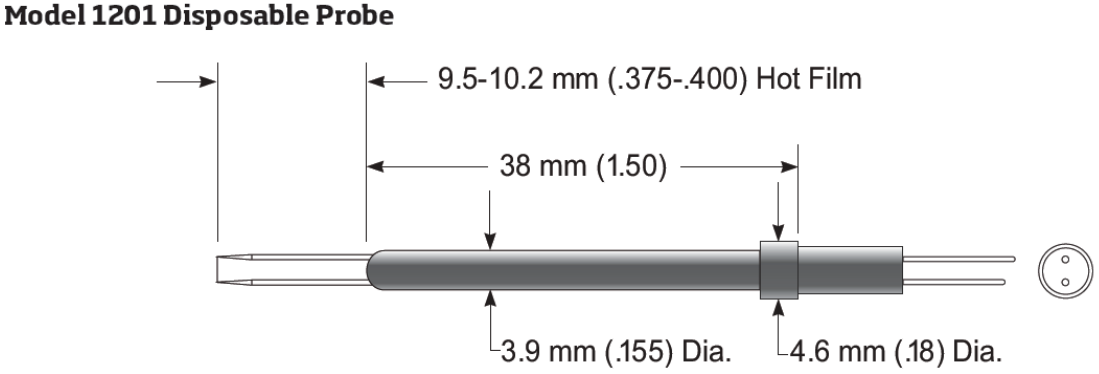

Figure 9: TSI hotfilm probe used for turbulence measurements (adopted from TSI website)

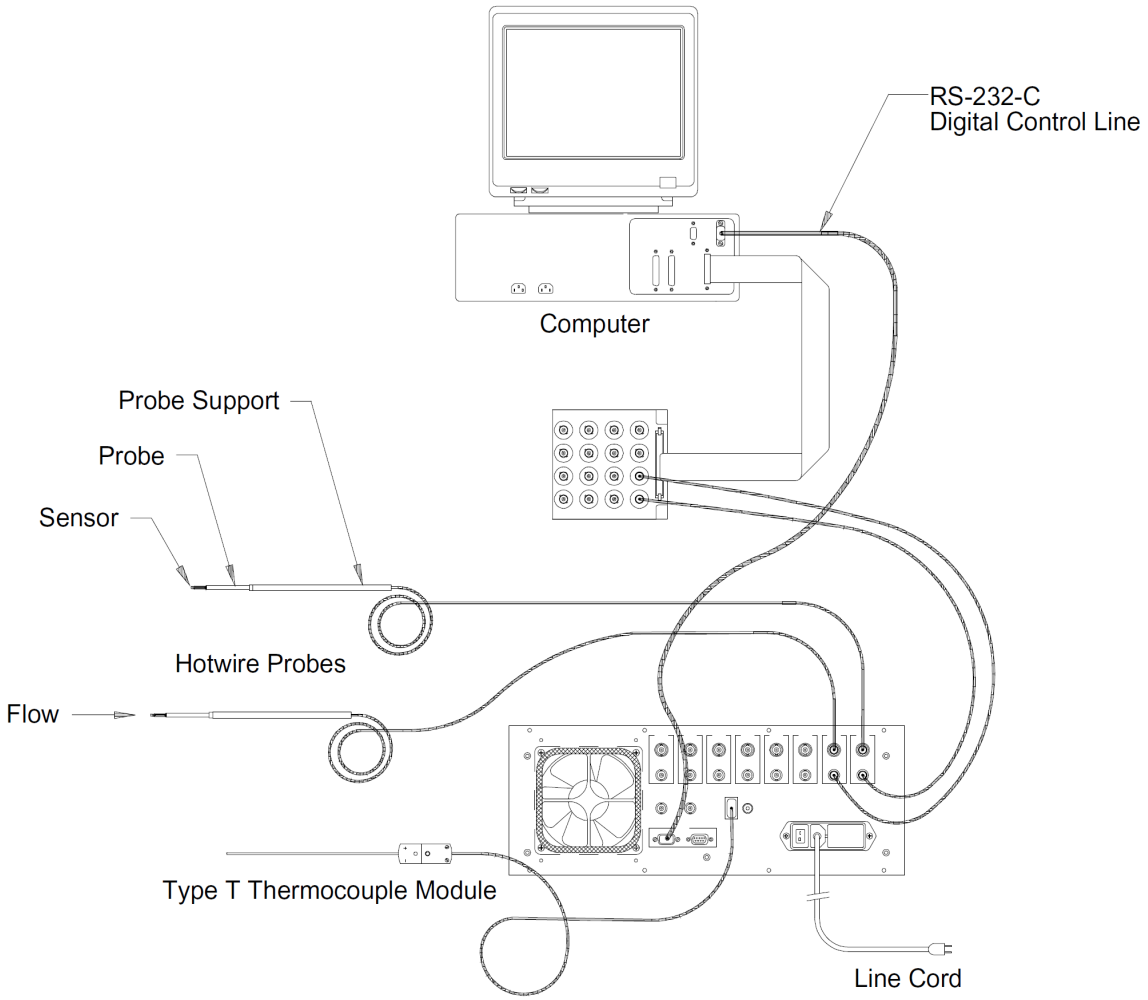

Figure 10: Constant temperature anemometry wiring diagram for turbulence intensity measurements taken from TSI CTA manual

CHAPTER II

DYNAMIC STALL - SEPARATION AND REATTACHMENT

2.1 Introduction and prior work

As discussed earlier, dynamic stall (DS) occurs on lifting surfaces experiencing unsteady motion typically beyond the static stall angle [75, 17]. Dynamic stall is a subset of unsteady aerodynamics which is of great interest in engineering and has been studied for close to a century now. The earliest known work in unsteady aerodynamics dates back to 1922 when Katzmayr [57] experimentally demonstrated the effect of periodic changes of angle of attack on the behavior of airfoils. This was followed by separate theoretical investigations by Wagner, Theodorsen, Küssner, von Kármán, Sears, and Loewy. Leishman [67] reviews further investigations in unsteady aerodynamics.

2.1.1 Early history of dynamic stall (Prior to 1970)

Kramer [64] in 1932 was the first to demonstrate the enhanced lift associated with highly unsteady airfoils/wings. Bailey [4] in 1939 captured the first recorded evidence of stall being observed on the retreating part of the rotor blade. He captured photographs of the stalled flow over the rotating blades of an autogiro rotor during flight tests. In 1951 Halfman [45] extended Katzmayr's idea to represent a helicopter rotor blade as an oscillating airfoil in both pitch and/or plunge. Halfman was successful in measuring the loads on an oscillating airfoil confirming Kramer's observation of enhanced lift. However, it should be noted that these cited investigations were primarily focused on the aeroelastic problem of rotor stall flutter.

Following these pioneering studies, Ham [49] demonstrated the vortical nature of the stalled flow field on a retreating rotor blade using pressure measurements on the airfoil surface. These experiments demonstrated the existence of a strong vortical disturbance on the upper surface of a rotor blade in forward flight. Further investigations of the phenomenon allowed Ham to link the occurrence of stall flutter to the phenomenon of dynamic stall [47].

Following which Ham and Garelick [48] made a strong case for dynamic stall considerations in helicopter rotor performance and design.

2.1.2 Recent developments (Since 1970) and dynamic stall mechanisms

The early investigations on stall flutter and the eventual realization of dynamic stall phenomenon on helicopter rotors in forward flight was followed by investigations shifting gears to focus on the fundamental understanding of dynamic stall. McCroskey [75] and Carr [17] followed in the footsteps of Halfman to conduct experiments on oscillating airfoils to gain further understanding of the phenomenon of dynamic stall. These investigations primarily focused on defining a parameter space for dynamic stall attributes on an oscillating airfoil. McCroskey and Carr evaluated parameters such as amplitude of oscillation, reduced frequency, Mach number and Reynolds number. While other investigations evaluated the effect of airfoil geometry [78, 77], effect of pitch axis location [55] and varying forcing conditions [19]. For a thorough review on dynamic stall please refer to Carr [13].

Although dynamic stall has been studied extensively, predicting the precise timing, extent and hence the phase of a dynamic stall event and reattachment on a rotating blade remains elusive. Predicting the delayed onset of flow separation and reattachment resulting from unsteady aerodynamics remains a tough challenge. This is especially true when the Reynolds number of the blade boundary layer is high enough so that the boundary layer upstream of separation is turbulent. In this case, studies show that stall initiation is a localized three dimensional phenomenon, even if the blade itself has zero sweep and taper, and is not rotating. Hence, researchers were then interested in identifying the physics of separation delay and onset of dynamic stall. The onset is attributed to several and often conflicting schools of thought including: *a*) classic trailing edge separation, *b*) shock induced separation, and *c*) bursting of a separation bubble. From the experimental observations McCroskey proposed one of the schools of thought on the mechanism for dynamic stall onset called trailing edge separation. Essentially he hypothesized that the separation begins at the trailing edge and gradually moves towards the leading edge and then transitions into full stall.

The investigations cited earlier were primarily performed below Mach numbers of $M \leq 0.3$. However, McCroskey's work [78, 77] clearly demonstrated that compressible Mach numbers ($M \geq 0.3$) were achieved on rapidly pitching airfoils. This was mainly due to acceleration of the fluid around the leading edge of the airfoil reaching high Mach numbers although the onset Mach number was as small as 0.18. This established a strong need to investigate dynamic stall under compressible flow conditions. Chandrashekara and Carr [14, 21, 16, 15] made the most significant contributions to the current understanding of compressible dynamic stall. They proposed a second school of thought on dynamic stall onset that the timing of the dynamic stall event depends on shock-vortex interaction phenomena in the accelerated flow over the leading edge. However, it should be noted that although compressible flow modifies the timing of the dynamic stall event, the flow field downstream of the separation is clearly incompressible. This fact comes into picture during the design of the experimental setup in this work, where compressibility of the fluid is *not* considered in the experiments conducted.

Early theories on the third school of thought on dynamic stall onset mechanism were proposed by Sears [99] followed by Van Dommelen et al. [105]. The theories predicted the development of a singularity at the onset of separation, followed by focused, sudden eruptions of boundary layer fluid into the outer stream, propagating the stall event. Recent advancements proposed by Haller [46, 104] also suggest that the separation location is variable in the case of unsteady flow separation. The implication of these theories for dynamic stall is that the precise timing of such events varies from cycle-to-cycle and in the spanwise location along the blade in the case of a helicopter in forward flight, even if the flight condition is nominally steady. In the case of wind turbines, it has been observed that the dynamic stall vortex initiation strongly depends upon local inflow angle [97]. This essentially makes the timing of the dynamic stall difficult to predict and control.

The recovery (reattachment) from the process of dynamic stall is delayed in a hysteresis loop. Just like the onset of separation, reattachment has been shown to be a non repeatable process with significant differences from cycle-to-cycle. The process of reattachment after the dynamic stall event has been investigated by Ahmed [3] and Green [41]. Both the studies

noted that the dynamic reattachment is a continuous process, unlike reattachment during a steady separated flow. Flow field level details using PIV measurements by Wernert [110] helped conclude that the extent of non-reproducibility was contingent on the size of the separated wake and the reduced frequency of the oscillation.

2.1.3 Rotating blade dynamic stall

Hitherto, most of these experimental investigations of dynamic stall have been limited to two-dimensional flows over oscillating airfoils in wind and water tunnels [75, 17, 78, 13] and on oscillating finite wings [77, 70, 18]. Computational fluid dynamics (CFD) investigations have proceeded from inviscid formulations to full Navier-Stokes simulations [60, 103, 65, 80] (see [31] for a thorough review). However, in reality the occurrence of dynamic stall is influenced by three-dimensional effects that are unique to the rotating environment [95, 79]. Such effects included viscous interactions associated with rotational augmentation, as well as inviscid ones such as finite wing and local yaw effects. Centrifugal effects are expected to drive a strong radial flow and the coupled effects of centrifugal and Coriolis forces in the rotating environment add more complexity to the flow characteristics [96]. McCroskey's [74] experimental evidence confirms that the fluid in the stalled region does move outward due to the centrifugal forces. According to Corten [25] the dynamic stall region of wind turbine blades also exhibits substantial radial pressure gradients. Radial acceleration appears to have a strong influence on post-stall lift and pitching moment evolution. Deviations from two-dimensional behavior of the dynamic stall vortex initiation kinematics on a wind turbine have been demonstrated by Schreck [97]. These three-dimensional influences include viscous interactions associated with rotational augmentation, as well as inviscid ones like local sweep effects. Hence, understanding the nature of the near-surface flow under the influence of these coupled forces is crucial to predicting dynamic stall, to the accuracy needed for high advance ratio rotor design as well as wind turbine design.

Investigations of dynamic stall on rotating blades have been sparse mainly due to the cumbersome nature of performing experiments or numerical simulations. The earliest work

was to study the effects of rotation on laminar separation over rotating blades. Himmelskamp [51] performed experiments showing that rotation postponed stalling to a higher lift coefficient than that would be expected from two-dimensional case. Later, Banks [5] developed an analytical model ascertaining the delaying effect of rotation on laminar separation. However, these pioneering investigations did not include unsteady motion of the lifting surface and hence this needed further investigation. Ham [49] was one of the first to measure pressure data over a rotating blade undergoing unsteady motion in retreating blade stall conditions. McCroskey and Fisher [76] made similar measurements on a rotor blade in retreating blade stall and concluded that the forces and moments are not predictable after the blade completely stalls. Soon after this dynamic stall on wind turbines also became a significant research area, and until recently most rotating blade dynamic stall studies were conducted on wind turbines. Fraunie [34] was the first one to accomplish velocity measurements to study the characteristics of dynamic stall on a VAWT. Butterfield [11] measured the performance of a HAWT and compared them to predictions using two-dimensional blade element theory (note that this was simple two-dimensional airfoil data and not airfoil data under dynamic stall conditions). He concluded that the delayed stall during rotation resulted in a significant increase in peak power levels over the predicted levels.

In the late 1990's and early 2000's Shreck and Robinson [98, 97] gathered extensive pressure measurement in field experiments to demonstrate the effect of dynamic stall on the performance of a HAWT. He observed that the DSV on a HAWT was highly reminiscent of those observed on three-dimensional wings (the omega-shaped DSV). He postulated that the DSV at the midspan location would rise above the surface and convect with the freestream. However, at inboard and outboard of the midspan, the vortex would remain close to the surface and shielded from freestream, impeding vortex convection. These disparities he claimed, "would engender rapid three-dimensional deformation of the DSV". At around the same time frame Bousman [7, 8] performed flight tests to gather pressure measurements on rotating blades of a helicopter during dynamic stall conditions (primarily maneuvers). The most striking observation in the flight tests was the occurrence of three dynamic stall events over the whole rotor azimuth, two on the retreating side and one in the advancing

side. The data suggested that only the initial dynamic stall cycle was first observed inboard and it then moves out to the tip of the blade and for subsequent stall cycles, the formation of the DSV occurred simultaneously all over the blade.

2.1.4 Instantaneous velocity fields during dynamic stall

Most of the experimental investigations cited hitherto have primarily involved gathering pressure distribution data over the surface of the airfoil/wing. In a few investigations velocity measurements were gathered using constant temperature anemometry and laser Doppler velocimetry. However, to study the mechanisms involved in such an unsteady flow, it would be advantageous to gather instantaneous velocity field data. Flow field velocity data will allow a better interpretations of the kinematics and dynamics of the DSV. This is where PIV would play a significant role since it is a "global" velocity measurement technique. Flow field velocity details of dynamic stall on oscillating airfoils/wings has been accomplished using PIV [90, 38, 83, 82]. However, there are very few experimental investigations of the flow field veloicty details of dynamic stall on rotating blades.

Flow field details of dynamic stall on rotating blades has been investigated experimentally in the past using PIV by Fujisawa [35, 36] and Ferreira [33, 32]. However, in these experiments the rotating blades were set up to operate as a VAWT, in which case the effect of centrifugal forces is unlike that on rotating helicopter rotor blades. In the case of rotating VAWT blades the centrifugal forces act perpendicular to the blade planform, while in the case of rotating helicopter and HAWT blades the centrifugal forces act along the span of the blade. Recently, rotating helicopter rotor blades have been used to experimentally study flow field details of dynamic stall [30, 81, 94], followed closely by numerical investigations on rotating configurations [93, 44, 37]. DiOttavio et al. and Raghav both studied the characteristics of the radial flow on a dynamically stalled rotor blade. Mulleners et al. conducted experiments on a model scale fully equipped helicopter model. They observed only small cycle-to-cycle variations of the DSV, and hypothesized that the radial forcing due to rotation effects was stabilizing the DSV.

2.2 Outlook and objectives

As discussed in the previous section there are only a few investigations where instantaneous velocity fields over a rotating blade in dynamic stall have been captured. At Georgia Institute of Technology, this work started off as an investigation to measure radial velocity over a rotating blade in dynamic stall and has been continued to study the three-dimensional dynamic stall vortex. Hence, the primary objective in this chapter to measure and characterize the dynamic stall event on a rotating blade. The specific objectives are:

1. Identify the azimuthal angles for dynamic separation and reattachment.

2. Study the development of dynamic stall from the point of separation to reattachment.

3. Characterize the cycle-to-cycle variations in the dynamic stall event.

2.3 Experimental methods

2.3.1 Experimental setup and flow conditions

The experiments were conducted in the high advance ratio facility (see Figure 11 also refer to Section 1.5.2 for a detailed description of the facility) constructed in the test section of the John Harper 2.13m×2.74m low speed wind tunnel (please refer to section 1.5.1 for details) at the Georgia Institute of Technology.

Given the objectives and motivation of capturing the dynamic separation and reattachment of the flow under dynamic stall conditions, a rotor rotation rate of 200RPM (Ω = 20.94 rad/s, U_T = 18.62 m/s) was chosen. To study the effects of advance ratio on the dynamic separation and reattachment, experiments were conducted at three free stream velocities of U_∞ = 4.65, 6.7, and 7.44 m/s which yielded advance ratios of μ = 0.25, 0.35, and 0.4. which is sufficient to induce dynamic stall as demonstrated by [30] using flow visualization. A collective pitch of 10° and a cyclic of −5° were used to create a 15° pitch on the retreating blade at $\psi = 270°$. However, due to flapping of the blade, the effective angle of attack observed on the retreating blade at $\psi = 270°$ was 16.8° for an advance ratio of 0.35. The chordwise velocity measurements were made at three locations in the range

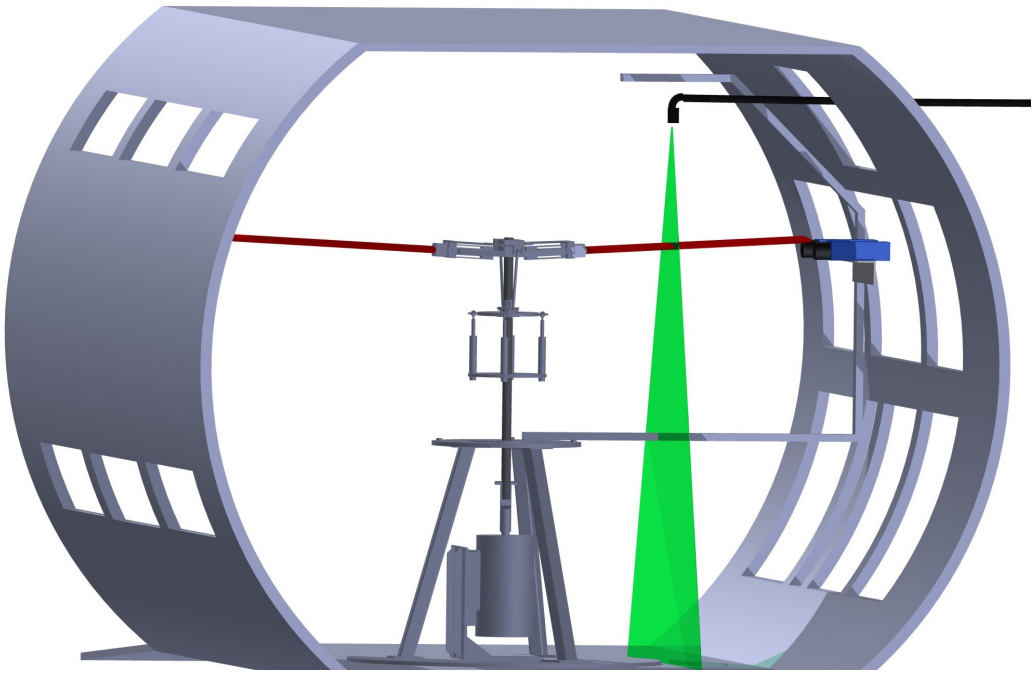

Figure 11: Setup of the retreating blade dynamic stall experiment with Stereo-PIV measurements

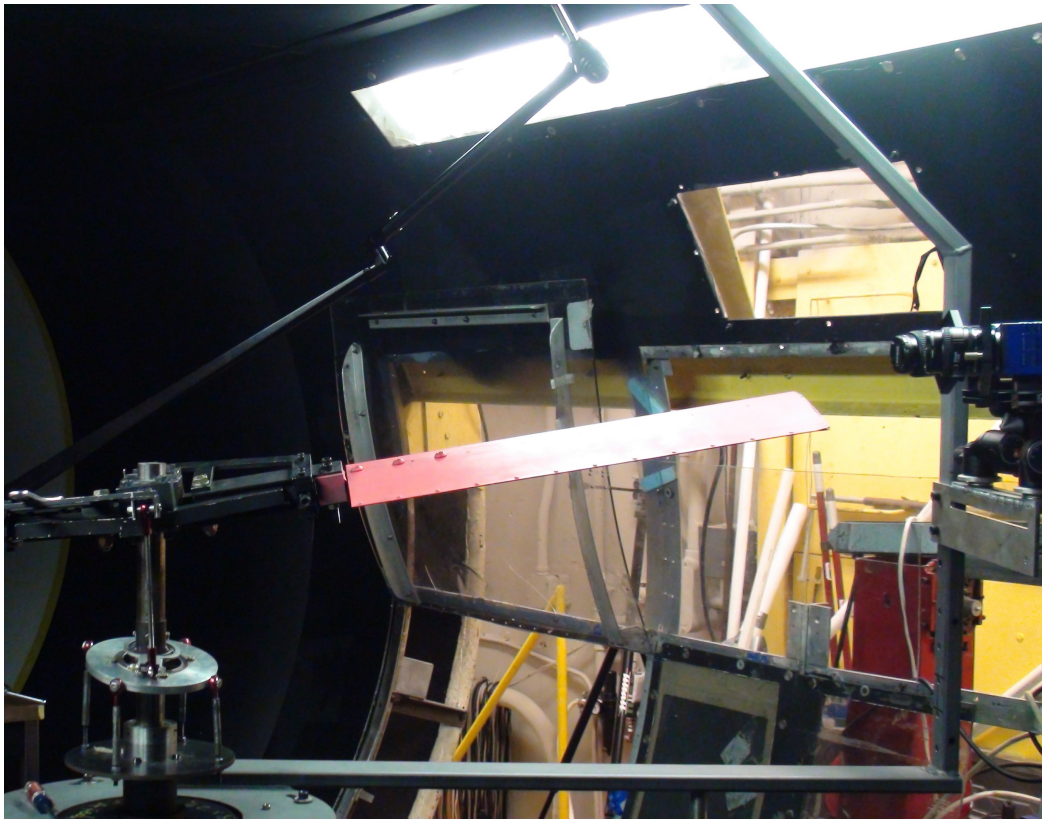

Figure 12: Setup of the retreating blade dynamic stall experiment with Stereo-PIV measurements

$0.5 \leq r/R \leq 0.7$ with spatial resolution of r/R = 0.1 as shown in Figure 13. Each measurement azimuthal and radial location is listed in Table 6 and each measurement point has a reduced frequency (k) and Reynolds number (Re) associated with it which is computed using the following expressions:

$$k = \frac{\Omega c}{2U_e} \tag{2a}$$

$$Re = \frac{U_e c}{\nu} \tag{2b}$$

$$U_e = U_T \frac{r}{R} + U_\infty \; sin\psi \tag{2c}$$

where Ω is the rotational rate, c is the chord length, ν is the kinematic viscosity of air, r/R is the non dimensional radial location, ψ is the azimuthal angle, and U_e is the effective velocity at a particular r/R and ψ.

Table 6: Experimental test points for $\Omega = 20.94$ rad/s : A is $\mu = 0.35$, B is $\mu = 0.40$, C is $\mu = 0.25$

ψ	r/R = 0.5	r/R = 0.6	r/R = 0.7
220°	ABC	ABC	–
230°	ABC	ABC	AB
235°	–	ABC	ABC
240°	–	ABC	–
255°	ABC	ABC	AB
265°	ABC	ABC	ABC
270°	ABC	ABC	ABC
280°	ABC	ABC	ABC
290°		ABC	ABC
300°	ABC	ABC	ABC
310°	ABC	ABC	ABC
315°	ABC	ABC	ABC
320°	ABC	ABC	–

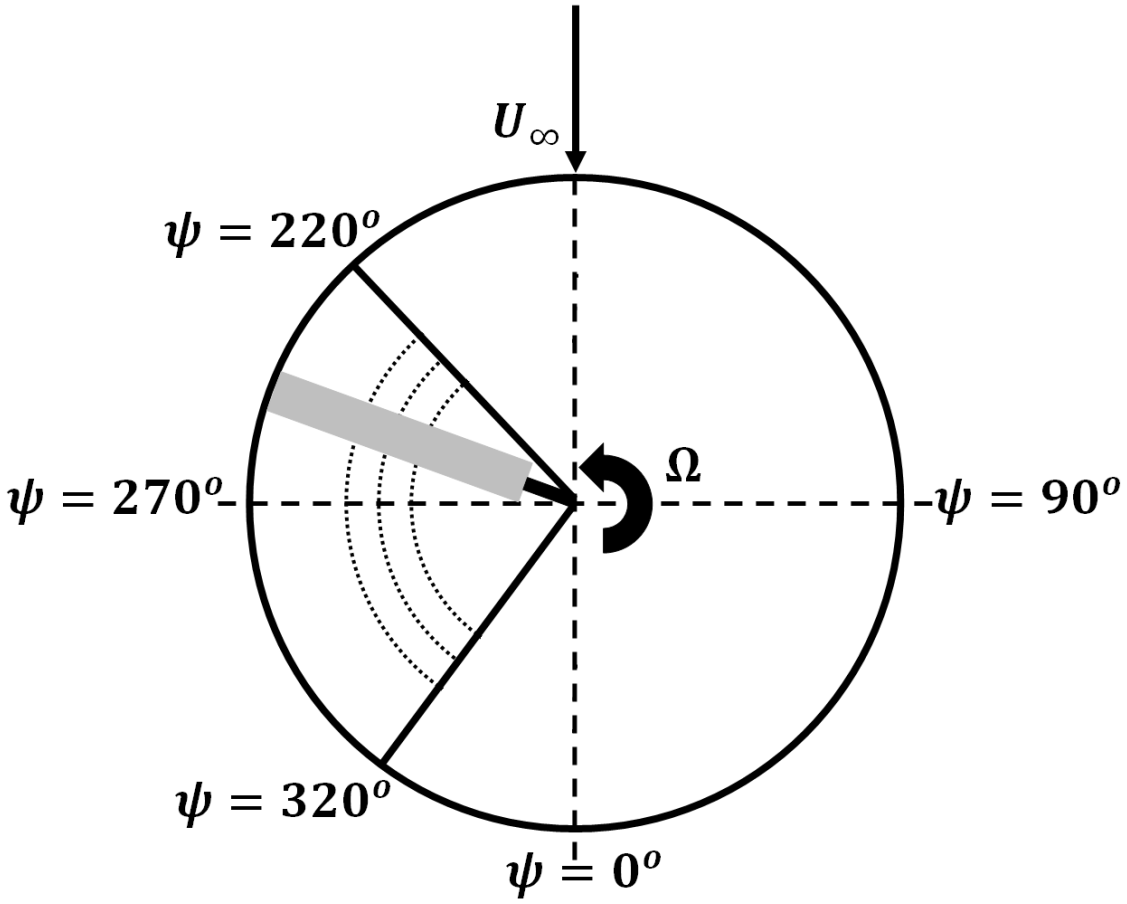

Figure 13: Figure illustrating the radial locations and azimuthal range for the experiments conducted - the inner most dotted circle is r/R = 0.5 and outermost is r/R = 0.7

2.3.2 PIV instrumentation

Due to the three-dimensional nature of the velocity field three component velocity measurements would give a better insight into the flow field dynamics. Hence, stereo-PIV was used to measure the velocity fields over the retreating rotor blade. The illumination was provided by a double-cavity Nd:YAG laser with a pulse energy of 200 mJ. The resulting beam diameter was about 3 mm with a pulse width of 5ns. A laser arm (a covered beam path) was used to deliver the laser beam to the measurement plane. Sheet optics was used at the end of the laser arm to generate a light sheet of 3 mm thickness. The flow was continuously seeded with approximately $10\mu m$ droplets generated by a Laskin-nozzle type indigenous aerosol generator.

McAlister [73] showed that fifty pitch cycles yielded converged statistics in the case of

force measurements during dynamic stall. Hence, drawing a similar parallel on the safer side a series of 100 image pairs were acquired at each measurement point using two PRO-X 2M camera which has a 1600×1200 pixel resolution and a pixel size of $7.4 \times 7.4 \mu m^2$. Due to limited optical access, the angle of the two cameras for the stereo-PIV setup was limited to between 15°–20° (the errors introduced due to this are computed in the accuracy estimates section). The particle size in the camera image ranged from 1.76 pixels to 2.81 pixels. The focal length of the lens system was 50 mm and the aperture on the camera was set at f/8. In order to improve the signal to noise ratio of the PIV data, the blade was coated with Rhodamine paint and a bandpass filter was used on the camera to minimize laser reflections from the upper surface of the blade. In addition, the unavoidable laser reflections were masked during the velocity vector computations.

DaVis 7.2 software provided by LaVision was used to process the PIV data, the velocities were calculated from the spatial cross-correlation of the images. An interrogation window overlap of 50% and a second interrogation pass with a reduced window size was used to increase the signal-to-noise ratio of the correlation peak. The first pass utilized an interrogation window of 64×64 pixels while 32×32 pixel window was used on the second pass. This yielded a velocity vector resolution of 1.8mm–2.1mm $\sim$ 0.01c–0.012c. Post-processing of the vector images consisted of an applied median filter and light smoothing for better visualization (3×3). As erroneous vectors appeared at the edges of the camera viewing window, these processes greatly reduced this noise.

2.3.3 Accuracy estimates

The uncertainty in flow conditions resulted in a Reynolds number uncertainty of ± 984. The uncertainty in collective pitch and cyclic pitch angle settings, which were measured using a digital protractor, is ±0.05°. The error in measurement of the angle of the tip path plane arises mainly due to the pixel size in image processing, and the uncertainty is 0.035°. The uncertainty in phase locking also estimated by image processing was ±0.05°.

The uncertainty in velocity measurements is computed using methods described in Appendix A.3. However, for stereo-PIV technique the errors introduced due to the angle of the

two cameras have to be accounted. Lawson [66] discusses the error introduced in the out-of-plane component of velocity (spanwise/radial velocity (w)) due to angle of the cameras. Although he suggests an angle between 20°–30° to minimize error, the error due to angle between 15°–20° can be computed from the results presented by Lawson. For the angles used in these experiments the RMS error for the out-of-plane component of displacement is between 2.8%–6%. Given that the light sheet thickness was maintained between 3–4mm and the magnification of the camera was $\frac{1}{16}$. Based on W_p measured in the radial plane (found to vary between 3.8–7.1 m/s) and U_p measured to be around 10.2 m/s the error in out-of-plane velocity component was computed using Equation 14. The error in out-of-plane component of velocity varies between 0.74% in the best case to 3.95% in the worst case. This amounts to an absolute error of 0.028 m/s–0.281 m/s based on W_p. It should be noted that this is only the error in the out-of-plane velocity component, the total error in measurements is to be derived from additional analysis of in-plane velocity component.

The in-plane velocity measurement errors are computed using methods described in Appendix A.3. Bias error was determined by plotting the probability density histograms of the instantaneous velocity data. With a resolution of 0.01 m/s the histograms did not reveal any peak-locking or any other experimental artifact. The lag error was estimated by considering the relaxation time of the seed particles (10μm) to changes in velocity. The characteristic time was defined as the time available for seed particle to respond to rapid changes in the flow, which was determined from the vorticity contours. A comparison showed that the characteristic time was 5–10 times greater than the relaxation time, indicating that the particle lag error was insignificant. Random error (σ_e) was computed by using Equation 13. For this experiment the random error ranged from 0.088 pixels in the best case (0.05×1.76 pixels) to 0.281 in the worst case (0.10×2.81 pixels).

Total measurement error for in-plane velocity measurements is quantified with Equation 14 from [91]. W_p was measured in the radial plane and was found to vary between 3.8–7.1 m/s, U_p was measured to be around 10.2 m/s, Z_s was maintained between 3-4 mm, M of the camera was $\frac{1}{16}$. σ_i amounted to $7.4 \times 10^{-6} \times \sigma_e$ ranging between 6.5×10^{-7} and 2.1×10^{-6}. Using these relations the total measurement error ϵ_m was estimated between

0.06% and 0.2%. This amounted to an absolute error of 0.006 m/s and 0.02 m/s based on U_p.

The total velocity measurement error is computed as a percentage by computing the magnitude of all the % measurement errors and it amounts to 0.75% in the best case and 3.96% in the worst case. It is no surprise that the total error is dominated by the out-of-plane measurement error which is much greater than in the in-plane velocity measurement error. Uncertainties in the velocity measurements are summarized in Table 7. The reader should note that the total measurement error reported here as a % is based on different base values (for example U_p for in-plane velocity error and W_p for out-of-plane velocity error). Hence the reader should excerise *caution* while interpreting these *total measurement errors.*

Table 7: Summary of uncertainty estimates for stereoscopic-PIV measurements

Type	Error
In-plane random error	0.088–0.281 pixels
Bias Error	0.01 m/s
Bias Error ($\%U_p$)	0.098%
Lag Error	Insignificant
In-plane velocity error	0.006 m/s–0.02 m/s
In-plane velocity error ($\%U_p$)	0.06%–0.2%
Out-of plane velocity error	0.028 m/s–0.281 m/s
Out-of plane velocity error ($\%W_p$)	0.74%–3.95%
Total measurement error (%)	0.75%–3.96%

2.4 Results and discussion

In all the PIV vector fields presented in this work, the axis of the camera images is fixed in the wind tunnel coordinate system and has not been corrected for the pitch angle of the blade. However, the origin (0,0) is the location of the leading edge in all the vector fields. The x axis is positive to the right, the z axis is positive downwards and the y axis positive out-of-plane of the paper completing the right handed coordinate system. All the dimensions are normalized by chord length, where x/c = 0 is the leading edge and x/c = -1

is the trailing edge of the blade. With the y axis as defined, out-of-plane velocity is positive and it indicates the radially outwards flow towards the tip of the blade. Negative out-of-plane velocity indicates a radially inward flow towards the root of the blade. In addition, for better visualization and analysis the corresponding freestream velocity component (velocity in the x direction) has been subtracted from the velocity vector fields.

2.4.1 Phase-averaged velocity fields

In this section, the analysis is performed assuming the existence of a dominant phase-locked average flow field. In this section the phase-averaged characteristics of process of dynamic stall is discussed. At $\psi = 180^\circ$ the blade begins the up stroke part of the oscillatory motion (with datum as the collective angle), it reaches its maximum pitch angle at $\psi = 270^\circ$ and there onwards undergoes the down stroke motion. Beginning with dynamic separation which occurs for yaw angles $225^\circ \leq \psi \leq 230^\circ$, moving on to the dynamic stall event itself for yaw angles $235^\circ \leq \psi \leq 315^\circ$ and finally the dynamic reattachment for yaw angles $315^\circ \leq \psi \leq 320^\circ$. In addition, using this velocity field data, pressure distribution data is obtained by solving for various levels of the Navier-Stokes equations.

2.4.1.1 Dynamic separation

Earlier, the mechanisms of dynamic stall onset and dynamic separation were discussed as the following: *a*) classic trailing edge separation, *b*) shock induced separation, and *c*) bursting of a separation bubble. It would be critical to first assess the expected mechanisms in play on the rotating blade in the experiments in this work. The experiments are conducted at very low Mach numbers and hence we can safely assume that the shock-induced separation mechanism would *not* be in play. However, the other two mechanisms a) and c) could be manifesting themselves in these experiments. Due to the nature of these two mechanisms, the classical trailing edge separation mechanism would be easier to identify, since it is a progressive mechanism and has a slow onset time. Since the bursting of the separation bubble is a random event and has a significant cycle-to-cycle variation, the role of this mechanism in the dynamic separation event would be harder to ascertain.

The first indication of the dynamic separation was observed at $\psi = 220°$. Figures 14–15 illustrate the phase-averaged velocity field overlaid on the contours of two dimensional velocity magnitude for the retreating blade at $\psi = 220°$, r/R = 0.5 at two advance ratios. Very clearly the flow close the trailing edge has separated, evident by the unattached flow close the surface of the wing for $x/c \leq -0.3$ in Figure 14 and for $x/c \leq -0.11$ in Figure 15. A primary difference that can be observed is that with the increase in advance ratio the onset of trailing edge separation is quicker. In other words at higher advance ratio (μ=0.4) the trailing edge separation onset is at a earlier azimuthal angle when compared to the lower advance ratio (μ=0.35).

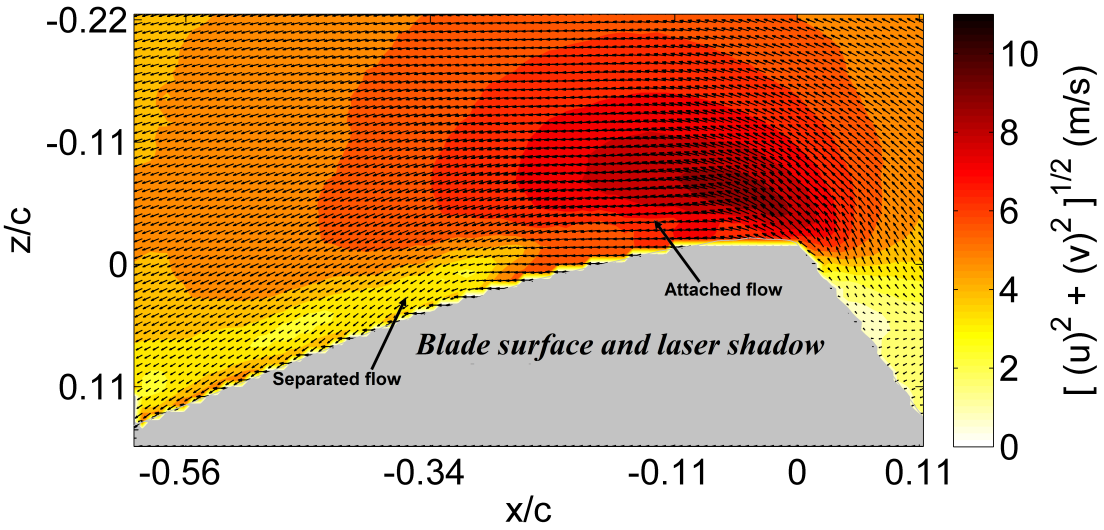

Figure 14: Velocity field at $\psi = 220°$, r/R = 0.5, $\mu = 0.35$ showing separation at trailing edge

On moving outboard to r/R = 0.6 at the same flow conditions the trailing edge separation is less apparent. Figures 16–17 illustrate the phase-averaged velocity field overlaid on the contours of two dimensional velocity magnitude for the retreating blade at $\psi = 220°$ and r/R = 0.6. The effect of moving outboard can be clearly observed by comparing Figure 16 with Figure 14. At r/R = 0.5 the separated flow has progressed further towards the leading edge than at r/R = 0.6, which indicates that the separation first begins at inboard locations and then progresses to outboard locations.

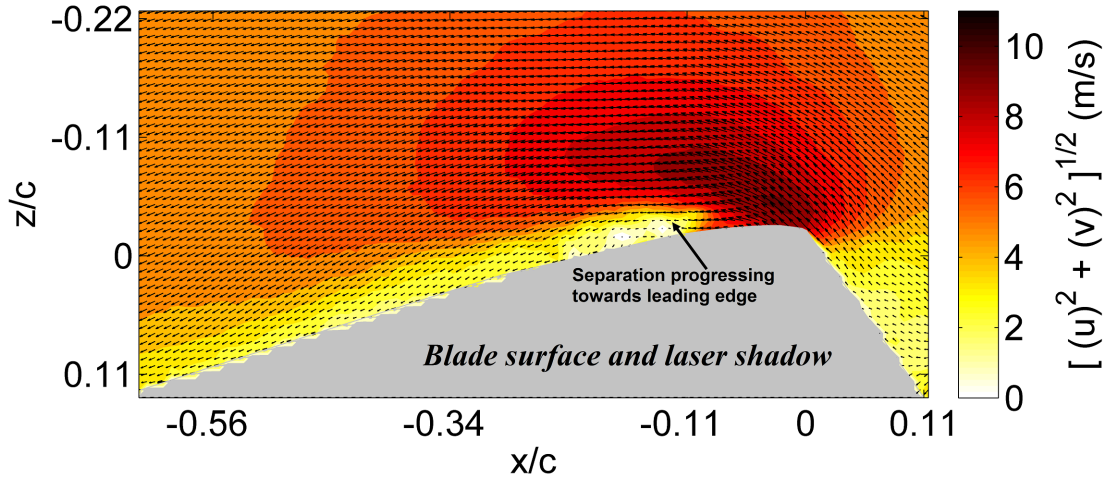

Figure 15: Velocity field at $\psi = 220°$, r/R = 0.5, $\mu = 0.4$ showing the progression of separation at trailing edge at higher advance ratio

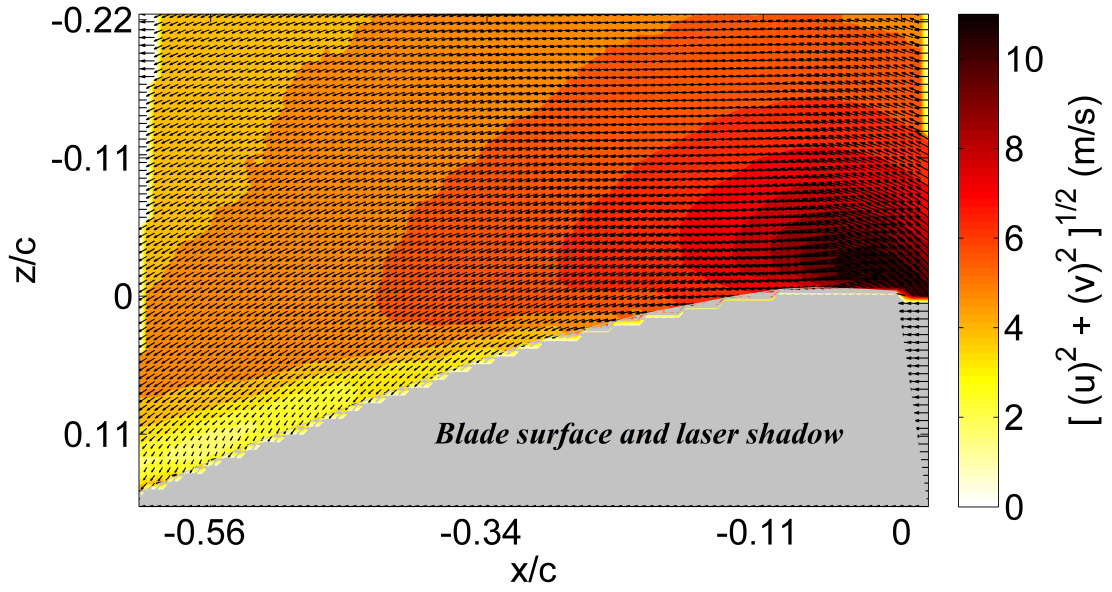

Figure 16: Velocity field at $\psi = 220°$, r/R = 0.6, $\mu = 0.35$ indicating the delayed onset of trailing edge separation

In summary, the analysis of the phase-averaged data clearly indicates that the separation begins at the trailing edge and slowly progresses upstream towards the leading edge. The trailing edge separation onset was clearly initiated well before $\psi = 220°$, but it should be noted that this angle is not classified as the onset of dynamic stall. In addition, the data

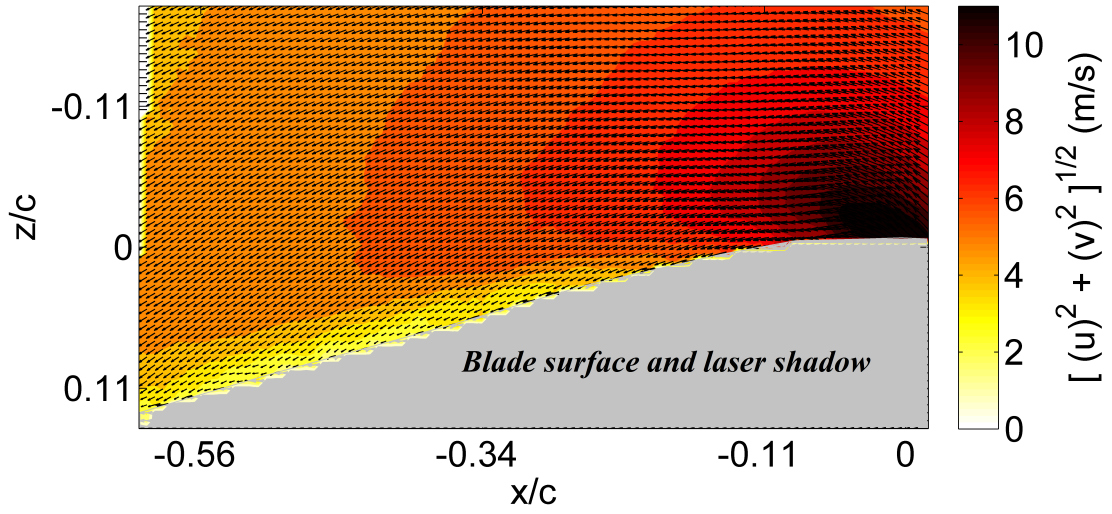

Figure 17: Velocity field at $\psi = 220°$, r/R = 0.6, $\mu = 0.4$ indicating the delayed onset of trailing edge separation

also indicates that the separation occurs at an earlier azimuthal location at higher advance ratios. Furthermore, the separation appears to first occur at inboard radial locations and then move to outboard locations.

The onset of stall in this work was classified as the time instant when leading edge separation was established. Hence, further measurements were made between $226.4° \leq \psi \leq 230°$. At $\psi = 230°$, the phase-averaged velocity field indicates that at r/R = 0.5 the separation has progressed to the leading edge and the complete upper surface of the wing is now separated. The separation at the leading edge at both advance ratios $\mu = 0.35$ and $\mu = 0.4$ at r/R = 0.5 can be observed in Figures 18 and 19. Again the differences between the two advance ratios can be observed by the fact that the separation appears stronger (the separated layer is thicker) for $\mu = 0.4$.

However, on moving outboard to r/R = 0.6 the velocity field (see Figure 20) shows striking difference when compared to the r/R = 0.5 location (see Figure 18) for the same flow condition ($\mu = 0.35$). These figures provide clear evidence to support the earlier conclusion that at the same flow conditions separation first occurs at inboard location and then progresses to outboard locations. Similar differences can be observed at $\mu = 0.4$

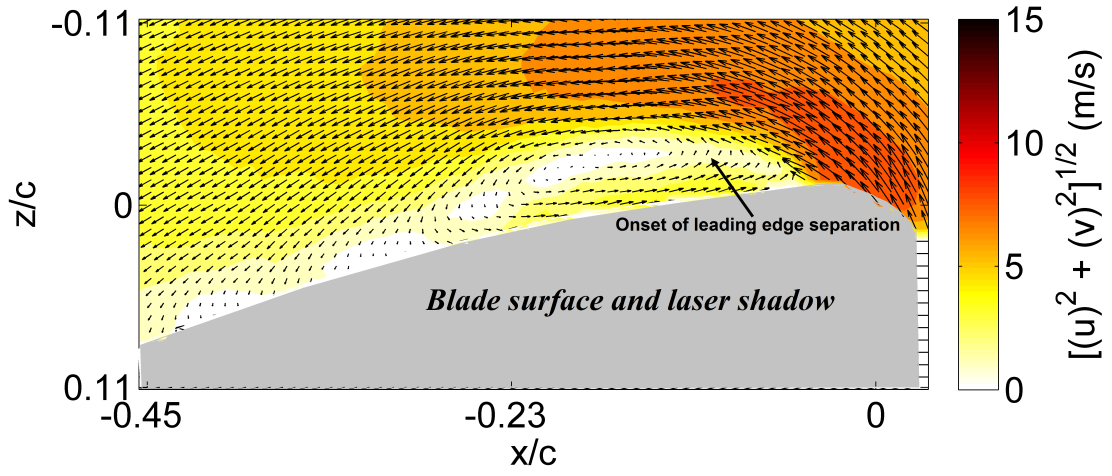

Figure 18: Velocity field at $\psi = 230°$, r/R = 0.5, $\mu = 0.35$ illustrating leading edge separation and onset of dynamic stall

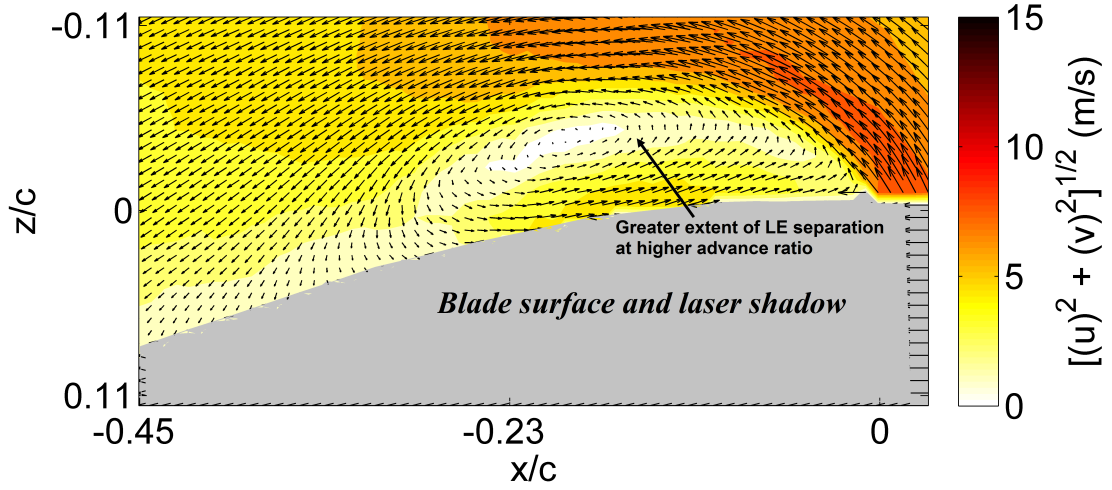

Figure 19: Velocity field at $\psi = 230°$, r/R = 0.5, $\mu = 0.4$ illustrating leading edge separation and onset of dynamic stall

between r/R = 0.5 and 0.6 (see Figures 19 and 21), where for r/R = 0.5 the leading edge separation appears to be more developed than at r/R = 0.6.

As mentioned earlier, the analysis in this section was performed assuming a dominant phase-averaged velocity field. Although this analysis provides a general indication of the

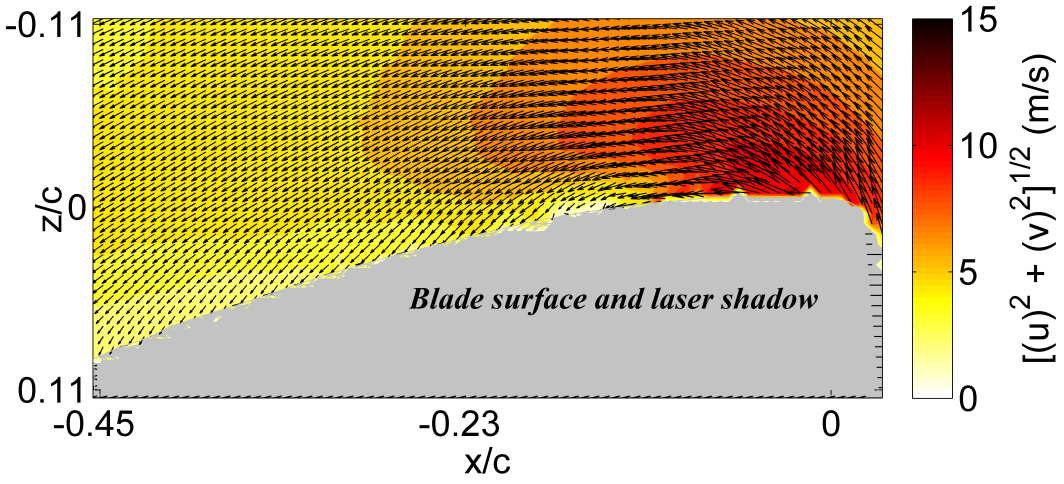

Figure 20: Velocity field at $\psi = 230°$, r/R = 0.6, $\mu = 0.35$

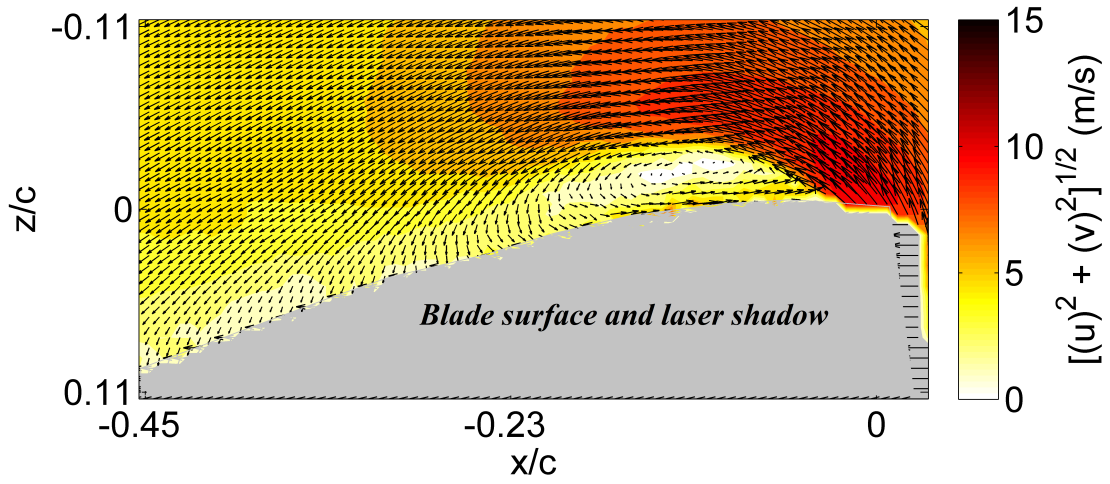

Figure 21: Velocity field at $\psi = 230°$, r/R = 0.6, $\mu = 0.4$

behavior of the averaged flow field, it does represent the exact details of the cycle-to-cycle variations of the separation event. Cycle-to-cycle variations were observed to an extent where certain instants had no indication of separation. Hence, if the phase-averaged velocity fields exhibit evidence of separation it only means that the majority of the instantaneous velocity fields were separated. To determine a more accurate representation of the cycle-to-cycle separation a conditional averaging could be used.

2.4.1.2 Dynamic stall (DS) event

The DS event in this thesis is referred to the event after leading edge separation occurs and before leading edge reattachment occurs that is for yaw angles $235^\circ \leq \psi \leq 305^\circ$. Having characterized the general details of the dynamic separation with respect to advance ratio and radial location. Clearly, the dynamic separation event varies with both the parameters advance ratio and radial location. To simplify the presentation and understanding of the DS event, the analysis will be performed through the yaw angles at one specific radial location (r/R = 0.6) and allow for limited variation of the advance ratio ($\mu = 0.35$ and $\mu = 0.4$). Choosing one radial location eliminates one extra variable (radial location) and allows for a systematic understanding by varying one other variable (advance ratio). This choice is preferred mainly because this section deals with gaining a fundamental understanding of the DS life cycle, which would be "similar" at any radial location.

In addition, detecting vortices in a flow is a challenge especially using iso-vorticity contours which can yield itself to substantial errors. Hence, in order to effectively characterize the vortical structure a vortex detection technique via metrics such as Γ_1 (also called Normalized Angular Momentum (NAM)) proposed by [40] was used. Γ_1 is defined as the following and described in detail in Appendix D.1.

$$\Gamma_1(P) = \frac{1}{N} \sum_{S} \frac{(PM \times U_M) \cdot z}{\|PM\| \cdot \|U_M\|} \tag{3}$$

a value of N = 3 yielded appropriate results with sufficient detail to discern the vortex.

A. $\psi = 235^\circ$

Figures 22 and 23 illustrate the phase-averaged velocity field overlaid on vorticity contours at $\psi = 235^\circ$ at r/R = 0.6 for advance ratios 0.35 and 0.4 respectively. Both the velocity fields comprise of a dominant vortical structure in the flow field, although the relative position of the vortex is different at the two advance ratios. The difference in the position of the vortex is attributed to the timing of the onset of dynamic stall, which was shown to occur earlier at higher advance ratio and the flow field is hence more evolved at $\mu = 0.4$. A comparison of the velocity vectors in Figures 21 and 23

demonstrates the evolution of the flow field after the onset of the leading edge separation. The phase-averaged vortex appears to have enlarged and convected away from the leading edge towards the trailing edge of the wing.

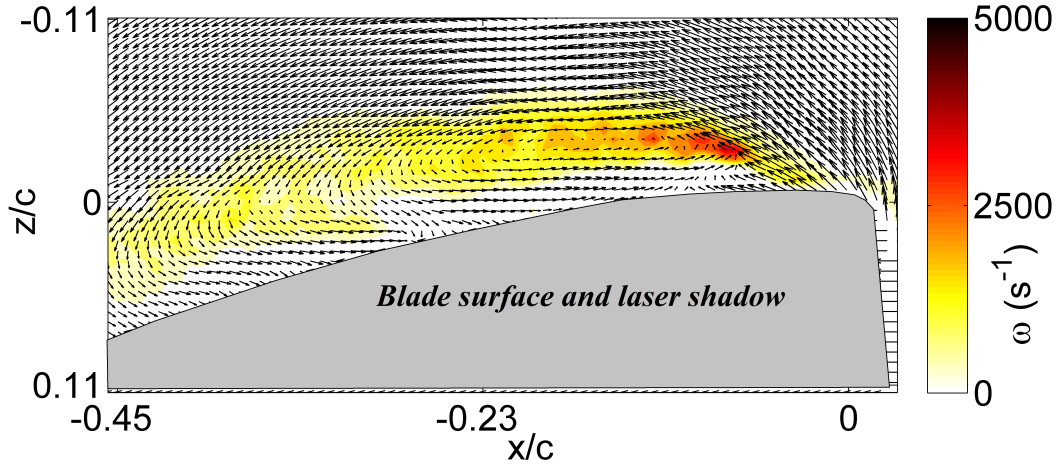

Figure 22: Velocity field at $\psi = 235°$, r/R = 0.6, $\mu = 0.35$

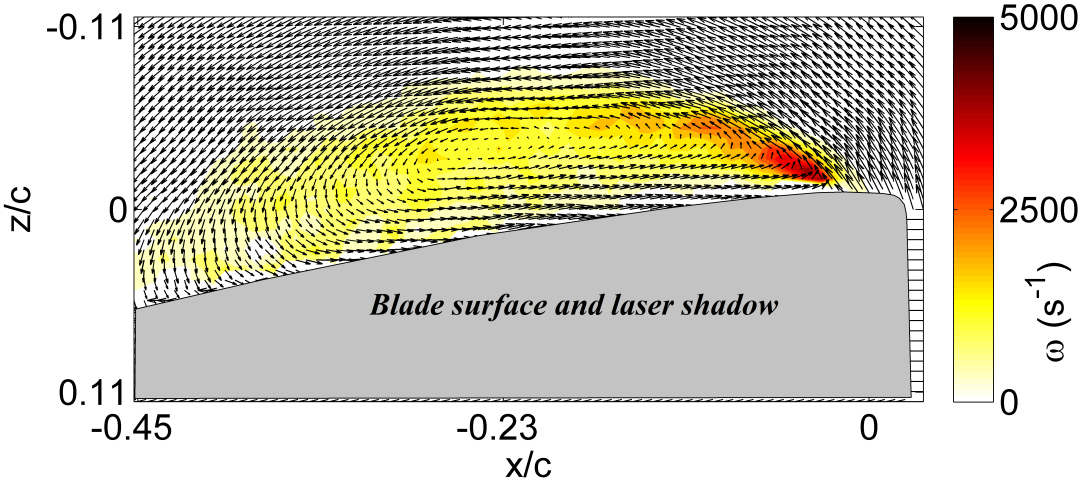

Figure 23: Velocity field at $\psi = 235°$, r/R = 0.6, $\mu = 0.4$

The phase averaged vortical structure can be observed in the NAM plots shown in Figures 24 and 25. The region with the highest value of Γ_1 is defined as the center of the vortex. Due to the unsteady nature of the flow field the phase-averaged velocity field

might have more than one maximum value in the flow field. This does not indicate the existence of two vortices, instead it indicates a spatially diffused version of the unsteady nature of the flow field. The NAM plots confirm the observation that the vortex appears to have have enlarged and lifting off the surface at the higher advance ratio ($\mu = 0.4$).

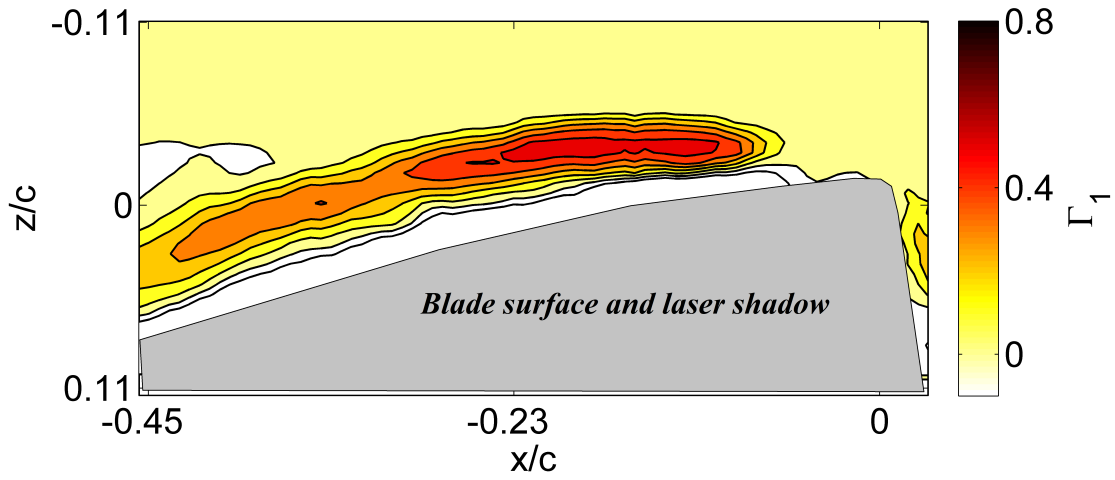

Figure 24: NAM plot at $\psi = 235°$, r/R = 0.6, $\mu = 0.35$

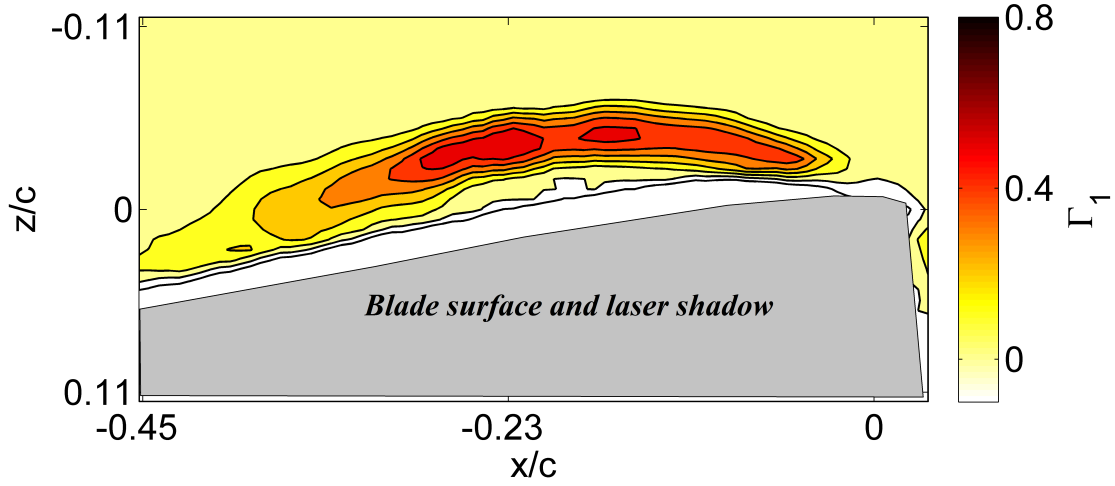

Figure 25: NAM plot at $\psi = 235°$, r/R = 0.6, $\mu = 0.4$

B. $\psi = 252.6°$

Figure 26 illustrates the velocity vector field overlaid on vorticity contours at $\psi = 252.5°$ for r/R = 0.6 and $\mu = 0.4$. The phase-averaged vortical structure has evidently lifted off the surface of the wing and has enlarged in size. Evidence of the vortex lifting off the surface of the wing and enlarging is also evident from Figure 27, which illustrates the NAM plot for the flow field.

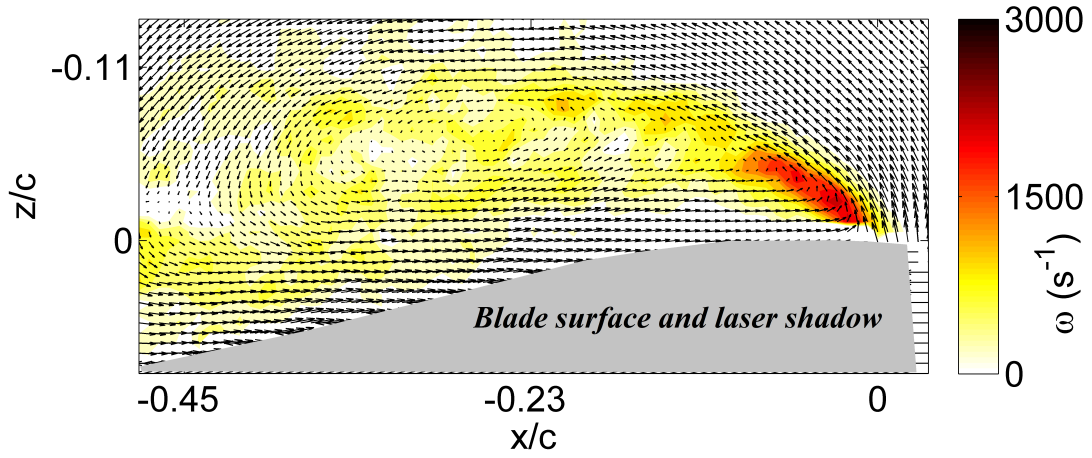

Figure 26: Velocity field at $\psi = 252.6°$, r/R = 0.6, $\mu = 0.4$

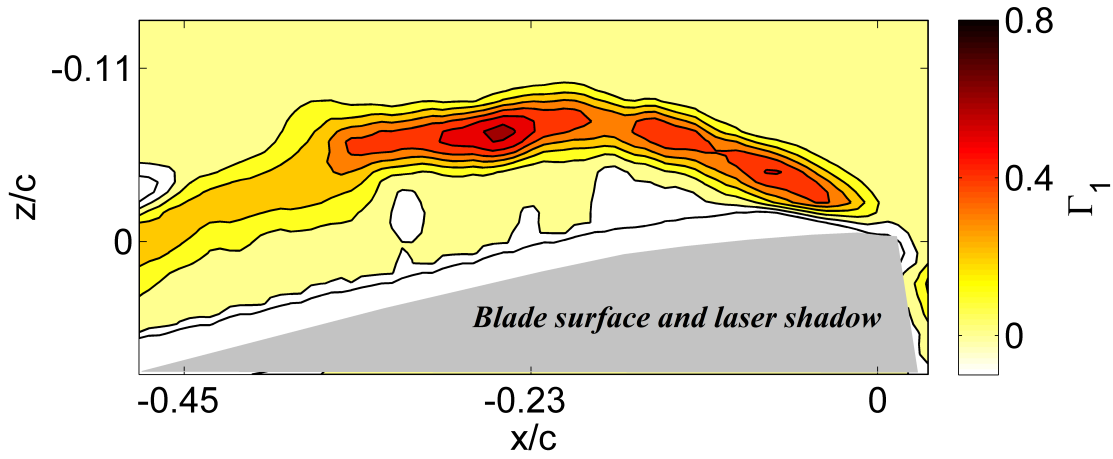

Figure 27: NAM plot at $\psi = 252.6°$, r/R = 0.6, $\mu = 0.4$

C. $\psi = 262.6°$

At the next yaw angle of $\psi = 262.6°$, the flow field has evolved some more in that the velocity field shows the enlargement of the vortical structure more than at $\psi = 252.6°$ as seen in Figure 28. In addition, the NAM plots show 2–3 distinct locations where the Γ_1 has a maximum value as observed in Figure 29. As discussed earlier this indicates that the instantaneous flow field has a significant cycle-to-cycle variation which causes the phase-averaged vortex to appear spatially diffused with multiple centers. Furthermore, scrutinizing Figures 25, 27 and 29 it is apparent that the cycle-to-cycle variations of the flow field *increases* as the DS cycle progresses in yaw angle which can be interpreted as the time line DS life cycle.

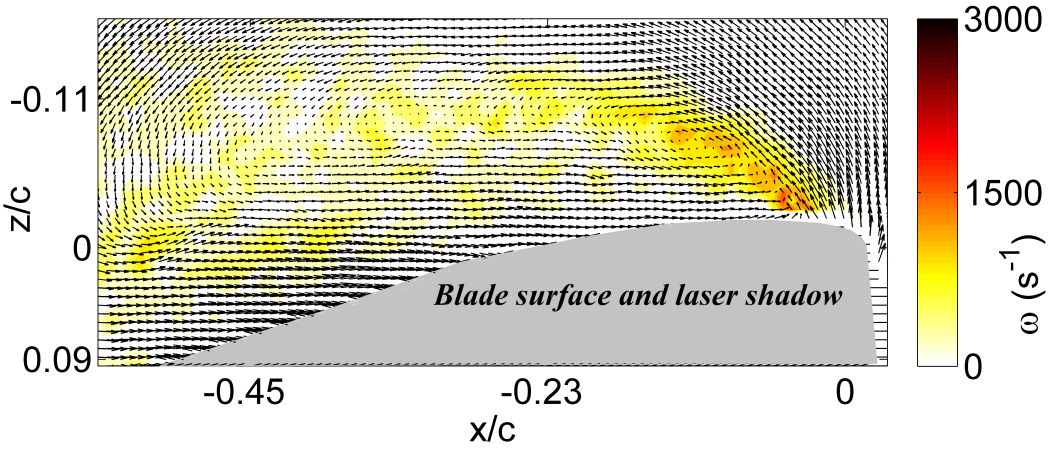

Figure 28: Velocity field at $\psi = 262.6°$, r/R = 0.6, $\mu = 0.4$

D. $\psi = 270°$

This particular yaw angle is a critical and interesting time instant in the life cycle of the DS event over a rotating blade. The reason for this is that at $\psi = 270°$ the spanwise flow (radial flow) is purely due to the reactive centrifugal forces rather than the yaw

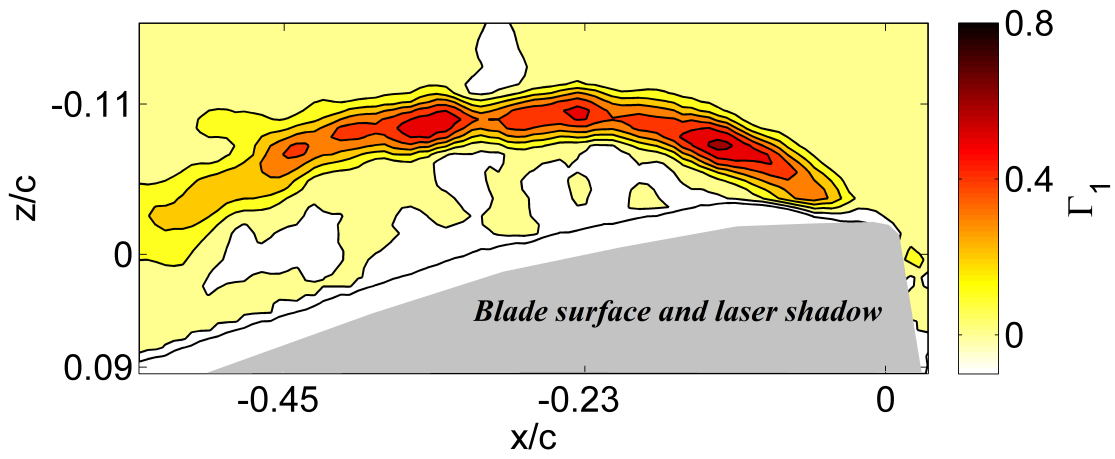

Figure 29: NAM plot at $\psi = 262.6°$, r/R = 0.6, $\mu = 0.4$

induced spanwise flow which occurs at all other yaw angles. Hence this particular yaw angle allows for a systematic study of the effect of "pure" radial flow (due to reactive centrifugal forces) on the DS event at $\psi = 270°$. This investigation is performed in detail in Chapter 3 using 2D PIV measurements with finer resolution spanwise measurements. Since this chapter deals with just the life cycle of DS event, the flow at $\psi = 270°$ is discussed as a part of the life cycle of the DS event. At this yaw angle the pitch angle has reached a maximum of $\theta = 15°$, hence this would be the maximum angle of attack over the whole rotor azimuth. Hence the flow field at this yaw angle is expected to depict the zenith of the separated flow field over the blade. The Figure 30 illustrates the velocity vector field overlaid on iso-vorticity contours, which again show an enlargement of the vortex over the blade. The NAM plot at this yaw angle (31) indicate that the location of the center of the vortex above the surface of the blade has increased.

E. $\psi = 280°$

For $\psi \geq 270°$ the blade is undergoing the down stroke motion and hence represents the time instants where the process of reattachment would start. This can be clearly

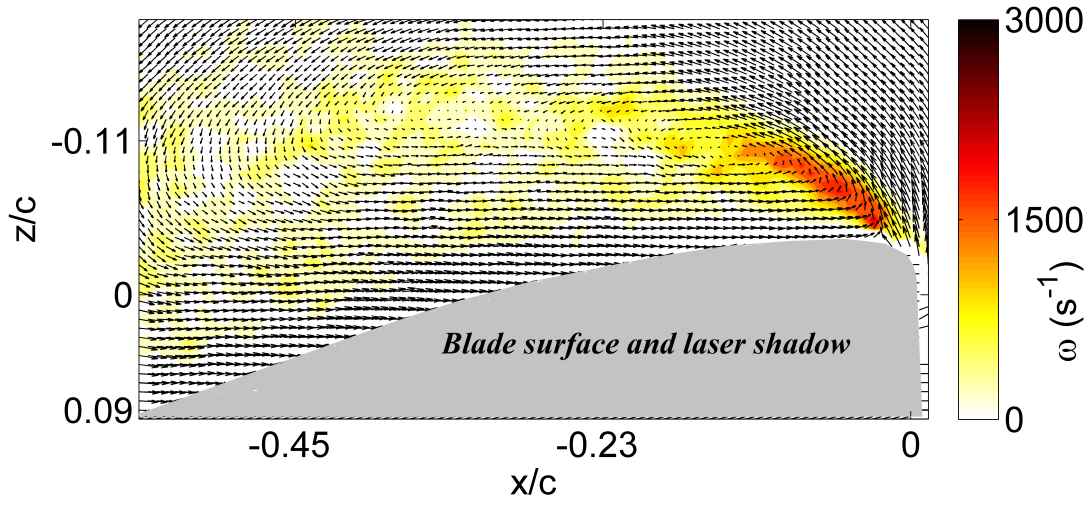

Figure 30: Velocity field at $\psi = 270°$, r/R = 0.6, $\mu = 0.4$

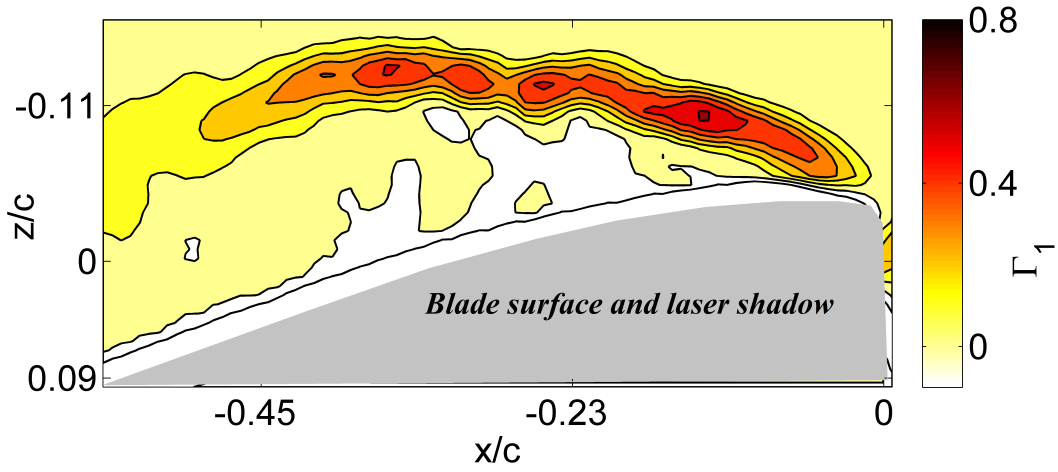

Figure 31: NAM plot at $\psi = 270°$, r/R = 0.6, $\mu = 0.4$

observed in the plots shown in Figures 32 and 33. A cursory look at the velocity field data does not indicate any significant differences between $\psi = 270°$ and $\psi = 280°$. However, the height of the separated region above the surface of the wing has reduced, which is also clearly evident in the NAM plot. One other critical observation in the NAM plot is the concentration of angular momentum at around x/c = -0.45, this could

indicate that it is around this stage when the vortex separates from the surface of the blade and convects with the freestream. However, these plots are only an indication of the phase-averaged behavior, the instantaneous velocity field analysis will allow for a better interpretation of the data.

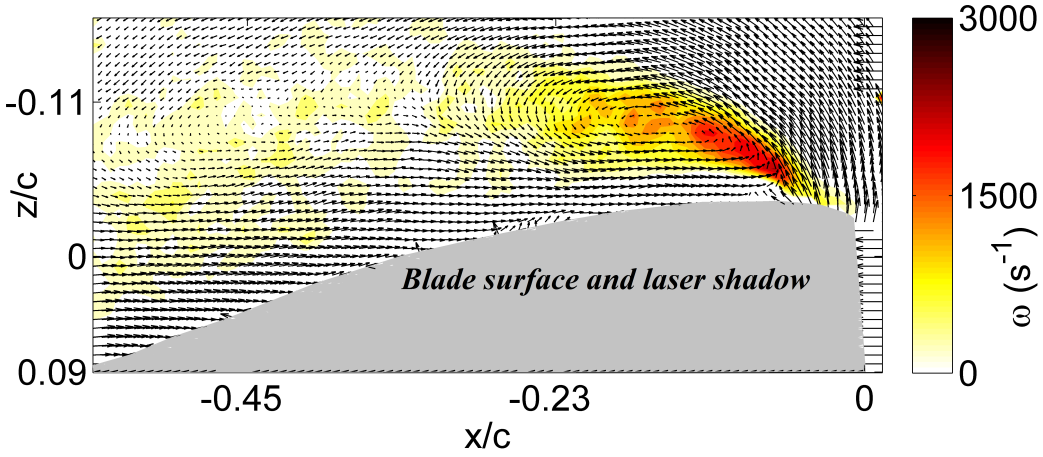

Figure 32: Velocity field at $\psi = 280°$, r/R = 0.6, $\mu = 0.4$

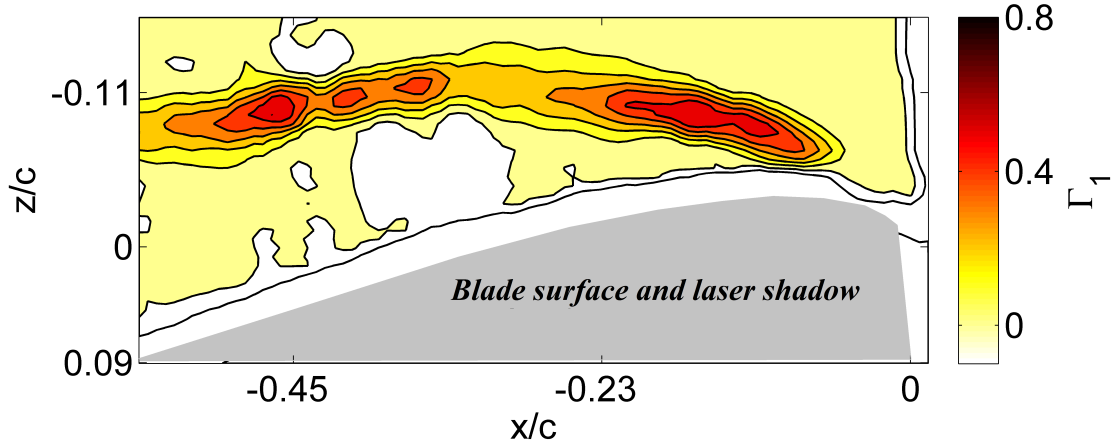

Figure 33: NAM plot at $\psi = 280°$, r/R = 0.6, $\mu = 0.4$

F. $\psi = 290°$

At this yaw angle the measured velocity field indicates that the extent of flow separation is lesser than at the yaw angle where the angle of attack was the highest. The phase-averaged velocity vector field illustrated in Figure 34 suggests that the vortical structure over the surface of the blade is shrinking in size. In addition, the NAM plot illustrated in Figure 35 reveals that the vortical structure is also moving closer to the surface of the blade. Furthermore, it also shows that there is one predominant peak in the Γ_1 value, which following arguments made earlier about the cycle-to-cycle variations of the flow field, indicates that the cycle-to-cycle variations is only nominal.

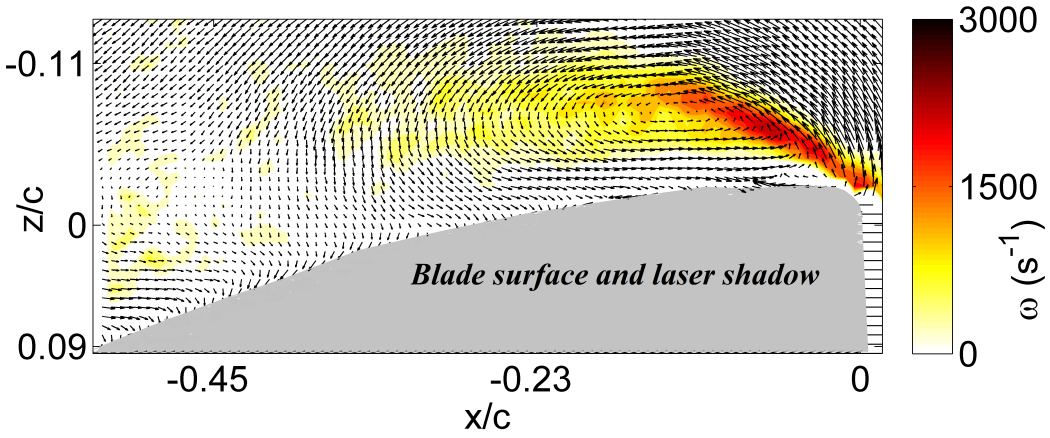

Figure 34: Velocity field at $\psi = 290°$, r/R = 0.6, $\mu = 0.4$

The Figure 36 summarizes the phase-averaged NAM plots at each yaw angle measurements were made during the DS cycle. In summary, an apparent trend can be observed in the behavior of the phase-averaged vortex over the retreating blade in dynamic stall conditions. Soon after separation the vortex is formed and appears elongated and pinned to the surface of the blade at $\psi = 235°$. As the yaw angle increases the vortex lifts off the blade surface and reaches its peak height at $\psi = 270°$ which is the yaw angle at which the blade has achieved the maximum angle of attack. Thereafter, the blade undergoes the down stroke motion and the vortex proceeds to descend towards the blade surface and is

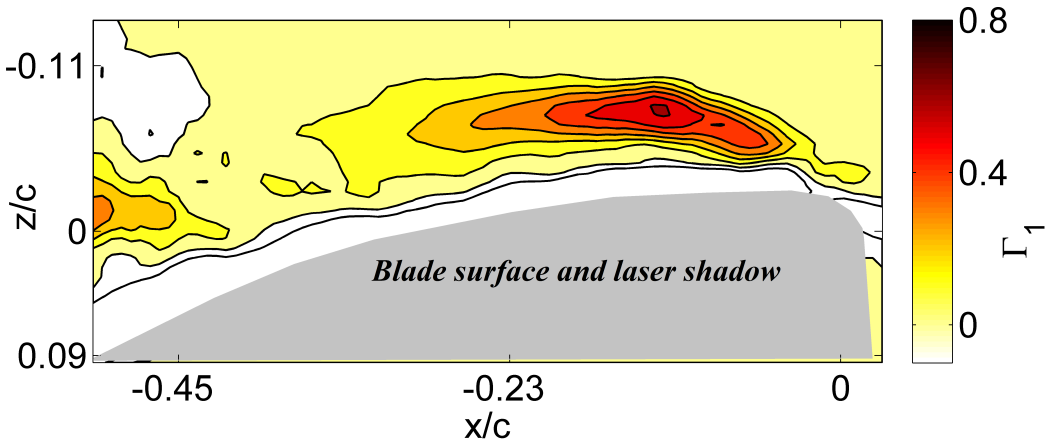

Figure 35: NAM plot at $\psi = 290°$, r/R = 0.6, $\mu = 0.4$

again appears pinned to the surface at $\psi = 290°$. In addition, as the yaw angle increases the NAM plots indicate that the angular momentum is a maximum at several locations within the phase-averaged vortex. The fact that there are multiple maximum values indicate that the cycle-to-cycle variations is significant and hence presents itself as a spatially diffused vortical structure with multiple maximas in the phase-averaged data. Again a clear trend can be observed with respect to the magnitude of the cycle-to-cycle variations. As yaw angle increases the cycle-to-cycle variations appear to increase up to yaw angle $\psi = 270°$, it then proceeds to decrease.

Since, the measurements gathered in this investigation comprise three components of velocity, the variation of the out-of-plane velocity component (radial velocity) can also be analyzed. The out-of-plane velocity has been corrected for the yaw induced spanwise velocity by using the following expression:

$$U_r = U_y - U_\infty cos\psi \tag{4}$$

where U_y is the out-of-plane velocity, U_∞ is the freestream velocity, ψ is the yaw angle at which the measurements are made. This corrected velocity allows for a better interpretation of the out-of-plane velocity component by accounting for the spanwise flow induced due to

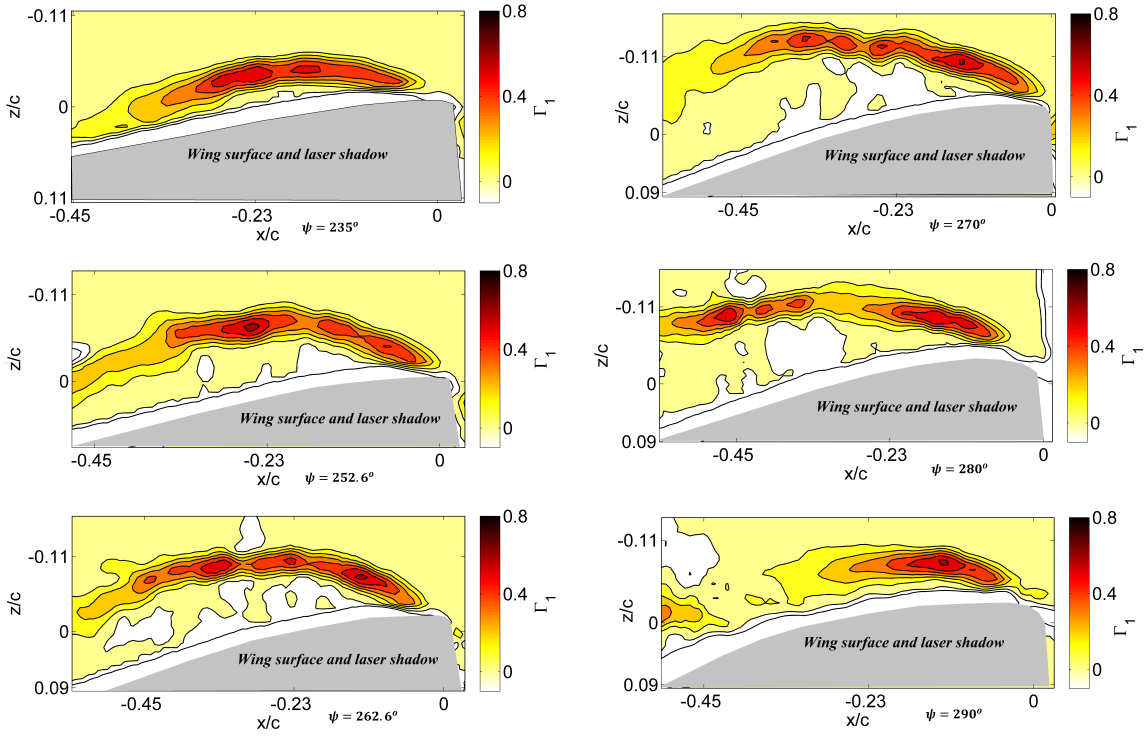

Figure 36: Summary of phase-averaged NAM plot for DS cycle at r/R = 0.6 and $\mu = 0.4$

yaw angle of the blade. The velocity component that remains, is the out-of-plane velocity that is induced to reactive centrifugal forces. Moreover, the corrected out-of-plane velocity component far away from the blade surface should be expected to maintain a value close to zero. Figure 37 illustrates the velocity field overlaid on contours of the out-of-plane velocity for various yaw angles $230° \leq \psi \leq 310°$ at r/R = 0.6 and $\mu = 0.4$ flow condition. With the axis defined as x positive to the right and z positive downwards, a positive out-of-plane velocity indicates flow from the root to the tip of the blade and vice versa. Evidently, the radial velocity component of flow is significant only in the separated flow regions, especially at yaw angles where the complete upper surface of the blade is separated. In addition, radial velocity is positive (towards the tip of the blade) closer to the surface of the blade mainly due to reactive centrifugal forces due to rotation of the blade. As expected, the radial velocity far away from the surface of the blade subsides to zero velocity. The magnitude of maximum radial velocity increases with yaw angle and reaches a peak at $\psi = 270°$, which is also the yaw angle at which the flow is massively separated and is the most unsteady (please

refer to Figure 36). This is convincing evidence that the separated flow region on a rotating blade typically has a significant radial flow (induced due to centrifugal forces) from the root to the tip of the blade.

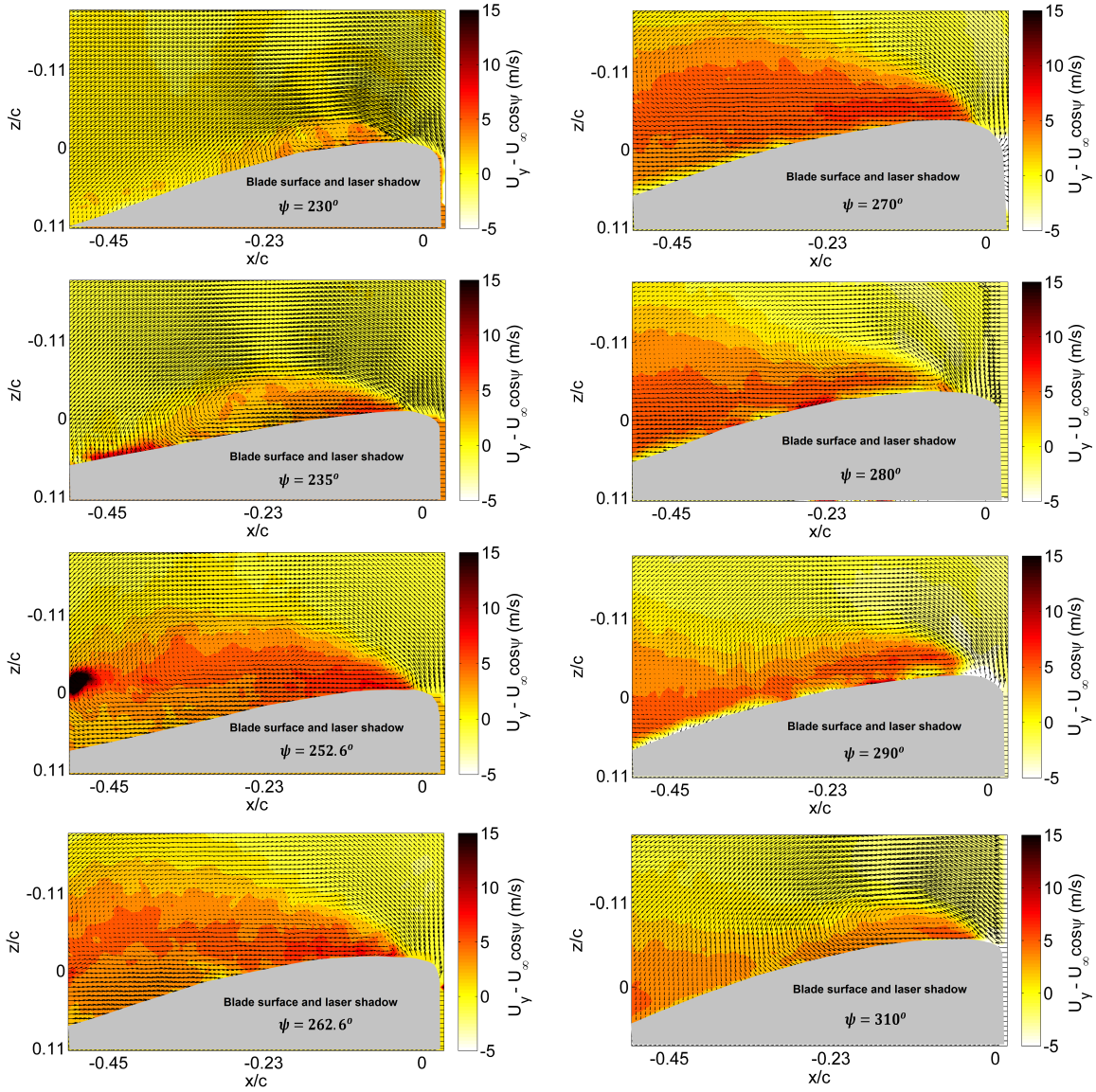

Figure 37: Summary of phase-averaged velocity overlaid on out-of-plane velocity component for DS cycle at r/R = 0.6 and $\mu = 0.4$

2.4.1.3 Dynamic reattachment

Following the DS event the blade undergoes the down stroke motion by reducing its pitch angle, at a sufficiently low pitch angle the angle of attack is conducive for the commencement

of the reattachment phase. As observed in the previous section (see Figure 36), the dynamic stall vortex shrunk in size after reaching it's peak at around $\psi = 270°$. For the flow conditions investigated in this work, reattachment is defined as the time instant in the DS life cycle where the leading edge flow reattaches. In these investigations reattachment was observed to occur between $315° \leq \psi \leq 320°$.

Figures 38 and 39 illustrate the velocity field and the NAM field over the rotating blade at $\psi = 315°$, r/R = 0.6 and $\mu = 0.4$. When compared to $\psi = 310°$, the flow has completely attached on all sections of the blade except at the leading edge, where the existence of a vortical structure indicates separated flow. The NAM field confirms the existence of a vortical structure very close to leading edge.

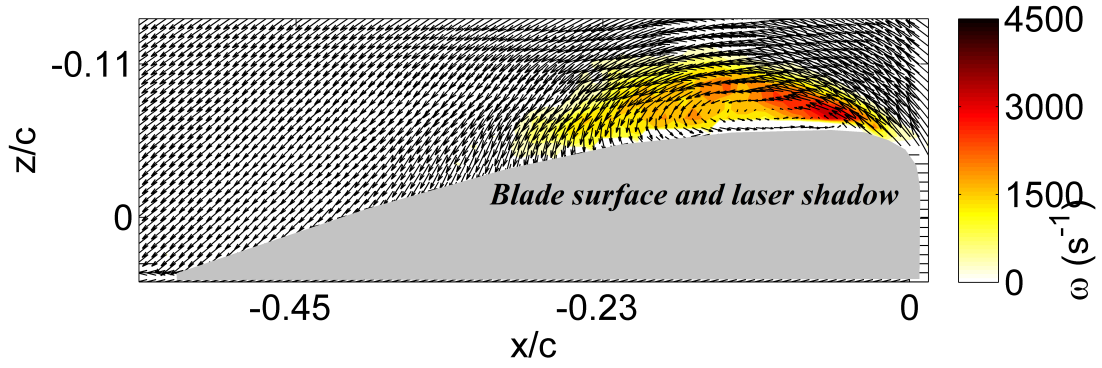

Figure 38: Velocity field at $\psi = 315°$, r/R = 0.6, $\mu = 0.4$

On moving to $\psi = 320°$ the phase-averaged flow field shows minimal evidence of separation over the blade. As observed in Figures 40 and 41 the flow is predominantly attached on all sections of the blade. This is also again confirmed from the NAM field where there is no evidence of a vortical structure in the flow field, indicating attached flow all over the surface of the blade.

2.4.2 Instantaneous velocity fields

Phase-averaged analysis provides a good general understanding of the velocity field over a rotating blade in dynamic stall. However, as discussed earlier dynamic stall is a highly

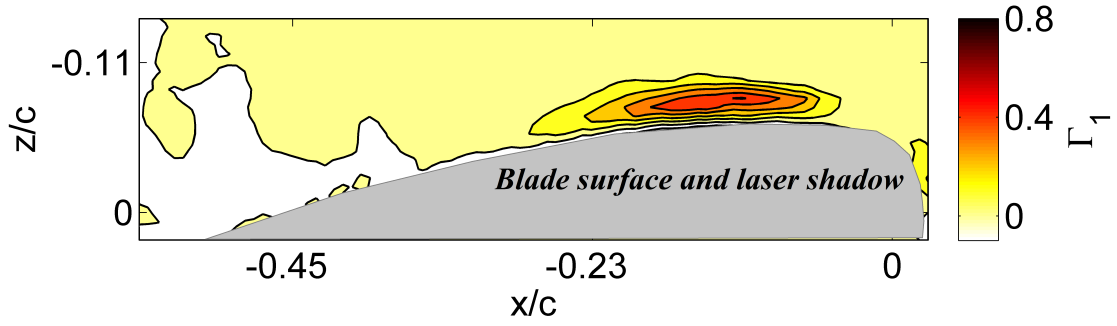

Figure 39: NAM plot at $\psi = 315°$, r/R = 0.6, $\mu = 0.4$

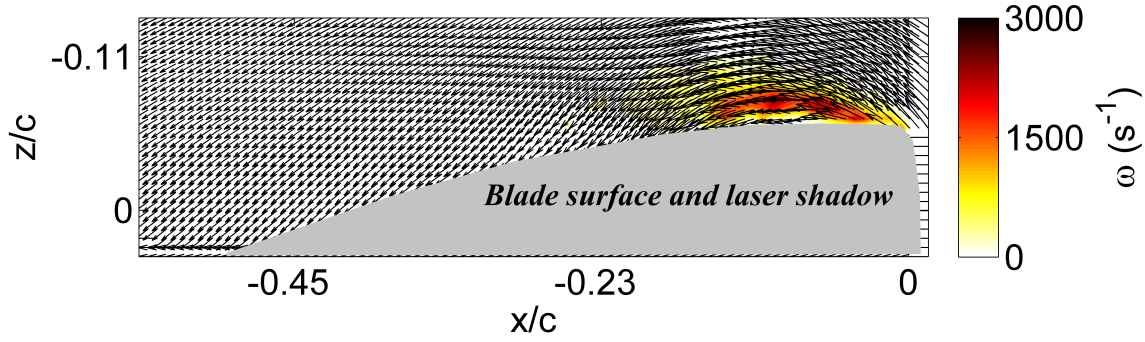

Figure 40: Velocity field at $\psi = 320°$, r/R = 0.6, $\mu = 0.4$

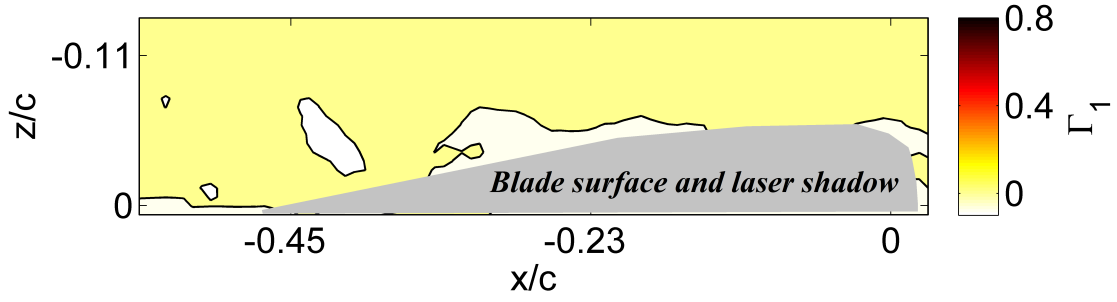

Figure 41: NAM plot at $\psi = 320°$, r/R = 0.6, $\mu = 0.4$

unsteady phenomenon and hence typically the cycle-to-cycle variations are significant. For example, prior work by Liiva [68] concluded that the scatter common to stalled-flow data during dynamic stall was not a function of wind tunnel turbulence or model imperfections. Hence, instantaneous velocity field analysis is critical to the complete understanding of the dynamic stall event over a rotating blade. In order to justify the instantaneous results, it is imperative to quantify the cycle-to-cycle variations far away from the blade. The blade flapping in PIV image was very consistent with only $\pm 0.5\ mm$ movement which translates to an uncertainty in flapping angle of around $\pm 0.05°$. In addition, velocity measurements away from the blade surface suggest that the cycle-to-cycle variations is negligible. With insignificant cycle-to-cycle variations in the far field properties, any variations observed on the flow over the blade should be entirely due to the dynamic stall event itself and not an artifact of far field properties. In this section, a case is made for the unsteady nature of the flow field.

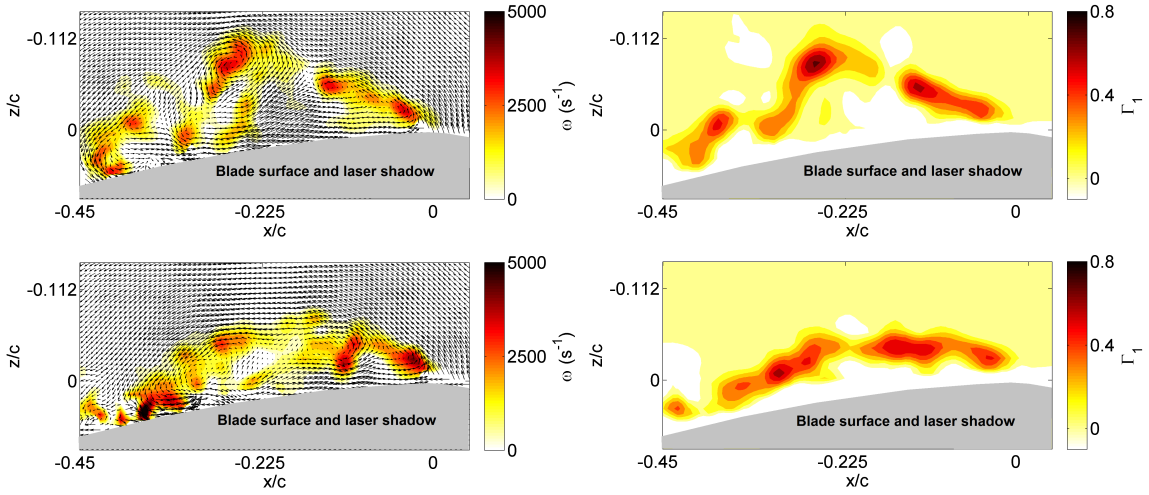

Figure 42: Two instants of the dynamically stalled velocity field with the corresponding NAM field at $\psi = 235°$, r/R = 0.6 and $\mu = 0.4$

General observations of the instantaneous velocity fields suggests that the phase-averaged vortical structure is very spatially compact when compared to the chaotic instantaneous flow field.

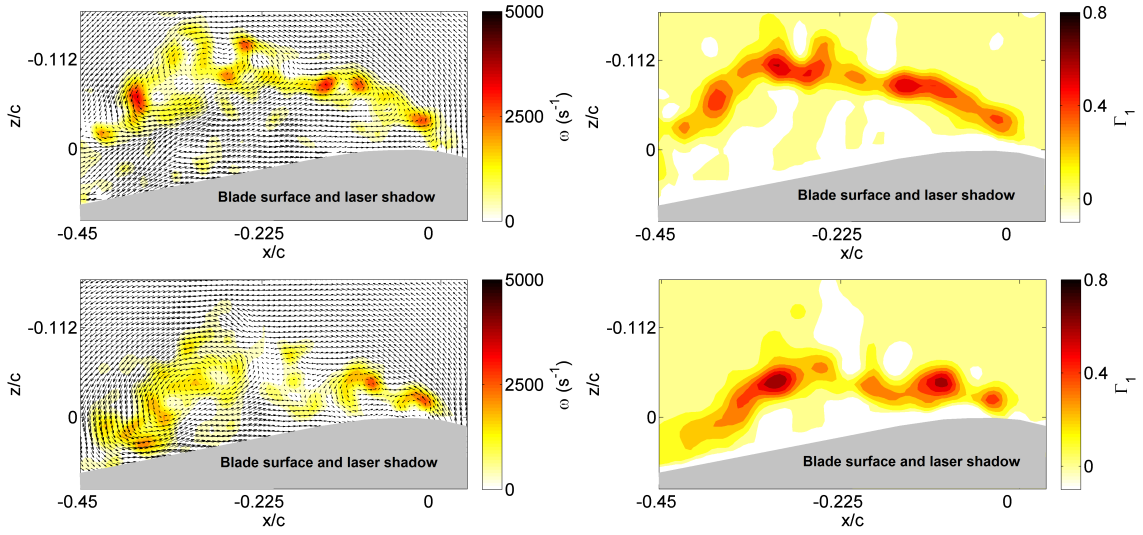

Figure 43: Two instants of the dynamically stalled velocity field with the corresponding NAM field at $\psi = 252.6°$, r/R $= 0.6$ and $\mu = 0.4$

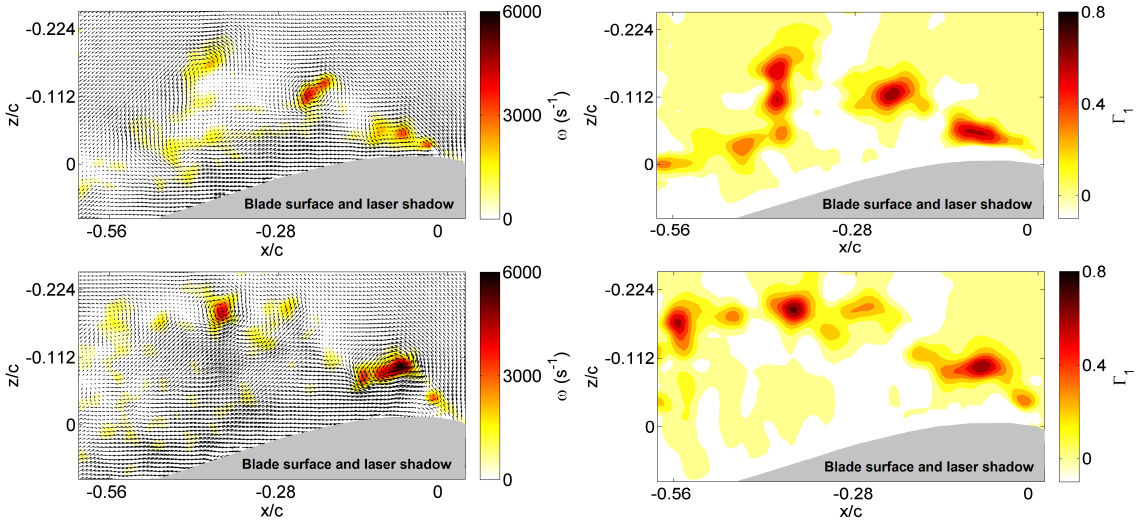

Figure 44: Two instants of the dynamically stalled velocity field with the corresponding NAM field at $\psi = 270°$, r/R $= 0.6$ and $\mu = 0.4$

2.4.2.1 Proper orthogonal decomposition

The instantaneous velocity fields presented in the previous section are typically complicated with multiple shear layer roll-up and secondary vortices superimposed on a large scale coherent vortical structure. The analysis of the dominant behavior of such a flow field is hard due to the finer vortical structures superposed on a large scale coherent structure.

Hence, in order to analyze the most dominant features of the instantaneous velocity fields a technique was sought which would help uncouple the dominant flow structures from the finer non-dominant structures based on the energy contained in the structures.

One approach to extract flow structures in an unsteady flow field is based on proper orthogonal decomposition (POD) of the flow field. The fundamental idea is to represent the random spatiotemporal signal as a seres of deterministic spatial functions with the temporal functions as random coefficients such that the original signal is approximated as accurate as possible based on an energy-weighted measure. Further details of the implementation and background of the technique is provided in Appendix D.2. To a certain degree this technique draws similar parallel to Fourier decomposition. The spatial modes can be used to approximate the flow fields to varying degrees. For example, using only the first spatial mode the velocity field will be approximated to a first degree, which most of the time is the most dominant mode of the flow field. Adding more modes to the approximation typically improves the accuracy of the reconstructed velocity field, such that an approximation with all the modes included would yield a velocity field very close the original instantaneous velocity field. However, the higher modes typically have lesser energy associated with them, and hence neglecting them is justified, as long as the analysis is restricted to the dominant flow modes.

Using POD each mode can be assigned a energy content level for example Figure 45 illustrates the energy contained in the each spatial eigenmode of the flow at $\psi = 270^\circ$ and r/R = 0.6 at two different advance ratios. The inset is a zoomed in view of the same data showing the differences between the advance ratios in the first 4–5 modes. The energy contained in the higher modes equalize very quickly between the advance ratios, indicating the that the finer flow structures which typically have lesser energy associated with them are essentially the same in both the flow fields. However, the main difference albeit trivial exists between the dominant modes, which have larger energies associated with them. Essentially the effect of a change in advance ratio is on the most dominant modes of the flow rather than on the finer structures which have lower energies associated with them. Hence, analyzing the flow using the first 3 eigenmodes to reconstruct the approximated instantaneous velocity

field would be sufficient to draw conclusions on the dominant behavior of the flow and hence extrapolated to the complete flow field.

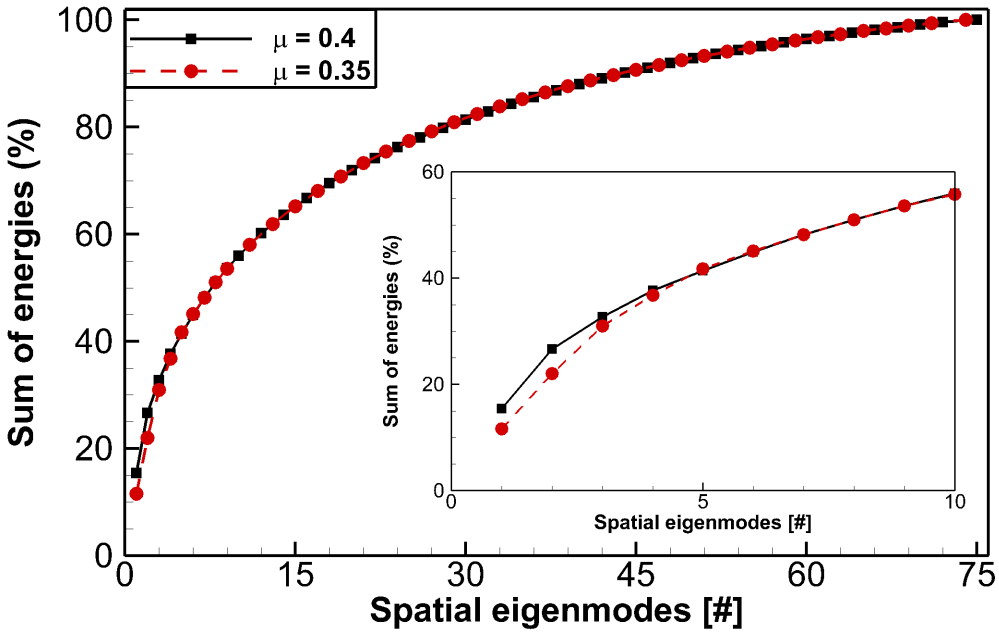

Figure 45: Sum of energies associated with each eigenmode of the flow at $\psi = 270°$ and r/R = 0.6

In this section only one azimuthal location is analyzed to understand the unsteady nature of the flow field. Earlier it was shown that the flow at $\psi = 270°$ is massively separated, which is the maximum extent of separation possible on the retreating blade. Hence if a azimuthal location has to be chosen to understand the unsteady nature of the flow field, it is best to look at the $\psi = 270°$ location. Figure 46 depicts the unsteady behavior of the flow by illustrating 10 consecutive approximated instantaneous NAM fields using 3 most dominant eigenmodes which is roughly 30% of the total energy of the flow field. The approximated flow is observed to exhibit a "cyclic behavior" between moderate separation to massive separation, as seen in Figure 46 (only one cycle is shown for brevity). If one considers the separated shear layer as making an angle with surface of the blade, at this flow condition the separated flow oscillates with a peak-to-peak angle of around 24.5°.

On increasing the advance ratio, the unsteady flow field illustrated in Figure 47 exhibits

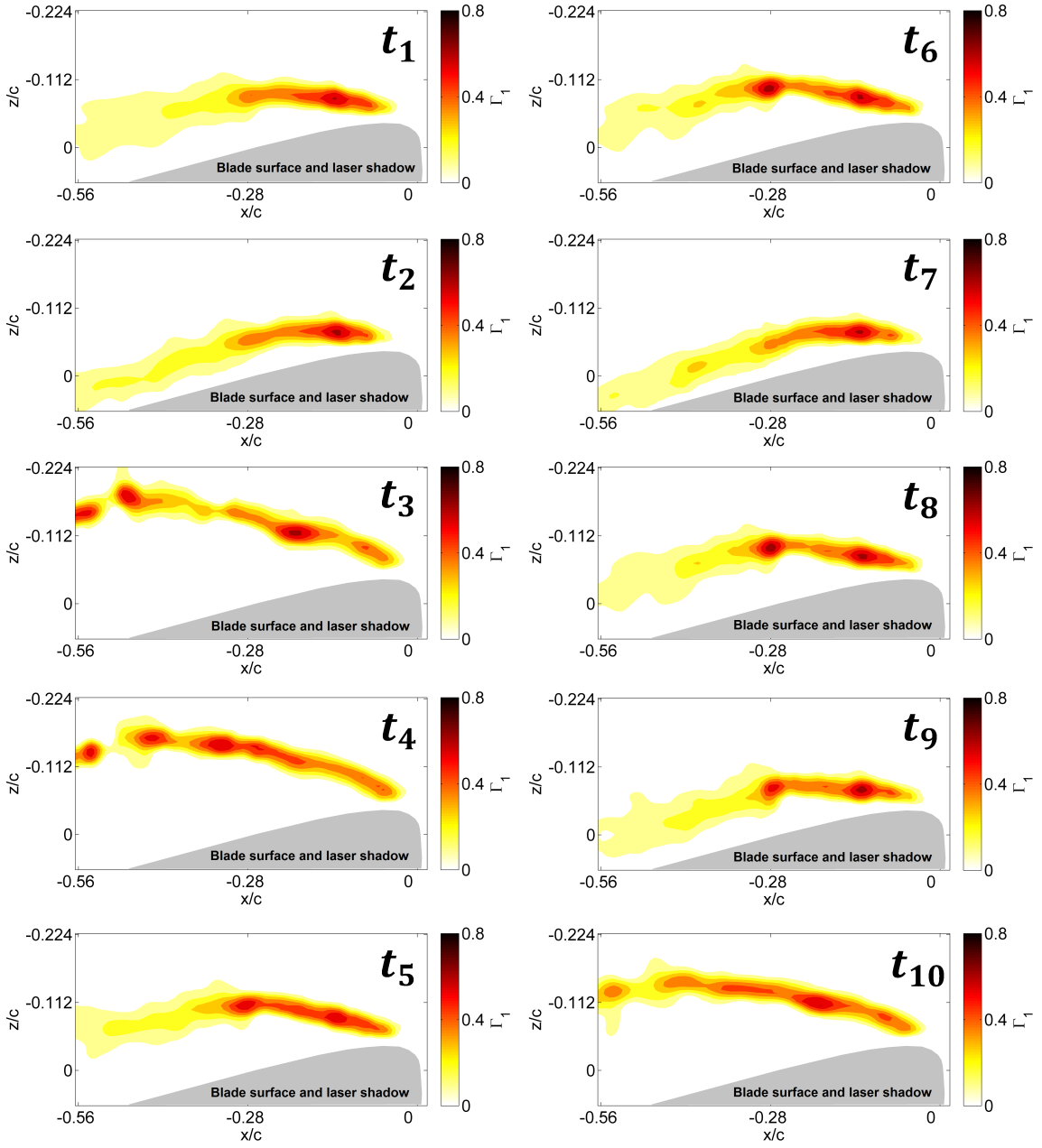

Figure 46: 10 snapshots of the approximated instantaneous NAM fields using 3 dominant eigenmodes of the flow at $\psi = 270°$, r/R = 0.6 and $\mu = 0.35$

a decrease in the cycle-to-cycle variations. Again considering the angle the shear layer makes with the surface of the blade, the peak-to-peak angle of oscillation of the shear layer reduces to around 12.8°. This essentially indicates that the flow fields cycle-to-cycle variations reduced upon increasing advance ratio. However, it should be noted that this reduction implies that the separated shear layer moved towards the massively separated

regime, reducing the cycle-to-cycle variations. Massive separation again means that on an average the dynamic stall event is more severe.

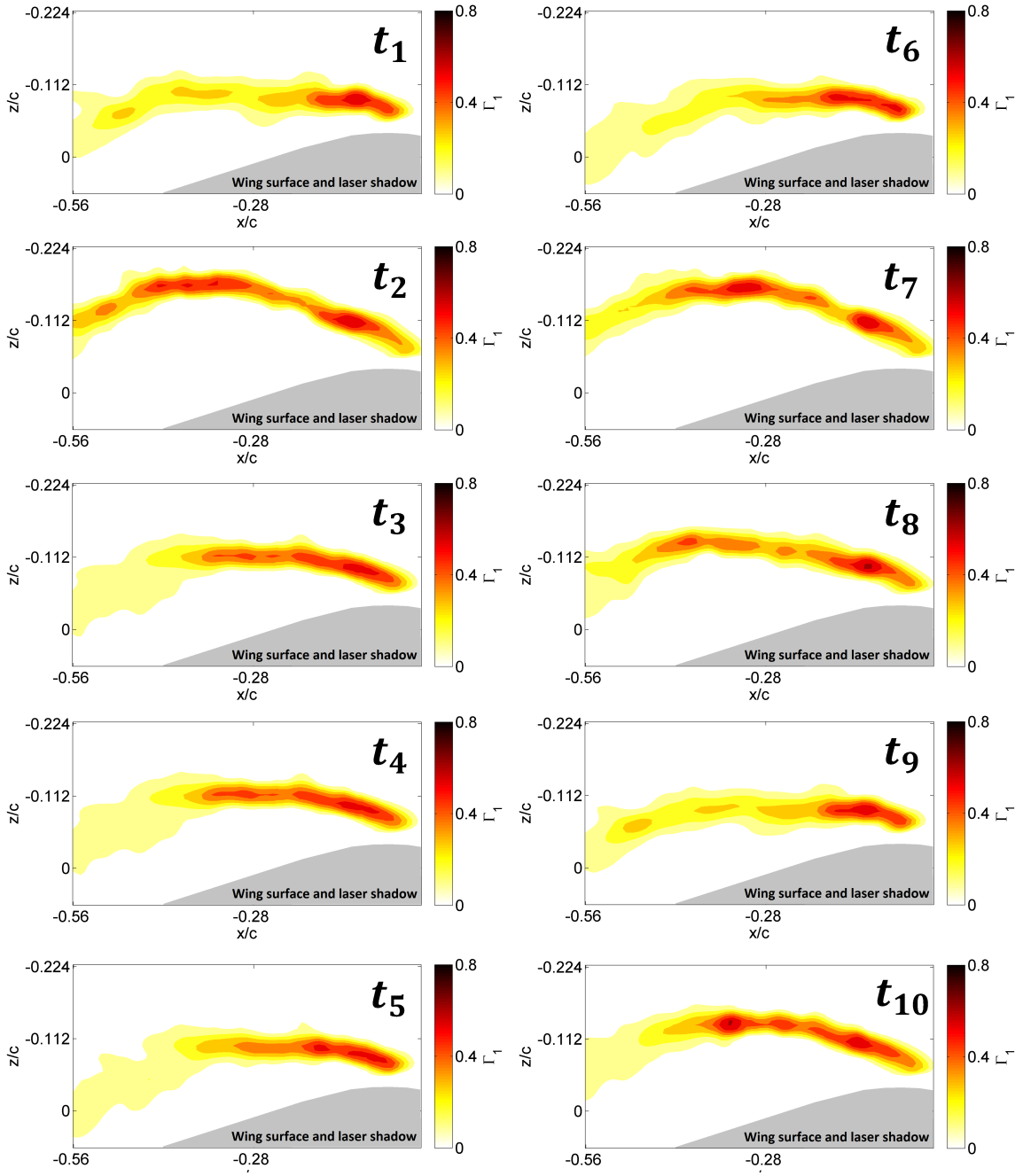

Figure 47: 10 snapshots of the approximated instantaneous NAM fields using 3 dominant eigenmodes of the flow at $\psi = 270°$, r/R = 0.6 and $\mu = 0.40$

2.4.3 Circulation computations

One other useful metric that can be derived from phase-averaged velocity fields is the circulation of the flow field on the upper surface of the blade (Γ_V). Circulation is defined as the vorticity flux in the flow field and is computed by evaluating Stokes theorem numerically:

$$\Gamma_V \quad = \quad \iint_S \omega \cdot dS \quad = \quad \sum_S \omega \; dxdy \tag{5}$$

where ω is vorticity and S is a closed surface chosen such that it surrounded the same area on each velocity field.

The circulation was computed on the upper surface of the blade for the different yaw angles where velocity measurements were made. Figure 48 illustrates the variation of circulation of the flow over the upper surface of the rotating blade with azimuthal angle for two separate advance ratios. The circulation of the flow over the upper surface of the blade at azimuthal angles close to separation and reattachment is evidently lower than at other azimuthal locations. This is expected in either case (close to separation or reattachment) primarily because the dynamic stall event has either uninitiated or concluded. As the dynamic stall event occurs for $230^\circ \leq \psi \leq 310^\circ$ the circulation in the flow over the upper surface increases which is expected during a dynamic stall event because of the associated lift over shoot. However, the interesting observation here is that the circulation for $260^\circ \leq \psi \leq 290^\circ$ is lower than the circulation for $\psi = 310^\circ$, which does not make sense intuitively. This anomaly can be reconciled by the observations in Section 2.4.2, where the flow is shown to be highly unsteady with a large spatial variation from cycle-to-cycle. The phase-averaging process of this highly unsteady flow field will cause the dynamic stall vortex to appear spatially diffused (in other words the vortex is weaker due to phase-averaging). This elucidates why the circulation in the flow over the upper surface of the blade for $260^\circ \leq \psi \leq 290^\circ$ derived from phase-averaged velocity field is unexpectedly lower.

To overcome this problem, the circulation around the flow field at each instant should be computed and then compared to the phase-averaged analysis. In addition, conditional

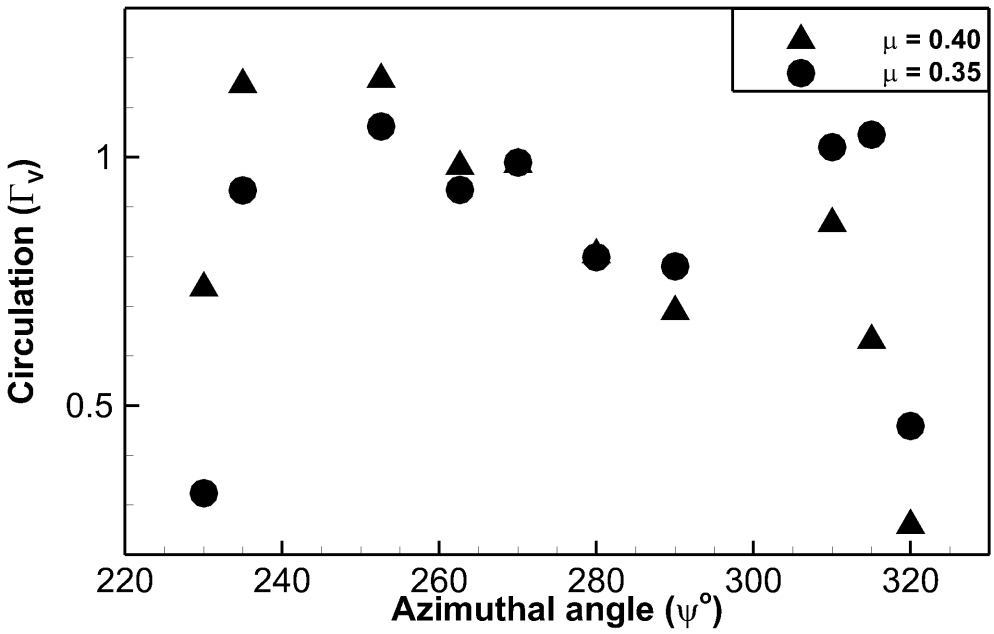

Figure 48: Variation of circulation of the flow over the upper surface of the rotating blade with azimuthal angle at r/R = 0.6 and $\mu = 0.35$ and $\mu = 0.4$

statistics can be used to derive average circulation over the the blade surface which will improve the circulation estimates. Figure 49 illustrates the difference between circulation computed using phase-averaged velocity field compared to that computed using instantaneous velocity fields and then averaged. Circulation was computed for the flow measurements at r/R = 0.6 and $\mu = 0.4$ and the error bars indicate the standard deviation of the circulation computed using instantaneous velocity fields. As discussed earlier, it is evident that the phase-averaging of the instantaneous velocity field spatially diffuses the vortex and reduces its strength. The anomaly observed in Figure 48, where the circulation exhibited a minima at around $\psi = 290°$ for $\mu = 0.4$ is hence demonstrated as an artifact of phase-averaging of the velocity field.

Figure 49 also furnishes more insights into the dynamic stall event on the rotating blade at r/R = 0.6 and $\mu = 0.4$. Circulation around the flow over the upper surface of the blade can be considered as a direct indication of the extent of dynamic lift overshoot that is expected on the blade "section". Based on this supposition, the dynamic lift overshoot

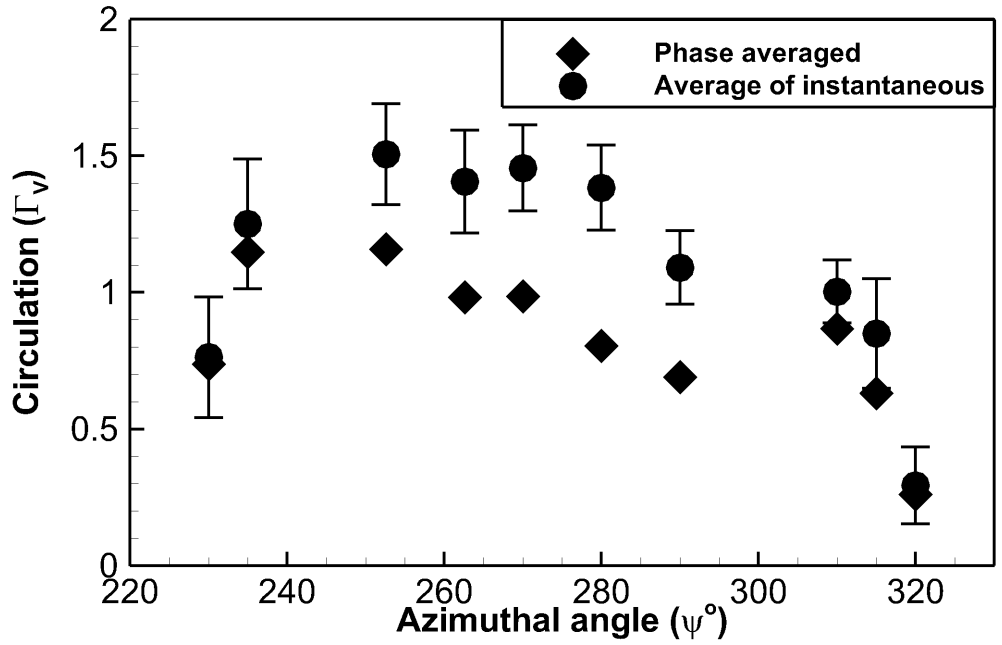

Figure 49: Variation of circulation of the flow over the upper surface of the rotating blade with azimuthal angle computed using phase averaged and instantaneous velocity fields at r/R = 0.6 and $\mu = 0.4$

occurs between $240° \leq \psi \leq 260°$, then the dynamic stall event enters a stage where the dynamic lift overshoot is maintained over a fair amount of the azimuthal angle. Eventually, there is a drastic drop in the dynamic lift close to reattachment.

2.5 Summary of results

In this chapter the velocity field over a retreating blade in dynamic stall conditions was measured to identify the azimuthal angles for dynamic separation and reattachment. The development of the dynamic stall life cycle on a rotating blade was also investigated. In addition, the cycle-to-cycle variations in the dynamic stall event due to the unsteady nature of the flow field is analyzed and quantified. A summary of the results and analysis is as follows:

1. Dynamic separation

   (a) The azimuthal angle for dynamic separation (defined in this work as evidence of leading edge separation) was determined to occur between $225° \leq \psi \leq 230°$. The

phase-averaged PIV measurements revealed that the mechanism of separation that was in operation was the classical trailing edge separation mechanism. The the trailing edge was observed to separate first, which slowly progressed up to the leading edge.

(b) Analysis of the separation event using phase-averaged velocity fields for a set of parameters such as radial location and advance ratio helped characterize the general behavior of dynamic separation. At a given azimuthal angle, separation was first observed to occur at inboard locations (closer to the root of the blade) and then progress to the outboard locations. And at a given radial location, the separation was observed to occur at an earlier azimuthal location for the case of a higher advance ratio.

(c) However, cycle-to-cycle variations were observed to an extent where certain instants had no indication of separation, while others showed clear evidence of separated flow. Hence, the phase-averaged velocity fields only provide a general indication of the behavior of the flow field. Instantaneous velocity field analysis would be needed for a more accurate representation of this unsteady event.

2. Dynamic stall event

(a) The phase-averaged velocity field was used to deduce conclusions on the DSV. Soon after separation the vortex appears to elongated and pinned to the surface of the blade at around $\psi = 235°$. As the yaw angle increases the vortex lifts off the blade surface and reaches its peak height above the blade surface at $\psi = 270°$. Beyond $\psi = 270°$ the blade undergoes the down stroke motion and vortex proceeds to descend towards the blade surface and the separated flow finally reattaches.

(b) One other critical observation is about the unsteady nature of the flow field. The NAM fields between $250° \leq \psi \leq 280°$ indicate a maximum value of NAM at several x/c locations within the phase-averaged vortex. This fact indicates that the cycle-to-cycle variations is quite significant and hence the phase-averaged

vortex presents itself as a spatially diffused vortex with multiple maximas. Again a clear trend is observed with respect to the magnitude of the cycle-to-cycle variations with yaw angle. As yaw angle increases the cycle-to-cycle variations appear to increase up to yaw angle $\psi = 270°$, it then proceeds to decrease.

(c) The three component velocity measurements allowed for an interpretation of the radial flow during dynamic stall event. Evidently, radial flow (corrected for spanwise flow induced due to yaw) is significant only in the separated flow regions, especially as the extent of separation increases. This is convincing evidence that the separated flow region on a rotating blade typically has a significant radial flow (induced due to centrifugal forces) from the root to the tip of the blade.

3. Following the DS event, the blade undergoes the down stroke motion via reduction of its pitch angle. In this investigation the phase-averaged velocity fields indicated that the reattachment occurred between $315° \leq \psi \leq 320°$.

4. With insignificant cycle-to-cycle variations in the far field properties, the unsteady nature of the flow is only attributed to the dynamic stall event itself and not to the far field properties. General observations of the instantaneous velocity fields suggests that the phase-averaged vortical structure is very spatially compact when compared to the chaotic instantaneous flow field.

5. Proper Orthogonal Decomposition

   (a) POD analysis was successfully used to analyze the instantaneous velocity fields. The first three dominant modes of the flow were used to reconstruct the approximated velocity fields which allowed for clearer interpretation of the unsteady flow field. The unsteady flow field at $\psi = 270°$, r/R = 0.6 and $\mu = 0.35$ was observed to exhibit a "cyclic behavior" between moderately separated to massively separated flow.

   (b) Considering the angle between the separated shear layer and the surface of the blade, at this flow condition the peak-to-peak angle was around 24.5°. However,

upon increasing the advance ratio the peak-to-peak angle reduced to around 12.8°. This essentially indicated that the cycle-to-cycle variations reduced with increase in advance ratio, more to the point it makes sense that upon increasing advance ratio the unsteady flow should transition towards massively separated regime.

6. Circulation computations around the flow over the upper surface of the rotating blade during dynamic stall revealed some more useful insights. The circulation around the flow over the upper surface of the blade can be considered as a direct indication of the extent of dynamic lift overshoot on that blade "section" during the DS event. Based on this supposition, the dynamic lift overshoot occurs between $240° \leq \psi \leq 260°$, then the dynamic stall event enters a stage where the dynamic lift overshoot is maintained over a fair amount of the azimuthal angle. Eventually, there is a drastic drop in the dynamic lift close to reattachment.

CHAPTER III

EFFECT OF ROTATION ON DYNAMIC STALL

3.1 Introduction

The previous chapter dealt with the general features of dynamic stall over a rotating blade including aspects of dynamic separation, the dynamic stall event, and the dynamic reattachment. However, the effect of radial flow on the dynamic stall event and the DSV itself still remains unexplored. In addition, the cycle-to-cycle variations of the DS event on a rotating blade are important for predicting the lift overshoot and the associated pitching moment variations. In this section experiments are conducted on the retreating part ($\psi = 270°$) of the rotating blade in forward flight in a low speed wind tunnel using two-dimensional PIV. The flow field at $\psi = 270°$ is one time instant in the life cycle of the DS event. However, the choice of $\psi = 270°$ decouples the effect of yaw induced span-wise flow from the centrifugally induced span-wise (radial) flow. Hence this enables a systematic study of the effect of "pure" radial flow due to centrifugal forces.

3.2 Objectives

The effect of radial flow on the dynamic stall event is investigated in this chapter. The specific objectives are:

1. To identify and characterize the large-scale coherent vortical structure on the rotating blade in dynamic stall conditions at $\psi = 270°$ using vortex detection techniques.

2. Classify the vortex as the DSV.

3. Investigate effect of radial flow on the DSV by studying its spanwise characteristics and comparisons to 2D DSV.

4. Study the cycle-to-cycle variations of the DSV on a rotating blade.

3.3 Experimental methods

3.3.1 Experimental setup and flow conditions

The experiments were conducted in the high advance ratio facility (see Figure 50 also refer to Section 1.5.2 for a detailed description of the facility) constructed in the test section of the John Harper 2.13m×2.74m low speed wind tunnel (please refer section refsec:lswt for details) at the Georgia Institute of Technology.

Given the objectives and motivation of capturing and studying the stall vortex on the retreating rotor blade, a rotor rotation rate of 200RPM ($\Omega = 20.94$ rad/s, $U_T = 18.62$ m/s) and a free stream velocity of $U_\infty = 6.1$ m/s were chosen. The operating advance ratio was $\mu = 0.33$, which is sufficient to induce dynamic stall as demonstrated by [30] using flow visualization. By trial and error DiOttavio determined the collective and cyclic pitch needed to induce dynamic stall on the retreating blade at $\psi = 270°$. A collective pitch of 10° and a cyclic of $-5°$ were used to create a 15° pitch on the retreating blade at $\psi = 270°$. However, due to flapping of the blade, the effective angle of attack observed on the retreating blade at $\psi = 270°$ was 16.8°. The chordwise velocity measurements were made at eleven locations in the range $0.514 \leq r/R \leq 0.971$ with spatial resolution increasing towards the tip, as shown in Fig. 50(b). Each measurement radial location is listed in table 8 with the associated reduced frequency ($k = \frac{\Omega c}{2U_e}$) and Reynolds number based on chord length ($Re = \frac{U_e c}{\nu}$), where $U_e|_{\psi=270°} = U_T \frac{r}{R} - U_\infty$.

3.3.2 PIV instrumentation

Two-dimensional PIV (in contrast to Stereo-PIV as in the previous chapter) was used to measure the velocity fields over the retreating rotor blade at $\psi = 270°$. The illumination was provided by a double-cavity Nd:YAG laser with a pulse energy of 200 mJ. The resulting beam diameter was about 3 mm with a pulse width of 5ns. A laser arm (a covered beam path) was used to deliver the laser beam to the measurement plane. Sheet optics was used at the end of the laser arm to generate a light sheet of 3 mm thickness. The flow was continuously seeded with approximately $10\mu m$ droplets generated by a Laskin-nozzle type aerosol generator. A series of 100 image pairs were acquired at each measurement

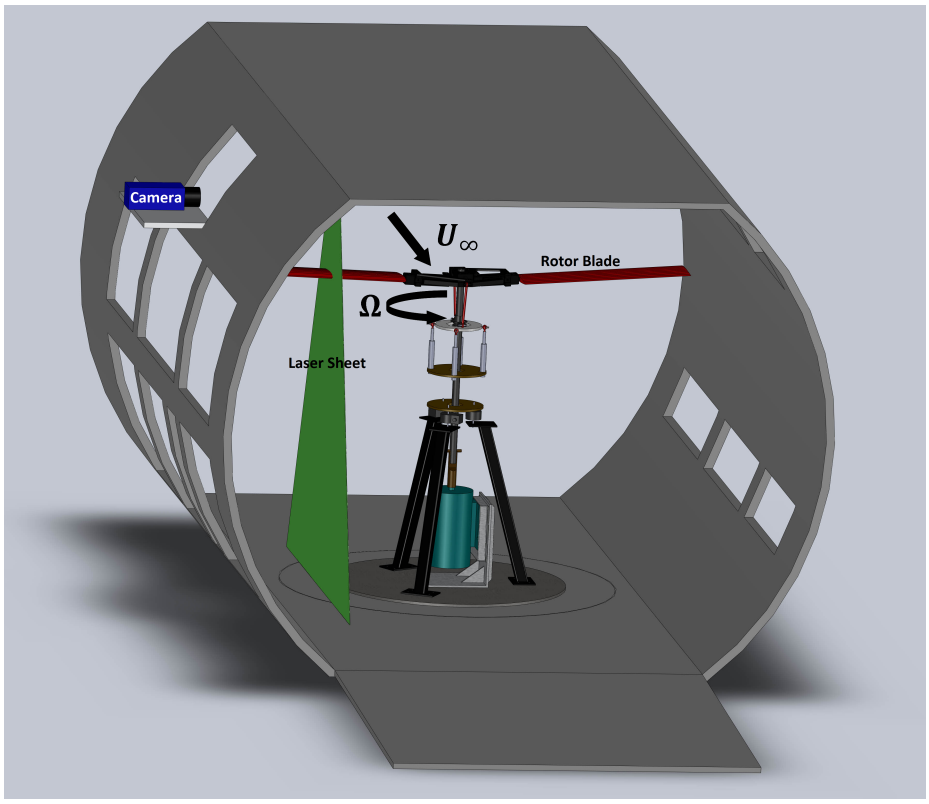

(a) View of the experimental setup from downstream of the wind tunnel test section

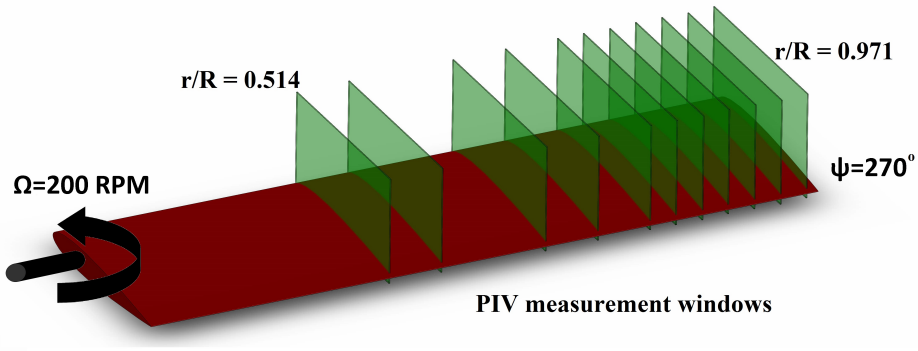

(b) PIV interrogation windows over the radius of the blade

Figure 50: High advance ratio facility - configured for chordwise flow experiments

plane using PRO-X 2M camera which has a 1600×1200 pixel resolution and a pixel size of $7.4\times7.4\mu m^2$. The particle size in the camera image ranged from 1.47 pixels to 2.52 pixels. The focal length of the lens system was 50 mm and the aperture on the camera was set at f/4. The blade was coated with Rhodamine paint and a bandpass filter was used on the camera to minimize laser reflections from the upper surface of the blade and improve

Table 8: Radial locations where PIV measurements were made at $\psi = 270°$

r/R	U_e (m/s)	k	Re
0.514	3.48	0.54	39,455
0.571	4.54	0.41	51,533
0.686	6.67	0.28	75,689
0.743	7.73	0.24	87,767
0.8	8.8	0.21	99,845
0.829	9.33	0.2	105,884
0.857	9.86	0.19	111,923
0.886	10.39	0.18	117,962
0.914	10.92	0.17	124,001
0.943	11.46	0.16	130,040
0.971	11.99	0.16	136,079

signal-to-noise ratio. Unavoidable laser reflections were masked during the velocity vector computations

DaVis 7.2 software provided by LaVision was used to process the PIV data. The velocities were calculated from the spatial cross-correlation of the images. An interrogation window overlap of 50% and a second interrogation pass with a reduced window size were used to increase the signal-to-noise ratio of the correlation peak. The first pass utilized an interrogation window of 64×64 pixels while a 32×32 pixel window was used on the second pass. This yielded a velocity vector resolution of 1.8mm–2.1 mm $\sim$ 0.01c–0.012c. Post-processing of the vector images consisted of an applied vector range and a median filter. These processes greatly reduced the noise due to erroneous vectors appearing at the edges of the viewing window.

3.3.3 Accuracy estimates

The uncertainty in flow conditions resulted in a Reynolds number uncertainty of ± 468. The uncertainty in collective pitch and cyclic pitch angle settings, which were measured using a digital protractor, is ±0.05°. The error in measurement of the angle of the tip path plane arises mainly due to the pixel size in image processing, and the uncertainty is 0.035°.

The uncertainty in phase locking also estimated by image processing was $\pm 0.05^{\circ}$.

The uncertainty in velocity measurements is computed using methods described in Appendix A.3. Bias error was determined by plotting the probability density histograms of the instantaneous velocity data. With a resolution of 0.005 m/s the histograms did not reveal any peak-locking or any other experimental artifact. The lag error was estimated by considering the relaxation time of the seed particles (10μm) to changes in velocity. The characteristic time was defined as the time available for seed particle to respond to rapid changes in the flow, which was determined from the vorticity contours. A comparison showed that the characteristic time was 5–10 times greater than the relaxation time, indicating that the particle lag error was insignificant. Random error (σ_e) was computed by using Eq. 13. For this experiment the random error ranged from 0.074 pixels in the best case (0.05×1.47 pixels) to 0.252 in the worst case (0.10×2.52 pixels).

The total measurement error (ϵ_m) was quantified with Eq. 14 from [91]. W_p was measured in the radial plane and was found to be 3.5 m/s, U_p was measured to be 10.2 m/s, Z_s was maintained between 3-4 mm, M of the camera was $\frac{1}{16}$. σ_i amounted to $7.4 \times 10^{-6} \times \sigma_e$ ranging between 5.5×10^{-7} and 1.9×10^{-6}. Using these relations the total measurement error ϵ_m was estimated between 0.26% and 0.89%. This amounted to an absolute error of 0.027 m/s and 0.091 m/s based on U_p. Uncertainties in the velocity measurements are summarized in Table 9.

Table 9: Summary of uncertainty estimates

Type	Error
Random Error	0.065–0.212 pixels
Bias Error	0.005 m/s
Lag Error	Insignificant
Total Measurement Error	0.26%–0.89%

3.4 Results and discussions

3.4.1 Phase-averaged analysis

The following analysis of the flow is performed assuming the existence of a dominant periodic flow field that is captured by the phase locked average flow field (this assumption is examined later). In all the PIV vector fields presented in this work, the axes of the camera images are fixed in the wind tunnel coordinate system and have not been corrected for the pitch angle of the blade. The origin (0,0) is the location of the leading edge in all the vector fields. All the dimensions are normalized by chord length, where x/c = 0 is the leading edge and x/c = -1 is the trailing edge of the blade. As mentioned earlier the experiments were performed only at $\psi = 270^{\circ}$ because this azimuthal angle enables the decoupling of the effect of yaw induced span-wise flow from the centrifugal forces induced span-wise (radial) flow. Hence, a systematic study on the effect of "pure" radial flow (due to centrifugal forces) on the DS event can be conducted. Again, the main aim of these experiments was to capture the dynamic stall vortex, study it's variation across the span and it's cycle-to-cycle variations at $\psi = 270^{\circ}$.

3.4.1.1 Identification of the vortex

The phase-averaged velocity field shows evidence of a large coherent vortical structure only at inboard locations $0.514 \leq r/R \leq 0.743$ at $\psi = 270^{\circ}$. In order to observe the vortical structure the free stream velocity ($U_{\infty} = 6.1\ m/s$) had to be subtracted from the phase-averaged velocity field. This can be observed very clearly from the velocity field measured at $\psi = 270^{\circ}$ and r/R = 0.514 and 0.743 depicted in Fig. 51 and Fig. 52. On moving outboard ($r/R > 0.8$) the phase-averaged velocity field showed no indication of a vortical structure due to the strong tip vortex effect. Figure 53 illustrates the velocity field at r/R = 0.971 where the effect of the tip vortex on the flow field can be clearly observed with all the velocity vectors predominantly having a downward flow component.

In order to effectively characterize the vortical structure a vortex detection technique via metrics such as Γ_1 (also called Normalized Angular Momentum (NAM)) proposed by [40] was used. Γ_1 is defined as:

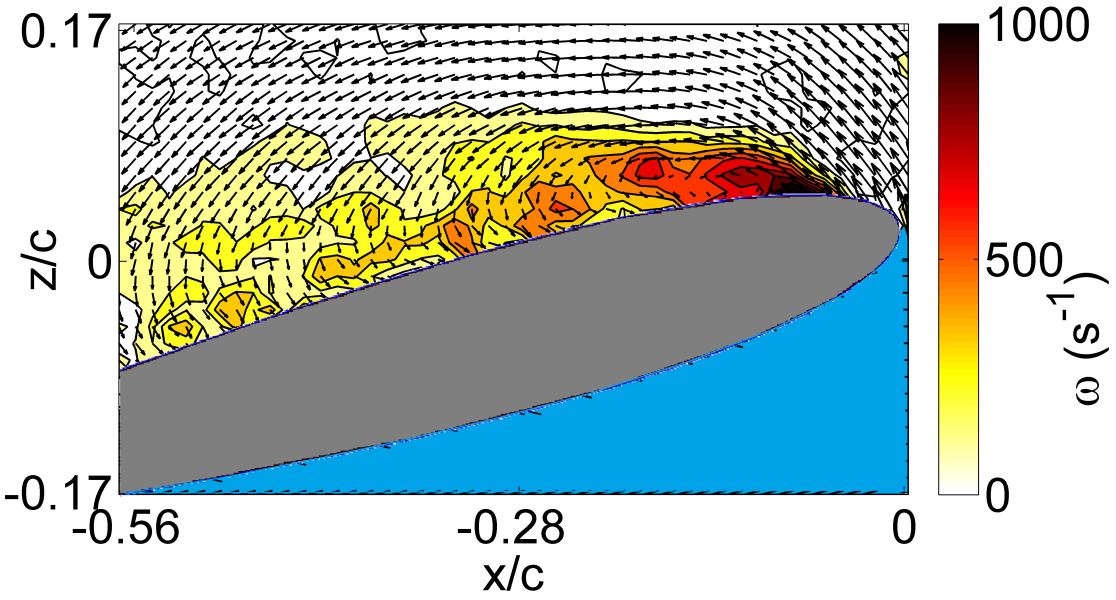

Figure 51: Velocity field at r/R = 0.514, k = 0.54, Re = 39,455

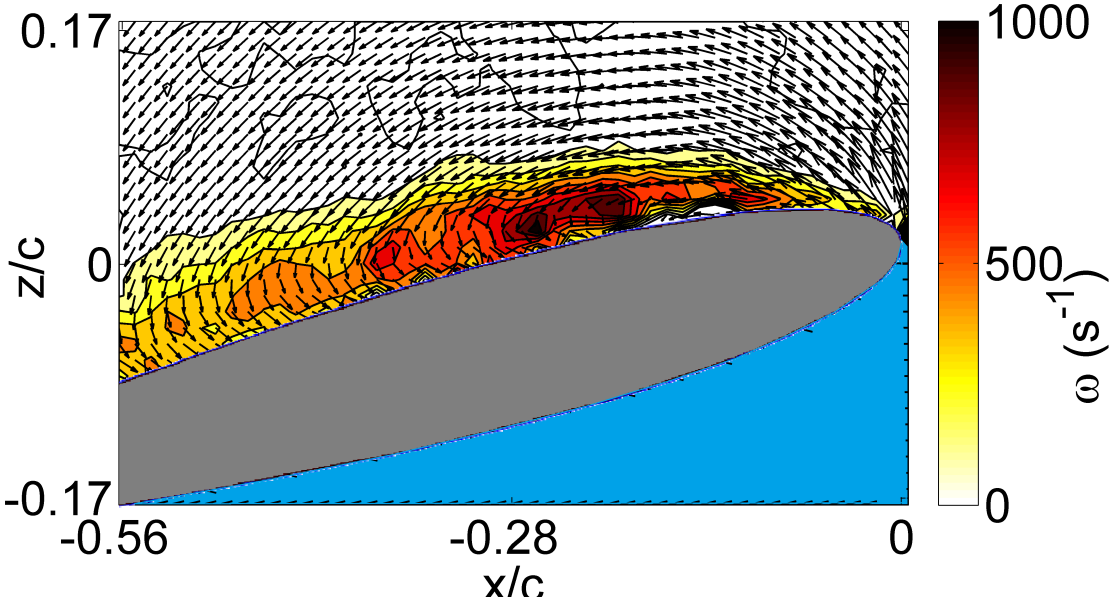

Figure 52: Velocity field at r/R = 0.743, k = 0.24, Re = 87,767

$$\Gamma_1(P) = \frac{1}{N} \sum_{S} \frac{(PM \times U_M) \cdot z}{\|PM\| \cdot \|U_M\|} \tag{6}$$

where N is the number of points in the two-dimensional neighborhood of S of any given point P in the measurement plane. M lies in S and z is the unit vector normal to the measurement plane. The parameter N plays the role of a spatial filter, but affects the

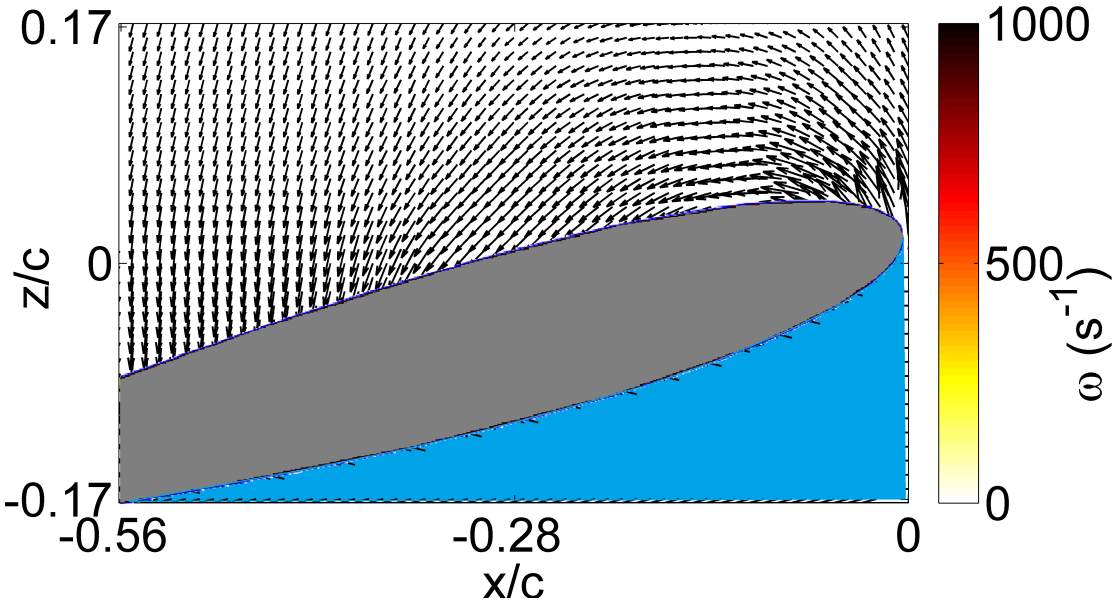

Figure 53: Velocity field at r/R = 0.971, k = 0.16, Re = 136,079

location of maximum Γ_1 weakly. See Appendix D.1 for more details on normalized angular momentum.

A value of N = 2 yielded appropriate results with sufficient detail to discern the vortex. The vortex can be clearly observed in the normalized angular momentum of the phase-averaged velocity fields shown in Fig. 54–Fig. 56. On moving outboard the location of the center of the vortex is moving towards the trailing edge, confirming the observations from the velocity fields. At slightly further outboard locations (not shown here) there is no evidence of the vortical structure. This indicates a strong dependence of the DS event on the azimuth angle of the blade. At far outboard locations (close to the tip of the blade) the significant effect of the tip vortex (see Fig. 53) greatly modifies the chordwise flow, suppressing the vortical structure.

3.4.1.2 Classification of the vortex as the DSV

The coherent vortical structure identified in the flow field could be a regular stall vortex occurring on the retreating blade. Hence, in order to classify the vortical structure as the DSV, circulation of the structure (Γ_V) on the upper surface of the blade was computed. If it is the DSV, it should contain a circulation that is of the order of the circulation equivalent of

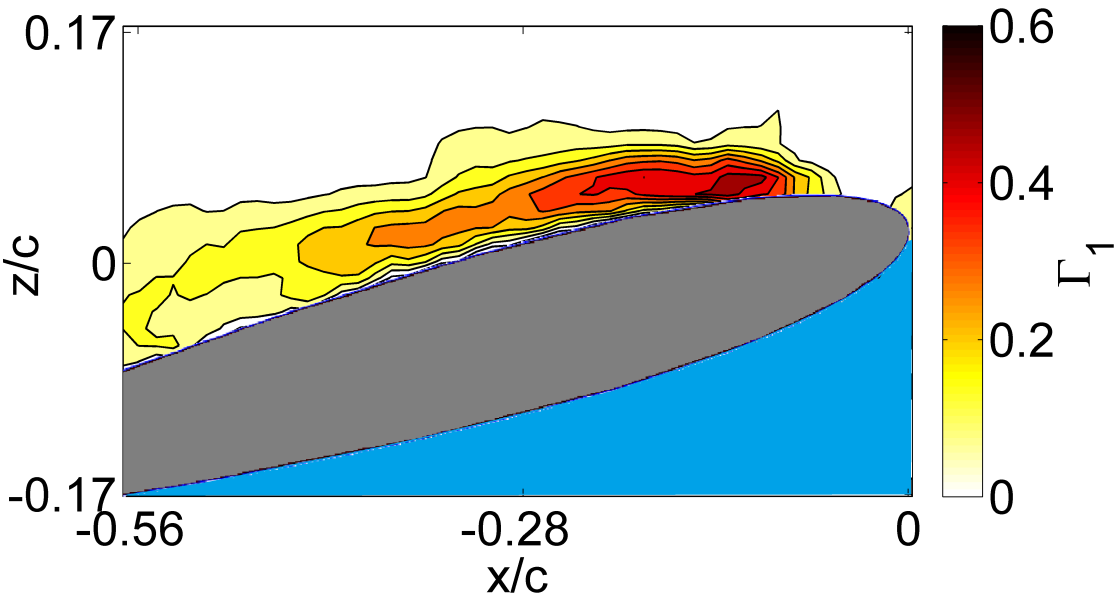

Figure 54: NAM at r/R = 0.514, k = 0.54, Re = 39,455

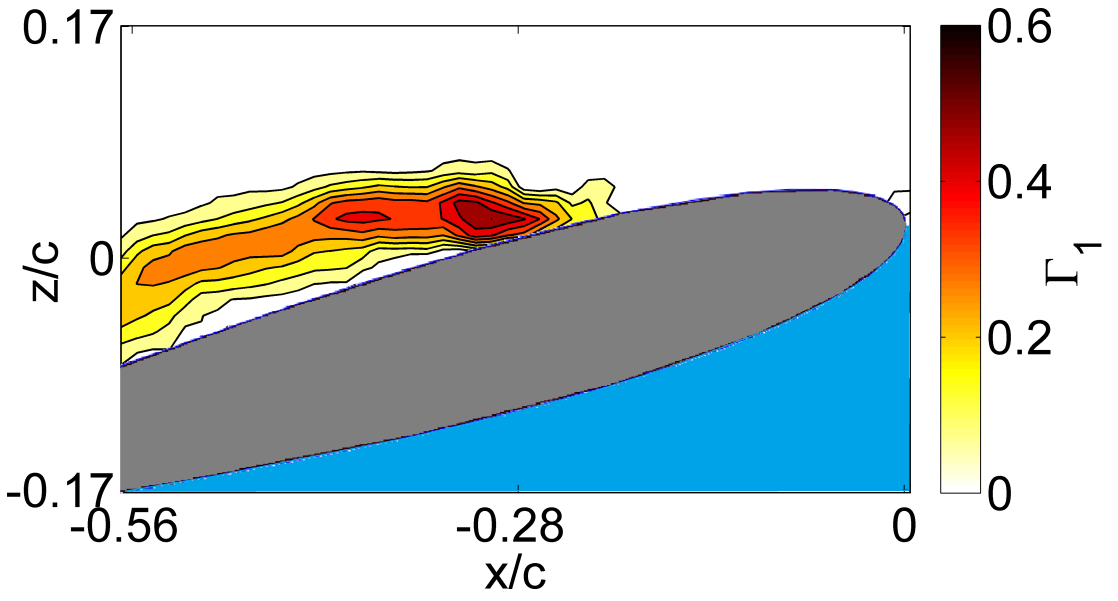

Figure 55: NAM at r/R = 0.686, k = 0.28, Re = 75,689

the lift overshoot (dynamic lift) measured on unsteady airfoils/wings. Figure 58 illustrates the dynamic lift component during DS which is primarily due to the circulation of the vortex on the upper surface of the wing.

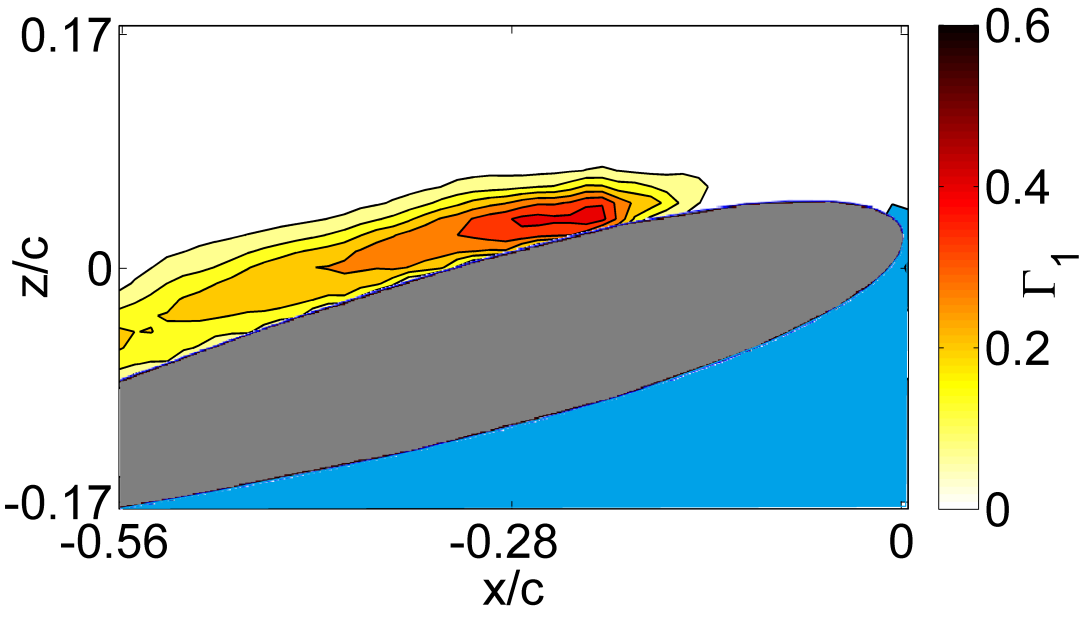

Figure 56: NAM at r/R = 0.743, k = 0.24, Re = 87,767

The bound circulation expected (Γ_a) was computed at maximum steady state C_L of the wing. Maximum C_L was determined to be 0.9 by measuring the lift curve of the wing in steady state at Re = 1.7×10^5. It follows that the sum of the expected bound circulation on the wing section (Γ_a) and circulation of the vortex (Γ_V) is proportional to the total lift on that wing section. Hence the ratio of the Γ_V to the total circulation on the wing section will indicate the extent of the dynamic nature of the DS event.

Circulation of a velocity field is defined as the amount of vorticity flux in it and is computed by evaluating Stokes theorem numerically

$$\Gamma_V \quad = \quad \iint_S \omega \cdot dS \quad = \quad \sum_S \omega \; dxdy \tag{7}$$

where ω is vorticity and S is a closed surface chosen such that it surrounded the vortical structure observed from the NAM plots.

The circulation around the vortex increased on moving outboard, which is expected because of the increase in velocity on moving outboard. Table 10 summarizes the computed values of Γ_a and Γ_V at several radial locations. The percentage of lift contribution arising

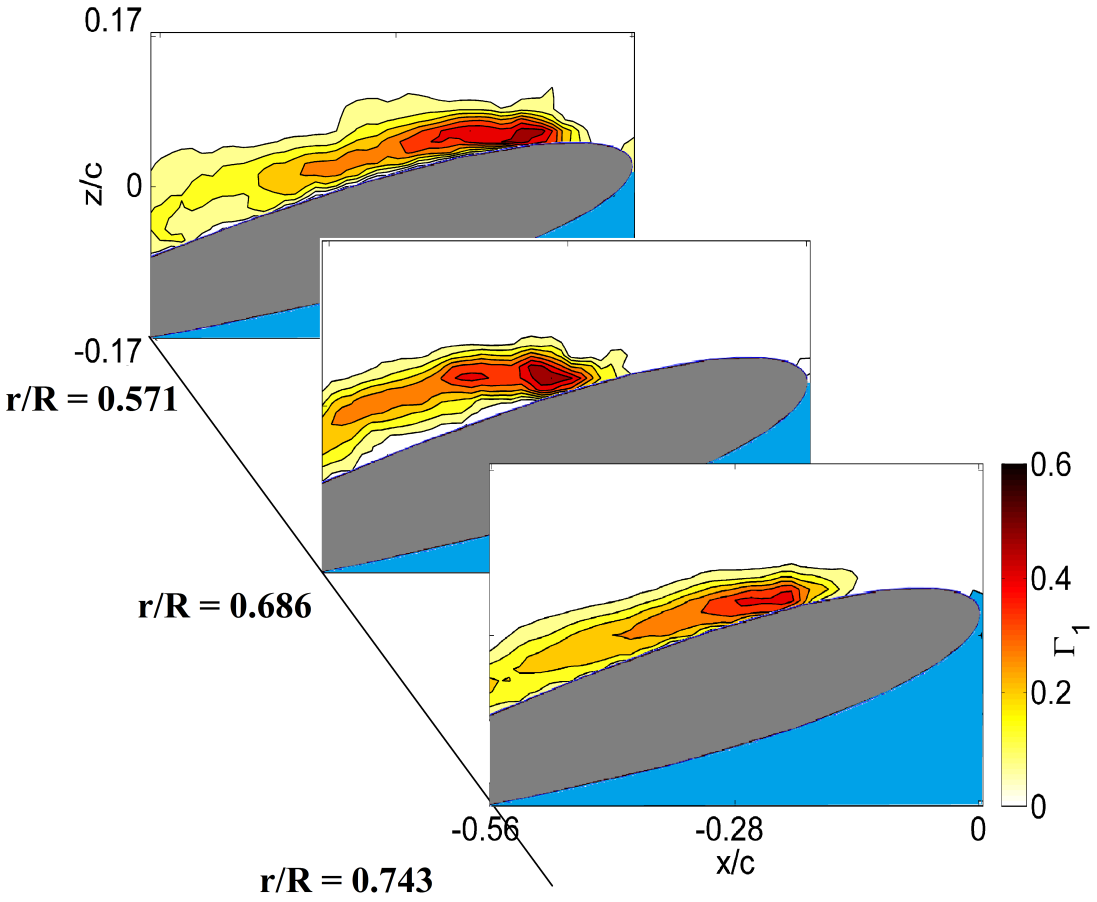

Figure 57: Illustration of the variation of the vortex at several radial locations

from the vortex was determined to be between 57.5% and 48.3%. Given the high reduced frequency conditions (see Table 8) and a fairly low aspect ratio blade, this level of overshoot is expected as observed by [75, 18]. The overshoot decreases on moving outboard indicating a decrease in dynamic lift, which indicates the weakening of the DS event.

3.4.1.3 Characteristics of the DSV

In two-dimensional studies, the DSV has been observed to form and uniformly arch away from the airfoil surface (see [75, 17, 82]). However, due to the effect of rotation in this investigation the DSV was observed to be "pinned" to the surface at all radial locations. In addition, the DSV observed on the rotating blade was noticeably stretched along the chord.

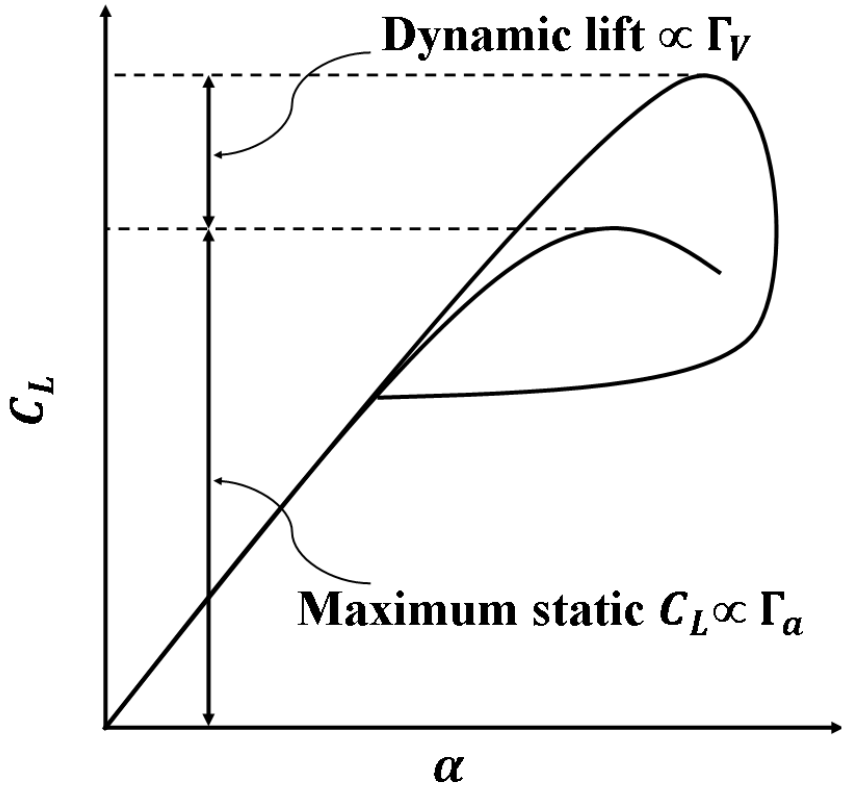

Figure 58: Illustration of dynamic lift on a unsteady airfoil/wing

Table 10: Circulation comparison at various radial location

r/R	Γ_a (m^2/s)	Γ_V (m^2/s)	$\frac{\Gamma_V}{\Gamma_a+\Gamma_V}$
0.514	0.28	0.38	57.5%
0.571	0.36	0.43	54.4%
0.686	0.53	0.51	49.0%
0.743	0.62	0.58	48.3%
0.800	0.70	0.36	33.9%

These observations are in *slight* contrast to [81] who found that the DSV was flatter only at outboard location (r/R = 0.6) than at midspan. However, their measurements also suggest that the DSV is in close proximity to the blade in contrast to two-dimensional DSV. The core of the vortex was observed to have a strong radial flow component as per observations in prior phase-averaged radial flow analysis by [94]. The strong radial flow that exists on the surface of the blade is expected to sweep the DSV outward and restrain the DSV close

to the blade surface.

The location of the DSV was determined by computing the coordinates of the maximum NAM at radial locations $0.514 \leq r/R \leq 0.8$. Figure 59 illustrates the variation of the non-dimensional chordwise location of the DSV varying with radial location. The chordwise location x/c = 0 corresponds to leading edge and x/c = -1 corresponds to trailing edge. There was a global shift of the location of the DSV towards the trailing edge on moving outboard which mimicked the trend of the separation line. Between r/R = 0.5 and 0.6 the location of the DSV did not change *significantly*, which agrees with the limited observations by [81] at r/R = 0.5 and 0.6. They attributed the span-wise invariance to stabilization due to radial forcing. However, the results in our investigation indicate that the chordwise location of the DSV displays a random behavior for $r/R \geq 0.686$. On moving further outboard ($r/R > 0.8$) there is no evidence of the vortical structure.

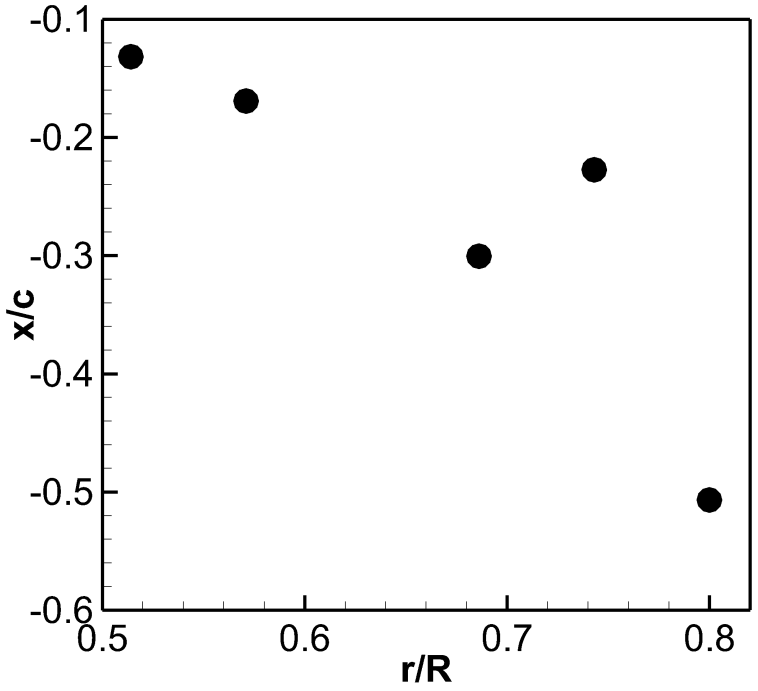

Figure 59: Span-wise variation of chordwise location

This span-wise variation of the vortical structure is expected since:

1. Dynamic stall on a rotating blade is a three-dimensional event - and the exact timing

of the DSV will vary as a function of both radial location and azimuth.

2. The dynamic stall event also depends on the reduced frequency of the blade section. The reduced frequency of the blade section decreases on moving outboard on the blade, this span-wise variation will also affect the DS event.

3. At most outboard locations the effect of the tip vortex is significant and it interacts with the flow over the upper surface of the blade suppressing the vortex.

4. Due to the substantial radial flow existing in this flowfield, the dynamic separation may be expected to propagate outward along the radial direction, and hence occur at later azimuths at outboard stations.

3.4.1.4 Separation line

The other notable feature in the chordwise plane is the location and behavior of the separation line. At each radial station examined, the separation point was determined by plotting the normal velocity 2mm from the blade surface and determining the point where an abrupt increase in its magnitude was observed. This is a practical way of determining separation from velocity data where resolving the boundary layer itself is impractical. Figure 60 shows the radial variation of the ensemble-averaged separation line with the error bars showing the standard deviation of the location of the separation point. At inboard locations ($r/R < 0.6$), which indicates the severity of dynamic stall. This is a classic feature also observed by other studies (McCroskey [78]). On the outboard sections of the blade the separation point moved aft towards the trailing edge. This is attributed to the influence of the downwash induced by the tip vortex.

3.4.2 Instantaneous velocity field analysis

The analysis of instantaneous velocity fields will provide further insights into the DS event. Due to the rotating environment, the phase of the DS event varies simultaneously with azimuthal angle and radial location. Hence observations at a particular azimuth and radial location is localized to that section and cannot be extrapolated. However, observations at

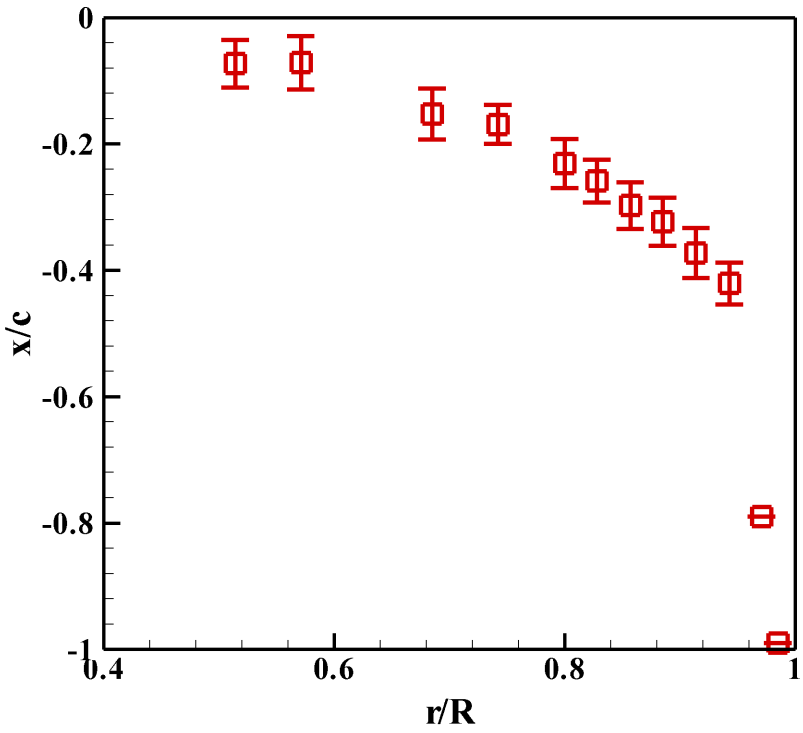

Figure 60: Radial variation of the phase-averaged separation line, with error bars showing standard deviation, the $x/c = 0$ location is the blade leading edge, while $x/c = -1$ is the blade trailing edge

various radial locations at one azimuthal angle could be used to derive conclusions on the span-wise variation at other azimuthal angles.

In order to quantify the cycle-to-cycle (CTC) variations of the DSV, the variations induced on the flow field due to other artifacts in the experiment had to be quantified. The phase locking error was quantified and as mentioned earlier the error in position of the blade is approximately $\pm 0.05°$. Next, the CTC variations in the far field were investigated by computing the standard deviation of the velocity measured at $\psi = 270°$ when the blade was located at $\psi = 290°$. The standard deviation was of the order of 0.25–0.37 m/s which indicated an insignificant amount of CTC variation in the flow field conditions. Next the variation of the tip vortex effect from one cycle to another was quantified, again by computing the standard deviation of the tip vortex induced velocities at r/R = 0.971. The fluctuations were determined be of the order of 0.27–0.62 m/s, again this indicates a

low level of tip vortex induced CTC variation. This analysis suggests the the far field has very low cycle-to-cycle variations. The above analysis was performed to isolate the CTC variations observed over the surface of the blade from other artifacts of the experiment. Having isolated the other CTC variations, the measured variations should be only due to the dynamic nature of the DS event rather than due to external factors.

Earlier it was discussed that the analysis of the phase-averaged velocity fields indicated a coherent DSV. However, the instantaneous velocity fields paint a different picture. The investigation of the instantaneous flow fields at $\psi = 270^\circ$ and r/R = 0.514 and 0.686 indicate that the so measured/observed coherent structure is a spatially diffused version of an instantaneous rolled up shear layer. At r/R = 0.514 the shear layer roll up breaks up into secondary vortices due to an instability. Following the nature of the instability, the secondary vortices were observed to be completely random in spatial location. A typical instantaneous shear layer roll up with a shear layer instability causing the secondary vortices over the rotating blade in dynamic stall conditions is shown in Fig. 61. However, on moving outboard to r/R = 0.686 the instantaneous velocity fields showed evidence of a single prominent vortical structure as seen in Fig. 62. As stated earlier, this variation implies that the timing of the DS event varies across the span of the blade. Similar behavior of shear layer during two-dimensional DS event has been observed at Re = 920,000 at different time instants of the airfoil upstroke (see Fig. 63 adopted from [82]). Mulleners's observation clearly indicates that the measurements in our experiments *cannot* be an artifact of the lower Reynolds number regime.

To quantify the CTC variations of the strength of the vortex, circulation around a fixed contour was computed for each instantaneous velocity field at r/R = 0.514 and 0.686. The contour was chosen such that it covered the rolled-up shear layer near the leading edge in every instantaneous velocity field. The average of the circulation computed around the vortex on 100 instantaneous velocity fields was determined to be 0.513 m^2/s with a standard deviation of 0.078 m^2/s at r/R = 0.514 and 0.739 m^2/s with a standard deviation of 0.126 m^2/s at r/R = 0.686. The low value of standard deviation (15%-17% of the mean) suggests that the strength of the vortex is stable from cycle-to-cycle to a certain

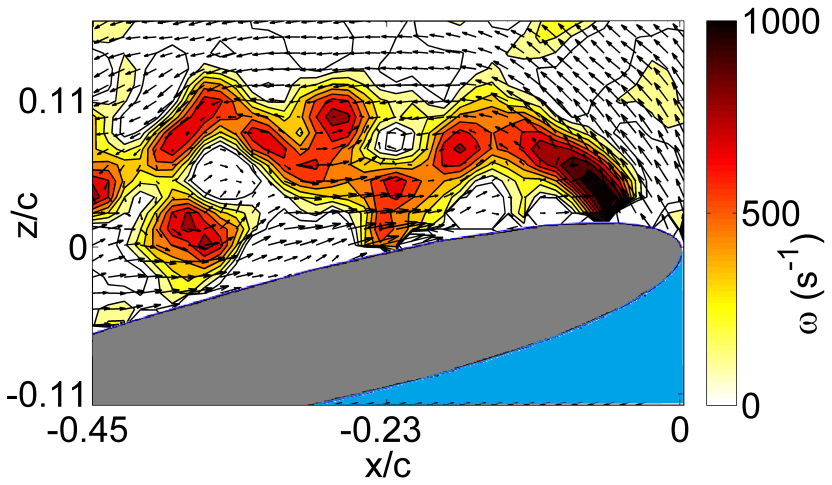

(a) Velocity field superimposed over the vorticity

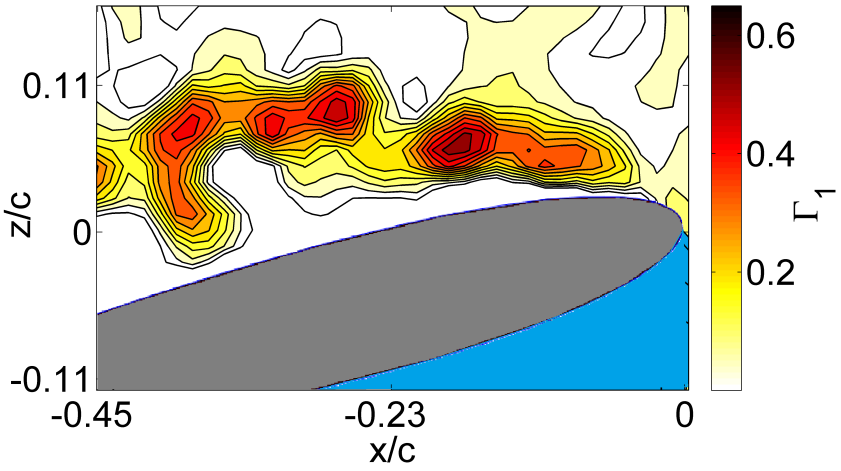

(b) Γ_1 of the shear layer roll up

Figure 61: Zoomed in view of the instantaneous velocity field at r/R = 0.514 showing shear layer instability with secondary vortices

degree. However, the average circulation obtained from instantaneous velocity fields was substantially higher (34.2%-44.9%) than the circulation of the vortex obtained from the phase-averaged velocity plots. The first implication is that the lift overshoot during the instantaneous DS event is higher than the overshoot obtained from the phase-averaged data. The second implication is that although the radial flow is relatively stabilizing the vortex strength from cycle-to-cycle, the vortex location is not stabilized, causing the vortex to be spatially diffused in the phase-averaged analysis. The fact that the spatial location of

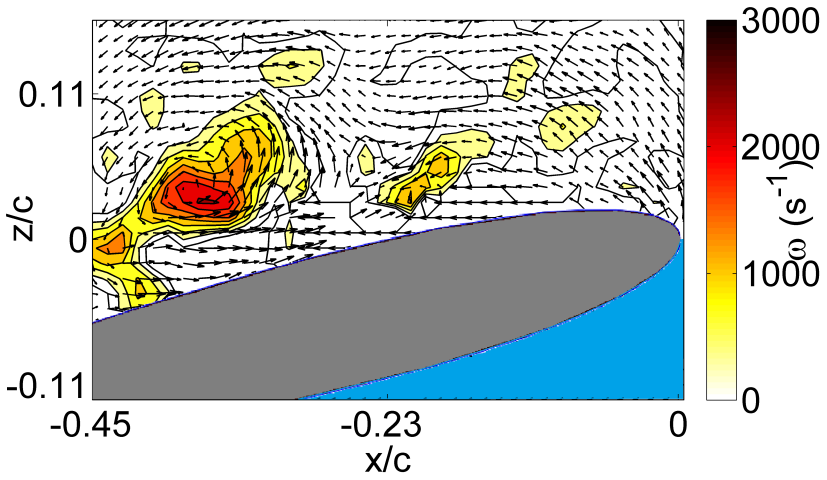

(a) Velocity field superimposed over the vorticity

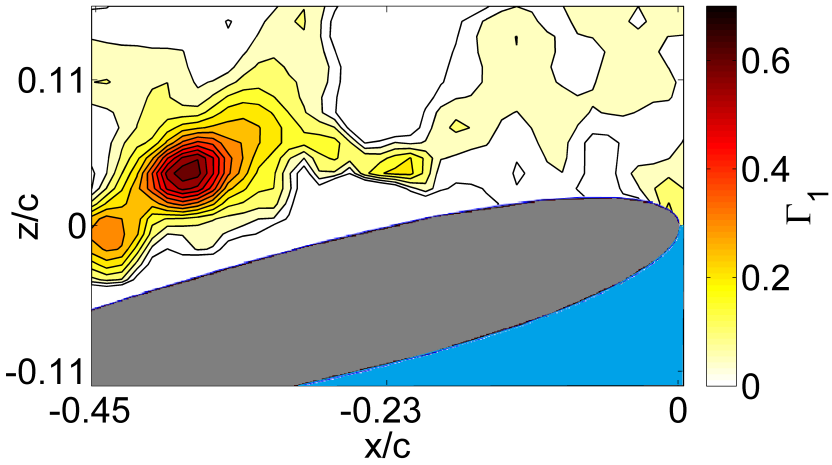

(b) Γ_1 of the shear layer roll up

Figure 62: Zoomed in view of the instantaneous velocity field at r/R = 0.686 showing a prominent vortex being shed

the vortex is erratic was also confirmed by computing the standard deviation from the phase-averaged data which was at around 32% of the mean value for r/R = 0.514. In summary, although the radial flow is stabilizing the strength of the vortex to a certain degree, the spatial location of the vortex from cycle-to-cycle is not stabilized. Hence, the consequences are twofold: *a*) If the strength of the vortex is relatively stable, the lift overshoot from cycle-to-cycle should also be stable and hence easily predictable. *b*) However, the erratic spatial location of the vortex implies that the associated pitching moment spike is not stable

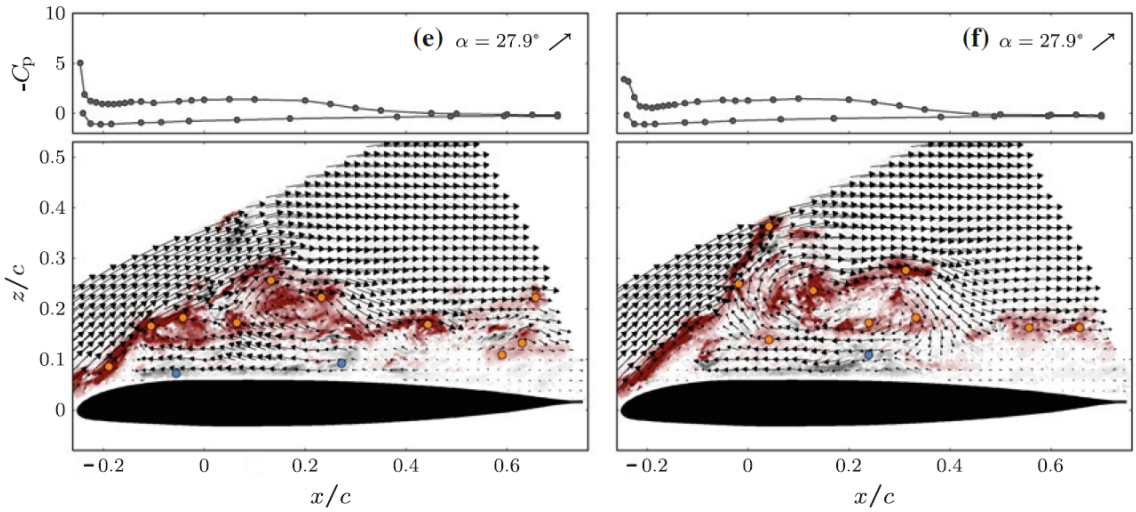

Figure 63: Shear layer instability of the DSV on a 2D oscillating airfoil at Re = 920,000 from [82]

and is harder to predict.

3.5 Summary of results

The characteristics of the unsteady flow field over a retreating rotor blade of low aspect ratio in dynamic stall conditions was investigated using PIV in a low speed wind tunnel. The findings of this investigation are summarized as follows:

1. A large-scale coherent vortical structure was detected in the phase averaged velocity field on the retreating rotor blade at $\psi = 270°$ using normalized angular momentum computations of the flow field.

2. The coherent vortex was classified as the DSV by virtue of the circulation of the vortex which is proportional to the lift overshoot during the DS event. The lift overshoot reduced on moving outboard indicating the weakening of the dynamic nature of the DS event.

3. The phase-averaged DS event was determined to have a strong dependence on radial location with the DSV being observed only at inboard locations $r/R \leq 0.8$.

4. The phase-averaged analysis of the DSV on the rotating blade indicated that it was pinned to the surface of the blade and elongated along the chord of the blade at all

locations where the vortex was observed. This result is in contrast to two-dimensional observations, where there is no radial velocity as in the rotating environment causing the vortex to occur in close proximity to the blade.

5. The instantaneous velocity fields painted a different picture. The coherent DSV observed in phase-averaged velocity plots were found to be a weaker and spatially diffused version of the instantaneous shear layer roll up.

6. A clear dependence of the DS event on the radial location was observed in the instantaneous velocity fields. At r/R = 0.514 the rolled up shear layer broke up into secondary vortices due to an instability whereas at r/R = 0.686 the instantaneous shear layer rolled up into a prominent vortical structure.

7. The radial flow relatively stabilizes the strength of the vortex from cycle-to-cycle but the vortex location is not stabilized causing the vortex to be spatially diffused and weaker in the phase-averaged analysis.

8. The main consequences of these implications are that the relative stability in the strength of the vortex makes it easy to predict the cycle-to-cycle variations in the lift overshoot. However, the erratic spatial location of the vortex implies that the associated pitching moment will not be stable from cycle-to-cycle and would be harder to predict.

CHAPTER IV

RADIAL FLOW DURING DYNAMIC STALL

4.1 Introduction

Initial experiments at The Georgia Institute of Technology [113] used a rotor in a hover facility, for the convenience in bringing the flow diagnostics close to the flowfield. Transient stall was induced by an "inflow obstructer" which was a plate in the shape of a sector of a circular disc, placed axially upstream of the rotor. The rotor blade was set at a pitch angle well above the static stall angle of attack of the airfoil section. When operated as a rotor, the induced inflow would ensure that the blade remained unstalled. The pitch was increased by trial and error until it was just under the angle where the rotating blade would stall as it entered the region where the inflow was obstructed. Laser sheet visualization confirmed that stall was occurring over the blocked sector, but the rotor was producing thrust elsewhere over the rotor disc. PIV data showed discrete structures developing in the velocity field when viewed in the axial-radial cross-flow section. These structures suggested a mechanism whereby the accelerated flow near the blade surface could be exchanged with the nearly stagnant flow away from the surface. In this particular experiment, the inflow obstruction was much more severe than what may be encountered in any practical engineered design of a rotating-blade device.

Following the "inflow obstructer" experiments, this study investigates the radial velocity field over a blade of a two-bladed teetering rotor in forward flight using extensive PIV studies.

4.2 Objectives

The radial flow field that exists on a rotating blade during dynamic stall has not been studied until recent measurements by our research group. The main objectives of this chapter are to:

1. Throw light on the rather unknown radial flow field on a retreating rotor blade in dynamic stall.

2. Study and characterize the physics of the radial flow using velocity measurements made at $\psi = 270°$.

3. Quantify the radial flow characteristics to estimate the effects of radial flow on the dynamic stall process.

4.3 Experimental methods

4.3.1 Experimental setup

The experiments were conducted in the high advance ratio experimental setup (please refer to Section 1.5.2 for a detailed description of the facility) constructed in the test section of the closed circuit John J Harper 7'×9' (2.13m×2.74m) low speed wind tunnel in the School of Aerospace Engineering.

Studies by Bousman [7, 8] correlating flight data with predictions show that the event of primary interest in load prediction is the large excursion in blade pitching moment that accompanies the separation and convection of the dynamic stall vortex. One school of thought suggests that the timing of dynamic stall on full-scale helicopter rotor blades depends on shock-vortex interaction phenomena in the highly accelerated flow over the leading upper surface of the blade [15]. The shock terminating this region may trigger or interact with the separation of the dynamic stall vortex. Thus it may be rightly extrapolated that experimental studies where the critical Mach number is not exceeded are irrelevant to predicting the stall line. But it should be noted that the flow field downstream of the stall line is incompressible, and studies in this region can be conducted ignoring compressibility. Further, the large aspect ratio that is typical of helicopter and wind turbine blades is not essential to study the physics of the radial flow. This is because the stalled regions develop well inboard, eliminating aspect ratio effects. Thus a moderate aspect ratio, low tip Mach number test case is adequate for the purposes of studying the radial flow on a rotating blade in dynamic stall. These reasons form the basis for the design of the experimental setup used in this work.

Given the objectives and motivation of studying radial flow behind the stall line, a rotor RPM of 200 and a tunnel speed of 20 ft/s (6.1m/s) was chosen. The operating advance ratio is 0.33, which was shown to be sufficient to induce dynamic stall [29]. This condition results in a chord-wise relative velocity of about 10.5 ft/s (3.21m/s) at the rotor mid-radius at the 270° azimuth of the 35-inch (0.889m) radius rotor. The angles determined for use in the experiment agreed with the angles corresponding to the onset of dynamic stall for a NACA0012 airfoil as reported by McCroskey et al. [75]. Further details of the facility and test are provided in Table 2.

The forward flight rotor results presented here started with extensive PIV studies of the radial velocity field over the retreating blade of a two-bladed teetering rotor in forward flight [29]. PIV was primarily used to study the radial flow over the dynamically stalled blade in forward flight using the setup depicted in Figure 4.3.1. Radial flow measurements were obtained at four stations using the apertures shown in Figure 64(b). To demonstrate the validity of the radial flow results, static stall tests were conducted on the blade at an angle of attack of 13.5° and a free stream velocity of $15ft/s$ $(4.6m/s)$.

The Laser was placed outside the test section and the TSI optical arm was used to deliver the laser light right above the rotor. The TSI optical arm is an articulated arm that offers flexibility in delivering the light sheet for PIV measurements or for other high energy laser applications. Featuring a beam path that can be fully enclosed from the laser to the measurement area, it is essential for safely delivering high energy, pulsed YAG laser beams. At the end of the arm, sheet optics provided by LaVision was used to generate the laser sheet of required thickness and divergence. The laser sheet was approximately 3mm thick and since the laser optics was very close to the blade a minimal focal length(focal length = -10 mm) lens was used to have a wide divergence angle so as to cover the whole blade.

Next the laser sheet was aligned with a particular r/R location on the blade and the free stream direction. The blade was then removed out of the position and the calibration plate provided by LaVision was placed in the test section and was aligned with the laser sheet, keeping in mind to make sure that the height was correctly adjusted to capture the flow field over the blade and slightly below the blade. At each position, a calibration was

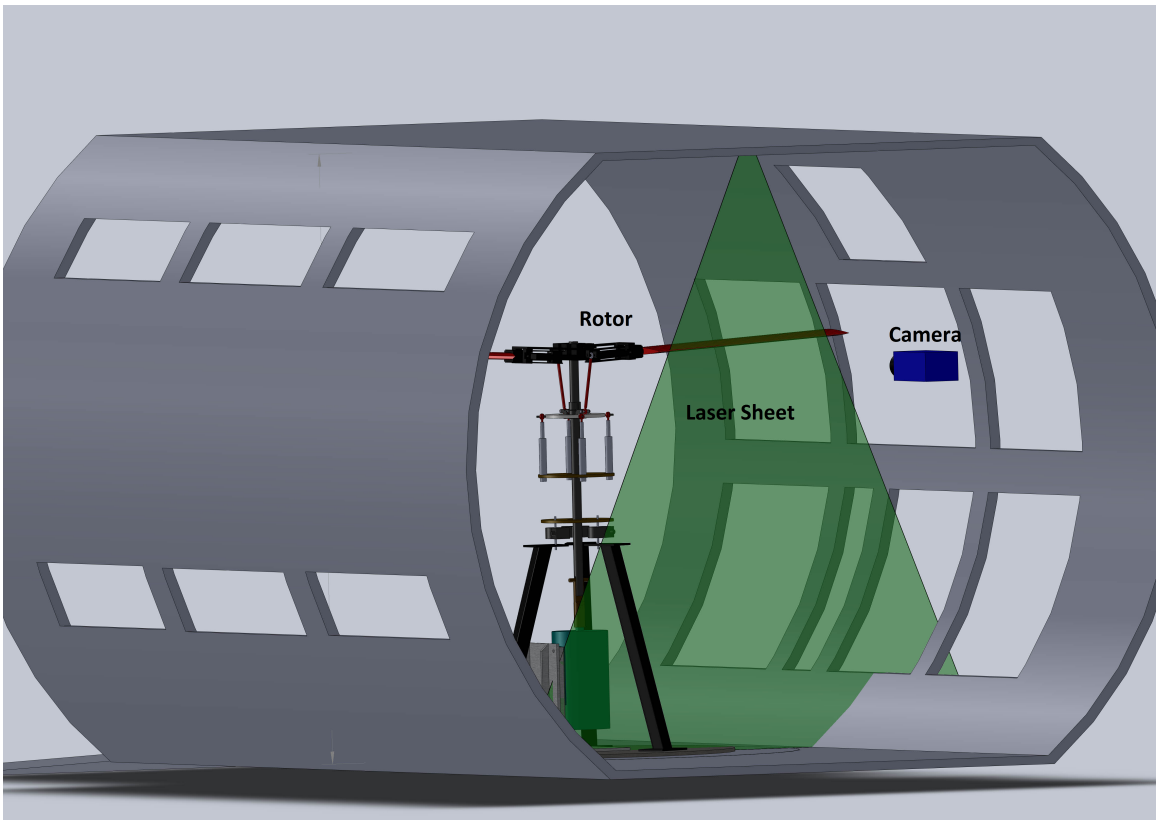

(a) Schematic of the PIV setup for Radial Flow looking from upstream

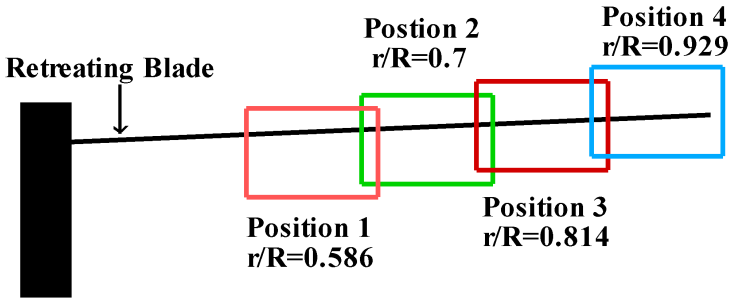

(b) PIV apertures over the radius of the blade.

Figure 64: High Advance Ratio Facility - configured for Radial Flow

performed. The correction for the tilt of the measuring window was applied. The RMS error of calibration was 0.315, generally an RMS error of less than 0.5 is considered a good calibration.

4.3.2 PIV Considerations

The recording method chosen was a double frame/double exposure (cross-correlation). This was basically done to achieve superior velocity vector fields over the auto correlation. To accomplish this double frame, the flash of the first laser illuminated the first frame and the flash of the second laser illuminated the second frame. All these functions are controlled by The Programmable Timing Unit (PTU) which is the central element for the timing of the system. The triggering mechanism was through a external cyclic trigger where the time delay was set to make sure the blade was located exactly at 270 degrees azimuth.

Since the mean flow direction was normal to the image plane, it was important to choose a pulse separation (Δt) that was short enough to ensure that the out-of-plane movement did not exceed 1/3 of the sheet thickness as discussed by Prasad [88]. A delay of 100 μs was chosen to produce sufficient frame-to-frame particle matching. Accurate PIV measurements also depended on the interrogation window size. Signal-to-noise ratio begins to degrade if particle displacements exceed one quarter of the interrogation window [88]. Optimally, 7 to 10 particles in each interrogation window are necessary [2]. Using results by Yang et al. [113] a maximum axial velocity of $8m/s$ was estimated while the radial velocity was limited to $3m/s$. A 32×32 pixel window would be sufficiently large so that particles traveling less than $10.6m/s$ would not travel more than 8 pixels or one quarter of the total interrogation window.

Velocities were calculated from the spatial cross-correlation of the images. The average particle displacement in each interrogation window was revealed by the location of the highest correlation peak. With the pixel size of the ImagerIntense camera averaging $6.5\mu m$, the particle size ranged from 1.06 pixels to 1.97 pixels. The optimal particle diameter for digital cross-correlation is approximately 2 pixels.

An interrogation window overlap of 75 percent and a second interrogation pass with a reduced window size increased the data yield and the signal-to-noise ratio of the correlation peak. Therefore, the first pass utilized an interrogation window of 64×64 pixels while a 32×32 pixel window was used on the second pass. Post-processing of the vector images consisted of an applied vector range and a median filter. As erroneous vectors appeared at

the edges of the camera viewing window, these processes greatly reduced this noise. Further details on the experimental methodology are presented in DiOttavio et al. [29].

4.3.3 Cross-flow plane downstream of trailing edge

The choice of the cross-flow plane and the instant immediately following the passage of the trailing edge enabled the capture of the velocity field just above and below the trailing edge without the blade surface obstructing or scattering the laser illumination. The flow at that station, measured much less than a millisecond after passage of the trailing edge, is negligibly different from the station immediately before the trailing edge. Certainly it is recognized that the wake of the blade changes rapidly, and the velocity field thus changes within a short distance of the trailing edge. However, recent computational results by Gross et al. [44] verify that the change immediately downstream of the blade is insignificant.

4.3.4 Flow Conditions

It was determined early in the experiment that a rotor RPM of 200 and a tunnel speed of 20 ft/s, which is an advance ratio of 0.33, would be a sufficient operating condition to capture dynamic stall. This condition would cause a chordwise velocity of about 19ft/s at mid-span at the 270 ° azimuth. As these conditions were kept constant, various cyclic and collective combinations were tried. A progression of separation can be seen in Figure 65 from attached flow to a total upper surface separation.

Therefore, it was decided to use the collective and cyclic setting of 10° and −5° respectively to produce a 15 degree angle of attack on the retreating blade. However, due to the flapping of the blade, the effective angle of attack seen by the retreating blade is 16.8° which matches the angles corresponding to the onset of dynamic stall for a NACA 0012 airfoil as reported by McCroskey et al. [75].

As mentioned earlier PIV was primarily used to study the radial jet over the dynamically stalled blade in forward flight. Flow measurements were made at four stations/windows(Figure 50(b)). The Figure 66 shows the view of PIV imaging from the camera. In addition to make sure that the results obtained were justifiable, static stall tests were conducted on the blade at an angle of attack of 13.5° and a freestream velocity of

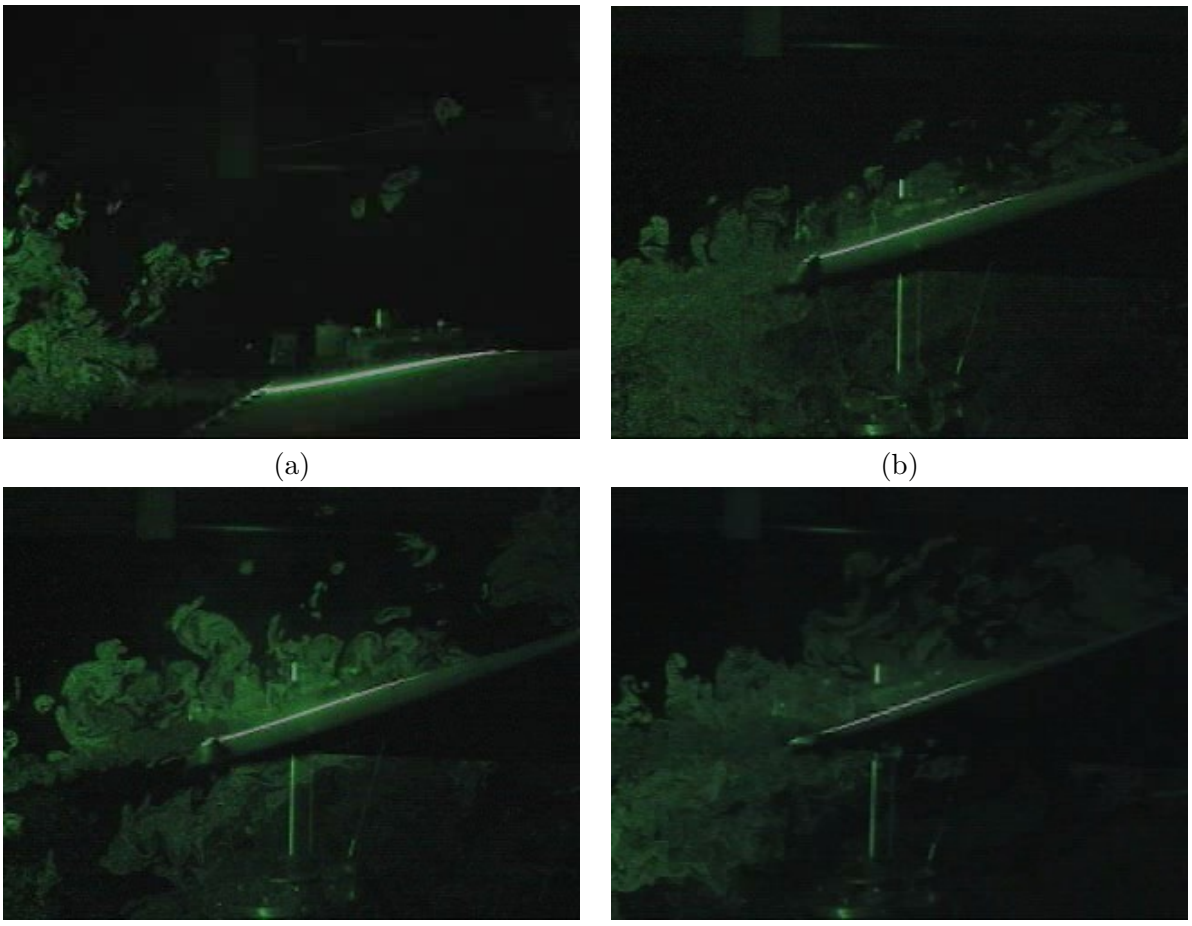

(a) (b)

(c) (d)

Figure 65: a) 5° Collective, 0° Cyclic b) 7° Collective, −5° Cyclic c) 8° Collective, −5° Cyclic d) 10° Collective, −5° Cyclic

15ft/s. Figure 67 shows the vector plot overlaid on the vorticity field. Definitely there were no visible signs of vortical structures and as expected a stalled flowfield was obtained.

4.4 Hypothesized flow features

The conceptual flow field is illustrated in Figure 68. In Figure 68(b) the $Z = 0$ plane represents a plane immediately above the blade surface and $Z = 1$ plane represents a plane farther above the blade surface. From the prior experimental results, the flow field in dynamic stall is hypothesized to have the following characteristics:

1. The flow downstream of the separation line over the blade is highly three dimensional and the Mach number remains low in the region downstream of the separation line.

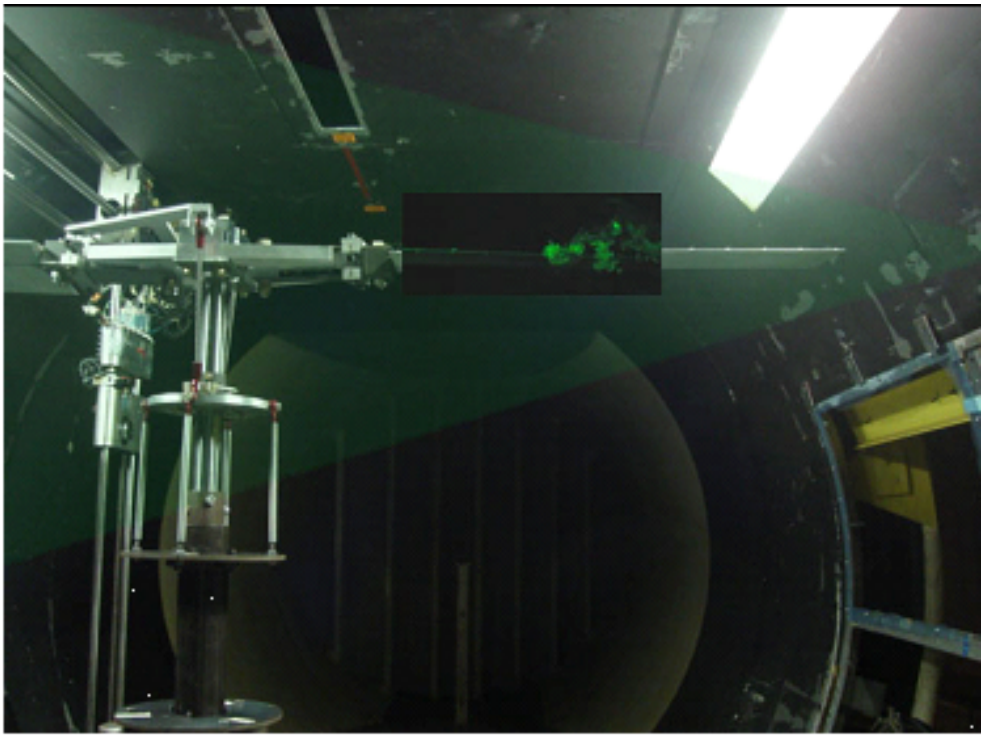

Figure 66: View of PIV imaging from camera

2. The nature of the separation line on a rotating blade will involve interaction between the stall line, tip vortices and the separated flow field downstream (see Figure 68(a)).

3. As the flow adjacent to the blade in the separated region moves at low speed relative to the rotating blade, the radial stresses at the surface may be transported to a substantial height above the surface into this flow, in contrast to the case of attached flow (see Figure 68(b)).

Using these results the following characteristics of the flow can be hypothesized:

1. The occurrence of a large radial flow can in turn have a strong influence on the separation process itself and thus have a role in determining the shape of the separation line (see Figure 68(a)).

2. The near-surface flow field will form a radial jet both above and below the blade surface due to the radial acceleration on the surface.

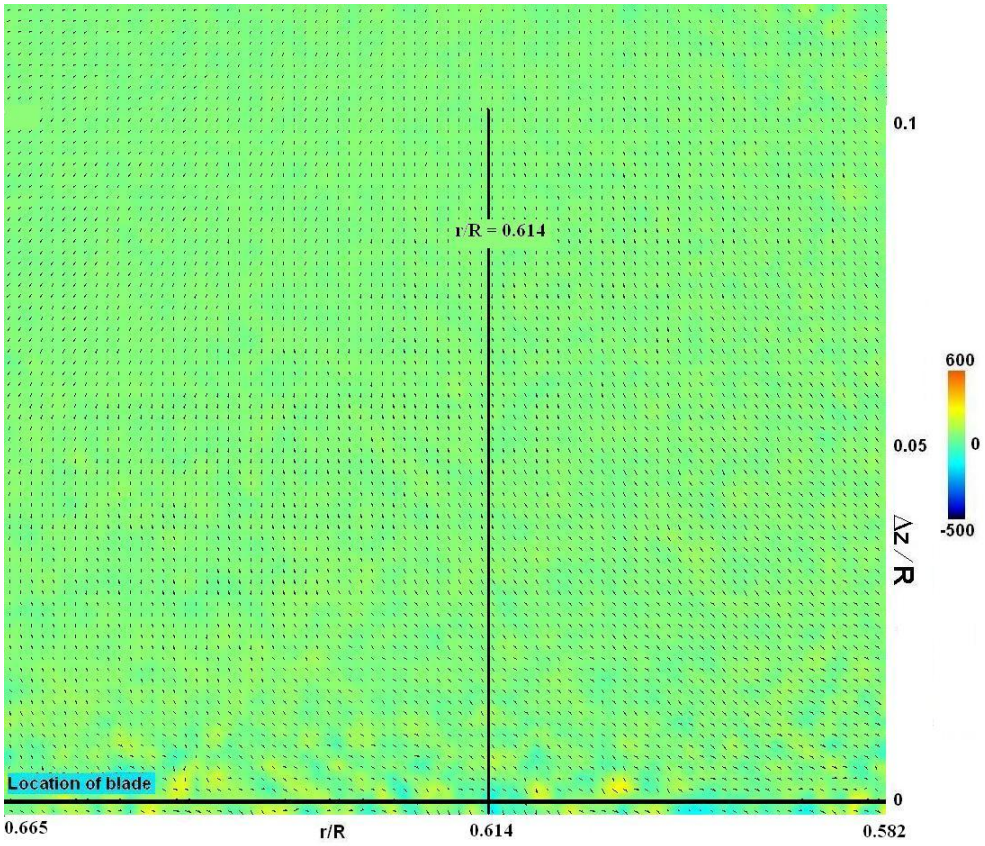

Figure 67:

3. This jet will itself be highly vortical as the flow at the blade surface obeys the zero-slip condition with respect to the rotating blade, while the flow immediately above that layer is accelerated radially outward (see Figure 68(b)).

4. The vortical jet is highly susceptible to shear layer instability due to the unsteady nature of the flow leading to break up of this layer.

From the above it can be concluded that not just the magnitude and profile of the radial velocity field in this region are of interest. Equally important are the characteristics and behavior of this radial jet which might contribute to the post-stall evolution of lift and pitching moment.

4.5 Results and Discussions

Radial flow over the rotor occurs as a result of centripetal and reactive centrifugal forces due to rotation, irrespective of blade stall. The influence of the centrifugal reactive or pumping

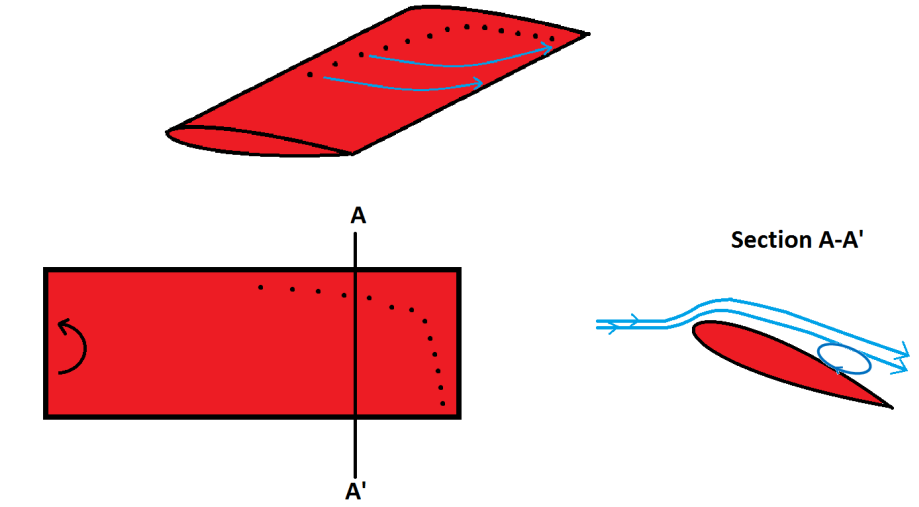

(a) Conceptual representation of the Separation line and separated flow

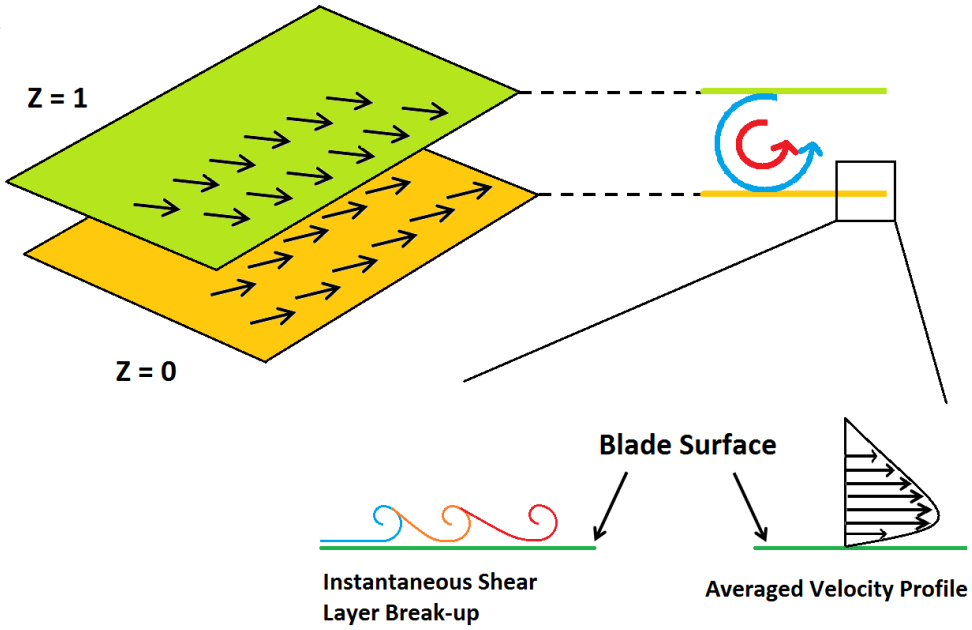

(b) Conceptual representation of shear layer and vorticity above the blade

Figure 68: Hypothesized flow features on a dynamically stalled rotating blade

force could be significant in adverse pressure gradients where the flow is retarded [79]. Although three-dimensional flow separation can itself manifest as fluctuations in spanwise flow, there exists no physical mechanism to develop a sustained flow in radial direction due to three-dimensional separation alone. The radial flow characteristics are discussed in detail in the following sections.

4.5.1 Radial velocity

As hypothesized, the rotation of the blade gives rise to a radial jet flow that develops over the surface. However, the no-slip condition must apply at the blade surface and thus, a viscous boundary layer exists. Moreover, the attached flow at the bottom surface of the blade also experiences the same radial acceleration. Therefore the radial flow velocity field should show radial jet layers adjacent to both the upper and lower blade surfaces. It is also noted that this boundary layer is very thin, and it is not expected that PIV will resolve this in the present experiments. Due to these reasons the double-peaked radial velocity profile adjacent to the blade surface appeared as a single peak at the middle of the blade thickness. This was observed at all the radial stations in Figure 69. It shows that the radial jet is confined to the region close to the blade. The jet appears to exist above and below the blade trailing edge. This is due to the fact that the measurement was taken 2mm downstream of the trailing edge, as indicated in the discussion regarding the inability to capture the blade boundary layer. For the moment, it can be assumed that the peak of the jet is what is seen, but that the radial velocity must drop from the maximum value to zero in the distance between the peak location and the surface of the rotor. This assumption is used to estimate the vorticity in the boundary layer above the blade. For the moment, the phenomena on the bottom surface of the blade are ignored.

The steps that went into producing the plots of radial velocity are: First, the velocity vectors were ensemble averaged. Second, using image processing, the blade surface is located from images of laser sheet visualization. Finally, the radial velocity component is transformed so that it is parallel to the blade surface (the blade is flapped up $+4^{\circ}$) in order to consider the vorticity in the boundary layer.

Figure 69 shows the axial variation of the averaged radial velocity profiles normalized by blade tip speed. The salient feature is that the magnitude of the radial velocity peak essentially decreases on moving outboard along the blade, quite the opposite of the expected increase in radial velocity. The uncertainty in the peak value due to spatial resolution is estimated to be less than 0.61% of the peak height of the velocity profile. The error was estimated by extrapolating the data after ignoring the peak to obtain an extrapolated peak

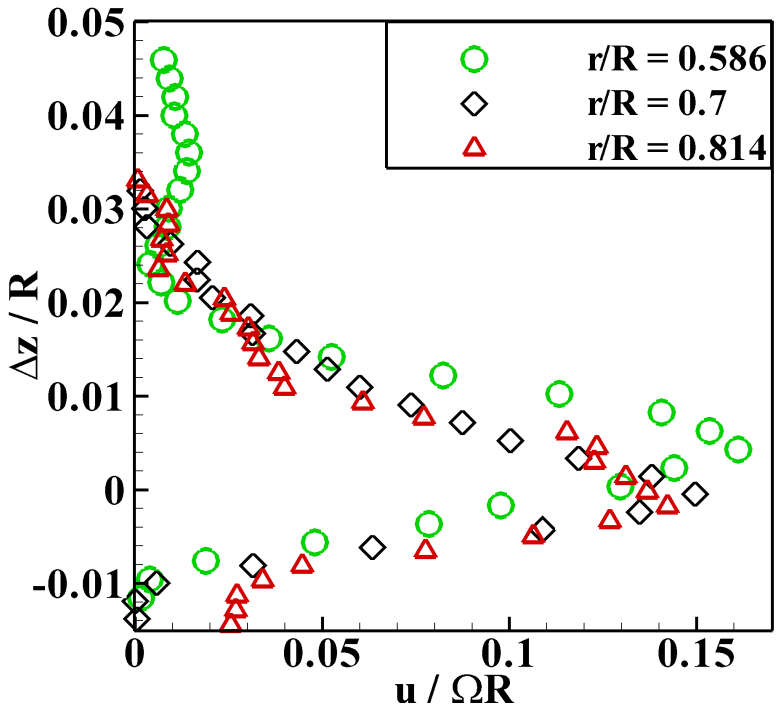

Figure 69: Profile of the variation of average radial velocity at various radial locations, normalized with respect to Blade Tip speed.

and then comparing it to the measured peak.

It should be mentioned here that direct comparisons to span-wise (radial) flow on an oscillating airfoil/wing during dynamic stall conditions should be done to understand the exact effect of rotation. However, this entails a whole new investigation of span-wise flow on oscillating wings with zero sweep and is left as a recommendation for future work.

4.5.2 Discrete structures in the cross-flow plane

A literature review on the separated flow over lifting surfaces revealed studies on stalled fixed wings, but very little on dynamic stall in flows over "true" rotating blades. Three-dimensional flow patterns were detected on airfoils based on surface visualizations by Gregory et al. [42] and surface oil streaklines by Winkelmann and Barlow [112]. Weihs and Katz [109] reported cells in the post-stall flowfield over straight wings. Similarly coherent structures and cells in the separated flow were observed by Yon [115, 116]. Yon also reported the fluctuations attributed to these cells in the wake of a stalled rectangular wing.

Low frequency oscillations were observed in the case of two-dimensional leading edge separation by Broeren [10]. Spanwise separation cells were seen to arise from trailing-edge separation, but this was primarily steady. Thus from the above discussion, it appears that spanwise cells have been observed in the stalled flow over fixed wings, even on nominally two-dimensional airfoil models. However, they are driven by the shear at the top of the separated flow region, which is the only source of vorticity in that situation once the flow is separated. This is very different from the case of a rotating blade where high shear stress in the form of radial stresses is present at the blade surface. In addition, recent numerical studies on a S822 wind turbine airfoil [44]) showed the effect of cross-flow on a rotating blade. The blade rotation resulted in a radial velocity component towards the blade tip in the separated flow region. The study postulated the existence of stationary and traveling cross-flow vortices over the span of the blade.

Figures 70–72 shows the vorticity contours in the cross-flow plane at three radial locations in the trailing edge plane. Clearly the jet shear layer has broken into several discrete structures in the windows shown. In addition, the vorticity entrained in the structures increases on moving outboard. Furthermore, the structures also appear to be lifting off the surface (referred to as "peel" or "jump" off) at the more outboard locations, a trend also seen in the measurement window centered at r/R = 0.814 and beyond.

An important aspect of these discrete structures is the variation of their size at different radial locations. In each of the PIV interrogation windows the average size of the structures was determined. This analysis was performed by measuring the major axis and minor axis of discrete structures appearing on 20 vector fields. The radial dimension was designated as the major axis (x/c) and the axial dimension was designated as the minor axis (y/c). With this designation if the major axis is equal to the minor axis the discrete structure is circular else it is elliptical. The variation of the major and minor axis (normalized by chord length (c)) on moving outboard is summarized in Table 11 and illustrated in Figure 73. However, it should be noted this analysis and discussion is statistical (averaged over 20 vector fields) and should not be misconstrued as instantaneous flow characteristics.

On moving radially outboard the size of major axis monotonously increases whereas the

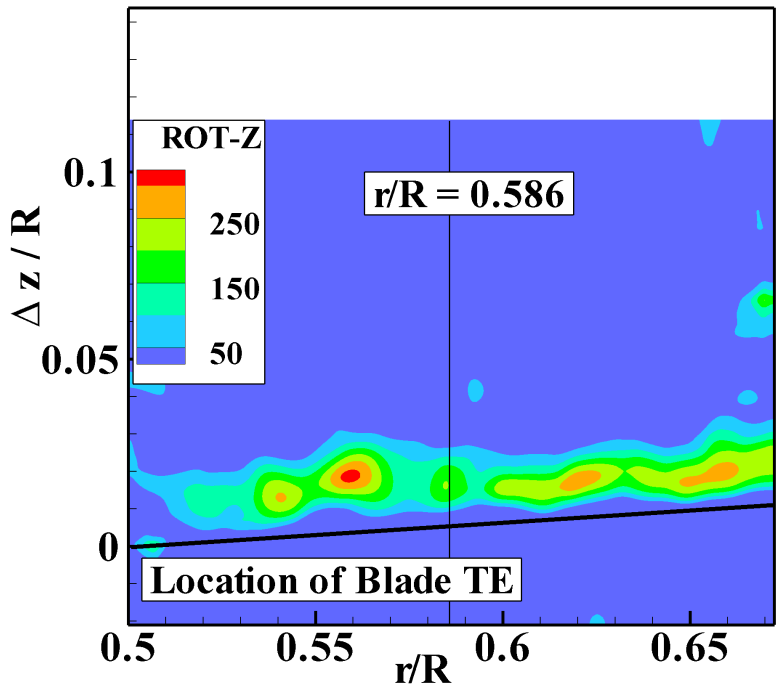

Figure 70: Contours of vorticity showing discrete structures above the blade at r/R = 0.586

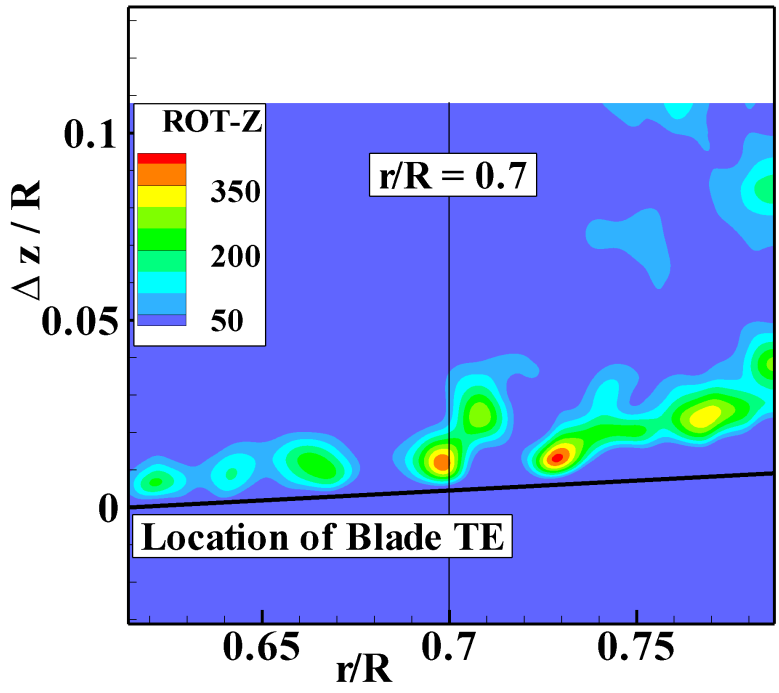

Figure 71: Contours of vorticity showing discrete structures above the blade at r/R = 0.7

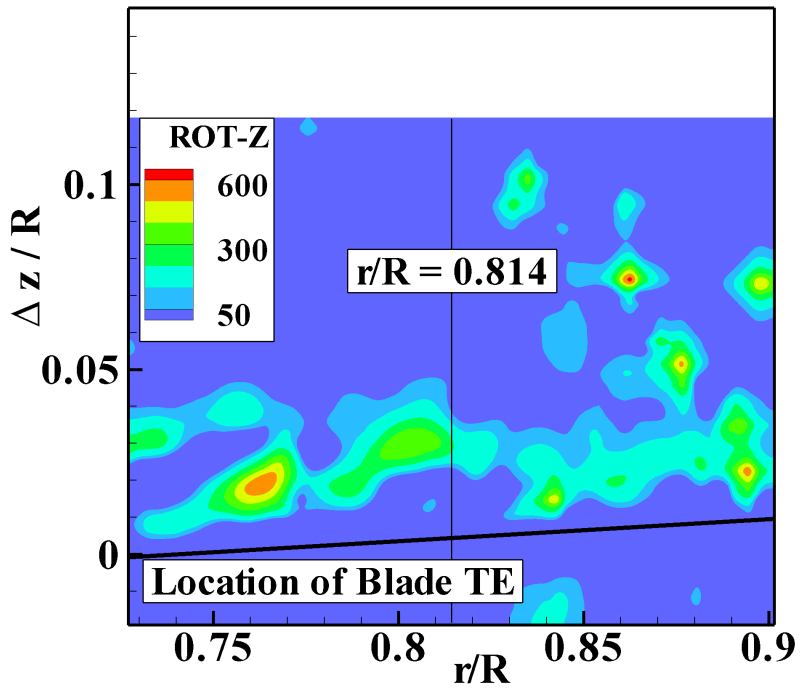

Figure 72: Contours of vorticity showing discrete structures above the blade at r/R = 0.814

Table 11: Variation of major (x/c) and minor (y/c) axis of the discrete structures with radial location

Window	Average		Standard deviation	
	x/c	y/c	x/c	y/c
r/R = 0.586	0.081	0.072	0.014	0.022
r/R = 0.7	0.088	0.063	0.022	0.018
r/R = 0.814	0.093	0.060	0.017	0.012

size of the minor axis monotonously decreases, suggesting two specific insights.

1. The discrete structures undergo a "stretching" due to the increase in radial stresses at outboard locations. It is conjectured that the "stretching" of these structures might have a causal relation to the "jumping" of the structures observed at outboard locations.

2. The above insight implies that these structures were formed at inboard locations and not in the window they were observed. This conclusion is premised on the fact that these structures need a finite amount of time (greater than time needed to convect

within the same window) to "stretch". In other words, the structures observed at the outboard locations originated inboard on the blade and convected radially outward.

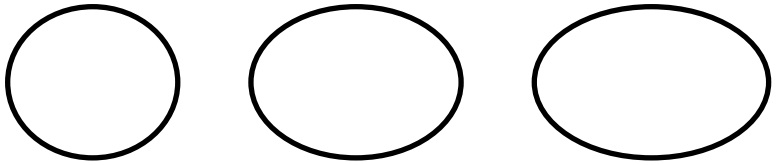

(a) r/R = 0.586 (b) r/R = 0.7 (c) r/R = 0.814

Figure 73: Illustration of the average size of discrete structures (not to scale)

In order to further understand the characteristics of these discrete structures, a statistical convergence test was performed on the data set. This sought to determine at what point during the ensemble averaging process would the discrete structures coalesce. First all the hundred vector fields collected at a given station were averaged. The vorticity of the discrete structures were observed to reduce to the local average vorticity level. Further, after averaging approximately 20 vector fields these discrete structures were no longer distinctly visible (see Figure 74). Distinctly visible was defined as the vorticity entrained in these structures being less than 20% higher than the local vorticity. This indicates a moderately rapid change in the precise locations of the structures, but also shows that their locations are not drastically different from one velocity field to the next.

The ensemble averaging analysis was aimed at identifying the precise location of these discrete structures. However, that analysis does not yield any information of the average vorticity contained in all the discrete structures in a particular window. This can be done by overlaying the centers of all the discrete structures occurring within an interrogation window over 30-40 vector fields. The results of this analysis is presented in the Figures 75–77. The negative vorticity observed below the structures is mainly because the averaging window chosen extended below the blade - which has negative vorticity. This ensemble averaging analysis has three important implications:

1. The averaging process applied to the discrete structures indicate that these structures are significant occurrences in the radial flow and further analysis is needed to quantify its significance in the radial flow field.

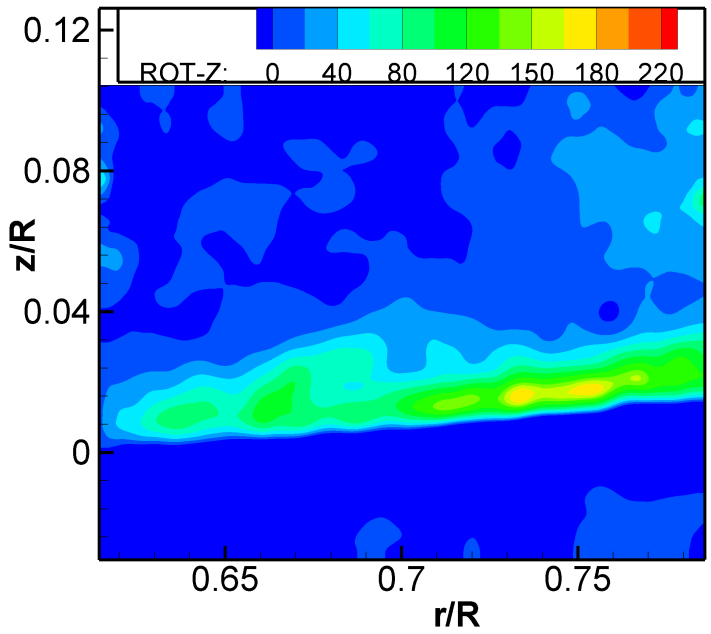

Figure 74: Ensemble averaged vorticity contours over 20 instantaneous vector fields

2. They also corroborates earlier findings of the "stretching" of these structures on moving radially outboard.

3. The fact that they all have comparable strengths, indicates that the process of initiation and formation of these discrete structures should be predictable by some means.

4.5.3 Significance of the discrete structures

The significance of the discrete structures is crucial to the understanding of the radial flow. In order to explore the significance of these discrete structures, first the question - what is the source of these instabilities? - must be answered. Hence in search for the answer, the root-mean-square (RMS) variation of the velocity vectors was investigated. The following hypothesis was made - "If the radial flow near the surface is the source of the instability, the fluctuation intensity in RMS should be high in the regions of higher radial flow. Else the fluctuations should be higher at the upper edge of the separated flow." The complete analysis of the ensemble averaged profiles showed that in all cases the RMS fluctuation peak essentially overlapped the peak of the radial velocity (Figure 78 shows the RMS peak close

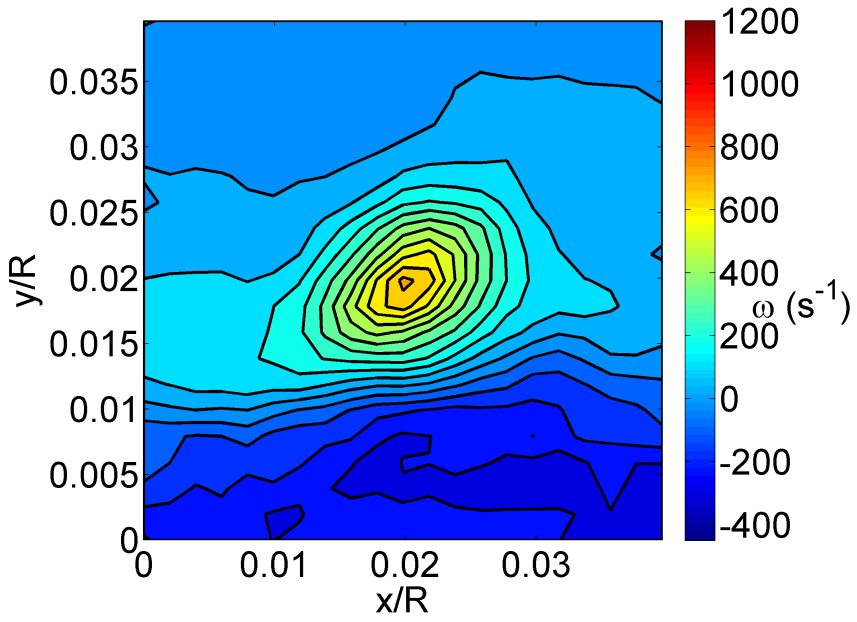

Figure 75: Ensemble averaged vorticity contour of discrete structures at r/R = 0.586

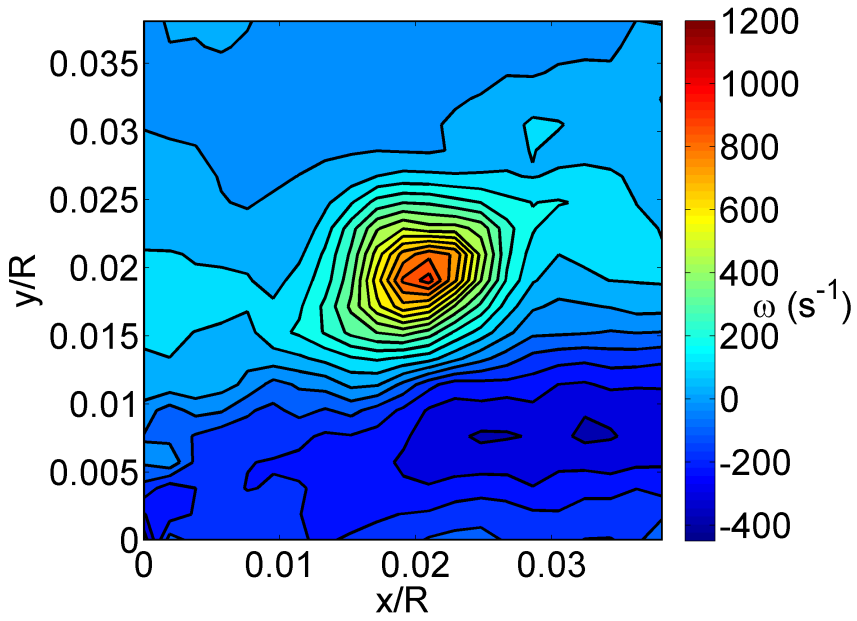

Figure 76: Ensemble averaged vorticity contour of discrete structures at r/R = 0.7

the blade surface). A significant implication of this analysis is that the discrete vortical structures are "driven" by the vorticity in the radial jet shear layer and not by the shear layer separating the upper edge of the separated/recirculating flow from the freestream.

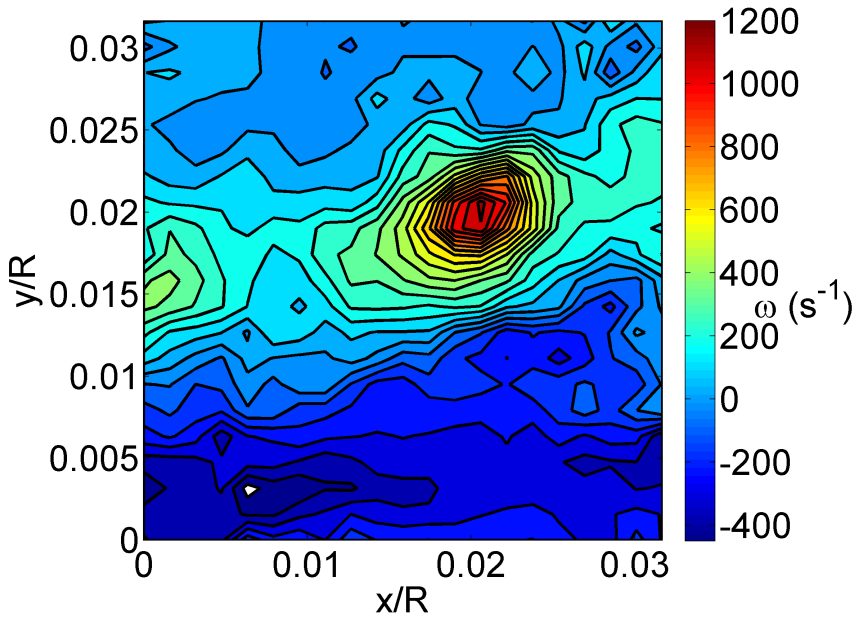

Figure 77: Ensemble averaged vorticity contour of discrete structures at r/R = 0.814

Moreover, the increasing RMS fluctuations indicates that they have a primary relationship to the increasing strength of the structures as one moves radially outboard on the blade.

4.5.4 Quantitative estimates

The average vorticity entrained in the discrete structures at various radial stations is depicted in Figure 79. This analysis was conducted by choosing 'a' radial location and averaging all the discrete structures that appeared at that location (in contrast to averaging all structures in a window). The key revelation is that the average strength of the structures and their variance increases on moving outboard on the blade. This fact along with the notion that the discrete structures are "driven" by the radial jet shear layer (discussed in previous section) can now be used to reconcile the behavior of the radial velocity. In other words higher amounts of vorticity generated from the surface is entrained in the discrete structures on moving outboard. Subsequently these discrete structures which were observed to "peel" or "jump" off the blade (see Figures 70–72) caused the evident decrease of peak magnitude of the radial velocity on moving outboard on the blade (Figure 69)

A quantitative comparison of the average strength of the structures to the average

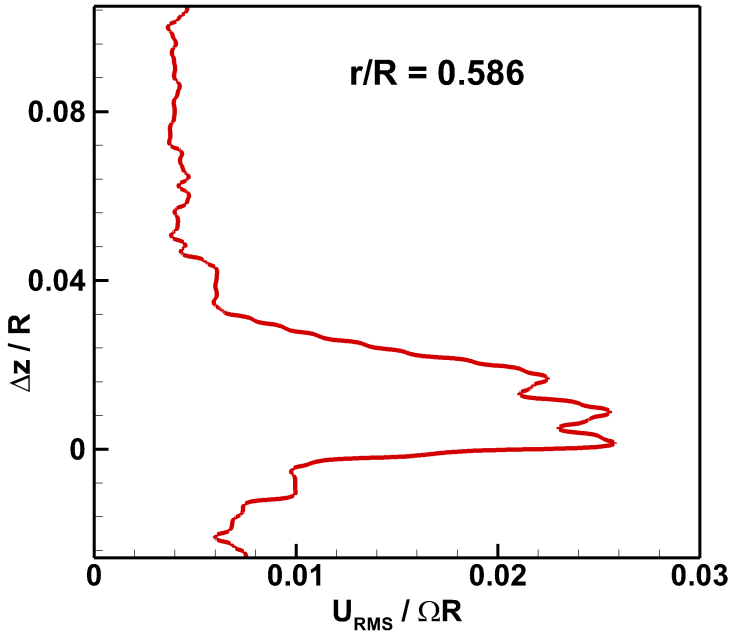

(a) r/R = 0.586

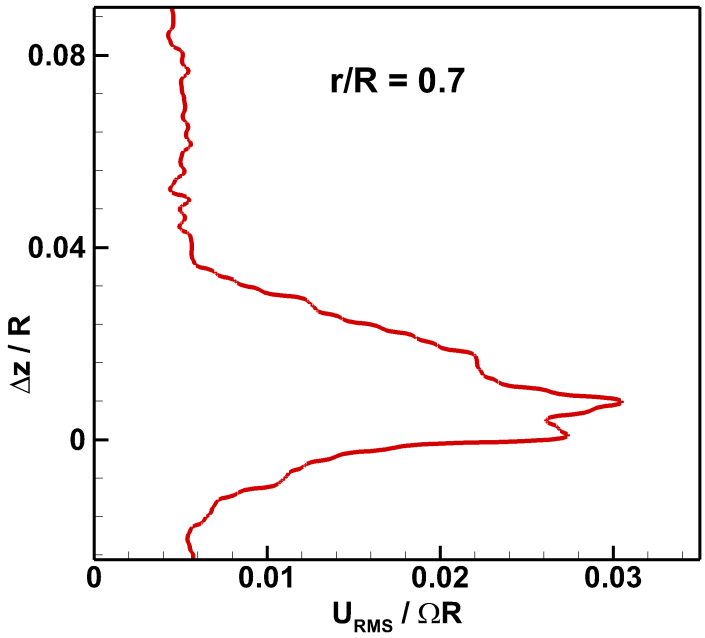

(b) r/R = 0.7

Figure 78: RMS fluctuations showing the peak occurring near the blade surface

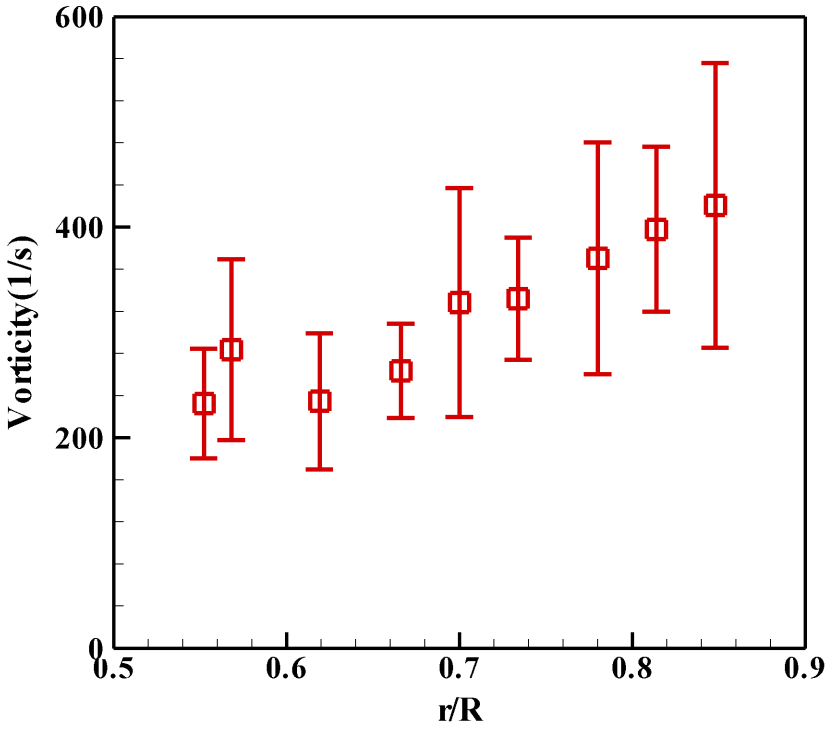

Figure 79: Radial Variation of the average vorticity of discrete structures, and their RMS variation in the trailing edge plane.

vorticity in the shear layers bounding the radial jet is illustrated in Figure 80. Two shear layers were considered for this analysis. First, the lower shear layer (LSL) is the boundary layer between the solid blade surface and the peak of the radial jet profile. It is produced by the shear between the radially accelerated flow and the no-slip condition at the surface and is the stronger of the two shear layers. Second, the upper shear layer (USL) is the layer of fluid above the point of peak radial velocity. It is produced by the jet velocity decay into the largely stagnant zone above it.

The LSL was observed to be almost an order of magnitude (factors of 7 or 8 have been observed) stronger than the discrete structures at inboard locations. It then weakens, even as the structures themselves get stronger, so that it is only 3 to 4 times as strong as the structures at the most outboard locations evaluated. Thus at these outboard locations, the discrete structures carry away 25% to 30% of the jet. However, the strength of the individual

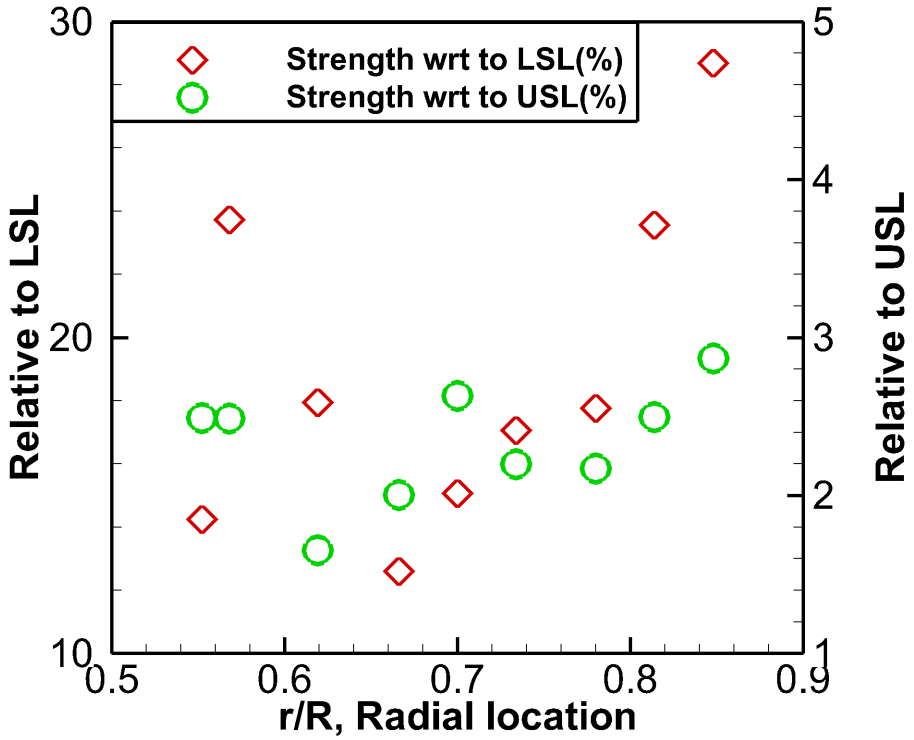

Figure 80: Average strength of Structures with respect to the Upper and Lower Shear layers

vortical structures is much less than 2% of the vorticity estimated from the radial velocity profile for the USL. Hence it can be inferred that this jet decay occurs mostly through the breakoff of the discrete structures.

4.6 Summary of results

1. In the separated flow over a rotor blade in retreating stall conditions, the radial velocity along the blade develops a sharp jet like profile pointing radially outward.

2. Discrete vortical structures occur in the separated flow field immediately above the blade, similar to those breaking off a shear layer.

3. The strongest RMS velocity fluctuation in the flowfield is near the peak of the radial velocity profile, indicating that the source of vorticity of the discrete structures is the radial jet shear layer rather than the freestream at the upper edge of the separated

flow.

4. The discrete vortical structures are observed to "jump" or "peel" off the blade and carry away roughly 30% of the vorticity in the shear layer between the radial jet and the blade surface.

5. The average shape of these discrete structures changes from being circular to elliptical on moving outboard. The structures seem to undergo "stretching" as they move outboard and might have a causal relationship to the "jumping" of the structures.

6. The ensemble averaged radial velocity profile data show that the averaged peak radial velocity decreases with increasing radial distance at a given chordwise location, contrary to what would be expected in the absence of the formation and breakup of the discrete vortical structures.

7. From the above, it is concluded that the breaking away of the discrete structures is the mechanism responsible for suppressing the growth of radial jet.

8. Order of magnitude comparisons show that the radial jet development is strength limited by the breakup into discrete structures, and the discrete structures themselves are first-order phenomena in the flow field of the rotor blade in retreating blade stall.

9. These flow characteristics may have significant effects on the evolution of lift and pitching moment of the blade during retreating blade stall.

CHAPTER V

ROTATING DISK ANALOGY FOR RADIAL FLOW

5.1 Introduction and motivation

As mentioned earlier, most studies of dynamic stall have been conducted using pitching and plunging airfoils in nominally two-dimensional settings [13, 82]. These cannot include the effects of reactive centrifugal forces that are present on a rotating blade. Especially under separated flow conditions, when the centrifugal forces on a rotating blade enhance the radial flow. Measurements during dynamic stall conditions on a rotating blade (see Chapter 4 and Mulleners [81]) demonstrated that the core of the dynamic stall vortex has a significant radial velocity component. In addition, the investigations also discuss the attenuation of the radial velocity on moving outboard towards the tip of the blade. Our work demonstrated that the physical mechanism by which the radial velocity attenuated was a shear layer instability of the radial flow. The instability led to the formation of co-rotating vortices (see Figure 71) above the radial velocity profile which broke away from the shear layer hence attenuating the radial flow. The observed structures are quasi-periodic, not quite repeating exactly from cycle to cycle of the rotor. In addition, these vortical structures were shown to have first-order significance to the flowfield and thus the air loads on a helicopter rotor undergoing dynamic stall in steady high speed forward flight. Predicting their occurrence and properties through large-scale computational fluid dynamics is difficult, as they appear to stem from instabilities developing from very small spatial and temporal scales in the radial jet layer. Hence an approach to provide guidance on their characteristics was sought which led to the investigation of an analogy with the rotating disk flow in a separated edgewise stream.

Hence, the experiments and work reported in this chapter were motivated by the discovery of discrete vortical structures above the radial jet layer (radial boundary layer) on

a rotor blade in retreating blade stall. We hypothesized that fundamental insights to predict the nature of these structures, could be developed from the flow over a rotating disk, which could in turn be linked to analytical solutions. An analytical solution is available for the steady axisymmetric three-dimensional boundary layer flow on an infinite rotating disk [56, 23]. This solution has been used in the past to help understand the flow over a rotating helicopter rotor blade at small angles of attack [79]. If structures similar to those observed on the rotor blade could be found over a rotating disk, that would open the way to link the rotor blade phenomena to quasi-analytical solutions and hence to derive fundamental relationships between parameters for the rotor blade problem. This would assist the development of computational prediction methods for helicopter rotors, among other applications.

Studies involving rotating disk boundary layer flow could provide useful insights into the fluid flow phenomena over a rotating blade. Boundary layer flow over rotating disks have well established analytical results [56, 23]. Moreover analytical results for laminar boundary layer flow on helicopter blades have also been studied [79]. These results provide a good test case for experiments to illustrate similarities between the flow on the disk to that on the blade. Earlier, rotating disk experiments and numerical computations were used to correlate boundary layers over a swept wing [43, 61]. The existence of spiral vortices in transition regimes of three-dimensional boundary layers on rotating axisymmetric bodies has been illustrated by studies [59, 62, 58]. These studies suggest that the spiral vortices have zero phase velocity in the cross-flow direction. A cross-sectional view of this vortex system is shown in the Figure 81. However, it should be noted that the instabilities we are "searching" is fundamentally different than the boundary layer instability observed in the previous citations.

5.2 Objectives

In this work experiments are conducted on a finite rotating disk in a uniform stream in a wind tunnel. Particle image velocimetry (PIV) is used to investigate the radial flow over the rotating disk with and without a freestream to study the differences. The primary

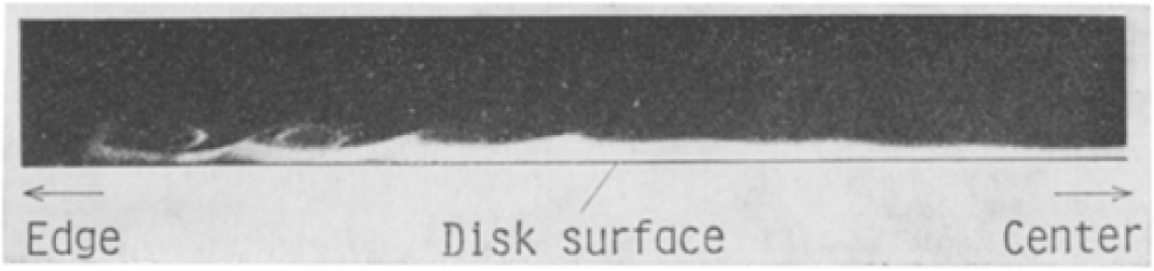

Figure 81: Cross-sectional view of the Spiral Vortices on a rotating disk [62]

objectives in this chapter are the following:

1. Measure the boundary layer over the rotating disk as a validation study.
2. Study the effect of a uniform stream on the radial velocity component on a rotating disk at zero angle of attack.
3. Study the instability of the radial flow on the rotating disk under separated flow conditions.
4. Develop correlation parameters to study the instability for different applications.

5.3 Experimental methods

5.3.1 Experimental setup

The experiments were conducted in the John Harper 2.13m×2.74m low speed wind tunnel at the Georgia Institute of Technology. The closed circuit tunnel is powered by a three-phase 600 hp induction motor controlled by a variable frequency drive which uses closed loop control to keep the error in fan RPM below 0.1 %. The turbulence intensity in the wind tunnel is 0.06 % measured at a freestream velocity of 110 ft/s (33.5 m/s). A drawing of the experimental setup is shown in Figure 82. It consists of a base platform made from aluminum. The base has a provision for holding a shaft using two high speed ball bearings to support the shaft at high rotation speeds. A factor of safety of 4 was used to determine the rated rotation rate of the high speed ball bearings.

The rotation rate of the shaft was measured using a US digital encoder with a accuracy of 1000 counts per revolution, yielding an accuracy of 0.36°. A 0.4hp (298.27 Watts) motor,

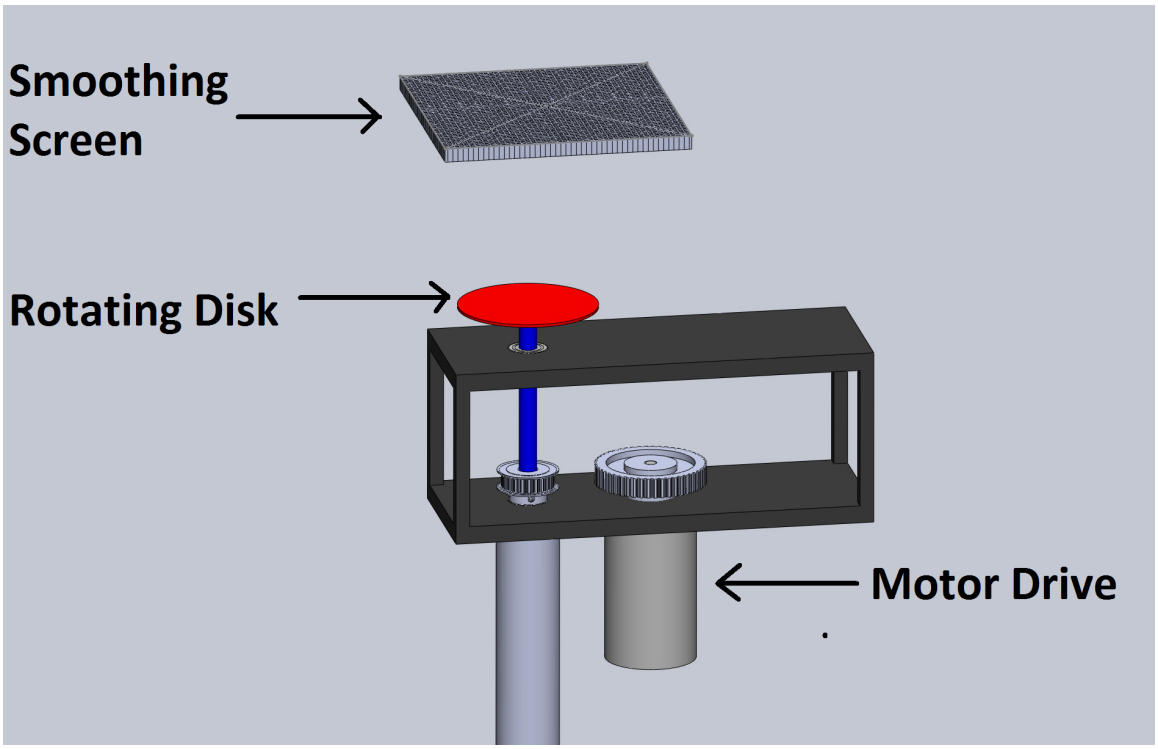

Figure 82: Drawing of the rotating disk setup

coupled with a high resolution timing belt drive was used to drive the shaft. The motor and timing gear coupling used a gear ratio of 1:2. The measured disk angular velocity Ω_d remained constant to within 0.12% of the total RPM. The disk was made of stainless steel and is 154 mm in diameter. It was ground and polished to a $0.001in$ $(0.0254mm)$ out of plane motion. To study the effect of freestream on the radial velocity of the rotating disk the setup was modified by adding a smooth ellipitcal surface to avoid effects of blunt body separation (see Figure 84). The interrogation area (field of view (FOV) size of 12mm×9mm) for the boundary layer measurements is shown by the dotted box in Fig. 94. To study the instability of radial flow with a uniform edgewise stream FOV was increased to 48mm×36mm.

5.3.2 PIV instrumentation

PIV was used to measure the velocity fields above the rotating disk. The flow investigation involved various levels of PIV since measuring the boundary layer of the rotating disk was

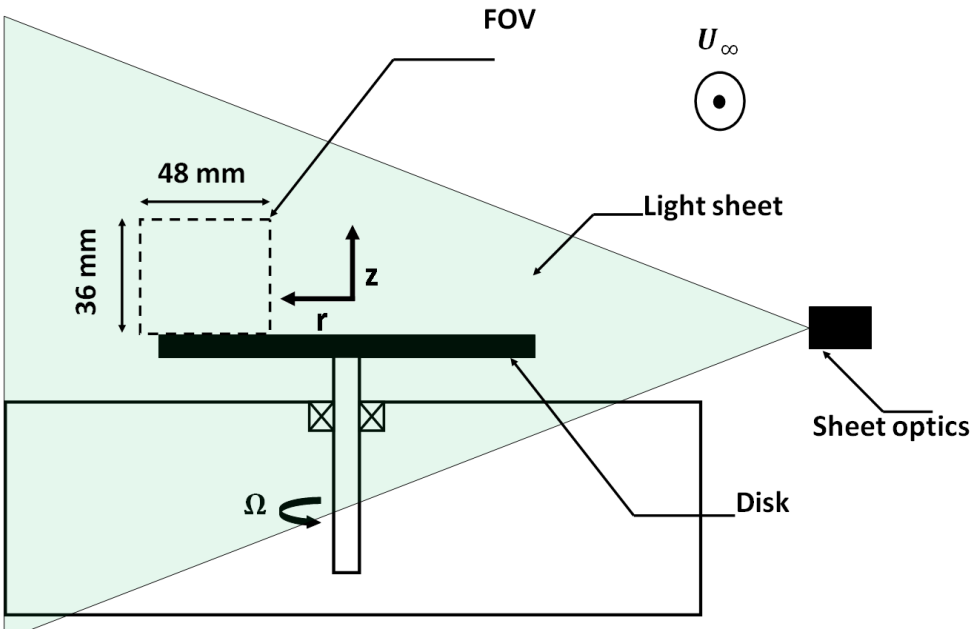

Figure 83: Schematic of the side view of PIV setup for boundary layer measurements (not to scale)

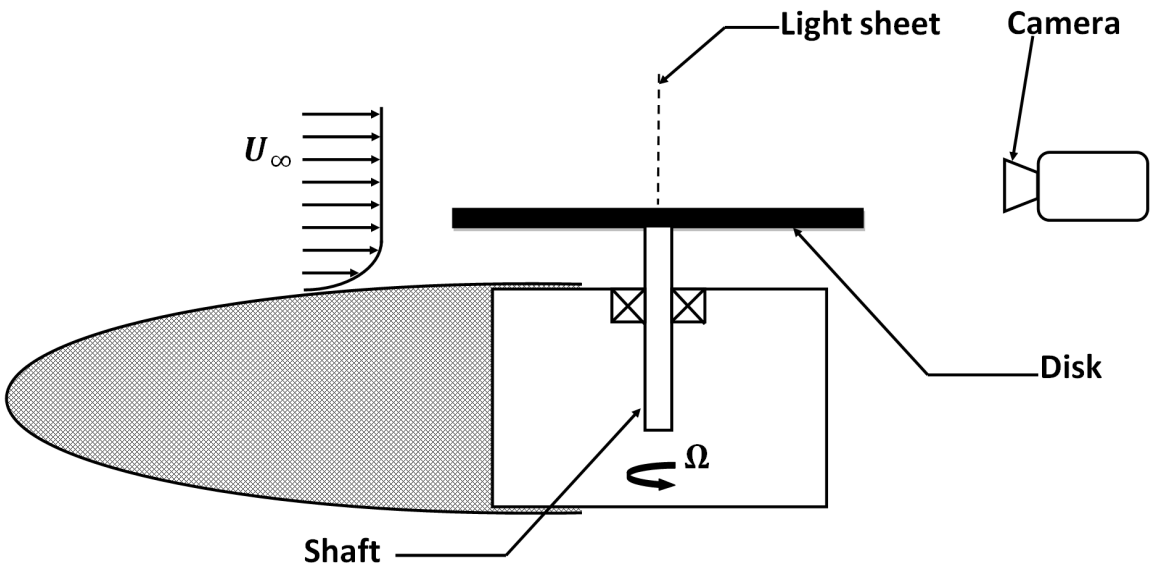

Figure 84: Illustration of the experimental setup with a uniform edgewise stream (not to scale)

a challenge with regular lens. Hence, μ-PIV was first used to measure the boundary layer on the rotating disk (see Figure 85 for μ-PIV setup). In addition, experiments were also conducted by using a micro lens (M-lens) to conduct the investigations with the uniform

edgewise stream (see Figure 86).

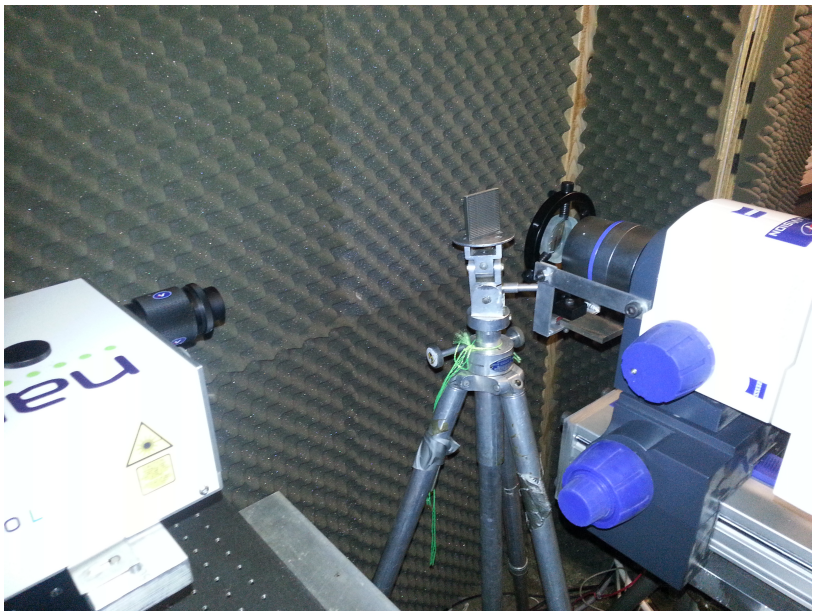

Figure 85: Photo of the μ-PIV setup during calibration process

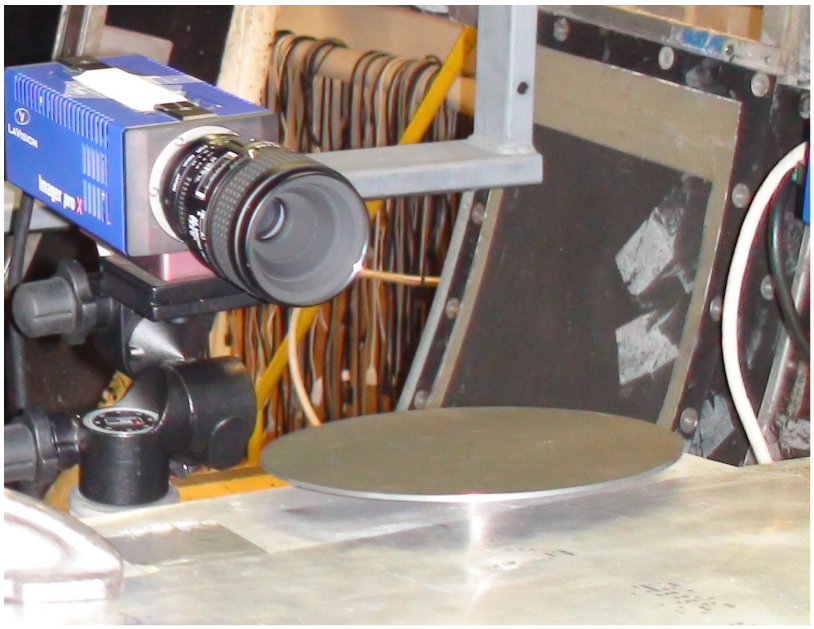

Figure 86: Photo of the Micro-Lens PIV setup inside the wind tunnel

The illumination was provided by a double-cavity Nd:YAG laser with a pulse energy of 200 mJ. A laser arm (a covered beam path) was used to deliver the illumination to the

measurement plane where sheet optics was used to generate a light sheet of 2 mm thickness. The laser alignment ensured that the center of the sheet was exactly coinciding with the disk. This was done to eliminate any laser scattering and reflections, thus enabling good PIV images. The flow was continuously seeded with $10\mu m$ droplets from a fog generator. A series of 100 image pairs was acquired at each measurement plane using PRO-X 2M camera which has a 1600×1200 pixel resolution and a pixel size of $7.4\times7.4\mu m^2$. The focal length of the lens system was 60 mm and the aperture on the camera was set at f/2.8. In order to improve the signal to noise ratio of the PIV data, the disk was coated with black paint and the unavoidable laser reflections at the disk surface were masked during the velocity vector computations. The time separation between subsequent exposures was set at 250μs for the boundary layer measurements. However, in the case of PIV investigations with a uniform edgewise stream, it was important to choose a pulse separation (Δt) that was short enough to ensure the out-of-plane movement did not exceed 1/3 of the sheet thickness [92].

DaVis 7.2 software provided by LaVision was used to process the PIV data, the velocities were calculated from the spatial cross-correlation of the images. 64×64 pixels interrogation window with 50% overlap and a second interrogation pass with a reduced window size (32×32 pixel) was used to yield a vector spatial resolution of 0.12 mm for boundary layer measurements and 0.48 mm for the "macro" flow field measurements. Post-processing of the vector images consisted of applying a median filter and light vector smoothing (3×3) for better visual presentation.

5.3.3 Challenges with μ-PIV

Measuring the boundary layer over a rotating disk is not an easy task, especially with optical diagnostic techniques and in a fluid with low viscosity. The low viscosity causes the boundary layer to be extremely thin typically of the order $\mathcal{O}(\leq 2mm)$. Capturing the boundary layer with PIV using the micro lens can lend itself to errors. However, using the microscope to measure the boundary layer on a surface is also challenging due to the following reasons:

1. The working distances are prohibitively small (60mm), which requires the microscope

to be very close to the measurement plane.

2. The short working distance results in flow interference between the optics (microscope objective) and the flow over the rotating disk.

3. Using the microscope enables measurement with resolution where pixel density is as high as 120 pixels/mm. However, it was observed that calibration error is around 2-3 pixels. This kind of error is prohibitive in regular PIV, but in the case of μ PIV with a high resolution 2-3 pixels error amounts to around of 0.025mm in displacement.

4. The depth of focus of the microscope objective is very small compared to regular lenses used for PIV. This is particularly challenging because the depth of focus is now of the order of the light sheet thickness. In three-dimensional flows this is particularly hard because the particles move out of the plane of the laser sheet and hence not yielding a useful correlation.

5.3.4 Test Conditions

Given the objectives of studying the boundary layer of the radial flow over the rotating disk and investigating the near surface flow specific test conditions were chosen. This decision was made based on a literature survey where various interesting phenomena were reported at different Reynolds numbers. The flow field variables are non-dimensionalized using the displacement thickness $\delta = \sqrt{\nu/\Omega}$ (where ν is the kinematic viscosity of the fluid), and the local tangential velocity of the disk $r\Omega$ (where r is the local radius) as reference quantities. Hence the dimensionless height above the surface, time averaged radial velocity component and Reynolds number are written as:

$$\eta = z\sqrt{\frac{\Omega_d}{\nu}} \tag{8a}$$

$$F(\eta) = \frac{u_r}{\Omega_d r} \tag{8b}$$

$$Re = R\sqrt{\frac{\Omega_d}{\nu}} \tag{8c}$$

where R is the radius of the disk. For the experiments with the uniform stream the velocity was non-dimensionalized using the tip speed of the disk $R\Omega_d$ and given by advance ratio $\mu_d = U_\infty/\Omega_d R$. Thus, a rotating disk in quiescent fluid would be indicated by μ_d=0 and a stationary disk in a freestream would be indicated by μ_d=∞. The test conditions are summarized in Table 12.

Table 12: Summary of experiments conducted at various test conditions

Type	Measurement	Technique	Re	μ_d
Validation	Radial jet	μ-PIV and M-lens PIV	88.9, 175.8	0
Freestream (α=0°)	Radial jet	M-lens PIV	175.8	0.71
Freestream (α=8°)	Macro flow field	M-lens PIV	126–199	0.35–1.39

5.3.5 Accuracy Estimate

The uncertainty in RPM of the disk, which is measured by the digital encoder is 0.1%. The error in the out of plane motion of the disk arising from the fabrication process is 0.01%. The measurement of the position of the disk in the PIV images is done using image processing in MATLAB, and the uncertainty is 0.01%. The uncertainty in velocity measurements was quantified using techniques summarized in Appendix XYZ. Table 13 summarizes all the PIV measurement errors for these experiments.

Table 13: Summary of PIV measurement errors

Type	Error
Random error	0.053–0.197 pixels
Bias error	0.005 m/s
Lag error	Insignificant
Total measurement error	0.34%–1.25%

5.4 Results and discussion

As mentioned earlier, validation experiments were first performed by measuring the radial component of velocity on a rotating disk in quiescent fluid. Measurements were gathered at two different Reynolds number (equivalent to two rotation rates). The theoretical values

for $F(\eta)$ the time averaged radial velocity over a rotating disk in quiescent fluid is obtained from the von Kármán similarity solution which were tabulated by Cochran [23]. Figure 87 compares the measured mean radial velocity on a rotating disk in quiescent fluid with analytical results.

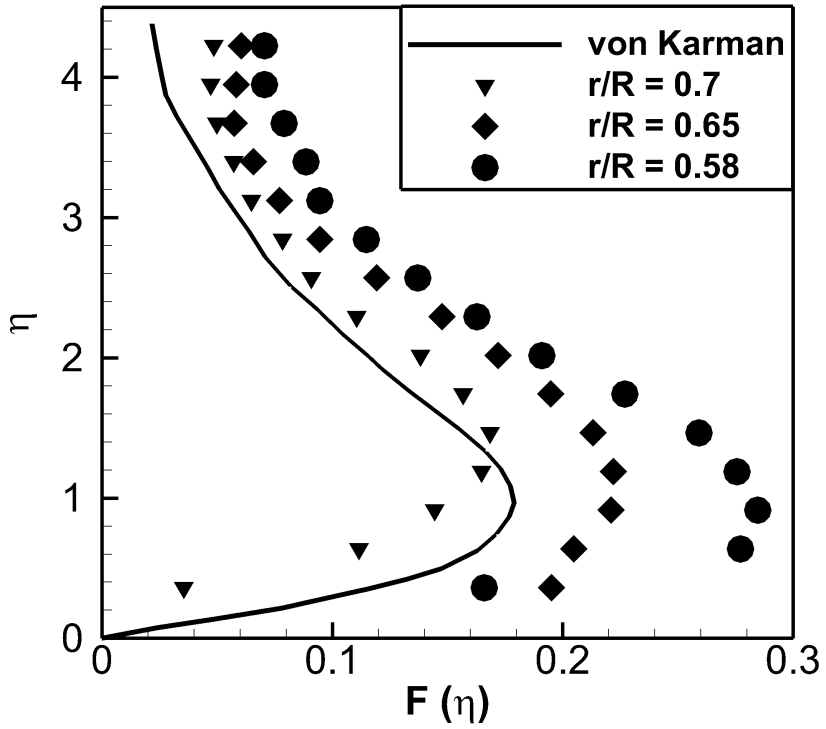

Figure 87: PIV measurement of the time averaged radial velocity profile at Re = 175.8, μ_d=0 and $\alpha = 0$

It can be clearly observed that the non dimensionalization does not yield a completely self similar solution. In order to investigate the "discrepancy" in the measured peak radial velocity several reasons were considered:

1. Vibration of the disk surface.

2. Surface roughness of the disk surface

3. Finite disk radius

.

The fore mentioned causes are investigated in detail to justify the results. First the any effect of vibration of the disk is investigated - the vibration of the disk surface allows the surface to move up into the boundary layer and hence causing errors in the measurement. A look at the histogram density (see Fig. 88) of the radial velocity (measured by μ-PIV) at the different heights above the disk surface suggests that the vibrations could only have an effect very close to the surface. The histogram distribution at a height z = 0.0287mm (the first point where velocity is measured) is more or less uniform suggesting that vibration could have contaminated the data. However, the distribution is no more uniform at higher locations (see Figs. 88(c) and 88(d)). Hence it can be concluded that the measured peak of the radial velocity is not contaminated due to vibration of the rotating disk.

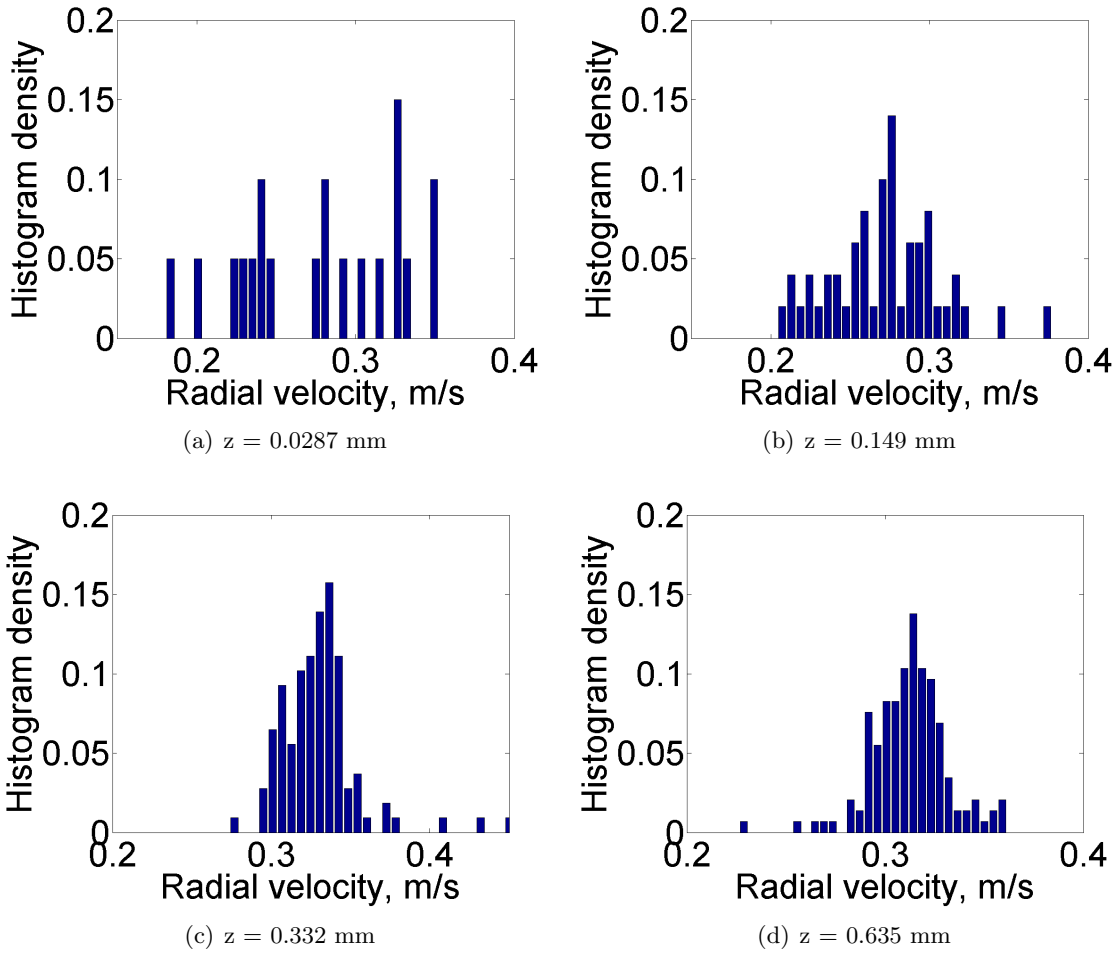

(a) z = 0.0287 mm

(b) z = 0.149 mm

(c) z = 0.332 mm

(d) z = 0.635 mm

Figure 88: Histograms of radial velocities at various heights above the disk surface

Surface roughness of the disk could contribute to a increased effective viscosity at the surface of the disk leading to higher measured radial velocities. The analytical solution obviously assumes a smooth disk surface and it might not be the same in experimental conditions. Most experiments have been conducted on mirror finished surfaces using hotwire measurements and have closely matched the analytical solutions. In this work since PIV was used for measurements - the surface had to be painted to avoid laser reflections in order to improve the signal to noise ratio. An average spray painted surface has a roughness factor of nearly 20 times that of a mirror finished surface (used in the hotwire experiments). See Table 14 adapted from [39] for a summary of roughness factors on different surfaces. Past work in centrifugal pumps [106] has shown that an increase in surface roughness causes an increased output (equivalent to an increased mass flow). The investigation involves a parametric sweep of the effect of roughness coefficient on the effective radial velocity outflow. The observations in that study suggest a 40% increase in radial velocity due to a 30× increase in roughness coefficient. However, it should be noted that the 40% increase of radial velocity is computed from the average mass flow which is very different from the just the mass flow through the radial flow near the peak of the profile. In the case of the rotating disk used in this work the increase in surface roughness due to the spray paint is around 20× which is of the same order of magnitude as seen in the literature and could explain the "anomaly" in the data. In addition, studies on the effects of roughness on a rotation disk have been conducted [117]) which clearly show that the peak radial velocity component increases with roughness.

A look at prior PIV measurements on rotating disks yielded only one investigation by Prasad [89]. Prasad in his investigation used Stereo-PIV to measure the radial velocity profile over a rotating disk, however the fluid used was glycerin. Glycerin is a highly viscous fluid and it can be argued that the viscosity effects in this fluid are much greater than the effect of surface roughness. However, this is not true in case of air where the viscosity is much lower than that of glycerin and surface roughness will effect the flow to a greater extent. From the above arguments it can be concluded that the observed higher radial velocity could be a direct consequence of surface roughness.

Table 14: Equivalent surface finish adapted from Gollos [39]

Type of Surface	k×10^3inches
Mirror finish	0-0.049
Polished Metal or Wood	0.05-0.09
Natural Sheet Metal	0.1-0.19
Optimum Paint-Sprayed	0.2-0.29
Average Paint-Sprayed	0.3-0.99

To further investigate the validity of the results a mass conservation integral around a selected control surface was performed. The difference in mass-inflow and mass-outflow was as small as 3.1% of the mass-inflow, this suggests that there are no gross errors in the measurement. However, it should be noted that the outplane velocity is not accounted here and it might give rise to the discrepancy. The results from μ-PIV are very systematic and very low in error and there is no reason to discount the veracity of the results. As a concluding note, it is recognized that the finite radius of the disk will definitely cause some non-linear effects on the radial velocity profile. These effects are not investigated in this study.

The next of experiments were performed to study the effect of a uniform stream on the radial component of velocity. The effect of a uniform stream on the radial velocity profile at Re = 175.8 is illustrated in Fig. 89. The addition of a freestream increases the total radial velocity component by a factor of two at r/R = 0.65. The *effective* radial velocity component (correcting the radial velocity far away from the disk so that the radial velocity far away from the disk is zero) increases by 87%. When a freestream is added at zero angle of attack, the presence of the strong radial flow causes the incoming flow to separate at the leading edge (as seen in Potts [87]). Furthermore, the influence of the freestream limited the growth of the peak radial velocity to half of the expected increase based on observations of the peak radial velocity without the freestream.

The above results showed that the addition of a freestream has a significant influence on the *effective* radial velocity component on the rotating disk. Next, the effect of a freestream on the "macro" flow field of the rotating disk was studied using a FOV of 48mm×36mm.

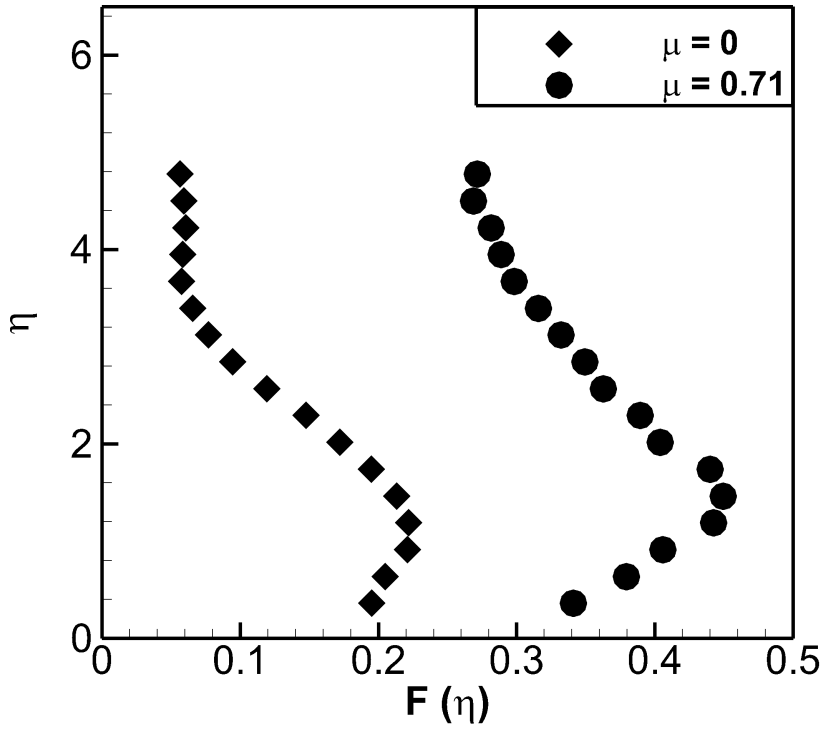

Figure 89: PIV measurement of the time averaged radial velocity profile at r/R = 0.65, Re = 175.8 and $\alpha = 0$

The rotational rate of the disk (expressed as advance ratio μ) was varied with the freestream held constant. An angle of attack of $\alpha = 8°$ was sufficient to induce a separated flow on the upper surface of the rotating disk. The separation was verified using PIV as observed in Fig. 90, which is a view from the side of the rotating disk with the uniform stream from the left to the right (refer to sketch 84 for clarification on the view). In the figure (0,0) is the location of the leading edge of the rotating disk.

Baseline experiments with a uniform stream at an angle of attack were conducted with no rotation of the disk. The separated flow had a small velocity component towards the disk surface, expected due to the separated flow conditions. With the disk rotating, the radial velocity component was observed to become unstable, revealing co-rotating vortical structures located above the radial jet layer. Note that this is instability of the layer above the radial jet, not the thin boundary layer between the radial jet and the solid surface. Figures 91 and 92 illustrate a typical set of co-rotating vortices observed in instantaneous

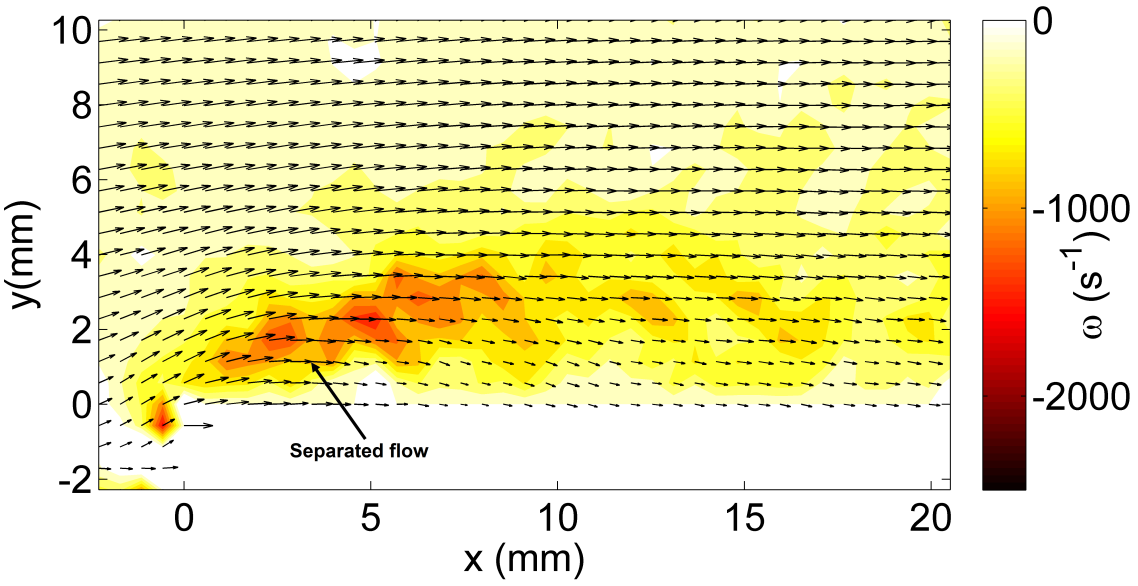

Figure 90: Evidence of separation over the rotating disk at Re = 178, $\mu = 0.69$ and $\alpha = 8°$ as viewed from the side

velocity fields for all flow conditions tested in this work at $\alpha = 8°$. To improve the spatial resolution, the PIV data in Fig. 91 were processed with a 75% overlap in contrast to the regular 50% overlap in Fig. 92. There are spurious velocity vectors close to the disk surface ($\eta \sim 0$) due to the laser reflections. The vortical structures were observed only during the rotation of the disk and not otherwise, firm evidence that the instability is due to the radial flow itself and not an artifact of separation. Furthermore, these co-rotating vortices were not observed on the rotating disk in a quiescent medium at the same rotation rates.

Previous work on instability of the radial flow layer on a rotating disk reveals that the layer is absolutely unstable for $Re \sim 507$ [69] and is unstable to non-stationary modes for $Re \sim 50$ [72]. A reviewer has pointed out that the co-rotating vortices observed here could as well be the non-stationary modes due to the convective instability of the radial boundary layer with a superimposed uniform stream. Against this plausible hypothesis, it should be noted that the rotating disk is operated at an angle of attack under separated flow conditions. The vortical structures observed here are *not* consistent in occurrence with respect to the radial location, spacing/frequency (between each vortical structure), appear

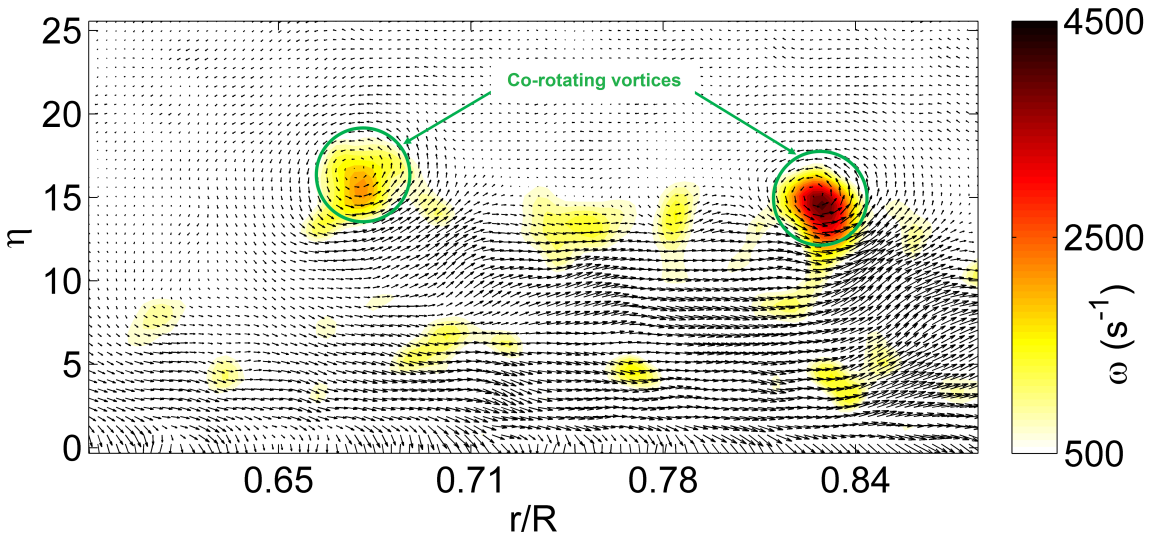

Figure 91: PIV velocity vector field illustrating a typical set of co-rotating vortices above the rotating disk at Re=178, $\mu = 0.69$ and $\alpha = 8°$

to convect at a finite phase velocity and are located at the upper edge of the radial jet layer. Due to the nature of these vortical structures all inferences are drawn from the conditional statistics of the PIV velocity fields. That is, only velocity fields where these structures appear are considered in the statistical analysis.

The conditionally averaged height of the vortical structures above the surface of the blade was determined for various angular velocities of the disk. The height above the disk surface at which these discrete structures were observed, increases as the angular velocity increases (summarized in Table 15). Although at first this is surprising, the analysis of the radial velocity profile at each rotation rate helped reconcile the observations. The time averaged radial velocity profiles for a rotating disk at $\alpha = 8°$ is illustrated in Fig. 93 for r/R = 0.59. Due to flow separation, the flow adjacent to the disk surface moves at relatively low speed and hence the centrifugal stresses at the surface are transported to a greater height above the surface, as clearly evident in Fig. 93. The critical observation here is that the inflection point of the time averaged radial velocity profile moves away from the surface of the disk with increasing rotational rate. This observation concurs with the average location of the co-rotating vortical structures, indicating that the vortical structures are due to

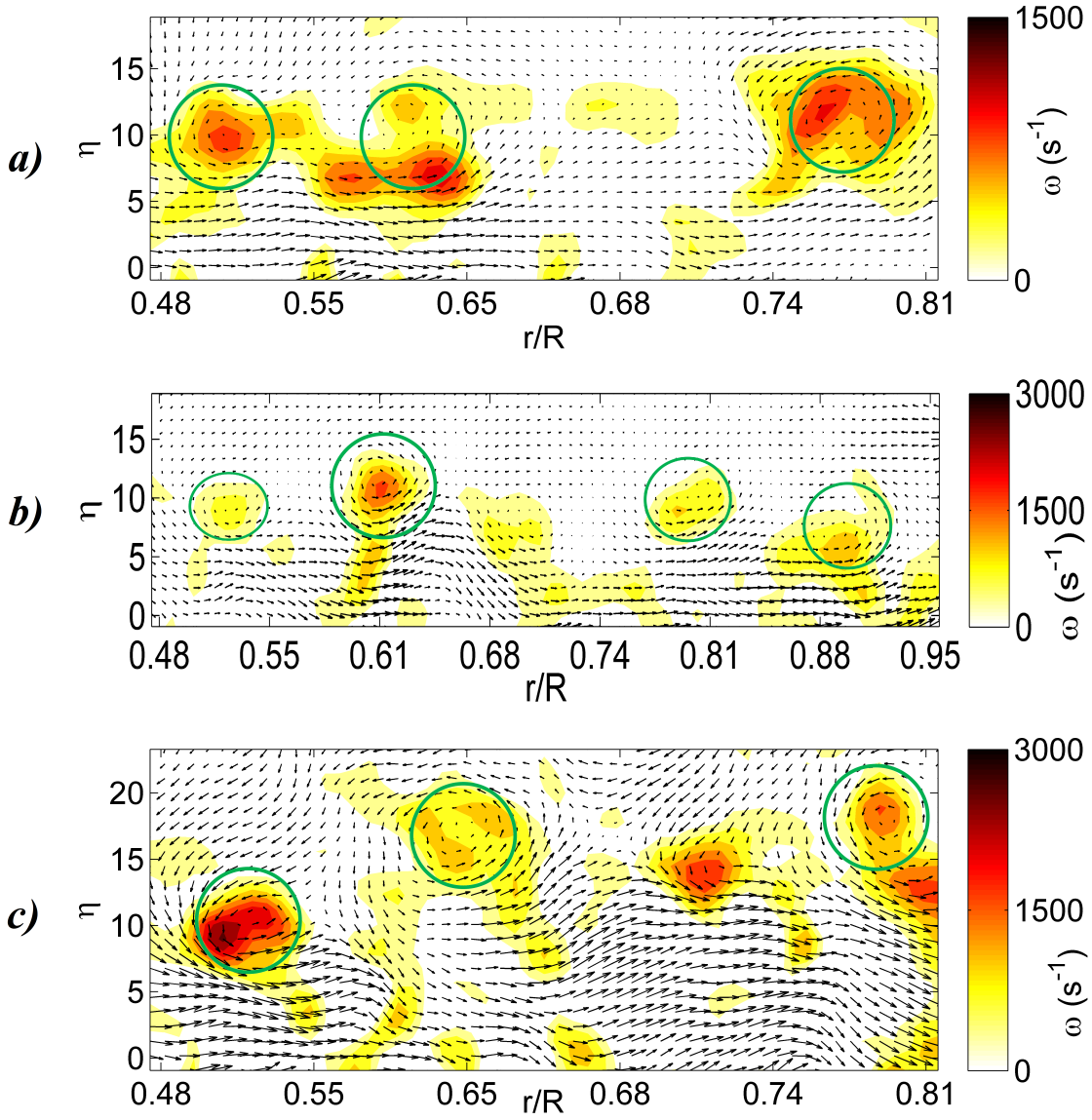

Figure 92: PIV velocity vector field illustrating a typical set of co-rotating vortices above the rotating disk at α=8° for a) Re=126 and μ = 1.39, b) Re=154 and μ = 0.92 and c) Re=199 and $\mu = 0.55$

an instability of the radial flow itself. At the writing of this letter, it appears that the instability is some form of the classical Kelvin-Helmholtz instability due to a shear layer with an inflection point.

Table 15: Summary of the mean (η_m) and standard deviation (η_s) of the height above the disk surface of the co-rotating vortical structures

Flow condition	η_m	η_s
Re = 126, μ = 1.39	6.88	2.82
Re = 154, μ = 0.92	12.05	2.97
Re = 178, μ = 0.69	16.17	4.21
Re = 199, μ = 0.55	23.21	6.85

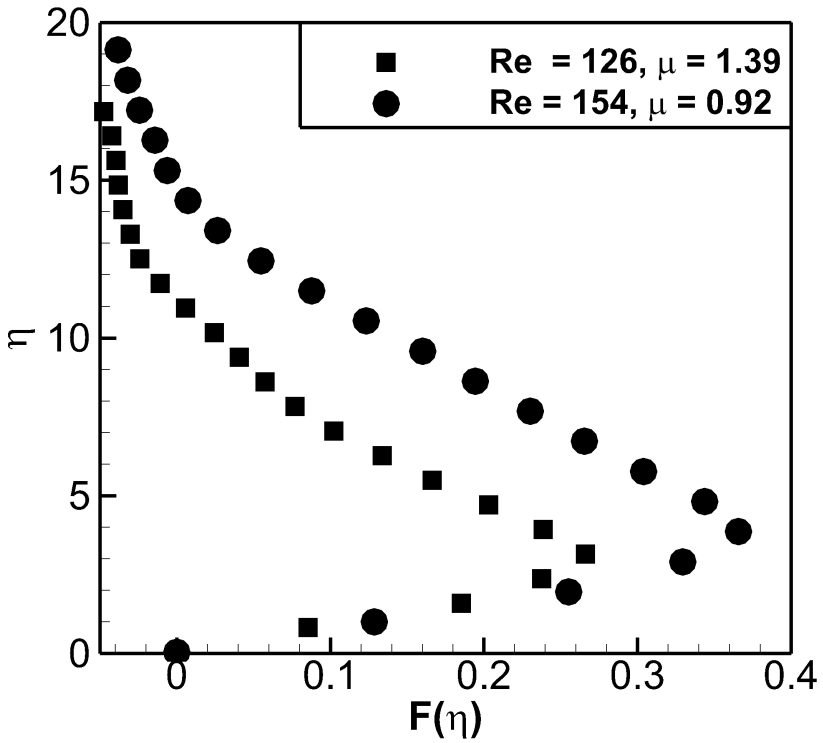

Figure 93: Mean radial velocity profiles on the rotating disk at $\alpha = 8°$ illustrating the increase in height of the inflection point at r/R = 0.59

Having established the cause and source of the instability, the co-rotating vortical structures were further characterized. The co-rotating vortical structures are defined by strength (vorticity), frequency and phase velocity. The angular velocity appears to have a

direct effect on the vorticity entrained in the structures with the vorticity magnitude increasing with rotation rate. This again supports the assertion that these vortical structures are an artifact of rotation and the associated radial flow. The vorticity entrained in these structures is expected to depend on the independent variables rotational rate Ω, freestream velocity U_∞, kinematic viscosity ν, and radius of the disk R. These variables can be grouped to form a non-dimensional voriticity given by $\omega^\star = \omega/\Omega$ which would be expected to scale with the following parameters:

$$\kappa = \frac{{U_\infty}^2}{\nu\Omega} \tag{9a}$$

$$\mu = \frac{U_\infty}{R\Omega} \tag{9b}$$

and $\omega^\star = f(\kappa, \mu)$. The dimensional and non-dimensional vorticity entrained in these structures are summarized in Table 16.

Table 16: Summary of the mean (subscript m) and standard deviation (subscript s) of vorticity entrained in the co-rotating vortical structures

Flow condition	ω_m (s^{-1})	ω_s (s^{-1})	${\omega^\star}_m$	${\omega^\star}_s$
$\kappa = 30422$, $\mu = 1.39$	1055.2	379.90	25.19	9.06
$\kappa = 20281$, $\mu = 0.92$	1341.5	358.15	21.35	5.70
$\kappa = 15211$, $\mu = 0.69$	1508.2	370.98	18.01	4.42
$\kappa = 12169$, $\mu = 0.55$	1698.4	545.45	16.22	5.21

The radial spacing Δ of the co-rotating structures determined by conditional averaging was found to be 9mm to 11mm for the different experimental conditions. With freestream held constant, an increase in angular velocity of the disk resulted in decreased spacing of the structures (i.e., increased spatial frequency). The spacing is non-dimensionalized as $\Delta^\star = \Delta\Omega/U_\infty$ with $\Delta^\star = f(\kappa, \mu)$, where κ, μ are non-dimensional parameters defined in expression 9. Initial analysis of the data to determine the phase velocity of the structures suggests that in some instances the structures are convecting at the "local" radial velocity which is a function of both r and η. However, a rigorous analysis could not be performed using the current data since these vortices were time dependent.

From the above observations and discussion it appears that the radial flow instability leading to the formation of co-rotating vortices is a fundamental behavior of the radial component of the velocity with a uniform edgewise stream. This allows for an analogy between the flow features on the rotating disk and the rotating blade in similar flow conditions defined by non-dimensional parameters κ and μ. It opens a path to systematically study the radial flow instability without having to perform large scale rotor blade experiments or computational analyses on rotating blades. The analytical solution can in principle be modified to account for the uniform stream to check for the instability and then incorporated into the radial flow model on rotating blades [79]. Various hypotheses still remain to be explored, for instance those suggested by the reviewers, to seek a closed-form analytical prediction of the quantitative spatial frequency and strength of these structures, as related to relevant operating parameters. This in turn would lead to models that predict the limiting effect of radial flow on the aerodynamic loads experienced by rotating blades, especially through the dynamic stall regime. Hence the urgency of this letter in establishing a promising avenue to make progress on the dynamic stall problem and related aeromechanics of rotors.

5.5 Summary of results

Experiments were conducted to test a hypothesis that the discrete vortical structures over a retreating rotor blade in dynamic stall could be captured on a rotating disk in the presence of a separated uniform stream. Validation was first carried out by measuring the time averaged radial velocity component on a rotating disk. Next, the "macro" flow field was investigated on the rotating disk in the presence of a separated uniform stream. The following is a summary of all the findings of the experiments conducted to test the hypothesis:

1. The radial flow velocity profile was measured over the rotating disk using μ-PIV and 2D PIV with micro lens. The μ-PIV was able to sufficiently resolve the boundary layer height, however there was a discrepancy in the peak radial velocity when compared to the analytical solution.

2. Various factors were identified which might cause the aforementioned discrepancy including disk vibrations, disk surface roughness and finite disk radius.

3. The finite disk radius aspect was not investigated in this work, although it is recognized that it could contribute to some non-linearity in the flow. In addition, the investigation of the histogram distributions of the radial velocity suggest that vibration of the disk cannot be a factor causing the anomalous results.

4. The dramatic increase in surface roughness caused due to spray painting the disk (necessary to improve the PIV results) might be causing the unexpected higher peak in radial velocity. Centrifugal pump literature suggests that a 30× leads to a 40% increase in radial velocity, which could explain the results observed in this work.

5. The presence of a freestream increases the *effective* radial velocity component. However, in the presence of the freestream the radial velocity component does not increase to the expected level on moving outboard. Suggesting that there is a physical mechanism causing the lower levels of radial velocity.

6. It was revealed that the radial flow on a radial flow on a rotating disk becomes unstable with the addition of a separated uniform stream.

7. The evidence of the instability was revealed by the co-rotating vortices at the upper edge of the radial jet. The average height above the surface where the co-rotating structures formed increased with increasing angular velocity.

8. This concurs with the increase in the height of the inflection point of the radial velocity profile above the surface. This clearly indicates that the source of the instability is the radial jet layer above the disk surface, and that the instability is *not* an artifact of separation of the freestream over the the rotating disk.

9. Vorticity entrained in these co-rotating structures has a direct correlation to the rotation rate with the vorticity magnitude increasing with increase in angular velocity of the disk.

10. Moreover, the spacing of these structures was determined to be inversely proportional to the angular velocity of the rotating disk. The co-rotating vortices appear to convect

with a finite phase velocity, however, a definite conclusion on the convection velocity has to be derived from time resolved data.

CHAPTER VI

EFFECT OF ROTATION ON REVERSE FLOW

6.1 Introduction

There are few studies on rotors at high advance ratios where reverse flow is significant. The earliest full scale investigations include: a Pitcairn PCA-2 autogyro rotor [111], a UH-1D teetering rotor [22], and an H-34 articulated rotor [71]. Current approaches to modeling rotor aerodynamics use aspect ratio and geometric yaw corrections to two-dimensional aerodynamic data for the reverse flow regime. The sweep correction assumes that only the velocity component perpendicular to the leading edge is significant. In addition, the rotation of the blade adds more complexity to the aerodynamic phenomena in this flow regime. Recent experiments [28] demonstrate evidence of large impulses in pitch-link loads on the retreating side of the rotor disc at high advance ratios. This suggests that two-dimensional assumptions are inadequate for reverse flow regimes.

Harris [50] performed correlation studies on full-scale data sets and showed that computational fluid dynamics (CFD) coupled with comprehensive analysis tools failed to adequately predict airloads in the reverse flow region and rotor performance at high advance ratios $\mu_a \geq 1.0$. Recent experimental work conducted by Datta et al. [28] on a slowed rotor showed large impulses in pitch-link loads on the retreating blades and evidence of "reverse chord dynamic stall" at advance ratios approaching unity. Comprehensive analysis using CAMRAD II performed by Yeo [114] on the slowed rotor dataset showed fair airload and structural load correlation. Coupled CFD and comprehensive analysis on the UH-60A dataset performed by Potsdam et al. [86] showed unconventional wake patterns, a lower surface vortex on the retreating blade which was attributed to "reverse chord dynamic stall", and poor prediction of the pitch link loads on the advancing and retreating blades. Much remains to be explored on several issues including the effect of three-dimensional flow, nonlinearities with increasing angle of attack and yaw, wing rotation, and finite wings.

6.1.1 Motivation and objectives

The motivation for this part of the work is two fold: *a*) To better understand the aerodynamic behavior of a yawed blade in reverse flow. The hypothesis considered in this work is that the trailing edge of the blade in reverse flow acts as a swept, sharp-edge delta wing, which produces a leading edge vortex. This leading edge vortex is expected to modify the characteristics of the aerodynamic loads on a yawed wing in reverse flow. *b*) To throw light on the effect of radial flow due to rotation on the aerodynamics of a blade in reverse flow. In order to test out the hypothesis the investigation was conducted in two parts summarized below:

1. The first is to understand the aerodynamic characteristics of a static yawed wing in reverse flow. The aerodynamic behavior of a rotating blade is very complex which include effects of yaw, aspect ratio, centrifugal forces and rotor vortex interaction. A static yawed wing experiment allows for the decoupling of rotational effects from the complex phenomenon present in the reverse flow region. The wing used in this study is from the two-bladed rotor that has been used in dynamic stall research (refer to section 1.5.2 for details) and is amenable to be used at high advance ratios to study rotation effects. Force measurements are reported on a finite wing at various yaw angles in the reverse flow regime. Tuft flow visualization was performed to qualitatively understand the surface flow pattern of yawed wings in reverse flow. In addition to flow visualization, PIV measurements were made on the static yawed wing to quantify the velocity field.

2. The second phase of the investigation was conducted on the same blade used in rotating tests at high advance ratios to study the effect of rotation on velocity field in reverse flow. Phase locked stereo-PIV measurements were gathered on the rotating blade to ascertain the existence of the vortex and throw light on the effect of rotation.

6.2 Experimental methods

The experiments were conducted in the John Harper 2.13m×2.74m low speed wind tunnel at the Georgia Institute of Technology. The closed circuit tunnel is powered by a three-phase 600hp induction motor controlled by a variable frequency drive. The drive is a closed loop controller with 0.1 % error in RPM setting. The turbulence intensity in the wind tunnel is 0.05 % measured at a freestream velocity of 110 ft/s (33.5 m/s). The turbulence intensity reported here is computed using velocity fluctuations data gathered after applying a 1Hz high pass filter and a 2.5kHz low pass filter.

6.2.1 Experimental setup

A finite wing with a NACA 0013 profile (see Table 2 for specifications) was used to conduct the experiments. A drawing and a photo of the setup in the wind tunnel is shown in Figure 94. The wing was mounted onto a two degree of freedom rig allowing the blade to yaw and pitch. The pitch (angle of attack (α) was controlled by a high torque stepper motor reduced with a 30:1 gearbox with a resolution of 0.1° in pitch. The yaw angle (ψ) was controlled by a high torque stepper motor which had a resolution of 1°. The stepper motors were controlled by a NI motion controller - nuDrive interfaced to a desktop computer via LABVIEW.

Figure 95 shows a photo of the stereo-PIV setup to measure the velocity field on the lower surface of the blade. The rotor was operated at a collective angle $\theta_0 = 6°$ and a cyclic angle $\theta_s = -6°$. The flow was seeded using atomized oil droplets ($10\mu m$) using a laskin nozzle type oil atomizer.

6.2.2 Instrumentation

The aerodynamic loads data on the static wing were gathered using a 6-DOF ATI Delta load-cell transducer interfaced to the computer via LABVIEW was used to measure force and moments on the wing. A three-dimensional rotation matrix was used to keep track of the forces and moments in each coordinate. The tuft flow visualization was performed using 2.5 cm long pieces of yarn taped at 2.5 cm spacing to the suction side of the wing. A

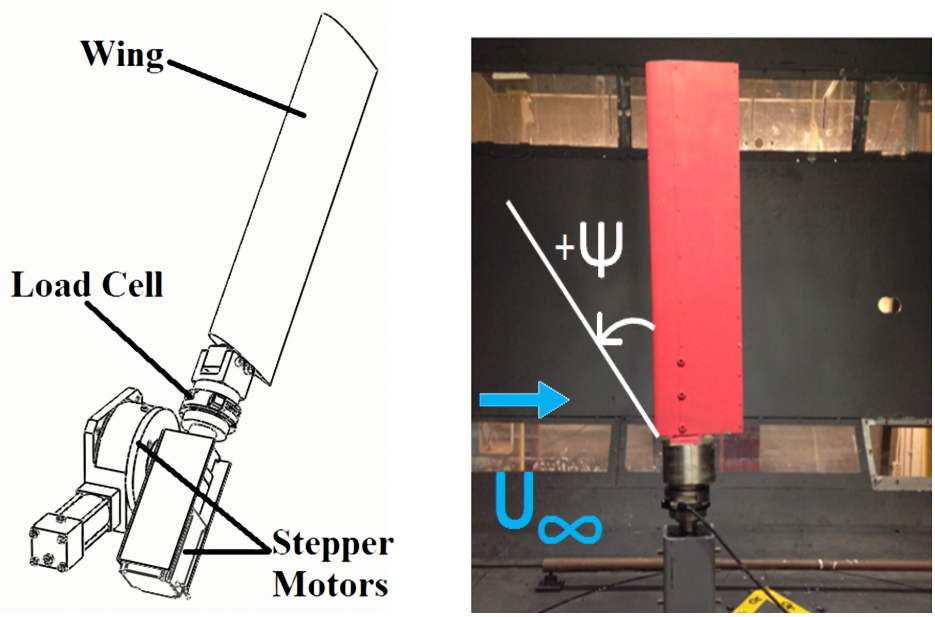

(a) Drawing of the wing setup

(b) Side view of the rotor blade setup in the wind tunnel

Figure 94: Experimental setup

high definition video camera was used to record the visualization.

The velocity field measurements were gathered using stereo-PIV on the lower surface of the rotating blade at high advance ratios. The angle between the two cameras was set at 20° due to limited optical access and space inside the wind tunnel. Rest of the PIV equipment used was the same as described in Section 2.3.1. The only modifications made to the setup were to align the laser sheet in the chordwise direction illuminating the lower surface of the blade and move the cameras to a lower location to measure the velocity field on the bottom surface of the blade.

6.2.3 Flow and Test Conditions

The tunnel dynamic pressure was measured using a Baratron, differential pressure transducer connected to a pitot-static tube located near the ceiling of at the upstream end of the test section. The tunnel speed and chord Reynolds number were calculated using the expressions in Table 19. The table also summarizes the flow conditions at a given ambient temperature and pressure for $R_e = 1.7 \times 10^5$. Chord Reynolds number was maintained at a constant by varying the freestream velocity as required depending on the measured

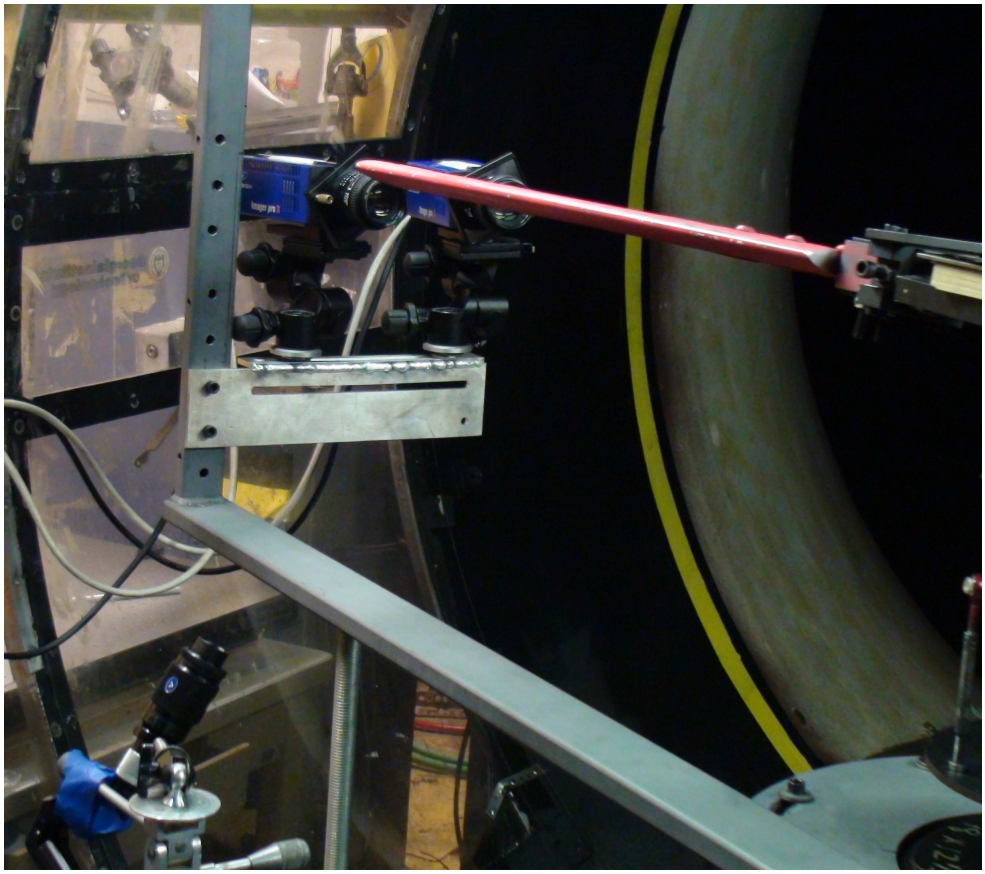

Figure 95: Photo of the stereo-PIV measurement setup inside the wind tunnel

temperature and pressure during each experimental run.

Table 17: Sample calculation of flow conditions

Property	Estimate	Value	Units
ρ	$\frac{P}{R_g T}$	1.184	kg/m^3
μ	$\frac{C_1 T^{3/2}}{T+S}$	1.91×10^{-5}	$Pa\text{-}s$
V_∞	$\sqrt{\frac{2q}{\rho}}$	15.41	m/s
R_e	$\frac{\rho V c}{\mu}$	1.7×10^5	

$C_1 = 1.458 \times 10^{-6}$ and $S = 110.4\ K$ are Sutherland's constants.

The aerodynamic loads data were gathered at a sampling rate of 10 kHz (which is far above the frequency response range of the load cell) and ensemble averaged over 300,000 samples. The chordwise velocity field measurements consisted of acquiring a series of 75

image pairs at each test condition using PRO-X 2M camera. The camera has a 1600×1200 pixel resolution and a pixel size of $7.4\times7.4\mu m^2$. The focal length of the lens system was 50 mm and the aperture on the camera was set at f/4. The time separation between subsequent exposures was chosen appropriately to enable the particles to move in 3 dimensions. DaVis 7.2 software provided by LaVision was used to process the PIV data, the velocities were calculated from the spatial stereoscopic cross-correlation of the images. 64×64 pixels interrogation window with 50% overlap and a second interrogation pass with a reduced window size (32×32 pixel) was used to yield a vector spatial resolution of 1.37mm which translates to 0.008c (where c is the chord length). Post-processing of the vector images consisted of applying a median filter and light vector smoothing (3×3) for better visual presentation. The various experiments conducted and the test conditions are summarized in Table 18 and described below.

1. Static wing experiments

   (a) The first test was to validate the experimental method for a static wing in regular flow against published data.

   (b) The second test explores the effects of yaw angle on the lift curve slope of the static wing in reverse flow conditions at two Reynolds numbers. The lift curve slope was determined by measuring the lift through a range of angle of attack as shown in Table 18. Angle of attack resolution was chosen appropriately to match the region of the lift curve being measured (lower resolution in the linear region and higher resolution near the stall region). The lift curve slope was determined over a range of yaw angles in increments of 5°.

   (c) The third test was tuft flow visualization at two Reynolds numbers and two yaw angles for the static wing. In this case, the wing was pitched through the angle of attack range in increments of 5°.

   (d) The fourth test was to measure the chordwise velocity field on the blade in reverse flow using PIV. A lower Reynolds number of 0.63×10^5 was chosen to match the effective Reynolds number of the rotating measurements to make direction

comparisons of the flow field.

2. Rotating wing experiments

   (a) Phase locked PIV measurements on a rotating wing at two advance ratios of $\mu = 0.8$ corresponding to $\Omega = 20.93\ rad/s$ and $\mu = 1.0$ corresponding to $\Omega = 15.7\ rad/s$. Measurements were made at one radial location of r/R = 0.5 and phase locked at $\psi = 240°$ and $\psi = 270°$ equivalent to $\psi = 30°$ and $\psi = 0°$ for the static blade.

Table 18: Summary of experiments conducted

Test	Data acquired	Conditions	Re ($\times 10^5$)
Static wing experiments			
Regular flow	Aerodynamic loads	$0° \leq \alpha \leq 30°$	1.7
Reverse flow	Aerodynamic loads	$180° \leq \alpha \leq 200°$ $0° \leq \psi \leq 60°$	1.7 and 3.0
Reverse flow	Flow visualization	$180° \leq \alpha \leq 210°$ $\psi = 30°, 45°$	1.7 and 3.0
Reverse flow	PIV - velocity field	$\alpha = 191.2°, 192°, 195°$ $\psi = 30°$	0.63 and 1.7
Rotating wing experiments			
Reverse flow	PIV - velocity field	$\psi = 240°, 270°$, $\mu = 0.8, 1.0$	0.63 (r/R=0.5)

6.3 Results and Discussion

As mentioned earlier, the aerodynamic loads validation was first performed by measuring lift, drag and pitching moment at a Reynolds number of 1.7×10^5 and angle of attack range of $0° \leq \alpha \leq 30°$. Figure 96(a) illustrates the validation data for the wing between $0° \leq \alpha \leq 20°$. The coefficient of lift (C_L), drag (C_D), and moment (C_M) are defined as the following:

$$C_L = \frac{L}{qS} \tag{10a}$$

$$C_D = \frac{D}{qS} \tag{10b}$$

$$C_M = \frac{M}{qcS} \tag{10c}$$

where q is the dynamic pressure ($\frac{1}{2}\rho {U_\infty}^2$), S is the surface area of the wing and c is the chord length. The slope of the linear portion of the lift curve (C_{L_α}) was determined to be $0.0692/deg = 3.956/rad$ by using a linear fit. This was compared with previously published data by Jacobs [53] for a two-dimensional airfoil (infinite wing) at a similar Reynolds number (1.7×10^5). Since the published data was for a two-dimensional airfoil, it was corrected for aspect ratio using the following equation:

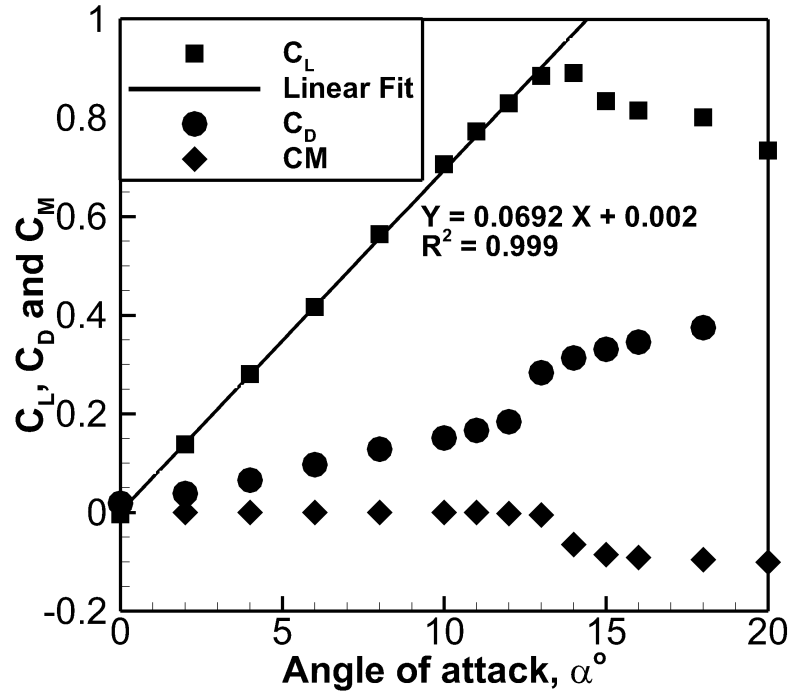

(a) Lift, drag and pitching moment

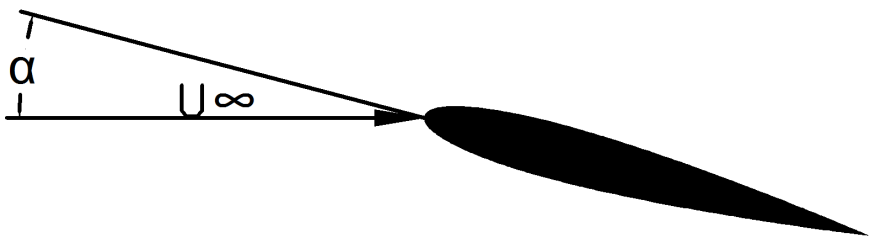

(b) Wing orientation

Figure 96: Regular flow at $Re = 1.7 \times 10^5$

$$C_{L_\alpha} = \frac{c_{l_\alpha}}{1 + \frac{57.3 c_{l_\alpha}}{\pi e AR}} \tag{11}$$

where, C_{L_α} is the lift curve slope corrected for aspect ratio, c_{l_α} is the lift curve slope of an infinite wing, e is Oswald's efficiency factor and AR is the aspect ratio of the wing.

The published lift curve for the infinite wing at $Re = 1.7 \times 10^5$ was $6.03/rad$, which was corrected for aspect ratio and determined to be $3.75/rad$. This is a close match to the lift curve slope obtained in these experiments considering the following: *a*) The corrections are accurate only for aspect ratio greater than 4.0 (while in these experiments aspect ratio of the wing is 3.5), *b*) The wing model used in this experiment has a rotor mount on one end which weakens the tip vortex at the blade root, causing a higher lift curve slope, and *c*) The mount interference with the lift force is not quantified at the writing of this technical note. One characteristic which was not picked up in these experiments was the sharp drop in lift around the static stall angle, which was attributed to the low aspect ratio of the wing.

6.3.1 Aerodynamic loads in reverse flow for static wing

Aerodynamic loads on the wing in reverse flow at $\psi = 0$ were measured; this is essentially the equivalent of a wing at a conventional angle of attack of 180°. Figure 97(a) illustrates the lift, drag and pitching moment of the wing in reverse flow. Here, the lift curve slope ($0.0684/deg = 3.92/rad$) was slightly lower than that of a wing in regular flow. An interesting observation is the linear increase of pitching moment with lift, which indicates that the center of pressure is no more located at the quarter chord (0.25c) of the wing with respect to the blunt leading edge. Instead, the data suggested that the center of pressure in reverse flow varies between 0.76c–0.82c with respect to the blunt leading edge.

The lift curve plots at various yaw angles in reverse flow are illustrated in Figure 98. The observed salient features of the wing in reverse flow are:

1. As expected the lift curve slope decreases with increasing yaw angle and the stall angle increases with increasing yaw angle.

2. At yaw angle $\psi \geq 15°$, the lift curves are observed to undergo a "soft-stall". In other

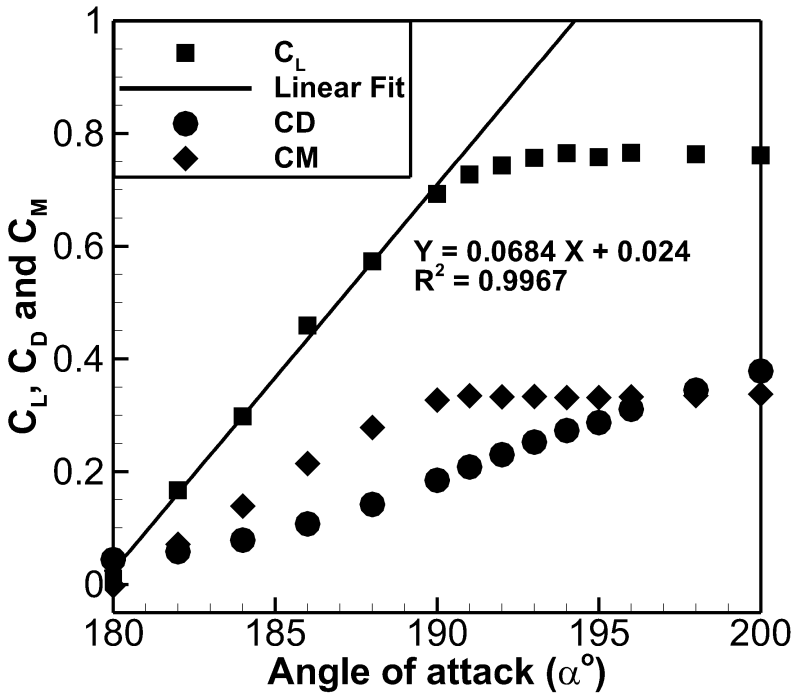

(a) Lift, drag and pitching moment

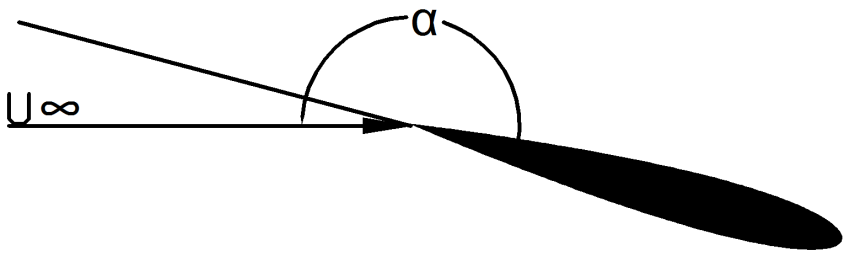

(b) Wing orientation

Figure 97: Regular flow at $Re = 1.7 \times 10^5$

words the there is no linear increase of lift with angle of attack. Instead is a small increase in lift with angle of attack. The physical reasoning for this trend could be explained by the behavior of the surface flow described in the next section.

There was a slight difference observed in the lift-curves at the two different Reynolds numbers, however the effect of Reynolds number of lift should not be discounted based on the limited data range in this work.

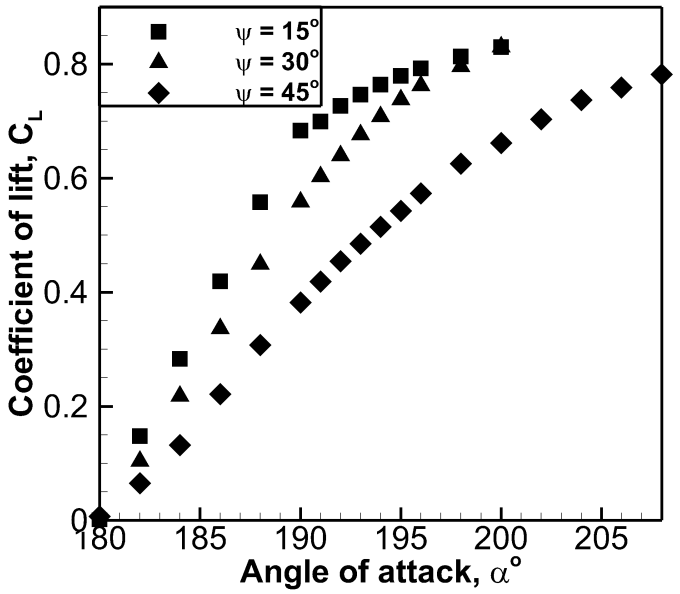

(a) $R_e = 1.7 \times 10^5$

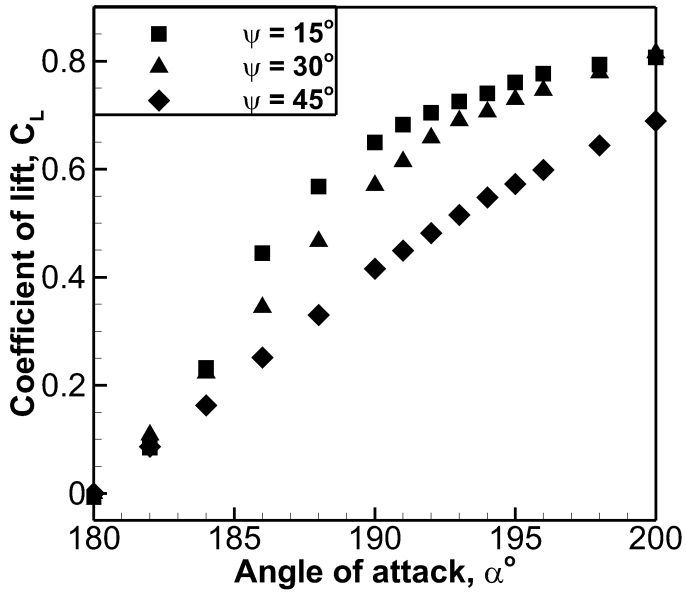

(b) $R_e = 3.0 \times 10^5$

Figure 98: Lift curves at varying yaw angles of the wing in reverse flow

A summary of lift curve slopes in regular flow and in reverse flow is illustrated in Figure 99. These plots are composed of multiple experiments with each data point showing the lift curve slope at each yaw angle.

1. The lift curve slope in regular flow exhibits the expected variation with yaw angle ($cos^2\psi$).

2. In reverse flow at $Re = 1.7 \times 10^5$ the lift curve slope starts out higher than the expected $cos^2\psi$ variation and maintains that behavior at higher yaw angles ($\psi \leq 50°$). In addition, at $Re = 3.0 \times 10^5$, the lift curve slopes at high yaw angles are also higher than the expected $cos^2\psi$ fit and the corresponding lift curve slope at $Re = 1.7 \times 10^5$. The slight increase in lift curve slope could be an effect of Reynolds number; however, the limited range of Reynolds number does not allow a complete interpretation of the effect of Reynolds number.This could suggest that there is an extra source of lift in the reverse flow regime at high yaw angles, most likely the initiation of vortex-induced lift at high yaw angles.

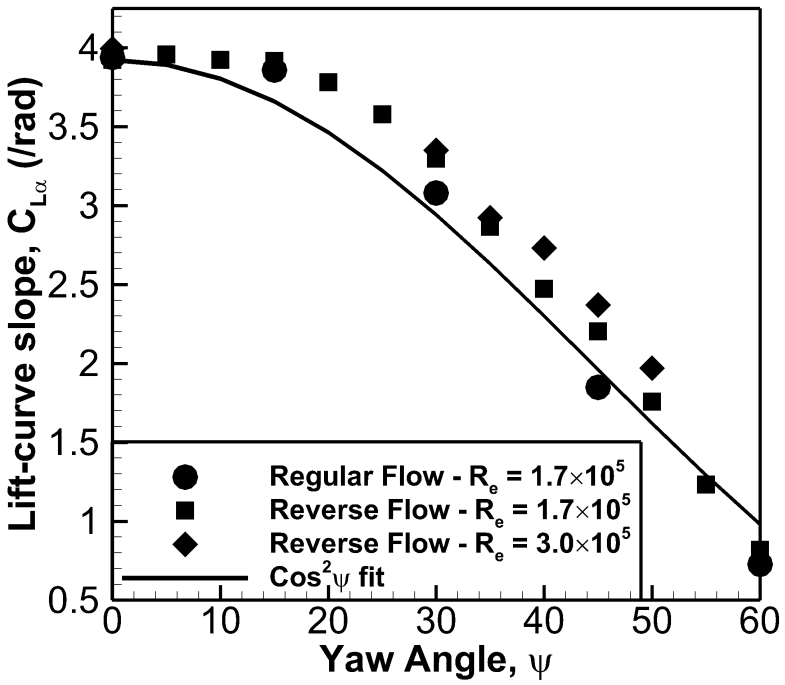

Figure 99: Variation of lift curve slope with yaw angle of the wing in reverse flow

6.3.2 Surface flow visualization in reverse flow for static wing

In order to further investigate the high lift curve slopes in reverse flow when compared to regular flow, tuft flow visualization was performed. The visualization was used to observe the nature of surface flow patterns on the yawed wing and to reconcile the lift force measurements in reverse flow. The flow visualization experiments were conducted at the test conditions indicated in Table 18 and only one test case for flow visualization is presented ($\psi = 45^\circ$ and $Re = 1.7 \times 10^5$). The data also shows signs of mount interference, which must be accounted for when drawing any conclusions. However, these are realities to be faced when trying to perform direct comparisons of a blade used in both fixed wing and rotorcraft applications. The variation of surface flow patterns with increasing angle of attack at a Reynolds number $Re = 1.7 \times 10^5$ and Yaw angle $\psi = 45^\circ$ is shown in Figure 100. In summary:

1. At $\alpha = 185^\circ$ the flow is attached on all sections of the wing and primarily in the freestream direction. A few tufts at the sharp trailing edge are moving in a clockwise, conical rotation pattern when looking from upstream. These could indicate the initiation of an attached vortex.

2. At $\alpha = 190^\circ$ the flow is still attached on all sections of the wing. However, the flow at the sharp trailing edge is predominantly in the span-wise direction showing signs of vortex growth (indicated with an oval in Figure 100(b)). The tufts aligned in the span-wise direction exhibit violent conical motions corresponding to the growth of an attached span-wise vortex.

3. At $\alpha = 195^\circ$ the surface flow exhibits three distinct flow patterns:

   (a) The surface flow is still attached on most parts of the wing, this is depicted with a solid triangle.

   (b) A significant portion of the surface flow is in the span-wise direction, signifying the expansion of an attached vortex.

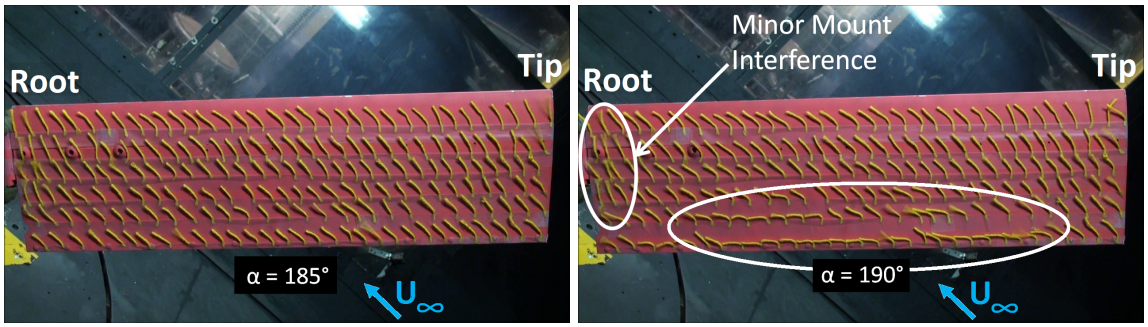

(a) $\alpha = 185°$

(b) $\alpha = 190°$

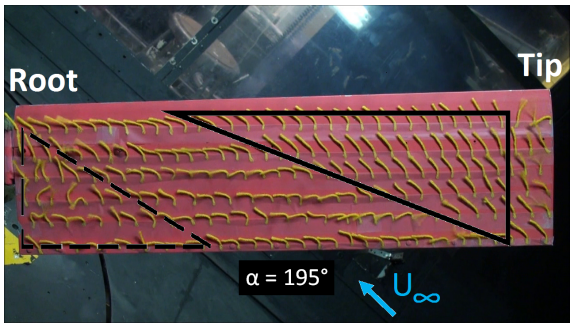

(c) $\alpha = 195°$

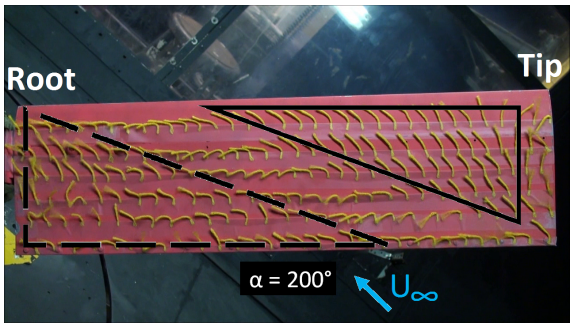

(d) $\alpha = 200°$

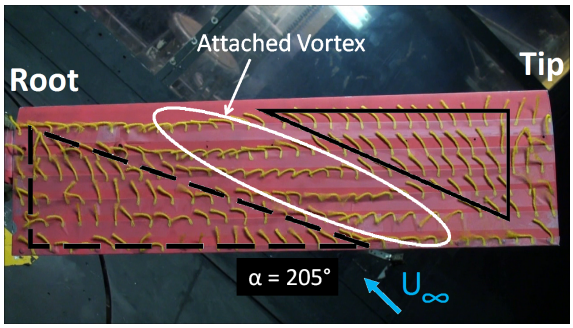

(e) $\alpha = 205°$

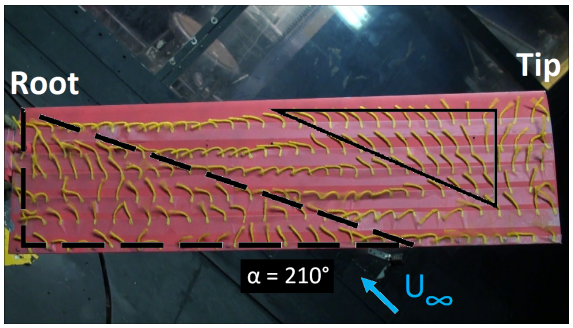

(f) $\alpha = 210°$

Figure 100: Flow visualization at $\psi = 45°$ and $Re = 1.7 \times 10^5$ in reverse flow

(c) The tufts in a small section of the wing near the root exhibit random chaotic motion suggesting flow separation (marked by a dashed triangle). As the flow reaches the root of the yawed wing it experiences an adverse pressure gradient due to a drop in span-wise velocity. This adverse pressure gradient results in flow separation and appears to cause vortex bursting as it would on a delta wing (Kohlman [63] and Payne [84]).

4. At $\alpha \geq 200°$ the surface flow does not show any significant changes. However, now

a clear demarcation is seen between attached and separated flow regions indicated by solid and dashed triangles respectively. Clearly as angle of attack increases the separated region is increasing in size and the attached region is decreasing in size, while the attached vortex flow maintains its size.

5. At this point it is also important to mention that the interference of the mount in a small aspect ratio wing (as in this case) would be significantly higher when compared to a larger aspect ratio wing. On a larger aspect ratio wing the separated flow near the root of the wing would be *expected* to be a smaller proportion of the total blade area.

The flow visualization observations can now used to reconcile the behavior of lift at high yaw angles $\psi \geq 20^{\circ}$. As observed in Figure 98, there is no post-stall drop in lift. This could be directly linked to the existence of an attached vortex on the yawed wing surface in reverse flow. In addition, the small regions of attached flow also help in producing lift. However, it is important to note that the surface flow patterns are specifically for a yawed wing which would be different than a swept wing.

Based on the flow visualization experiments the surface flow topology on a yawed wing in reverse flow is sketched in Figure 101. The flow topology shows the three distinct flow regimes - attached flow, vortex flow and separated flow demarcated by the dotted lines. It is worth noting that the position and shape of the attached span-wise vortex closely resembles that of the lower surface vortex predicted by Potsdam (see Figure 25 in [86]), which was attributed to "reverse-chord dynamic stall". The similar vortex observed in this investigation on a static yawed wing could suggest that the vortex predicted by Potsdam et al. may not be an artifact of rotation.

6.3.3 Chordwise velocity field in reverse flow for static wing

The motivation for measuring the chordwise velocity field in reverse flow for a static wing was to compare and contrast this flow to the flow over a rotating blade in similar conditions. PIV measurements were gathered on the static wing at $\psi = 30^{\circ}$ (equivalent to $\psi = 240^{\circ}$ for the rotating case) at test conditions summarized in Section 6.2.3. The angle of attack chosen

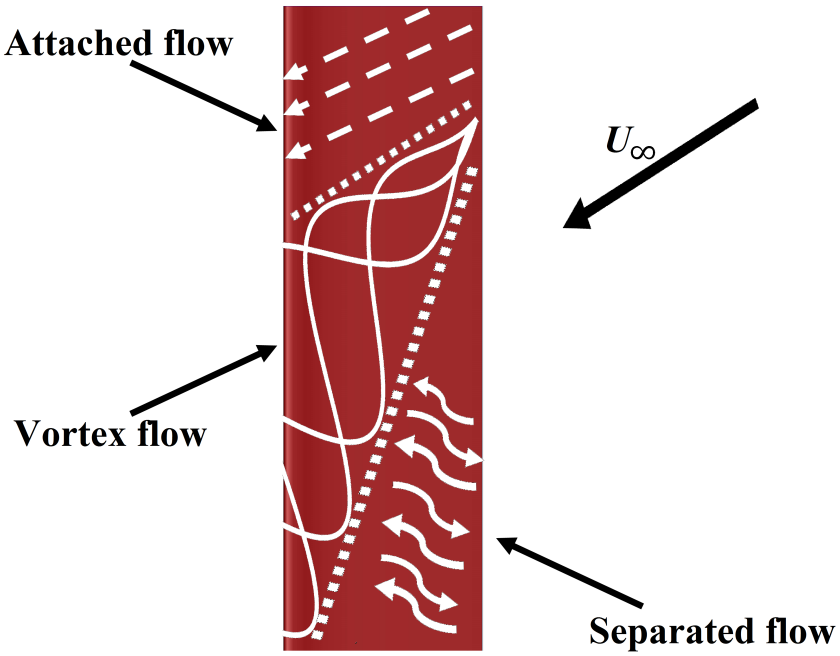

Figure 101: Proposed surface flow topology over a yawed wing in reverse flow

for the chordwise velocity measurements was to ensure the static wing was at the same effective angle of attack as the rotating blade (accounting for inflow and blade flapping). The pitch angle of the rotating blade at $\psi = 240°$ is 191.2° and the effective angle of attack is 192°. Hence the chordwise velocity measurements on the static wing were gathered at 191.2° and 192° and Re = 0.63×10^5 (the effective Reynolds number at r/R = 0.5 for $\mu = 0.8$ and $\Omega = 20.93\ rad/s$ is 0.63×10^5). The second Reynolds number was chosen to verify the surface flow visualization at Re = 1.7×10^5 and angle of attack 192° and 195° presented in the previous section.

In the all the velocity vector fields presented in this chapter, the axis of the vector fields are fixed in the wind tunnel coordinate system and has not been corrected for the pitch angle of the blade. The right hand coordinate system for the vector field is such that the positive y axis is out of the plane and hence negative radial (spanwise) velocity indicates a flow towards the root of the blade and vice versa. All dimensions are normalized by the chord length, where x/c = 0 is the leading edge and x/c = 1 is the trailing edge of the

blade. Figures 102–104 illustrates the time averaged velocity vector overlaid on contours of vorticity at $\psi = 30°$, $\alpha = 191.2° - -195°$, and $Re = 0.63 \times 10^5$ *and* 1.7×10^5. The velocity field data at $Re = 1.7 \times 10^5$ corroborates the surface flow visualization (see figure 100) which showed evidence of a vortex at the trailing edge of the blade.

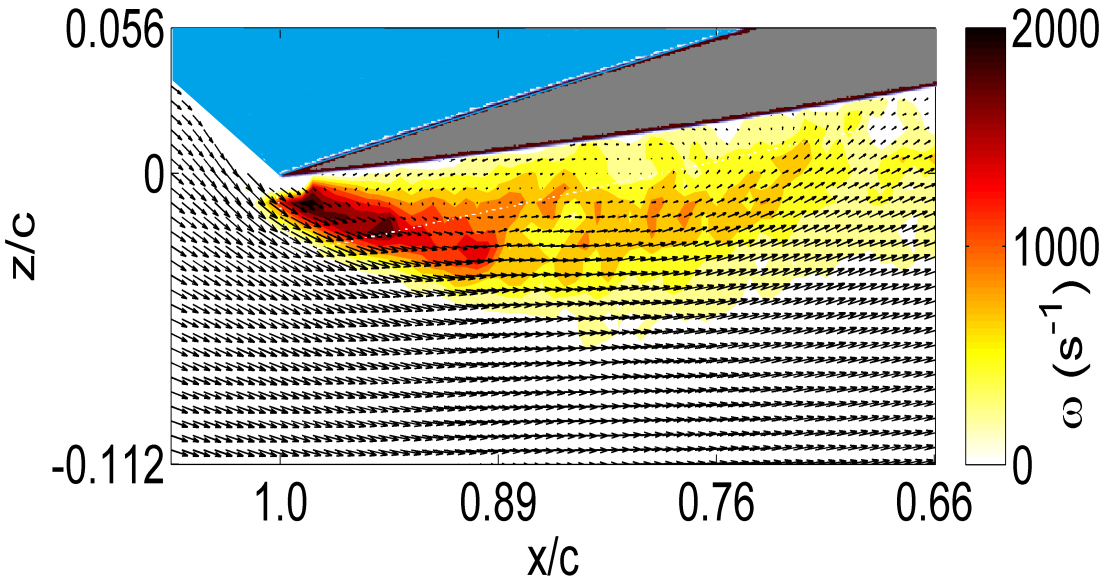

Figure 102: Velocity field on a static wing showing the existence of a vortex at $\psi = 30°$, $\alpha = 191.2°$, $Re = 0.63 \times 10^5$

The velocity field data gathered in these experiments (stereoscopic-PIV) allows for the interpretation of the third component of velocity (radial/spanwise). Figure 105 shows the time averaged velocity vectors overlaid on the time averaged radial velocity component (U_r positive for out of plane). It can be observed very clearly that the radial component of velocity is predominantly into the plane of the paper, indicating a spanwise flow towards the root which should be expected on a blade at forward yaw angle (see Figure 94(b) for definition of forward yaw). This is also observed in the surface flow visualization presented in section 6.3.2. The radial velocity has a lower magnitude closer to the surface of the blade, and increases on moving away from the blade surface. The radial velocity field data can now be used to analyze the effect of rotation, which is expected to predominantly affect the radial velocity component due to additional centrifugal effects during rotation.

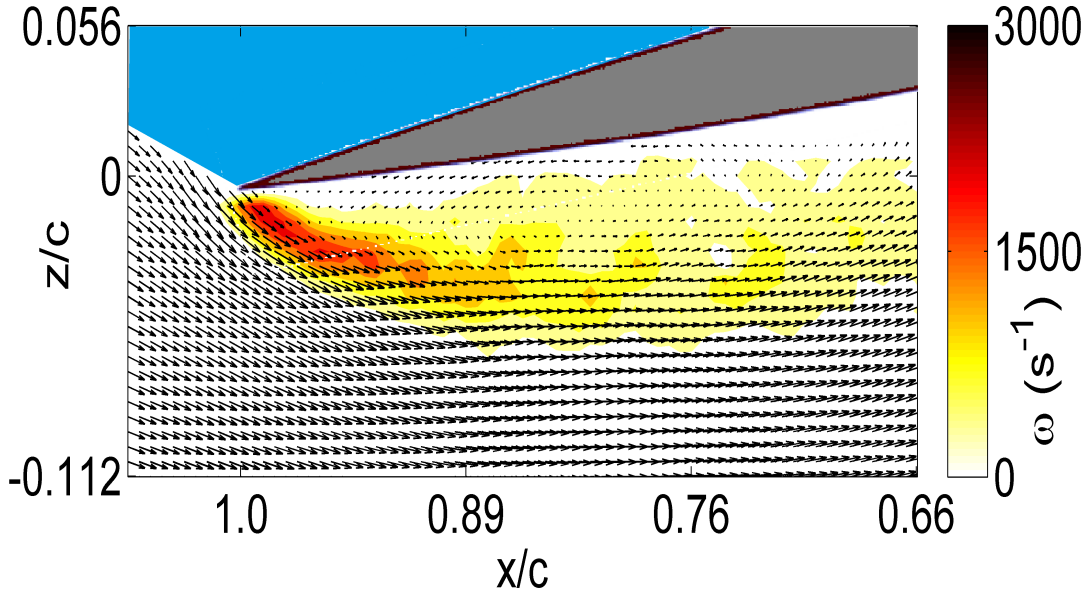

Figure 103: Velocity field on a static wing showing the existence of a vortex at $\psi = 30°$, $\alpha = 192°$, $Re = 0.63 \times 10^5$

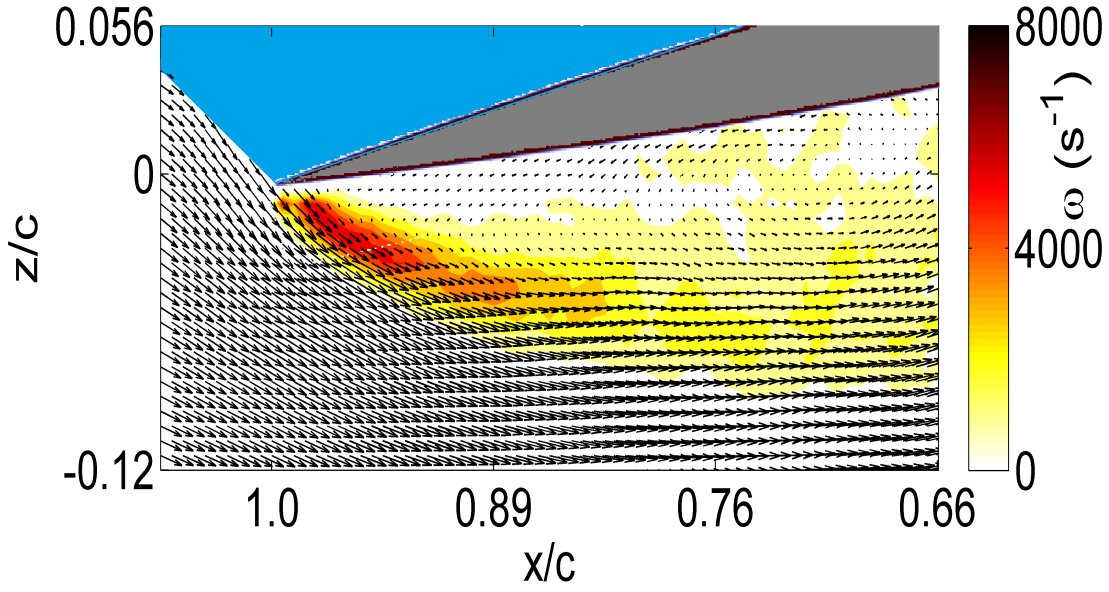

Figure 104: Velocity field on a static wing showing the existence of a vortex at $\psi = 30°$, $\alpha = 195°$, $Re = 1.7 \times 10^5$

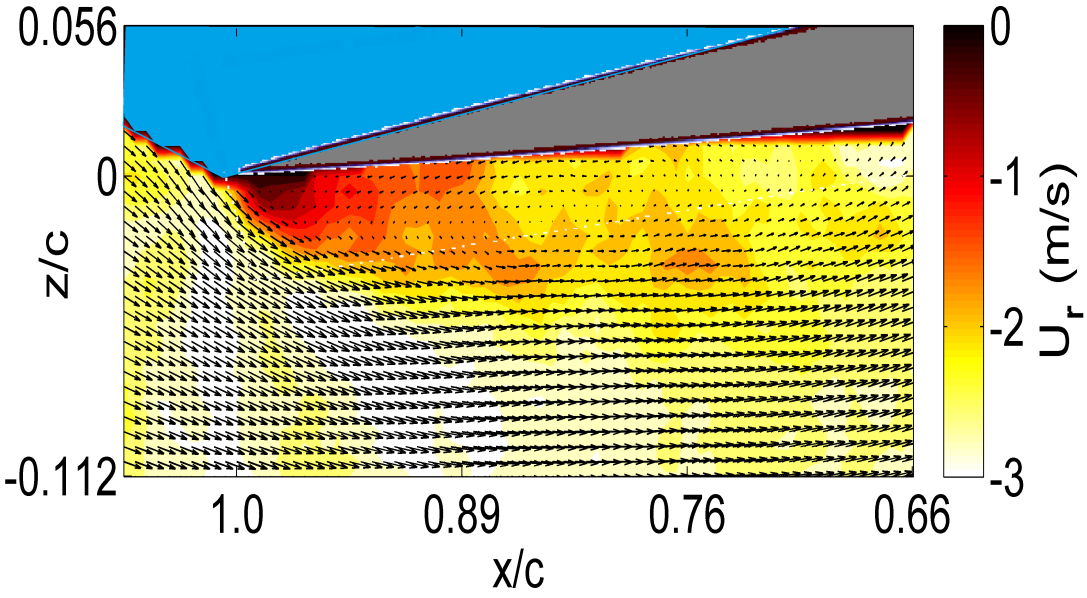

Figure 105: Velocity field on a static wing overlaid on the radial (spanwise) component of velocity at $\psi = 30°$, $\alpha = 192°$, $Re = 0.63 \times 10^5$

6.3.4 Chordwise velocity field in reverse flow for rotating wing

Velocity measurements on the rotating blade at $\mu = 0.8$, $\Omega = 20.93\ rad/s$ and r/R = 0.5 phase locked at $\psi = 240°$ (equivalent to static wing at $\psi = 30°$) is illustrated in Figure 106. Clearly, the radial velocity has a positive value (flow from the root to the tip of the blade) close to the blade surface, which is predominantly due to reactive centrifugal forces during rotation. The radial velocity then quickly transitions to a negative value (from from tip to the root of the blade), which is expected since the radial stress driving the radial flow does not extend to a great height above the blade surface. A comparison of Figures 105 and 106 demonstrates the effect of the rotation on the radial component of velocity in reverse flow conditions. Furthermore, a comparison of Figures 103 and 107 suggests that the additional radial velocity due to rotation delays the separation at the trailing edge at similar flow conditions ($Re = 0.63 \times 10^5$, $\alpha = 192°$ and $\psi = 30°$).

With the current collective and cyclic pitch settings ($\theta_0 = 6°$ and $\theta_s = -6°$) separation at trailing edge could not be observed until yaw angle $\psi = 270°$ (equivalent to static wing

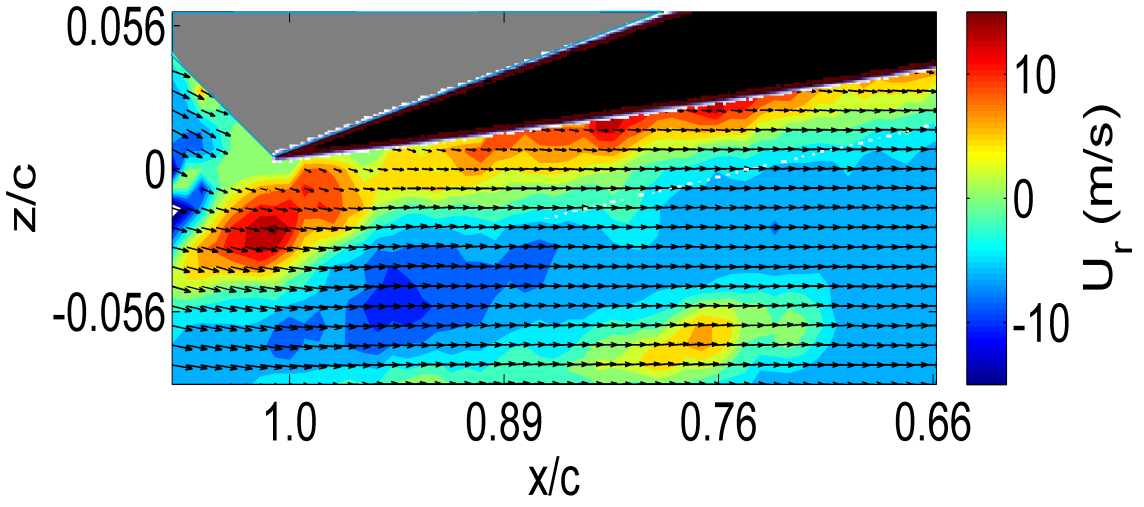

Figure 106: Velocity field on a rotating wing overlaid on the radial (spanwise) component of velocity at $\psi = 240°$, $\mu = 0.8$ and $\Omega = 20.93\ rad/s$ which yields $\alpha = 192°$ and $Re = 0.63 \times 10^5$ at r/R = 0.5

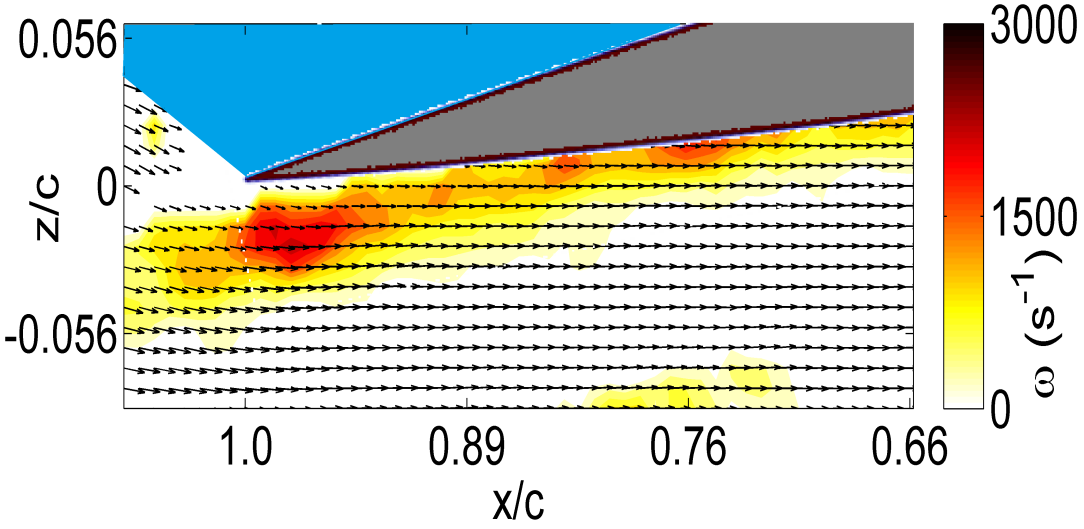

Figure 107: Velocity field on a rotating wing overlaid on vorticity contours at $\psi = 240°$, $\mu = 0.8$ and $\Omega = 20.93\ rad/s$ which yields $\alpha = 192°$ and $Re = 0.63 \times 10^5$ at r/R = 0.5

at $\psi = 0°$). Figure 108 illustrates a measured vortex in reverse flow on the lower surface of the blade. To clearly visualize the vortex the freestream velocity ($U_\infty = 14.88$ m/s) had to be subtracted from the velocity field. The circulation of the vortex (Γ_V) was computed using Stokes theorem (see Equation 7) and determined to be 0.354 m^2/s. The circulation of this vortex was compared to the maximum bound circulation (Γ_a) of the "airfoil" section of the wing. The bound circulation was computed using the following expression:

$$\Gamma_a = \frac{1}{2} U_\infty c C_{L_{max}} \tag{12}$$

where c is the chord length and $C_{L_{max}}$ is maximum static coefficient of lift and was taken from the aerodynamic loads measurement data (see Section 6.3.1. The computed bound circulation was 0.392, which is slightly higher than the circulation of the vortex at the trailing edge. The fact that the circulation in the vortex is of the same order of magnitude of the bound circulation could imply a significant lift contribution from the vortex developing on the lower surface of the blade in reverse flow.

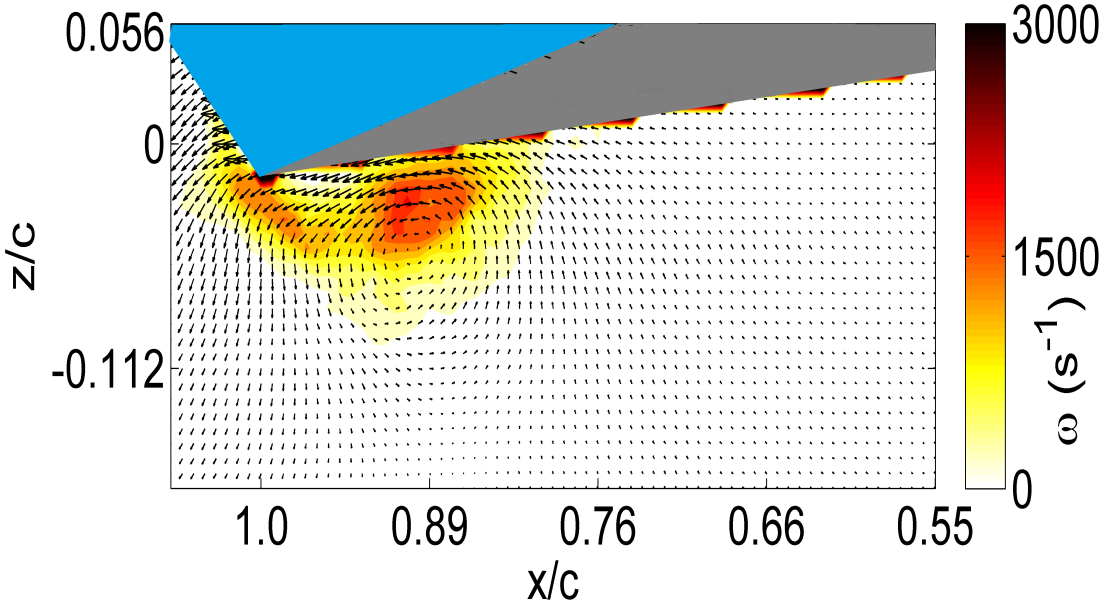

Figure 108: Velocity field on a rotating wing overlaid on vorticity contours at $\psi = 270°$, $\mu = 0.8$ and $\Omega = 20.93$ rad/s at r/R = 0.5

6.4 Summary of results

The motivation for this work was to better understand the aerodynamic behavior of a rotating blade in reverse flow by first understanding the aerodynamic characteristics of a static wing in reverse flow and then on the rotating blade. Lift forces on a finite wing in regular flow were measured and validated against published data. The same finite wing was then tested in reverse flow regimes at various yaw angles in order to understand the fundamental differences in behavior of the lift characteristics when compared to that in regular flow. In addition, the same blade was used in rotating blade experiments to study the reverse flow in a rotating environment.

The findings in this work are summarized as follows:

1. The lift behavior of the wing in reverse flow at yaw angles $\psi > 20^\circ$ indicates no post-stall drop in lift.

2. The lift curve slopes in reverse flow were observed to be higher than the corresponding regular flow lift curve slopes at yaw angles $\psi > 20^\circ$. It was also observed that the lift curve slopes at higher yaw angles displayed a small increase with Reynolds number.

3. The above two conclusions suggest that there is an extra source of lift in the reverse flow regime at high yaw angles ($20^\circ \leq \psi \leq 50^\circ$), indicating the possible initiation of vortex-induced lift at these yaw angles.

4. Surface flow visualization at $Re = 1.7 \times 10^5$ and $\psi = 45^\circ$ confirmed the existence of an attached vortex on the wing in reverse flow. The flow visualization also established the sequence of the development of surface flow patterns on the wing.

   (a) At lower angles of attack ($180 \leq \alpha \leq 190^\circ$) the surface flow was mostly attached. The flow at the sharp trailing edge was predominantly in the span-wise direction. The tufts aligned in the span-wise direction exhibited violent conical motions showing signs of an incipient and expanding span-wise vortex.

   (b) At higher angles of attack ($\alpha \geq 195^\circ$) the surface flow developed three distinct flow regimes - the attached flow, vortex flow and separated flow.

(c) The flow separation occurs due to the adverse pressure gradient induced by the mount at the root and appears to cause vortex bursting as it would on a delta wing.

(d) The area of the separated flow near the mount is *expected* to reduce for a larger aspect ratio wing since the mount induced adverse pressure gradient would be significantly lower.

5. The higher lift curve slopes in reverse flow and the lack of a post-stall drop in lift at high yaw angles is reconciled by the existence of the attached vortex and small regions of attached flow on the yawe wing in reverse flow at high angle of attack ($\alpha \geq 200^{\circ}$).

6. PIV measurements on a yawed static wing at angle of attack in reverse flow also confirmed the existence of an attached leading edge vortex as observed in the surface flow visualization.

7. PIV measurements on the rotating blade at similar angle of attack and yaw angle as that of the static wing showed no evidence of separation. The formation of the vortex was delayed to a higher angle of attack primarily due to rotational augmentation which hinders separation.

The work in this chapter was aimed at establishing the aerodynamics of a blade in reverse flow. The next logical step is to model the effect of reverse flow on rotating blades using a delta wing analogy. The analysis of the lift-to-drag ratio and pitching moment behavior is crucial to explaining the aerodynamic loads in the reverse flow regime and should be performed to gain further insights.

CHAPTER VII

CONCLUSIONS AND RECOMMENDATIONS

In this chapter, the main conclusions of the work presented in this thesis are outlined. First, the conclusions derived from the results of all investigations in this work are summarized and they are placed in context of the overall field of retreating blade aerodynamics. Next, a summary of significant contributions arising from this thesis is presented. Finally, recommendations for further work are proposed for future considerations.

7.1 Conclusions

In this thesis, two aerodynamic phenomena - dynamic stall and reverse flow, both that both occur on retreating rotor blades were investigated. The principal objective was to understand the effect of radial flow induced due to centrifugal forces on these phenomena. The flow field level details of the dynamic stall phenomenon on the retreating rotor blade was investigated by measuring the velocity field using a combination of SPIV and PIV techniques. The reverse flow investigation was conducted using aerodynamic load measurements, surface flow visualization via tufts and PIV. In this section the specific conclusions of each sub-investigation and their relevance to the rotorcraft community is listed and discussed.

1. The phase-averaged velocity field during the inception of separation suggests that the mechanism in operation was the classical trailing edge separation mechanism. This is similar to what was hypothesized and observed by McCroskey [75] on oscillating two-dimensional airfoils. However, in the rotating environment the separation first occurred at inboard radial locations first and then progressed to outboard locations. The radial flow appears to thus affect the onset of separation. The main implication here is that the different span-wise locations of the blade will undergo the DS cycle at different time instants, making it a truly three-dimensional event. The associated lift overshoot and pitching moment spike will hence not occur at the same phase on the

rotating blade. However, it is important to note here that the cycle-to-cycle variations were quite significant, which again has implications on the exact timing of onset of separation and hence of dynamic stall.

2. During the DS event a coherent vortical structure forms over the upper surface of the blade. While it initially it appears to be pinned to the surface of the blade, at the maximum angle of attack the vortex lifts off the surface of the blade. As the dynamic stall event progresses, the associated radial flow magnitude also increases. This brings into question the role of radial flow in the process of dynamic stall. The critical observation here is that the phase-averaged vortex is spatially diffused when compared to the instantaneous velocity fields. This was deduced by analyzing the POD approximated instantaneous velocity fields. It was also confirmed by computing circulation around the flow over the upper surface of the blade from phase-averaged velocity and comparing it to the circulation computed from instantaneous velocity fields and then averaged.

3. The flow field at $\psi = 270^{\circ}$ was thoroughly investigated by measuring the velocity field at several radial locations to quantify the effect of rotation on dynamic stall. The $\psi = 270^{\circ}$ azimuthal angle was chosen mainly because it allowed for a decoupling of the span-wise flow induced due to yaw and radial flow induced due to rotation. The coherent vortex observed on the upper surface of the blade was classified as the DSV by virtue of the circulation of the vortex which was expected to be proportional to the lift overshoot during the DS event. The lift overshoot decreased on moving radially outboard indicating the weakening of the dynamic nature of the DS event. The results suggested that the radial flow relatively stabilizes the strength of the vortex from cycle-to-cycle but the vortex location is not stabilized causing the vortex to be spatially diffused and weaker in the phase-averaged velocity fields. The main consequence here is that the relative stability in strength of the vortex makes it easy to predict the cycle-to-cycle variations of the lift overshoot. However, the erratic spatial location of the vortex implies that the associated pitching moment will not be stable

from cycle-to-cycle and hence harder to predict.

4. The results on the effect of rotation on dynamic stall motivated an investigation of the radial flow over the rotating blade during dynamic stall conditions. Again the $\psi = 270^{\circ}$ azimuthal angle was chosen mainly because it allowed for a decoupling of the span-wise flow induced due to yaw and radial flow induced due to rotation. Contrary to expectations the peak radial flow magnitude attenuated on moving radially outboard. Further investigations suggested the physical mechanism for this attenuation was an apparent shear layer instability. The instability caused the radial jet to break up with co-rotating vortices which carried away roughly 30% of the vorticity in the shear layer between the radial jet and the blade surface. This phenomenon was quantified to be of first order significance in the radial flow field, hence could be significantly modifying the evolution of lift and pitching moment during the DS event.

5. The significance of radial flow during the DS event prompted a fundamental investigation of the radial flow instability on a rotating blade in separated flow conditions. Since the radial flow on a rotating blade was primarily due to centrifugal forces, it was hypothesized that fundamental insights into the phenomenon on a separated rotating blade can be sought by studying the radial boundary layer of a rotating disk in a separated flow. PIV measurements indicated that a radial flow instability was triggered upon superimposing a uniform stream on a rotating disk. The instability was recognized by observing the evidence of co-rotating structures which occurred at the upper edge of the radial boundary layer coinciding with the inflection point of the radial velocity profile. The vortices were observed only during the rotation of the disk and not otherwise, firm evidence that the instability is due to the radial flow itself and not an artifact of separation. Furthermore, these co-rotating vortices were not observed on the rotating disk in a quiescent medium at the same rotation rates, presumably because the instability was weak enough not to get amplified under those conditions. Correlation metrics were proposed to develop an analogy between the flow features on the rotating disk and rotating blade operating in similar separated flow

conditions.

6. The final part of this thesis dealt with reverse flow over a yawed blade. A vortex flow hypothesis was proposed for a yawed blade at angle of attack in reverse flow, which was expected to operate similar to a sharp-edge delta wing at angle of attack. Aerodynamic load measurements in regular and reverse flow conditions on a static yawed blade at angle of attack suggested that the lift curve slopes in reverse flow were higher than the corresponding regular flow lift curve slopes. This suggested an extra source of lift in the reverse flow regime at highly yawed angles, indicating the possible initiation of vortex induced lift at these yaw angles. Surface flow visualization via tufts demonstrated evidence of an attached span-wise vortex validating the plausibility of the vortex flow hypothesis. The vortex flow hypothesis has significant implications in this exotic flow regime, it allows for the development of a analytical model to predict lift similar to the Polhamus suction analogy. PIV measurements of the flow on the lower surface of the rotating and static blade in reverse flow conditions clearly demonstrated the effects of rotation on the process of separation. Rotational augmentation appeared to delay the formation of the leading edge vortex to a higher angle of attack when compared to the static case.

7.2 Summary of significant contributions

The following is a summary of the key contributions:

1. For the case of an isolated teetering rotor, the dynamic stall event was characterized with detailed measurements from inception of separation through reattachment. Phase-averaged velocity fields were gathered for a set of parameters such as radial location and advance ratio through the various yaw angles, which helped characterize the general behavior of dynamic stall. These measurements were also used to quantify the cycle-to-cycle variations of dynamic stall on a retreating rotor blade.

2. The effect of rotation on the DS event was also investigated, this was compared and contrasted to the traditional two-dimensional DSV. This study also helped in

throwing light on the radial variation of the dynamic stall event at $\psi = 270°$ which is the azimuthal angle where radial flow is purely due to centrifugal forces unique to the rotating environment.

3. Radial flow measurements on the retreating blade during DS quantified the significance of radial flow. Contrary to expectations, the radial flow attenuated on moving outboard due to an apparent shear layer instability. Additionally, It was shown that the radial flow is of first order significance in the flow field and hence should have a significant impact on the evolution of lift and pitching moment during DS.

4. In search for a similar flow field that can be studied easily, the rotating disk similarity hypothesis was proposed and demonstrated. Investigations showed that the shear layer instability of a flow induced due to centrifugal forces on a separated surface is a fundamental behavior of the radial flow. This allows for a quasi-analytical way to predict the instabilities on a separated rotating blade hence enabling the derivation of fundamental relationships. It opens a path to develop analogies between the flow over a rotating disk and a rotating blade. In addition, it allows for a systematic study of the radial flow instability without having to perform large scale experiments or computational analyses.

5. A vortex flow hypothesis for yawed blades in reverse flow was proposed and demonstrated. This allows for the development of a vortex induced lift model for yawed wings in reverse flow, possibly using Polhamus suction analogy. PIV measurements on a static and rotating blade at similar flow conditions showed the effects of rotation, and confirmed the delay of separation due to rotational augmentation.

7.3 Recommendations for future work

Based on the results and conclusions of the investigations in this work, several recommendations for future work are proposed in this section.

1. Dynamic stall

(a) The dynamic stall event on a rotating blade was demonstrated to be a highly unsteady event. In this investigation phase-locking was used because of the limitation of the speed of the laser and camera. Further insights into this unsteady flow field can be sought using Time Resolved PIV (TR-PIV). This involves a high frequency laser and camera which would be capable of measuring consecutive instantaneous snapshots of the flow field.

(b) In addition, TR-PIV could also yield further insights into the radial flow instability, where the formation and convection of time dependent co-rotating vortical structures was observed as a physical mechanism via which the radial flow attenuated on moving radially outboard. In the same lines, TR-PIV could be used to investigate the radial flow instability on a rotating disk in a separated flow, which was also observed to be a time dependent phenomenon.

(c) In the case of the radial flow instability over a rotating disk in separated flow. Correlation parameters were proposed to develop an analogy, however the validity of the parameters were not thoroughly tested with further experimentation. Future experiments should be aimed at validating that hypothesis and completing the analogy to the rotating blade in separated flow.

(d) A common shortcoming of such an investigation which focuses on velocity measurements is that pressure data is not gathered along with the velocity data. However, PIV data can be used to further analyze the same flow fields by solving the Navier-Stokes equation to obtain pressure fields from velocity fields. This could be used to then determine the surface pressure distribution with sufficient accuracy.

2. Reverse flow

(a) The current experiments were limited in trim conditions due to the physical constraints of the experimental setup. Modification of the experimental setup with longer pitch links to enable better high advance ratio ($\mu \geq 1$) trim conditions. Preferably a collective of $\theta_o = 7^\circ$ and a cyclic of $\theta_s = -8^\circ$ would be ideal to

achieve pitch angles to induce separation at yaw angles $240^\circ \leq \psi \leq 260^\circ$, to study the formation of the vortex on the lower side of the rotating blade in reverse flow conditions.

APPENDIX A

UNCERTAINTY ESTIMATES

A.1 Flow condition and experimental setup uncertainty

The flow dynamic pressure was measured using a 10 Torr Baratron, a differential pressure transducer with a precision of 0.001 Torr (0.001 mm Hg = 0.133 Pa) connected to a pitot-static tube located near the ceiling of the middle of the test section. The ambient pressure and temperature measurements are then used to compute the density of fluid. The flow velocity is calculated using the dynamic pressure and density of the fluid. The equations are summarized in Table 19

Table 19: Sample calculation of flow conditions

Property	Estimate	Value	Units
ρ	$\frac{P}{R_g T}$	1.184	kg/m^3
μ	$\frac{C_1 T^{3/2}}{T+S}$	1.91×10^{-5}	$Pa\text{-}s$
V_∞	$\sqrt{\frac{2q}{\rho}}$	15.41	m/s
R_e	$\frac{\rho V_\infty c}{\mu}$	1.7×10^5	

$C_1 = 1.458 \times 10^{-6}$ and $S = 110.4\ K$ are Sutherland's constants.

The uncertainties in flow conditions arising from measurement inaccuracies are summarized in Table 20. In addition the table also lists the error in density calculation arising from measurement uncertainty of ambient pressure and temperature. The uncertainty in collective pitch and cyclic pitch angle settings, which were measured using a digital protractor, is 0.05°. The error in measurement of the angle of the tip path plane arises mainly due to the pixel size in image processing, and the uncertainty is 0.035°.

Table 20: Summary of errors

Parameter	Range Considered	Uncertainty
Freestream velocity	0-30 m/s	± 0.33%
Density	1.183 kg/m^3	± 0.025%
Load-cell calibration	0-15 N	±1.37%
Yaw and Pitch Angle	$0^\circ - 60^\circ$	± 0.05°
Reynolds Number	$1.7 \times 10^5 - 3 \times 10^5$	±0.3%

A.2 Aerodynamic loads uncertainty

The primary errors in the force measurement arises from the load sensor calibration. The least-squares technique to calibrate six axis load cells was used to achieve a low calibration error of 1.37%. Similarly the accuracy of the velocity and density were determined from the limitations of the apparatus used to measure the conditions. The total error in the measurement of drag, side force, and yaw moment coefficient was calculated to be ±1.21%. This value was calculated using the errors due to individual factors found in Table 20. The ensemble averaged data are very repeatable with minimal scatter at each measured point, as observed in the results and discussion section. In addition, a detailed analysis of the wing geometry used was performed by measuring the wing chord and thickness at over eighteen locations through the span of the blade. The average error of thickness and chord length when compared to the standard NACA 0013 was around 1.0% of each dimension, with the root mean square error around 0.5%. Please refer to Section 1.5.2 for further details of these measurements.

A.3 PIV uncertainty

The uncertainty in velocity measurements is computed using methods described in [92, 91]. Errors in PIV measurements can be of five types [88]. They are:

1. Random error due to noise and other measurement uncertainties.

2. Bias error due to sub-pixel interpolation.

3. Gradient error resulting from rotation and deformation of the flow withing an interrogation spot leading to loss of correlation.

4. Tracking error resulting from the inability of a particle to follow the flow.

5. Acceleration error caused by approximating the local Eulerian velocity from the Lagrangian motion of tracer particles.

Out of these five, the last three cannot be avoided. They can only be minimized by careful planning, by optimizing the size of the particles and the pulse separation to give the best results for the flow conditions. The steps that were taken to plan these aspects were outlined at the beginning of this chapter. It is also quite difficult to quantify the last three errors.

As far as the bias error is concerned, it is manifested by a phenomenon referred to as pixel locking, where the sub-pixel interpolation causes the velocity to be biased towards integer values of pixel shift. It has also been shown that bias error becomes sizable usually when particle image diameter > 1 diameter [1]. One way of preventing this phenomenon is to check the histograms of the pixel shift after each run to ensure that there is not a cluster around an integer value. The probability density histograms (see figure 109) of the instantaneous velocity data did not reveal peak-locking or any other experimental artifact, the highest resolution of velocity being 0.005 m/s. Therefore, one can make a reasonable conclusion that this error is not sizable in this study.

It has been shown that random error scales with the particle image diameter and is given by the relation in equation 13, where σ_e is the random error, d_p is the particle image diameter and c_e is an empirical constant usually lies between 0.05 and 0.10.

$$\sigma_e = c \times d_p \tag{13}$$

Calculations for sample experimental data is thus presented. For this experiment the random error ranged from 0.053 pixels in the best case (0.05×1.06 pixels) to 0.197 in the worst case (0.10×1.97 pixels).

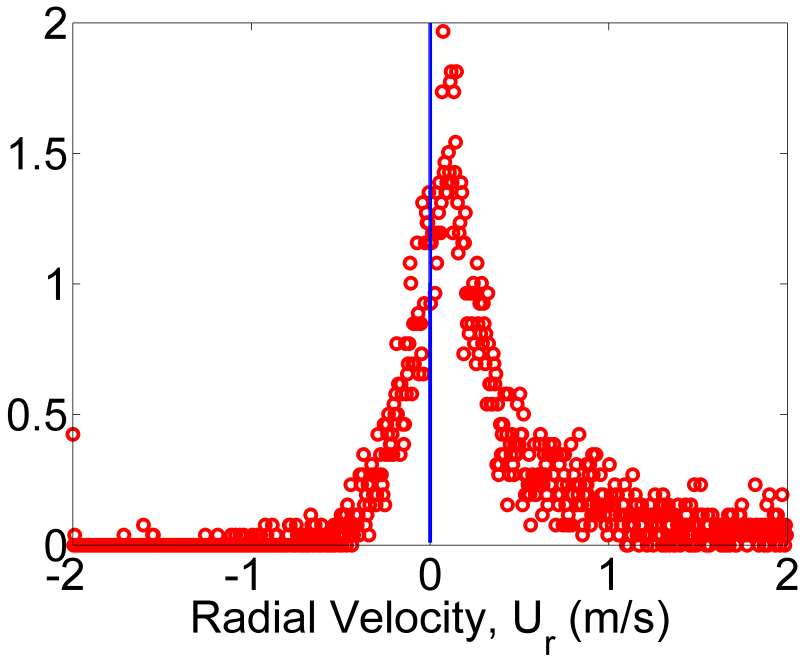

Figure 109: Histogram illustrating velocity distribution

The total measurement error, ϵ_m, was quantified with Eq. 14 from Ref. [91], where W_p is the maximum out-of plane component of flow velocity, U_p is the maximum in plane component of flow velocity, Z_s is the light sheet thickness, M is the magnification, and σ_i is the random measurement error in the image plane.

$$\epsilon_m \leq \frac{W_p}{U_p} \times \frac{3}{Z_s M} \times \sigma_i \tag{14}$$

W_p was measured in the chordwise plane and was found to be $2.5m/s$, U_p was measured to be $3.5m/s$, Z_s was maintained between 3-4mm, M of the camera was $\frac{1}{16}$. σ_i amounted to $6.5 \times 10^{-6} \times \sigma_e$ ranging between 3.45×10^{-7} and 1.28×10^{-6}.

Using these relations the total measurement error ϵ_m was estimated between 0.34% and 1.25%. This amounted to an absolute error of $0.012m/s$ and $0.043m/s$ based on U_p. The uncertainty in PIV measurements are summarized in Table 21.

A.3.1 Particle Size Considerations

During PIV measurements the particle size must be considered for each experiment to estimate any errors arising due to the particles not "following" the flow - called particle lag

Table 21: Summary of PIV errors

Type	Estimate	Error
Random Error	Eq. 13	0.053 - 0.197 pixels
Bias Error	Peak Locking Histogram	0.005 m/s
Lag Error	Relaxation Time	Insignificant
Total Measurement Error	Eq. 14	0.34% - 1.25%

error ([92]). There are primarily two competing forces that must be weighed in order to select an appropriate seed particle size.

1. The particles must be small enough to accurately track the flow

2. Large enough and plentiful enough to be tracked optically.

The particle lag error was determined to be insignificant after considering the particle dynamics in a viscous fluid. A transient solution for the response of the seed particles to changes in velocity was formulated as summarized below.

Using the stokes drag law the velocity lag of a particle in a continuously accelerating fluid was determined to be:

$$U_s = U_p - U = d_p^2 \frac{\rho_p - \rho}{18\mu} a \tag{15}$$

The step response of U_p typically follows an exponential law solution (see equation 21) if the density of the particle is much greater than the fluid density. In this case the particle density is 800 times the density of the fluid. The following is a derivation of the response of a seed particle to a velocity change. The seed particles were typically 1-10 microns in diameter. Hence a creeping flow assumption was used to solve for the velocity using stokes law.

Considering the momentum equation in the spherical polar coordinates (r, θ), with $\theta = 0$ in the direction of U, given by

$$\left(\frac{\partial^2}{\partial r^2} + \frac{1}{r^2} \frac{\partial^2}{\partial \theta} - \frac{cot\theta}{r^2} \frac{\partial}{\partial \theta} \right)^2 \psi = 0 \tag{16}$$

The pressure acting on the seed particle is found by integrating the momentum relation of the Navier-Stokes equations which gives

$$p = p_\infty - \frac{3\mu d_p U}{2r^2} cos(\theta) \tag{17}$$

where p_∞ is the uniform freestream pressure. Thus the pressure deviation is proportional to dynamic viscosity (μ) and antisymmetric, being positive at the front and negative at the rear of the sphere (seed particle). This creates a pressure drag on the sphere. There is also a surface shear stress which creates a drag force. The shear stress distribution in the fluid is given by

$$\tau_{r\theta} = \mu \left(\frac{1}{r} \frac{\partial u_r}{\partial \theta} + \frac{\partial u_\theta}{\partial r} - \frac{u_\theta}{r} \right) = -\frac{\mu U sin(\theta)}{r} \left(\frac{3{d_p}^3}{2r^3} \right) \tag{18}$$

The total drag is found by integrating pressure and shear around the surface.

$$F = -\int_0^\pi \tau_{r\theta}\Big|_{r=\frac{d_p}{2}} sin(\theta) \mathrm{d}A - \int_0^\pi p\Big|_{r=\frac{d_p}{2}} cos(\theta) \mathrm{d}A$$

$$\mathrm{d}A = \frac{1}{2}\pi {d_p}^2 sin\theta \mathrm{d}\theta$$

$$F = 2\pi\mu U d_p + \pi\mu U d_p = 3\pi\mu U d_p \tag{19}$$

The above result is the sphere drag formula of Stokes, consisting of two-thirds viscous force and one-third pressure force. The formula is strictly valid only for $Re \ll 1$. To include the particle dynamics, the differential equation governing the motion of the seed particles neglecting gravity is given by Equation 20. In this equation the inertia of the particles and the drag force are balanced.

$$m\frac{\partial U}{\partial t} + 3\pi\mu U d_p = 0 \tag{20}$$

The solution for the Equation 20 follows an exponential law, and under the given conditions of a step change of velocity the solution is as shown below and in Figure 110

$$U_p(t) = U \left[1 - exp\left(\frac{-t}{\tau_s} \right) \right] \tag{21}$$

with the relaxation time τ_s given by

$$\tau_s = d_p^2 \frac{\rho_p}{18\mu} \tag{22}$$

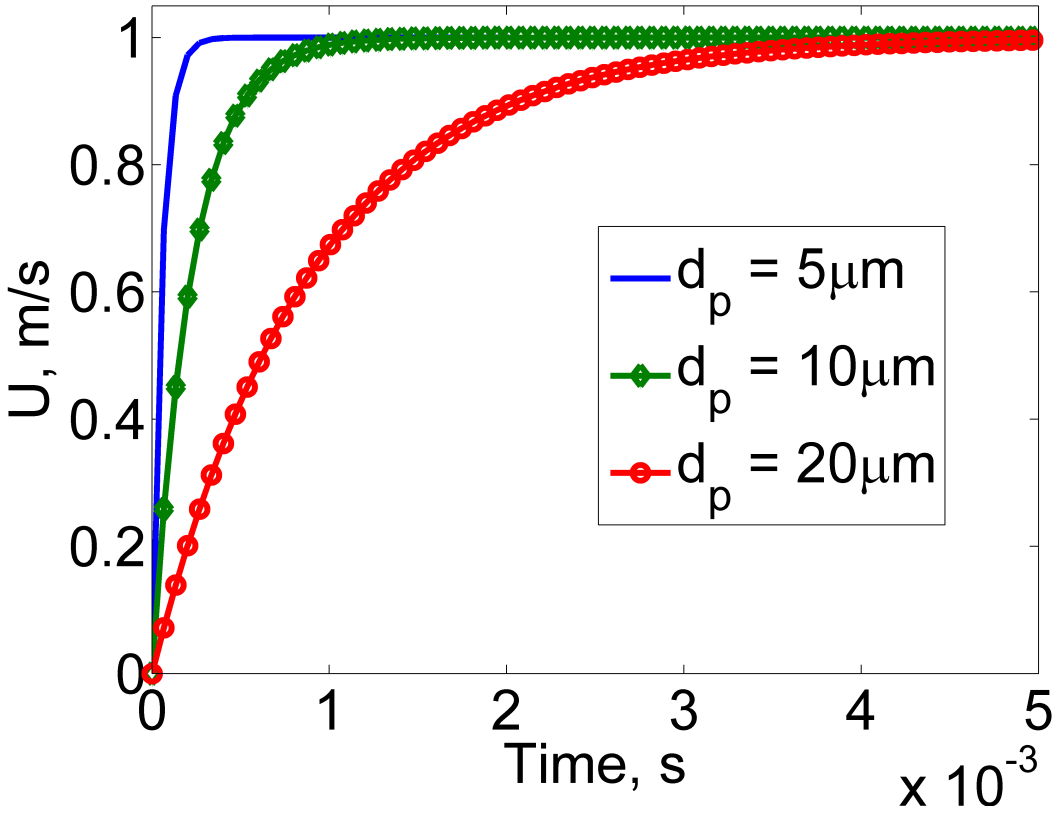

Figure 110: Seed particle response time for mineral oil of varying particle diameter

The characteristic time of the seed particles was determined from vorticity contours and compared to the the relaxation time for the seed particles. The characteristic time turned out be around 5-10 times that of the relaxation time, which indicates very small error in the measurements.

APPENDIX B

FREESTREAM TURBULENCE INTENSITY

The turbulence intensity of the John J Harper wind tunnel was measured using Constant Temperature Anemometry (CTA) (see section 1.5.5 for the details of the equipment used).

The hot-film probe was mounted on a traverse system to to automate the data measurement across the width of the test section. The data was initially recorded as voltages and then converted to velocities using the calibration coefficients. Both "raw" and "conditioned" voltage data were recorded at a sampling rate of 5,000 Hz for a total time of 30 seconds per recording. The raw data were conditioned by first passing it through a low pass filter set at 2,500 Hz then through a high pass filter set at 1 Hz and finally a 20 dB gain was applied to amplify the signal. The gain has been accounted for (removed) in the data presented in this work.

The raw data (mean flow velocity) is used to determine the calibration coefficients (see table 22) and the conditioned data (velocity fluctuations) is used to obtain energy spectra to deduce the turbulence intensity. The calibration coefficients are determined using the following expression:

$$E^2 = A + BU^n \tag{23}$$

where E is the measured voltage, U is the expected velocity, and A,B and n are constants tabulated for this experiment in Table 22, while figure 111 illustrates the calibration data acquired.

Table 22: Calibration coefficients for the hot-film used

Constant	Value
A	0.1952
B	1.2967
n	0.42

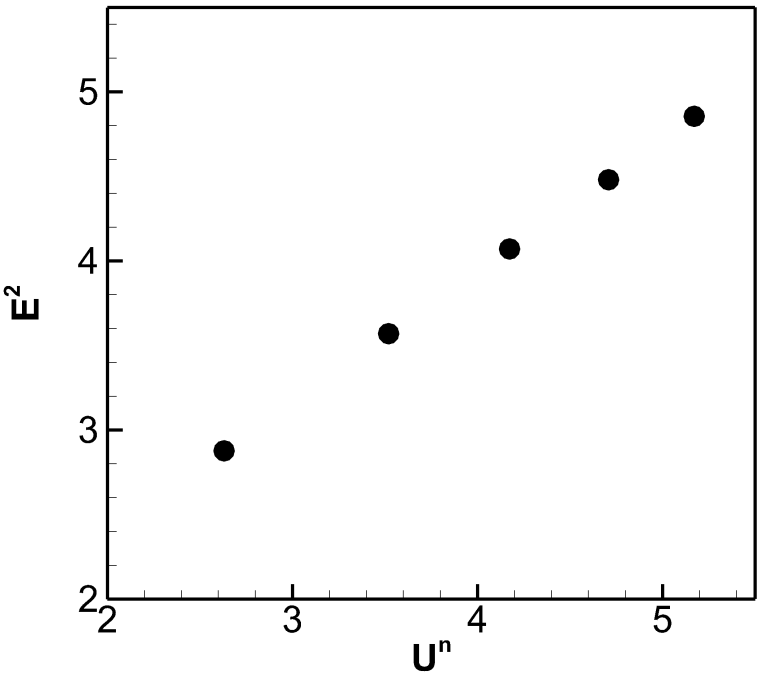

Figure 111: Calibration of the hotfilm used in the turbulence intensity measurements

Knowing the calibration coefficients, the fluctuation velocity is then determined using the following expression:

$$u_i = \left[\frac{2\bar{E}}{nB^{1/n} \left(\bar{E}^2 - A \right)^{\frac{n-1}{n}}} \right] e_i \tag{24}$$

where, E is the raw voltage and e is the conditioned voltage. The root mean square (RMS) velocity (u') is then calculated using the following expression:

$$u' = \sqrt{\frac{1}{N} \sum_{i=1}^{N} {u_i}^2} \tag{25}$$

The turbulence intensity defined as the ratio of the root mean square velocity (u') to the mean freestream (U) of the flow is the then computed using the following expression:

$$TI = \frac{u'}{U} \tag{26}$$

Figure 112 illustrates the power spectral density of the freestream at 22.35 m/s (50mph). Although, there are frequency spikes in the data at frequency greater than 1000 Hz, the contribution of those frequencies to the turbulence intensity is quite negligible.

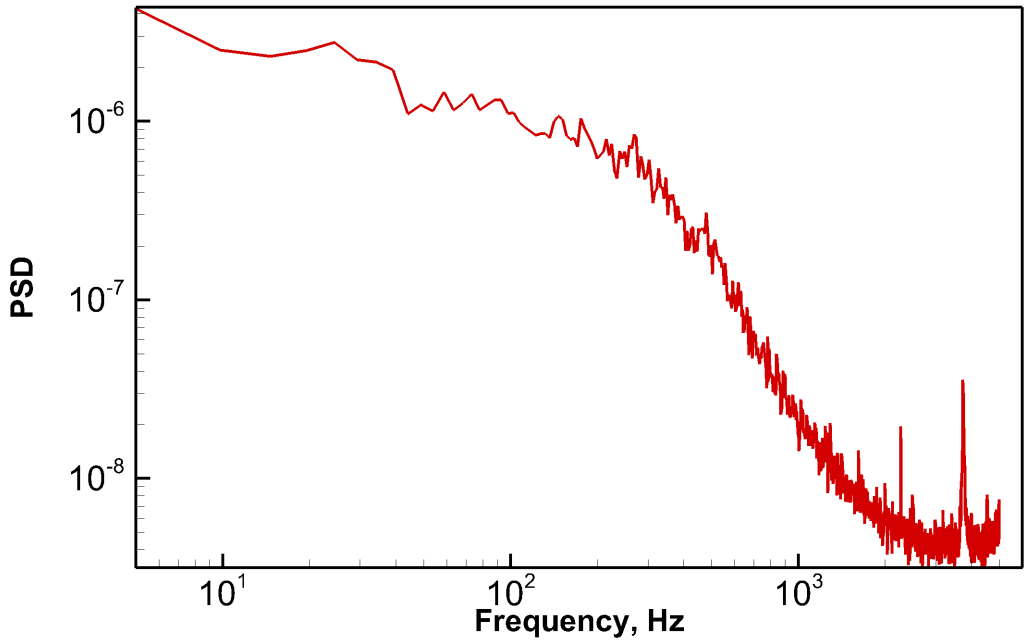

Figure 112: Power spectral density of the freestream at U_∞=22.35 m/s

APPENDIX C

WIND TURBINE CORRELATION

This section focuses on relating the occurrences on the rotor setup to a large HAWT. We start off with a discussion of the importance of dynamic stall on HAWT. Followed by a discussion of the similarities between the two cases, and the findings.

One limiter of the operating lifetime of horizontal axis wind turbines [100] is the dynamic loading on blades and generators, sometimes far in excess of their design loads [101]. This dynamic loading is attributed to variety of different sources such as unsteady aerodynamic effects, including dynamic inflow, turbulence, wind shear, and dynamic stall. These sources are suspected to be leading drivers of fatigue failure on a HAWT. However the problem of dynamic stall is of particular importance on wind turbines as the unsteady loads produced can be large enough to cause structural damage. It was showed that a 30% error in prediction of air load leads to a 70% decrease in life expectancy of a wind turbine [107]. Moreover large uncertainties still remain today in the prediction of dynamic stall air loads on a HAWT. It has been shown that two-dimensional data on oscillating airfoils from wind tunnel tests are insufficient to construct a good estimate of the structural loading on horizontal axis wind turbines [52]. Studies have showed that such data consistently under predict actual loading and power output [12]. Substantial differences in the pressure distribution of the inboard section of rotating wind turbine blades compared to 2-D models, preceding dynamic stall was reported [26]. Certain studies postulated structures and interactions responsible for these flow field enhancements.

The figure 113 shows the regime of flow that this work addresses and how it compares between the wind turbine case and the Georgia Tech rotor setup. A wind turbine - Grumman Wind Stream 33 Downwind HAWT, used by National Renewable Energy Laboratory in dynamic stall experiments [52] is compared to the experimental setup at Georgia Tech. For convenience of comparison to the rotor setup the azimuth angle ψ has been defined

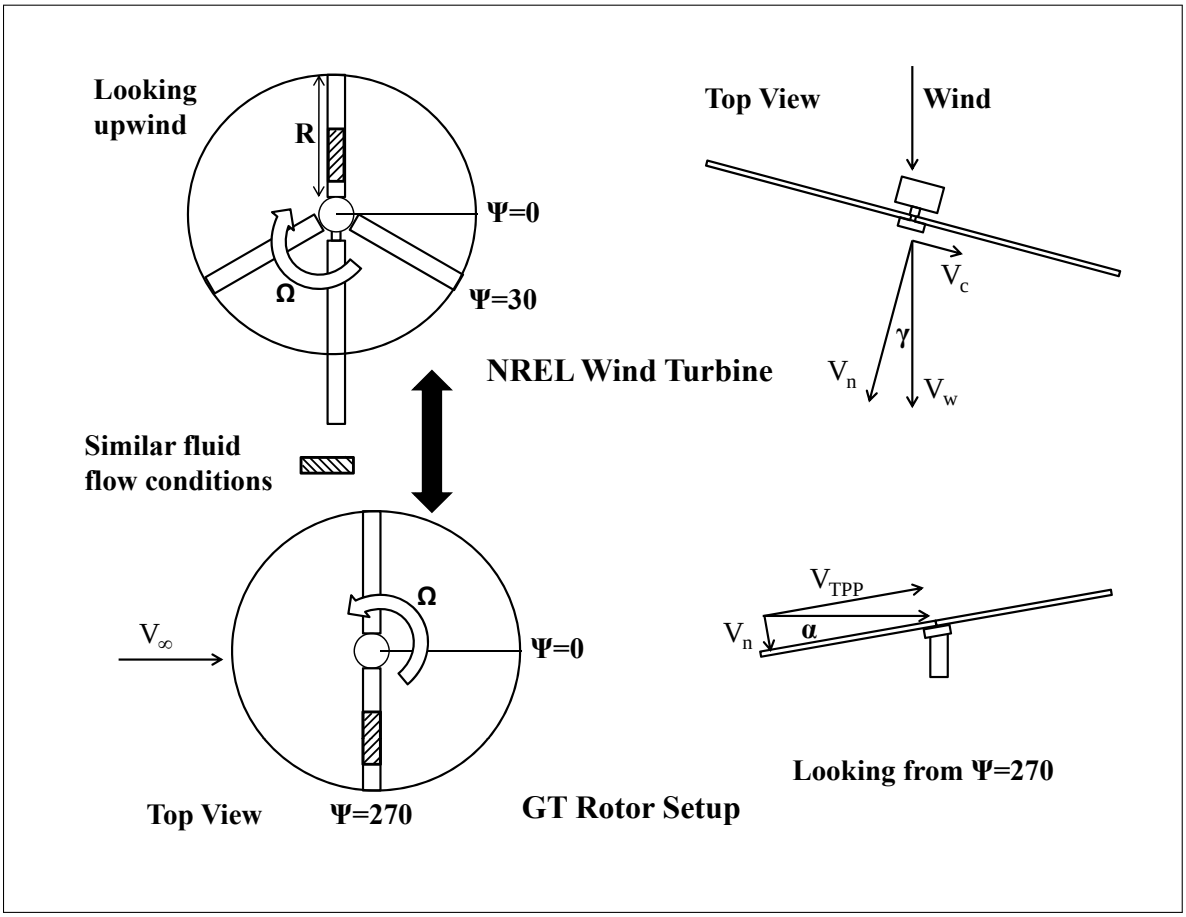

Figure 113: Schematic representation of similar fluid flow conditions.

differently than the regular convention. $\psi = 0$ starts at the right side of the turbine looking downwind.

To demonstrate similar fluid flow conditions over the rotating blades of the wind turbine and GT rotor setup, dynamic similarity parameters were defined and evaluated. They have been summarized in Table 23. The figure 114 illustrates the similarities in the dynamic parameters of tip speed ratio, reduced frequency and angle of attack. The experimental setup at the John Harper Wind Tunnel is in the same general operating regime as the wind turbine at yaw angles of $20° - 30°$.

Clearly the reduced frequencies and tip Speed ratios(as per the definition) are in the same regime. The angle of attack range that the blades experience is also observed to be comparable between both the setups. The main aim here was to show similar fluid flow

Table 23: Equations defining dynamic similarity parameters

- Tip Speed Ratio It was defined as the Ratio of local blade speed to the inplane component of velocity to the rotor.

$$TSR = \frac{\Omega r}{V_c} \tag{27}$$

- Angle of Attack

$$V_n = V_w \left(1 - a_o\right) \cos\gamma \tag{28}$$

a_o is a factor that accounts for deceleration of wind due to wind turbine operation(induced velocity).

$$V_c = V_w \sin\gamma \tag{29}$$

Tangential component of velocity to the blade is a function of the azimuth angle and defined as

$$V_t = \Omega r + V_c \sin\psi \tag{30}$$

Angle of attacks for the wind turbine blade(α_w) and the rotor setup(α_r) are then defined as

$$\phi_w = \arctan\frac{V_n}{V_t} \tag{31}$$

$$\alpha_w = \phi_w - \beta_w \tag{32}$$

$$\phi_r = \arctan\frac{V_i}{V_{t_r}} \tag{33}$$

V_{tr} is the tangential component of velocity to the blade in the rotor setup.

$$\alpha_r = \beta_r - \phi_r \tag{34}$$

- Reduced Frequency(ψ=270°)

$$\begin{aligned} k &= \frac{\omega_f c}{2U} \\ &= \frac{\Omega c}{2\left(\Omega r - U_\infty\right)} \\ &= \frac{c/2r}{\left(1 - U_\infty/\Omega r\right)} \end{aligned} \tag{35}$$

$\omega_f = \Omega$ for a teetering rotor

conditions giving rise to dynamic stall in each of the cases. Since the rotating blades in each case are subjected to the same conditions, the behavior and characteristics of the fluid

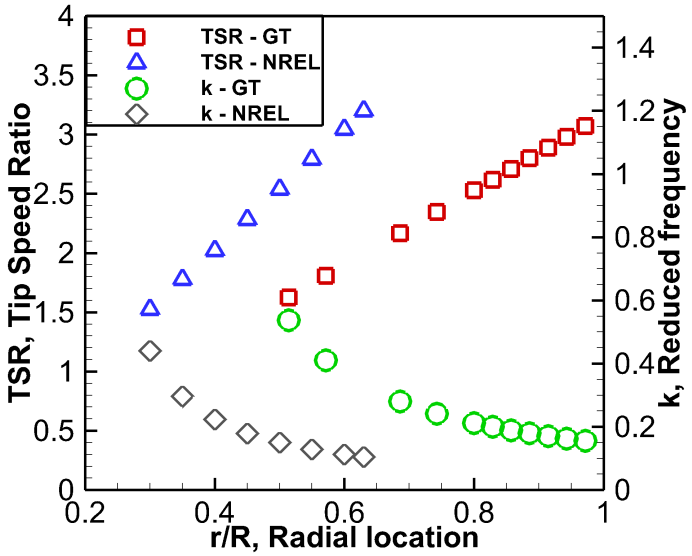

(a) Comparison of Tip Speed Ratio and Reduced Frequency at ψ=270° ($\gamma = 30°$ for wind turbine)

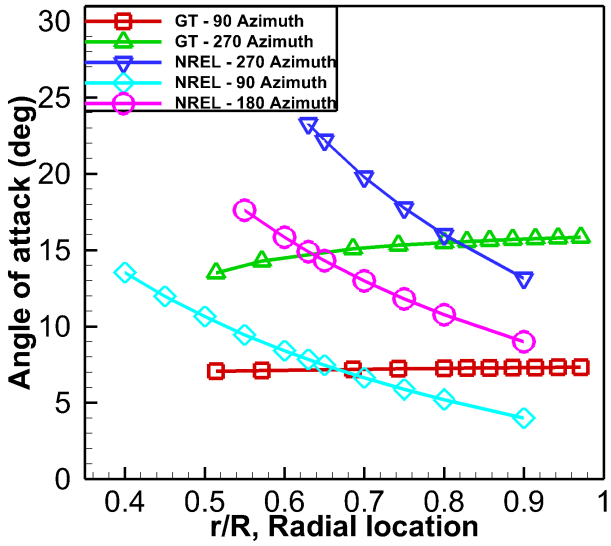

(b) Comparison of variation of Angle of Attack across the span at different Azimuths ($\gamma = 30°$) for wind turbine

Figure 114: Comparison of dynamic similarity parameters

flow over the blades should also be similar. In fact according to [25] the radial flow is more pronounced on the inboard sections of a wind turbine blade.

APPENDIX D

ADVANCED PIV DATA ANALYSIS TECHNIQUES

D.1 Vortex detection - Eulerian analysis

All the flows investigated in this work are surface flows which typically have high vorticity levels. In addition, there could be higher concentration of vorticity within a vortex occurring in the flow field. Detecting vortices in a flow is a challenge and using iso-vorticity contours to detect a vortex can yield itself to substantial errors. In addition in case of experimental data, especially PIV where experimental noise can effect of quality of data processing gradient based vortex detection methods perform poorly. For a comprehensive review of performance and robustness of gradient based vortex detection methods see e.g. [27, 54]. Most vortex identification criteria, such as vorticity concentration, λ_2, etc. require the evaluation of velocity field gradients and is there is susceptible to experimental noise.

However, vortex detection techniques proposed by Graftieaux et al. [40] via metrics such as Γ_1 and Γ_2 do not require the evaluation of gradients and is therefore less susceptible to experimental noise. Γ_1 is also called Normalized Angular Momentum (NAM). These functions are capable of characterizing the locations of the center and the boundary of the large-scale vortex, by considering only the topology of the velocity field and not its magnitude. In addition, the metrics proposed by Graftieaux et al. are in specific to identify a large scale vortex superposed on a small-scale turbulent velocity field. Which suits the requirements of vortex detection techniques required in this investigation. The following detailed description of the metrics is taken from Graftieaux et al.

D.1.1 The vortex center identification algorithm

If P is a fixed point in the measurement domain. The dimensionless scalar function Γ_1 at P is defined as:

$$\Gamma_1(P) = \frac{1}{S}\int_{M\in S} \frac{(PM \wedge U_M)\cdot z}{\|PM\|\cdot\|U_M\|} dS = \frac{1}{S}\int_S sin(\theta_M) dS \tag{36}$$

where S is a two dimensional area surrounding P, M lies in S and z is the unit vector normal to the measurement plane. θ_M represents the angle between the velocity vector U_M and radius vector PM. $|\Gamma_1|$ is bounded by 1.

For processing of PIV measurements where the velocity field is sampled at discrete spatial locations, S is a rectangular domain of fixed size and geometry, centered on P, and Γ_1 is then approximated by:

$$\Gamma_1(P) = \frac{1}{N}\sum_S \frac{(PM \wedge U_M)\cdot z}{\|PM\|\cdot\|U_M\|} = \frac{1}{N}\sum_S sin(\theta_M) \tag{37}$$

where N is the number of points M inside S. The parameter N plays the role of a spatial filter, but affects only weakly the location of maximum Γ_1. This location is determined by local maximum detection, based on a threshold computation. This definition of NAM is not Galilean invariant, but provides a simple and robust way to identify the locations of centers of vortical structures.

D.1.2 The vortex core identification algorithm

The vortex boundary identification method is derived from the previous algorithm and takes into account a local convection velocity U_P around P:

$$\Gamma_2(P) = \frac{1}{S}\int_{M\in S} \frac{[PM \wedge (U_M - U_P)]\cdot z}{\|PM\|\cdot\|U_M - U_P\|} dS \tag{38}$$

where $U_P = (1/S)\int_S U dS$. Note that in contrast to Γ_1, Γ_2 is Galilean invariant. Here, Galilean invariance holds the same meaning as in Newtonian mechanics - i.e. the laws of motion are the same in all inertial frames. Most vortical structures are essentially formed by the roll-up of shear layers and hence are composed of a multitude of small-scale vortices generated by a primary instability in the shear layers. The Γ_2 technique allows to identify these small-scale vortical structures within a larger vortical structure. Again for practical application, the approximation of Γ_2 is given by:

$$\Gamma_2(P) = \frac{1}{N} \sum_S \frac{[PM \wedge (U_M - U_P)] \cdot z}{\|PM\| \cdot \|U_M - U_P\|} \tag{39}$$

D.1.3 Validation of the algorithms

The validation for the algorithms was done by using the algorithm on a well known synthesized flow field with vortices of known strength placed in known locations. For this purpose a flow field with 6 Burgers vortices was generated. Figure 115(a) illustrates the synthesized flow field with six random burgers vortices. The vectors indicate the direction of the velocity and the color contour indicates the vorticity generated due to the vortices. Figure 115(b) illustrates the result obtained after computing NAM for the synthesized flow field with Burgers vortices.

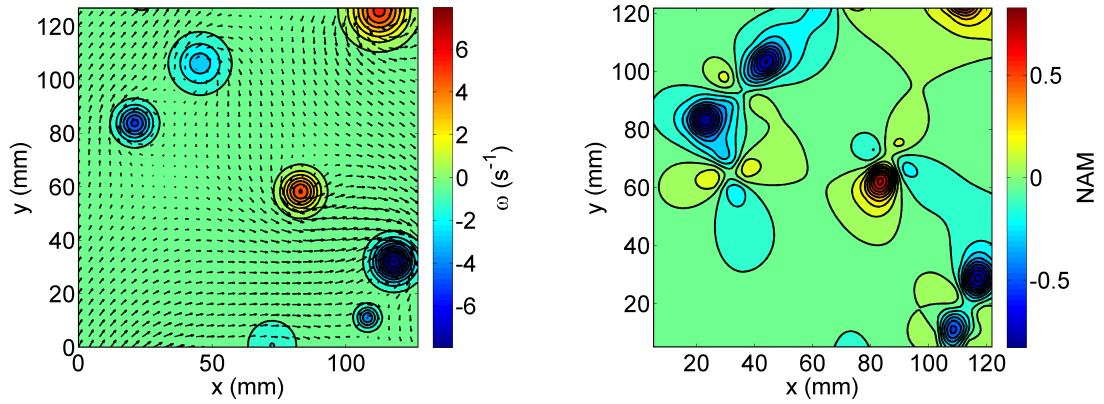

(a) Flow field synthesized with six Burgers Vortices (b) Γ_1 - Normalized Angular Momentum algorithm applied to the synthetic flow field

Figure 115: Validation of the Normalized Angular Momentum vortex identification technique (Γ_1)

D.2 Proper orthogonal decomposition (POD)

POD is a technique which extracts information via a statistical analysis of the velocity fields. The application of this technique can be done using two methods: the direct method [6] or the snapshot method [102]. Both these methods have been proven to have no significant differences as far as coherent structure analysis is concerned. Software provided by LaVision (Davis 8.0) was used to implement the POD technique for the velocity field. The

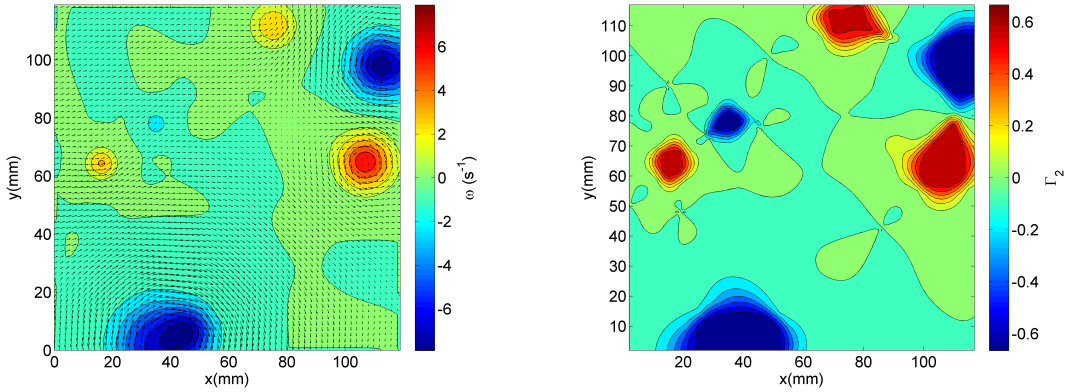

(a) Flow field synthesized with six Burgers Vortices (b) Γ_2 - Vortex core identification algorithm applied to the synthetic flow field

Figure 116: Validation of the vortex core identification technique (Γ_2)

software uses the snapshot technique since the velocity field is composed of a finite set of 'snapshots' sampled at discrete times and spatial locations. Typically, the POD proceeds in two steps: analysis and approximation.

D.2.1 Analysis

Given a set of N_p instantaneous velocity fields U_i, a correlation matrix $\mathbf{R}$ is first defined as the scalar product:

$$\mathbf{R}_{i,j} = \frac{1}{N_p} \int U_i(x).U_j(x)dx \tag{40}$$

Diagonalization of the matrix $\mathbf{R}$ yields N_p real positive eigenvalues λ_m, each which is associated with an eigenvector $\mathbf{V}_p$. If $\chi_k(x)$ is a linear combination of eigenvectors $\mathbf{V}_p$ and velocity fields $U_i(x)$, the spatial modes ϕ_k can be normalized to provide an orthonormal basis.

$$\phi_k(x) = \frac{\chi_k}{[(\chi_k, \chi_k)]^{1/2}} \tag{41}$$

here, λ_m is the contribution of the mode $\phi_m(x)$ to the energy of the flow. Equations 40 and 41 shows that the eigenmodes ϕ_m, called empirical eigenmodes, are deduced from a set of experimental snapshots U_i.

D.2.2 Approximation

Now the velocity fields are reconstructed as a linear superposition of modes, expressed as follows:

$$U_i = \sum_{j=1}^{N_p} a_{i,j}\phi_j \tag{42}$$

where the coefficient $a_{i,j}$ is obtained by projecting the raw velocity fields on the POD basis:

$$a_{i,j} = (U_i, \phi_j) \tag{43}$$

The POD exhibits some well known and interesting properties, *a*) The POD is optimal from an energetic point of view, and *b*) Both the original velocity fields and empirical eigenmodes respect the same boundary conditions.

REFERENCES

[1] Adrian, R. J., "Particle-imaging techniques for experimental fluid mechanics," *Annual review of fluid mechanics*, vol. 23, no. 1, pp. 261–304, 1991.

[2] Adrian, R. J., "Twenty Years of Particle Image Velocimetry," *Experiments in Fluids*, vol. 39, no. 2, pp. 159–169, 2005.

[3] Ahmed, S. and Chandrasekhara, M., "Reattachment studies of an oscillating airfoil dynamic stall flowfield," *AIAA journal*, vol. 32, no. 5, pp. 1006–1012, 1994.

[4] Bailey Jr, F. and Gustafson, F., "Observations in flight of the region of stalled flow over the blades of an autogiro rotor," tech. rep., DTIC Document, 1939.

[5] Banks, W. and Gadd, G., "Delaying effect of rotation on laminar separation," *AIAA journal*, vol. 1, no. 4, pp. 941–941, 1963.

[6] Berkooz, G., Holmes, P., and Lumley, J. L., "The proper orthogonal decomposition in the analysis of turbulent flows," *Annual review of fluid mechanics*, vol. 25, no. 1, pp. 539–575, 1993.

[7] Bousman, W. G., "A qualitative examination of dynamic stall from flight test data," *Journal of the American Helicopter Society*, vol. 43, no. 4, pp. 279–295, 1998.

[8] Bousman, W. G., "Evaluation of airfoil dynamic stall characteristics for maneuverability," *Journal of the American Helicopter Society*, vol. 46, no. 4, pp. 239–250, 2001.

[9] Bowles, P. O., *Wind Tunnel Experiments on the Effect of Compressibility on the Attributes of Dynamic Stall*. PhD thesis, 2012.

[10] Broeren, A. and Bragg, M., "Spanwise Variation in the Unsteady Stalling Flowfields of Two-dimensional Airfoil Models," *AIAA journal*, vol. 39, no. 9, pp. 1641–1651, 2001.

[11] Butterfield, C. P., "Aerodynamic pressure and flow-visualization measurement from a rotating wind turbine blade," tech. rep., Solar Energy Research Inst., Golden, CO (USA), 1988.

[12] Butterfield, C., Simms, D., Scott, G., and Hansen, A., "Dynamic Stall on Wind Turbine Blades," tech. rep., National Renewable Energy Lab., Golden, CO (United States), 1991.

[13] Carr, L., "Progress in analysis and prediction of dynamic stall," *Journal of aircraft*, vol. 25, no. 1, pp. 6–17, 1988.

[14] Carr, L. and Chandrasekhara, M., "Design and development of a compressible dynamic stall facility," *Journal of aircraft*, vol. 29, no. 3, pp. 314–318, 1992.

[15] Carr, L. and Chandrasekhara, M., "Compressibility Effects on Dynamic Stall," *Progress in Aerospace Sciences*, vol. 32, no. 6, pp. 523–573, 1996.

[16] Carr, L., Chandrasekhara, M., and Brock, N., "Quantitative study of unsteady compressible flow on an oscillating airfoil," *Journal of aircraft*, vol. 31, no. 4, pp. 892–898, 1994.

[17] Carr, L., McAlister, K., and McCroskey, W., "Analysis of the Development of Dynamic Stall Based on Oscillating Airfoil Experiments," 1977.

[18] Carta, F., "Dynamic Stall of Swept and Unswept Oscillating Wings," tech. rep., DTIC Document, 1985.

[19] Carta, F. O., *A comparison of the pitching and plunging response of an oscillating airfoil*, vol. 3172. National Aeronautics and Space Administration, Scientific and Technical Information Branch, 1979.

[20] Carter, J. and others, "Extreme mu rotor," Jan. 17 2006. US Patent 6,986,642.

[21] Chandrasekhara, M., "Interferometric Investigations of Compressible Dynamic Stall Over a Transiently Pitching Airfoil," tech. rep., DTIC Document, 1993.

[22] Charles, B. D. and Tanner, W. H., "Wind tunnel investigation of semirigid full-scale rotors operating at high advance ratios," tech. rep., DTIC Document, 1969.

[23] Cochran, W., "The flow due to a rotating disc," in *Mathematical Proceedings of the Cambridge Philosophical Society*, vol. 30, pp. 365–375, Cambridge Univ Press, 1934.

[24] Conlisk, A., "Modern helicopter aerodynamics," *Annual review of fluid mechanics*, vol. 29, no. 1, pp. 515–567, 1997.

[25] Corten, G., *Flow Separation on Wind Turbines Blades*. PhD thesis, University Utrecht, 2001.

[26] Coton, F., Wang, T., and Galbraith, R., "An Examination of Key Aerodynamic Modelling Issues Raised by the NREL Blind Comparison," *Wind Energy*, vol. 5, no. 2-3, pp. 199–212, 2002.

[27] Cucitore, R., Quadrio, M., and Baron, A., "On the effectiveness and limitations of local criteria for the identification of a vortex," *European Journal of Mechanics-B/Fluids*, vol. 18, no. 2, pp. 261–282, 1999.

[28] Datta, A., Yeo, H., and Norman, T. R., "Experimental investigation and fundamental understanding of a full-scale slowed rotor at high advance ratios," *Journal of the American Helicopter Society*, vol. 58, no. 2, pp. 1–17, 2013.

[29] DiOttavio, J., Watson, K., Cormey, J., Kondor, S., and Komerath, N., "Discrete Structures In The Radial Flow Over A Rotor Blade In Dynamic Stall," in *26th AIAA Applied Aerodynamics Conference*, August 2008.

[30] DiOttavio, J., Watson, K., Cormey, J., Komerath, N., and Kondor, S., "Discrete structures in the radial flow over a rotor blade in dynamic stall," in *Proceedings of the 26th applied aerodynamics conference, AIAA, Honolulu, Hawaii, USA*, 2008.

[31] Ekaterinaris, J. A. and Platzer, M. F., "Computational prediction of airfoil dynamic stall," *Progress in aerospace sciences*, vol. 33, no. 11-12, pp. 759–846, 1998.

[32] Ferreira, C. S., van Kuik, G., van Bussel, G., and Scarano, F., "Visualization by piv of dynamic stall on a vertical axis wind turbine," *Experiments in Fluids*, vol. 46, no. 1, pp. 97–108, 2009.

[33] Ferreira, C. S., Bijl, H., Van Bussel, G., and Van Kuik, G., "Simulating dynamic stall in a 2d vawt: Modeling strategy, verification and validation with particle image velocimetry data," in *Journal of Physics: Conference Series*, vol. 75, p. 012023, IOP Publishing, 2007.

[34] Fraunie, P., Beguier, C., Paraschivoiu, I., and Brochier, G., "Water channel experiments of dynamic stall on darrieus wind turbine blades," *Journal of Propulsion and Power*, vol. 2, no. 5, pp. 445–449, 1986.

[35] Fujisawa, N. and Takeuchi, M., "Flow visualization and piv measurement of flow field around a darrieus rotor in dynamic stall," *Journal of Visualization*, vol. 1, no. 4, pp. 379–386, 1999.

[36] Fujisawa, N. and Shibuya, S., "Observations of dynamic stall on darrieus wind turbine blades," *Journal of Wind Engineering and Industrial Aerodynamics*, vol. 89, no. 2, pp. 201–214, 2001.

[37] Gardner, A. and Richter, K., "Influence of rotation on dynamic stall," *Journal of the American Helicopter Society*, vol. 58, no. 3, pp. 1–9, 2013.

[38] Geissler, W. and Haselmeyer, H., "Investigation of dynamic stall onset," *Aerospace science and technology*, vol. 10, no. 7, pp. 590–600, 2006.

[39] Gollos, W., "Boundary layer drag for non-smooth surfaces," Tech. Rep. RM-1129, U.S. Air Force, 1953.

[40] Graftieaux, L., Michard, M., and Grosjean, N., "Combining piv, pod and vortex identification algorithms for the study of unsteady turbulent swirling flows," *Measurement Science and Technology*, vol. 12, no. 9, p. 1422, 2001.

[41] Green, R. and Galbraith, R. M., "Dynamic recovery to fully attached aerofoil flow from deep stall," *AIAA journal*, vol. 33, no. 8, pp. 1433–1440, 1995.

[42] Gregory, N., Quincey, V., O'Reilly, C., and Hall, D., "Progress Report on Observations of Three-Dimensional Flow Patterns obtained during stall development on aerofoils, and on the problem of measuring two-dimensional characteristics," *NPL Aero Report*, vol. 1309, 1970.

[43] Gregory, N., Stuart, J., and Walker, W., "On the stability of three-dimensional boundary layers with application to the flow due to a rotating disk," *Philosophical Transactions of the Royal Society of London. Series A, Mathematical and Physical Sciences*, vol. 248, no. 943, pp. 155–199, 1955.

[44] Gross, A., Fasel, H., Friederich, T., and Kloker, M., "Numerical Investigation of Rotational Augmentation for S822 Wind Turbine Airfoil," *Wind Energy*, 2010.

[45] Halfman, R. L., Johnson, H., and Haley, S., "Evaluation of high-angle-of-attack aerodynamic-derivative data and stall-flutter prediction techniques," tech. rep., DTIC Document, 1951.

[46] Haller, G., "Exact theory of unsteady separation for two-dimensional flows," *Journal of Fluid Mechanics*, vol. 512, pp. 257–311, 2004.

[47] Ham, N. D., "A stall flutter of helicopter rotor blades: A special case of the dynamic stall phenomenon," tech. rep., DTIC Document, 1967.

[48] Ham, N. D. and Garelick, M. S., "Dynamic stall considerations in helicopter rotors," *Journal of the American Helicopter Society*, vol. 13, no. 2, pp. 49–55, 1968.

[49] Ham, N. D. and Young, M., "Torsional oscillation of helicopter blades due to stall.," *Journal of Aircraft*, vol. 3, no. 3, pp. 218–224, 1966.

[50] Harris, F., "Rotor performance at high advance ratio; theory versus test," *NASA CR*, no. 215370, 2008.

[51] Himmelskamp, H., *Profiluntersuchungen an einem umlaufenden Propeller*. Max-Planck-Inst. f. Strömungsforschg [Auslfg auch], 1950.

[52] Huyer, S., Simms, D., and Robinson, M., "Unsteady Aerodynamics Associated with a Horizontal-Axis Wind Turbine," *AIAA journal*, vol. 34, no. 7, 1996.

[53] Jacobs, E. N. and Sherman, A., "Airfoil section characteristics as affected by variations of the reynolds number," Technical Report 586, National Advisory Committee for Aeronautics, 1937.

[54] Jeong, J. and Hussain, F., "On the identification of a vortex," *Journal of Fluid Mechanics*, vol. 285, no. 69, pp. 69–94, 1995.

[55] Jumper, E., Dimmick, R., and Allaire, A., "The effect of pitch location on dynamic stall," *Journal of fluids engineering*, vol. 111, no. 3, pp. 256–262, 1989.

[56] Kármán, V., "Über laminare und turbulente reibung," *ZAMM-Journal of Applied Mathematics and Mechanics/Zeitschrift für Angewandte Mathematik und Mechanik*, vol. 1, no. 4, pp. 233–252, 1921.

[57] Katzmayr, R., *Effect of periodic changes of angle of attack on behavior of airfoils*. National Advisory Committee for Aeronautics, 1922.

[58] Kobayashi, R. and Izumi, H., "Boundary-layer transition on a rotating cone in still fluid," *Journal of Fluid Mechanics*, vol. 127, no. -1, pp. 353–364, 1983.

[59] Kobayashi, R., Kohama, Y., and Takamadate, C., "Spiral vortices in boundary layer transition regime on a rotating disk," *Acta Mechanica*, vol. 35, no. 1, pp. 71–82, 1980.

[60] Koga, D. and Eaton, J., "Active Control of Unsteady and Separated Flow Structures," tech. rep., DTIC Document, 1989.

[61] Kohama, Y., "Some expectation on the mechanism of cross-flow instability in a swept wing flow," *Acta mechanica*, vol. 66, no. 1, pp. 21–38, 1987.

[62] Kohama, Y. and Kobayashi, R., "Boundary-layer transition and the behaviour of spiral vortices on rotating spheres," *Journal of Fluid Mechanics*, vol. 137, no. -1, pp. 153–164, 1983.

[63] Kohlman, D. and Wentz, W., "Vortex breakdown on slender sharp-edged wings," *Journal of Aircraft*, vol. 8, no. 3, pp. 156–161, 1971.

[64] Kramer, M., "Increase in the maximum lift of an airfoil due to a sudden increase in its effective angle of attack resulting from a gust," Technical Report TM-678, NASA, 1932.

[65] Larsen, J., Nielsen, S., and Krenk, S., "Dynamic Stall Model for Wind Turbine Airfoils," *Journal of Fluids and Structures*, vol. 23, no. 7, pp. 959–982, 2007.

[66] Lawson, N. and Wu, J., "Three-dimensional particle image velocimetry: experimental error analysis of a digital angular stereoscopic system," *Measurement Science and Technology*, vol. 8, no. 12, p. 1455, 1997.

[67] Leishman, J. G., *Principles of helicopter aerodynamics*. Cambridge University Press, 2006.

[68] Liiva, J. and Davenport, F. J., "Dynamic stall of airfoil sections for high-speed rotors," *Journal of the American Helicopter Society*, vol. 14, no. 2, pp. 26–33, 1969.

[69] Lingwood, R., "An experimental study of absolute instability of the rotating-disk boundary-layer flow," *Journal of Fluid Mechanics*, vol. 314, no. -1, pp. 373–405, 1996.

[70] Lorber, P., "Dynamic Stall of Sinusoidally Oscillating Three-Dimensional Swept and Unswept Wings in Compressible Flow," in *AHS, Annual Forum, 48 th, Washington, Proceedings.*, vol. 2, pp. 1307–1322, 1992.

[71] MacCloud, J. L., Biggers, J. C., and Stroub, R. H., *An Investigation of Full-Scale Helicopter Rotors at High Advance Ratios and Advancing Tip Mach Numbers*. National Aeronautics and Space Administration, 1968.

[72] Malik, M. R., Wilkinson, S. P., and Orszag, S. A., "Instability and transition in rotating disk flow," *AIAA Journal*, vol. 19, no. 9, pp. 1131–1138, 1981.

[73] McAlister, K., Pucci, S., McCroskey, W., and Carr, L., "An experimental study of dynamic stall on advanced airfoil sections. volume 2. pressure and force data.," tech. rep., DTIC Document, 1982.

[74] McCroskey, W., "Measurements of Boundary Layer Transition, Separation and Streamline Direction on Rotating Blades," *NASA TN D-6321*, 1971.

[75] McCroskey, W., Carr, L., and McAlister, K., "Dynamic Stall Experiments on Oscillating Airfoils," *AIAA Journal*, vol. 14, no. 1, pp. 57–63, 1976.

[76] McCroskey, W. and Fisher, R. K., "Detailed aerodynamic measurements on a model rotor in the blade stall regime," *Journal of the American Helicopter Society*, vol. 17, no. 1, pp. 20–30, 1972.

[77] McCroskey, W., McAlister, K., Carr, L., and Pucci, S., "An Experimental Study of Dynamic Stall on Advanced Airfoil Sections. Volume 1: Summary of the experiment," *NASA Technical Memorandum*, no. TM 84245, 1982.

[78] McCroskey, W., McAlister, K., Carr, L., Pucci, S., Lambert, O., Indergrand, R., and others, "Dynamic Stall on Advanced Airfoil Sections," *Journal of the American Helicopter Society*, vol. 26, p. 40, 1981.

[79] McCroskey, W. and Yaggy, P., "Laminar Boundary Layers on Helicopter Rotors in Forward Flight," *AIAA JOURNAL*, vol. 6, pp. 1919–1926, 1968.

[80] Meunier, M., "Simulation and Optimization of Flow Control Strategies for Novel High-Lift Configurations," *AIAA journal.*, vol. 47, no. 5, pp. 1145–1157, 2009.

[81] Mulleners, K., Kindler, K., and Raffel, M., "Dynamic stall on a fully equipped helicopter model," *Aerospace Science and Technology*, vol. 19, pp. 72–76, June 2012.

[82] Mulleners, K. and Raffel, M., "The onset of dynamic stall revisited," *Experiments in fluids*, vol. 52, no. 3, pp. 779–793, 2012.

[83] Ol, M. V., Bernal, L., Kang, C.-K., and Shyy, W., "Shallow and deep dynamic stall for flapping low reynolds number airfoils," in *Animal Locomotion*, pp. 321–339, Springer, 2010.

[84] Payne, F., *Structure of leading-edge vortex flows including vortex breakdown.* PhD thesis, University of Notre Dame, May 1987.

[85] Perry, F., "Aerodynamics of the helicopter world speed record," in *The American Helicopter Society 43rd Annual Forum Proceedings*, (Alexandria, VA), May 18–20 1987.

[86] Potsdam, M., Datta, A., and Jayaraman, B., "Computational investigation and fundamental understanding of a slowed uh-60a rotor at high advance ratios," in *American Helicopter Society 68th Annual Forum, Fort Worth, TX*, 2012.

[87] Potts, J. R. and Crowther, W. J., "The flow over a rotating disc-wing," in *RAeS Aerodynamics Research Conference Proc., London, UK*, 2000.

[88] Prasad, A., "Particle image velocimetry," *CURRENT SCIENCE-BANGALORE-*, vol. 79, no. 1, pp. 51–60, 2000.

[89] Prasad, A. and Adrian, R., "Stereoscopic particle image velocimetry applied to liquid flows," *Experiments in Fluids*, vol. 15, no. 1, pp. 49–60, 1993.

[90] Raffel, M., Kompenhans, J., and Wernert, P., "Investigation of the unsteady flow velocity field above an airfoil pitching under deep dynamic stall conditions," *Experiments in Fluids*, vol. 19, no. 2, pp. 103–111, 1995.

[91] Raffel, M., Richard, H., Ehrenfried, K., Van der Wall, B., Burley, C., Beaumier, P., McAlister, K., and Pengel, K., "Recording and Evaluation Methods of PIV Investigations on a Helicopter rotor model," *Experiments in fluids*, vol. 36, no. 1, pp. 146–156, 2004.

[92] Raffel, M., Willert, C. E., and Kompenhans, J., *Particle Image Velocimetry: A Practical Guide; with 24 Tables*. Springer, 1998.

[93] Raghav, V., Richards, P., Komerath, N., and Smith, M., "An exploration of the physics of dynamic stall," in *Proceedings of AHS Aeromechanics Specialists Conference, AHS, San Francisco, CA, USA*, 2010.

[94] Raghav, V. and Komerath, N., "An exploration of radial flow on a rotating blade in retreating blade stall," *Journal of the American Helicopter Society*, vol. 58, no. 2, 2013.

[95] Robinson, M., Hand, M., Simms, D., and Schreck, S., "Horizontal Axis Wind Turbine Aerodynamics: Three-Dimensional, Unsteady, and Separated Flow Influences," in *Presented at the 3rd ASME/JSME Joint Fluids Engineering Conference, San Francisco, CA (US), 07/18/1999–07/23/1999*, Citeseer, 1999.

[96] Schlichting, H. and Gersten, K., *Boundary-layer theory*. Springer Verlag, 2000.

[97] Schreck, S. and Robinson, M., "Blade Three-Dimensional Dynamic Stall Response to Wind Turbine Operating Condition," *Journal of Solar Energy Engineering*, vol. 127, pp. 488–495, 2005.

[98] Schreck, S., Robinson, M., Hand, M., and Simms, D., "Hawt dynamic stall response asymmetries under yawed flow conditions," *Wind Energy*, vol. 3, no. 4, pp. 215–232, 2000.

[99] Sears, W. and Telionis, D., "Boundary-layer separation in unsteady flow," *SIAM Journal on Applied Mathematics*, vol. 28, no. 1, pp. 215–235, 1975.

[100] Shipley, D., Miller, M., and Robinson, M., "Dynamic Stall Occurrence on a Horizontal Axis Wind Turbine Blade," tech. rep., National Renewable Energy Lab., Golden, CO (United States), 1995.

[101] Shipley, D., Miller, M., Robinson, M., Luttges, M., and Simms, D., "Evidence that Aerodynamic Effects, Including Dynamic Stall, Dictate HAWT Structural Loads and Power Generation in Highly Transient Time Frames," in *Presented at the American Wind Energy Association Annual Conference and Exhibition, Minneapolis, MN, 9-13 May 1994*, pp. 9–13, 1994.

[102] Sirovich, L., "Turbulence and the dynamics of coherent structures. i-coherent structures. ii-symmetries and transformations. iii-dynamics and scaling," *Quarterly of applied mathematics*, vol. 45, pp. 561–571, 1987.

[103] Spentzos, A., Barakos, G., Badcock, K., Richards, B., Wernert, P., Schreck, S., and Raffel, M., "Investigation of three-dimensional dynamic stall using computational fluid dynamics," *AIAA journal*, vol. 43, no. 5, pp. 1023–1033, 2005.

[104] Surana, A., Jacobs, G. B., Grunberg, O., and Haller, G., "An exact theory of three-dimensional fixed separation in unsteady flows," *Physics of Fluids*, vol. 20, p. 107101, 2008.

[105] Van Dommelen, L. and Shen, S., "The Genesis of Separation," in *Symposium on Numerical and Physical Aspects of Aerodynamic Flows*, 1981.

[106] Varley, F., "Effects of impeller design and surface roughness on the performance of centrifugal pumps," *Proceedings of the Institution of Mechanical Engineers*, vol. 175, no. 1, pp. 955–989, 1961.

[107] Veers, P., "The Effect of Aerodynamics Analysis on Fatigue Life Estimation," in *Wind Turbine Aerodynamics Seminar*, 1985 - March 26-29.

[108] Walsh, D., Weiner, S., Arifian, K., Lawrence, T., Wilson, M., Millott, T., and Blackwell, R., "High Airspeed Testing of the Sikorsky X2 Technology™ Demonstrator," in *The American Helicopter Society 67th Annual Forum Proceedings*, 2011.

[109] Weihs, D. and Katz, J., "Cellular Patterns in Poststall Flow over Unswept Wings," *AIAA journal*, vol. 21, no. 12, pp. 1757–1759, 1983.

[110] Wernert, P., Koerber, G., Wietrich, F., Raffel, M., and Kompenhans, J., "Demonstration by piv of the non-reproducibility of the flow field around an airfoil pitching under deep dynamic stall conditions and consequences thereof," *Aerospace science and technology*, vol. 1, no. 2, pp. 125–135, 1997.

[111] Wheatley, J. B. and Hood, M. J., "Full-scale wind-tunnel tests of a pca-2 autogiro rotor," 1935.

[112] Winkelman, A. and Barlow, J., "Flowfield Model for a Rectangular Planform Wing Beyond Stall," *AIAA Journal*, vol. 18, pp. 1006–1008, 1980.

[113] Yang, J., Balakrishnan, G., and Komerath, N., "Radial Flow Measurements Downstream of Forced Dynamic Separation on a Rotor Blade," in *36 th Fluid Dynamics Conference and Exhibit, AIAA, AIAA Paper*, vol. 3377, 2006.

[114] Yeo, H., "Investigation of uh-60a rotor performance and loads at high advance ratios," *Journal of Aircraft*, vol. 50, no. 2, pp. 576–589, 2012.

[115] Yon, S., *Coherent Structures in the Wake of a Stalled Rectangular Wing*. PhD thesis, University of California, San Diego and San Diego State University, 1995.

[116] Yon, S. and Katz, J., "Cellular Structures in the Flow Over the Flap of a Two-Element Wing," *Journal of aircraft*, vol. 35, no. 2, pp. 230–232, 1998.

[117] Zoueshtiagh, F., Ali, R., Colley, A., Thomas, P. J., and Carpenter, P. W., "Laminar-turbulent boundary-layer transition over a rough rotating disk," *Physics of Fluids*, vol. 15, p. 2441, 2003.

VITA

Vrishank Raghav S was born in Bangalore, India. Raised with his sister Parimala, he completed his schooling at National Public School - Rajajinagar, Bangalore between 1990–2004. He then graduated from National Institute of Technology - Warangal, India, with a Bachelor of Technology degree in Mechanical Engineering in 2008. He was recognized for his overall achievements during his bachelors degree with the Outstanding Senior Award at NIT - Warangal. In 2008 he secured an admission in the graduate program at Georgia Institute of Technology in the School of Aerospace Engineering. He spent most of his time in the basement of the Guggenheim Building where he conducted and supervised wind tunnel experiments. In 2010 he received a Master of Science degree in Aerospace Engineering from Georgia Tech. He is the recipient of the Vertical Flight Foundation (VFF) Scholarship in 2010, the United Technologies Research Center (UTRC) Fellowship in 2011, and the Robert Wolfe Fellowship in 2012. While at Georgia Tech, he also pursued a Master in Business Administration degree between 2011 and 2012. In the Fall of 2013 he presented his dissertation and in the Spring of 2014 he was awarded his Doctor of Philosophy degree at Georgia Institute of Technology in Aerospace Engineering.